NTNU

The Norwegian University of Science and Technology
Norges teknisk-naturvitenskapelige universitet

Report no.
2002:09
Classification
Open

POSTAL ADDRESS
NTNU
DEPARTMENT OF THERMAL ENERGY AND HYDROPOWER
Kolbjørn Hejes vei 1A
N-7491 TRONDHEIM

TELEPHONE
Switchboard NTNU: +47 73 59 40 00
Department office: +47 73 59 27 00
Hydropower section: +47 73 59 38 57

TELEFAX
Department office: +47 73 59 83 90
Hydropower section: +47 73 59 38 54

Title of report	Date
Shock tube experiments on nitromethane and Promotion of chemical reactions by non-thermal plasma	03.06.2002
	No. of pages/appendixes 328
Author Morten Seljeskog	Project manager Otto K. Sønju
Division Faculty of Engineering Science and Technology Department of Thermal Energy and Hydropower	Project no.
ISBN nr. 82-471-5464-1	Price group

Client/sponsor of project	Client's ref.
The Norwegian Defense Construction service, TOTAL Norge AS, Elf Petroleum Norge AS	

Abstract

This dissertation was undertaken to study two different subjects both related to molecular decomposition by applying a shock tube and non-thermal plasma to decompose selected hydrocarbons. The first approach to molecular decomposition concerned thermal decomposition and oxidation of highly diluted nitromethane (NM) in a shock tube. Reflected shock tube experiments on NM decomposition, using mixtures of 0.2 to 1.5 vol% NM in nitrogen or argon were performed over the temperature range 850-1550 K and pressure range 190-900 kPa, with 46 experiments diluted in nitrogen and 44 diluted in argon. By residual error analysis of the measured decomposition profiles it was found that NM decomposition ($CH_3NO_2 + M \rightarrow CH_3 + NO_2 + M$, where M = N_2 /Ar) corresponds well to a law of first order. Arrhenius expressions corresponding to NM diluted either in N_2 or in Ar were found as $k_{N2} = 10^{17.011} \times \exp(-182.6$ kJ/mole / R×T) <cm^3/mole×s> and $k_{Ar} = 10^{17.574} \times \exp(-207$ kJ/mole / R×T) <cm^3/mole×s>, respectively. A new reaction mechanism was then proposed, based on new experimental data for NM decomposition both in Ar and N_2 and on three previously developed mechanisms. The new mechanism predicts well the decomposition of NM diluted in both N_2 and Ar within the pressure and temperature range covered by the experiments.

In parallel to, and following the decomposition experiments, oxidative experiments on the ignition delay times of NM/O_2/Ar mixtures were investigated over high temperature and low to high pressure ranges. These experiments were carried out with eight different mixtures of gaseous NM and oxygen diluted in argon, with pressures ranging between 44.3-600 kPa, and temperatures ranging between 842-1378 K. The oxidation experiments were divided into different categories according to the type of decomposition signals achieved. For signals with and without emission, the apparent quasi-constant activation energy was found from the correlations, to be 64.574 kJ/mol and 113.544 kJ/mol, respectively. The correlations for the ignition delay for time signals with and without emission were deduced as $\tau_{emission} = 0.3669 \times 10^{-2} \times [NM]^{-1.02}[O_2]^{-1.08} \times [Ar]^{1.42} \times \exp(7767/T)$ and $\tau_{no\ emission} = 0.3005 \times 10^{-2} \times [NM]^{-0.28}[O_2]^{0.12} \times [Ar]^{-0.59} \times \exp(13657/T)$, respectively.

The second approach to molecular decomposition concerned the application of non-thermal plasma to initiate reactions and decompose/oxidize selected hydrocarbons, methane and propane, in air. Experiments with a gliding arc discharge device were performed at the university of Orléans on the decomposition/reforming of low-to-stoichiometric concentration air/CH_4 mixtures. The presented results show that complete reduction of methane could be obtained if the residence time in the reactor was sufficiently long. The products of the methane decomposition were mainly CO_2, CO and H_2O. The CH_4 conversion rate showed to increase with increasing residence time, temperature of the operating gas, and initial concentration of methane. To achieve complete decomposition of CH_4 in 1 m^3 of a 2 vol% mixture, the energy cost was about 1.5 kWh. However, the formation of both CO and NO_x in the present gliding discharge system was found to be significant. The produced amount of both CO (0.4-1 vol%) and NO_x (2000-3500 ppm) were in such high quantities that they would constitute an important pollution threat if this process as of today was to be used in large scale CH_4 decomposition.

Further experimental investigations were performed on self-built laboratory scale, single- and double dielectric-barrier discharge devices as a means of removing CH_4 and C_3H_8 from simulated reactive inlet mixtures. The different discharge reactors were all powered by an arrangement of commercially available Tesla coil units capable of high-voltage high-frequency output. The results from each of the different experiments are limited and sometimes only qualitative, but show a tendency that the both CH_4 and C_3H_8 are reduced in a matter of a 3-6 min. retention time. The most plausible mechanism for explaining the current achievements is the decomposition by direct electron impact.

	Indexing Terms: English	Indexing Terms: Norwegian
Group 1	Nitromethane decomposition	Nitrometane dekomponering
Group 2	Non-thermal plasma	Kaldt plasma
Selected by author	Nitromethane reaction mechanism	Nitrometane reaksjonsmekanisme
	Hydrocarbon decomposition	Hydrokarbon dekomponering

URN:NBN:no-3311

URN:NBN:no-3311

SHOCK TUBE EXPERIMENTS ON NITROMETHANE

AND

PROMOTION OF CHEMICAL REACTIONS BY NON-THERMAL PLASMA

By

Morten Seljeskog

A dissertation submitted for the degree of doktor ingeniør

Department of Thermal Energy and Hydropower

Norwegian University of Science and Technology

Submitted June 2002

URN:NBN:no-3311

URN:NBN:no-3311

SUMMARY

This dissertation was undertaken to study two different subjects both related to molecular decomposition by applying a shock tube and non-thermal plasma to decompose selected hydrocarbons. The first approach to molecular decomposition concerned thermal decomposition and oxidation of highly diluted nitromethane in a shock tube. The basic physical and chemical properties for nitromethane are reported together with some theory on nitromethane detonation structure, ignition process and the effect of additives on these parameters. The experimental part covered the calibration of experimental apparatus, UV spectrum analysis and shock tube experiments. Reflected shock experiments on nitromethane decomposition were studied. The experiments were performed in the transient region, which is in the region between pressure dependent and independent rate constants. By residual error analysis of the measured decomposition profiles, it was found that nitromethane decomposition corresponds well enough to a law of first order.

In this work, a new reaction mechanism is proposed, based on new experimental data for NM decomposition both in Ar and N_2. The new mechanism was based on three previously developed mechanisms. Arrhenius expressions were derived for the nitromethane decomposition at different wavelengths and diluents. These were derived from the plot of the best exponential fit of the experimental k-values versus the inverse of the temperature in the reflected shock. By comparing the experimental against the calculated results it was indeed clarified that decomposition of highly diluted nitromethane at higher temperature conditions could be explained by the unimolecular third body dissociation reaction alone.

Computer simulations of the thermal nitromethane decomposition were used to verify that the reaction mechanism indeed initiates through the third body decomposition of the nitromethane molecule as stated by previous authors. Three previously proposed reaction mechanisms were compared against the experimental data and used as basis for the simulations. After the decomposition of the nitromethane molecule the reaction proceeds by two major and parallel pathways, which both include radical reactions, to produce CH_2O. The latter acting as a source for further radicals when attacked by existing OH and H radicals, producing HCO radicals that will carry the reactions to completion. The simulated profiles corresponded well with those obtained experimentally.

URN:NBN:no-3311

Following the decomposition experiments, oxidative experiments on the ignition delay times of $CH_3NO_2/O_2/Ar$ mixtures were investigated over high temperature and low to high pressure ranges. These experiments were carried out with eight different mixtures of gaseous nitromethane and oxygen diluted in argon. The oxidation experiments were divided into three different types according to the type of decomposition signals achieved. For signals with emission and for slightly or non-diluted mixtures the apparent quasi-constant activation energy was found from experimental correlations. When the molar fraction of argon tends to unity and for slightly diluted mixtures, a different correlation was derived. A quasi-constant activation energy (ΔE) was also deduced from these correlations.

The second approach to molecular decomposition concerned the application of non-thermal plasma to initiate reactions and decompose/oxidize selected hydrocarbons, methane and propane, in air and was sectioned into one theoretical and two experimental parts. In such discharges, chemical change is driven by a variety of processes including ionization, molecular excitation, ion-electron recombination, fragmentation of ions and excited molecules, and reactions of radicals, atoms, and ions.

The first experimental section on non-thermal plasma was performed at the university of Orléans and covered a theoretical survey and experimental work done on the decomposition/reforming of low-to-stoichiometric concentration air/methane mixtures in a gliding arc discharge device. The basic theory and physical description of a gliding arc device are reported. Through experiments it was found that important quantities of NO_x were formed. When the discharge was run in pure air, the maximum concentration was achieved at the lowest flow-rate. Maximum NO_x concentration when cooling the reactor unit with either air or water, showed no significant differences. The NO_x production was found to be linear proportional to the air flow rate through the reactor, the highest flow rate giving the lowest NO_x concentrations. At lower flow rates the residence time increased and more energy was distributed to the reacting volume resulting in higher temperature and thereby higher chemical activity and faster conversion to final products. The maximum amount of NO_x produced was the same for both the air- and water-cooled reactor. Further, low-concentration methane in air was decomposed in the same reactor at varying residence times, the main products being CO_2 and CO (and H_2O, observed by not quantified). The CH_4 conversion rate was observed to increase with increasing residence

time in the reactor (decreasing flow rate). The experiments indicated that the CH_4 conversion increased with increasing CH_4 concentration, thus confirming experiments by previous authors. As for the pure-air experiments, important quantities of NO_x was formed. Because of the methane content additional CO was produced. The NO_x concentration showed to increase with increasing residence time but with an insignificant difference for different methane concentrations. It was observed that when the methane concentration passed the lower flammability limit, important quantities of condensate was formed.

The second experimental section on non-thermal plasma was performed at the Norwegian University of Science and Technology. Here, an experimental investigation was performed on a laboratory scale, single- and double dielectric-barrier discharge device as a means of removing CH_4 and C_3H_8 from a simulated reactive mixture inlet stream. The different discharge reactors were all powered by an arrangement of commercially available Tesla coil units capable of high-voltage high-frequency output. The results from each of the different experiments are limited and sometimes only qualitative, but show a tendency that the both CH_4 and C_3H_8 are reduced in a matter of a 3-6 *min.* retention time. The most plausible mechanism for explaining the current achievements is the decomposition by direct electron impact. The slow rate of decomposition can be attributed to the hydrocarbons being diluted in air and that much of the electrical energy therefore may have been wasted in producing unused radicals of the carrier gas. The initial experiments on ignition and flame propagation were performed on stoichiometric mixtures of CH_4 and C_3H_8 in air in a wire-to-plane reactor. By theory, the gas discharge would produce both high energy electrons and free radicals which could break up and decompose the hydrocarbon molecules. From the visual observations of flame propagation there were no measurable effects on the propagation velocity when this occurred. These experiments were more of a qualitative approach, with results of type; propagation occurred = YES and no propagation = NO, were no propagation was attributed to the effect of hydrocarbon decomposition by electron impact dissociation. The results showed that there was no distinct limit between when ignition and propagation occurred and not. With C_3H_8 and run times from 3.5 *min.* and upwards, experiments where no propagation was observed, started to occur. The mean run time for experiments with no propagation was found to 4.3 *min*. This could indicate that at least some of the

C_3H_8 had been completely or partly decomposed (or otherwise affected), so that the mixture was no longer flammable. The same pattern was found for the CH_4 mixture, with a necessary mean run time of 5.1 *min.* for experiments with no propagation to occur. Since direct electron impact dissociation is a slower process in diluted mixtures, we can presume that this mechanism was the most probable cause for the currently achieved results.

To actually quantify the capability of the barrier discharge to decompose either C_3H_8 or CH_4 in air, recycling circuit of tubes was set up. Experiments in a double parallel plate reactor were performed. A stoichiometric mixture of C_3H_8 in air was run in a loop for different periods of time. According to these results, very little change in composition had occurred, only some minor decrease in C_3H_8-concentration could be observed with increasing run-times. These indications of only very slow or non-existent decomposition can probably again be attributed to the direct electron impact dissociation. Further experiments were performed on stoichiometric CH_4 mixtures in a double annular reactor using the same loop as previously mentioned. This time ambient air was used, containing some amount of water vapour. The aim with this was to see if the assumed effect of radical production from H_2O would improve the rate of decomposition. These results showed some similar behaviour as for the results obtained with the wire-to-plane reactor. Complete removal of CH_4 was achieved after 5-6 *min.* in the discharge loop. This new double annular reactor seemed to be more effective compared to the previous double parallel plate reactor, where almost no decomposition of C_3H_8 was achieved. Decomposition of CH_4 could now be achieved even if this molecule apparently is much harder to destruct that C_3H_8, according to previous work. The decomposition obtained, can probably be attributed to a more effective reactor design, combined with the addition of water vapour to the mixture. The results obtained through all three types of experiments have indicated that a discharge system based on the Tesla coil principle, has the capability to completely or partly decompose both the investigated hydrocarbon components (C_3H_8 and CH_4) within a time exposure in the discharge between 3-6 *min*. The time for complete decomposition to occur is in accordance with earlier observations. The findings indicate that high voltage, high frequency Tesla coil systems, as power source for barrier discharge reactors, have a potentially reducing effect on the initial concentration of both CH_4 and C_3H_8.

ACKNOWLEDGEMENTS

My academic supervisors, Otto K. Sønju (NTNU) and Tom Engebretsen (Sintef) deserve gratitude for guidance and patience throughout the course of the thesis.

I also would like to thank Prof. Albin Czernichowski at GREMI (Université d'Orléans-France) and Prof. Gabrielle Dupre and Prof. Claude Paillard at CNRS/LCSR (Laboratoire de Combustion et Systémes Réactifs) for assisting me during the course of this work at the respective sites in France.

Arnfinn Jensen from The Norwegian Defence Construction Service, Dr. Ingar O. Moen at Defence Research and Development Canada and Dr. Dag Bjerketvedt from Telemark University College, have also provided invaluable assistance.

The staff in the laboratory at the department also deserve acknowledgement for their help on finding solutions to practical problems and for keeping up with me those years.

Kristian Ukkonen, graduated from Helsinki University of Technology as MSc. from laboratory of computer science and engineering, helpfully built and supplied the large tesla coil that was used during one of the experiments.

At last but not least, I would like to express my sincere appreciation to my wife for her support and understanding and for telling me that enough is enough!

This work was supported financially by The Norwegian Defence Construction Service and TOTAL Norge AS, Elf Petroleum Norge AS (through the International Department at the The Norwegian University of Science and Technology - NTNU).

* * *

TABLE OF CONTENTS

* * *

LIST OF FIGURES

* * *

LIST OF TABLES

* * *

CHAPTER 1.

INTRODUCTION

1.1 BACKGROUND

This thesis was undertaken to study the molecular decomposition of hydrocarbons in gaseous mixtures both by using shock tube experiments and by generating and applying non-thermal plasma. The shock tube experiments were used to thermally decompose and oxidate highly diluted nitromethane in a shock tube while the experiments with non-thermal plasma were used to initiate reactions and decompose/oxidize two selected hydrocarbons (methane and propane) in air. The latter topic comprised two different experimental approaches. In the following, some of the background for carrying out this work has been described.

Shock tube experiments are important when information for computer modelling reaction schemes is required. Despite many experimental developments, a detailed understanding of shock induced chemical decomposition in explosives at the molecular level remains an outstanding problem. Shock tubes are important tools when more in-depth understanding of the chemistry of decomposition for energetic materials and the effects of shock waves in condensed explosives is required, in order to produce safe and reliable explosives. To achieve this, one has to develop appropriate mathematical models for the physical and chemical processes involved in the initiation of chemical reaction in explosives and subsequent decomposition, as well as implementation of efficient computational techniques to solve these models.

The first approach to molecular decomposition addressed in this study covers the decomposition and oxidation kinetics of nitromethane (NM), which is a nitroparaffin. This is a topic which also previously has been investigated because of the role of the NM molecule in different domains including the chemistry of nitro-propellants, the mechanism of gas phase nitration of hydrocarbons or the mechanism of photochemical smog. This relatively stable explosive can be sensitized by introducing gas bubbles in the liquid. In this case, the mechanism of liquid explosive detonation initiated by rapid compression or shock waves implies the modelling of the gas phase reaction of NM diluted with inert gas.

Previous workers have agreed that the initial first order step is given as $CH_3NO_2 \rightarrow CH_3 + NO_2$. Cotrell, Graham and Reid (1951) first deduced the value of the rate constant as $k\ (s^{-1}) = 10^{+13} \times \exp(-26600/T(K))$, later adjusted by Crawforth and Waddington (1969) and then by Tricot, Perche and Lucquin (1981). Zaslonko et al. (1972) performed the first thermal decomposition study of NM in shock waves, using the mechanism from Cotrell, Graham and Reid (1951) to explain their results. Glänzer and Troe (1972) showed that the initial first order rate constant with respect to NM at highly diluted conditions, varied with pressure between 0.2 and 2 *MPa* at high temperature (900-1500 *K*). In the same temperature range, Hsu and Lin (1985) proposed a decomposition mechanism for NM, consisting of 37 chemical reactions with an initial step of first order as a third body reaction given as:

$$CH_3NO_2 + M \quad \rightarrow \quad CH_3 + NO_2 + M \tag{1-1}$$

This mechanism was then validated for the decomposition of highly diluted NM at low pressure (40-100 *kPa*) in shock waves. A complementary study was carried out by Guirguis et al. (1985) on the ignition mechanism of high temperature gaseous NM. Induction times were computed using a reaction mechanism consisting of 48 reactions, which was found to correctly predict the induction times for the experimental pressure and temperature ranges with pure or slightly diluted NM. When is comes to the oxidation of NM behind shock waves, very few studies have been reported in the literature. Experiments performed by Kang et al. (1991) provided a relation between the ignition delay time, temperature and densities of NM and O_2.

Based on these earlier studies, the aim of the present experiments on NM was to verify and establish a representative reaction mechanism for the simulation of thermal high-temperature decomposition and oxidation of NM in gas phase, close to detonation conditions. From before only few experiments on the pyrolysis behaviour of gaseous NM have been performed. This kinds of experiments are usually done to collect information on the decomposition behaviour of a selected component at different temperatures, pressures and concentrations. The most important information usually deduced from thermal decomposition, is the rate constant, given by the evolution of the species concentration behind the reflected shock. From the form of the concentration evolution versus time, calculated from the absorption signals registered by the monochromator, the reaction order may be deduced. Measured overall decomposition rates can be used to justify the

global rate derived from the modelling. Thermal decomposition experiments also gives valuable information on the molecular extinction coefficient, ε, which is a wavelength-dependent molar absorptivity coefficient with units of 1/(*mol*cm*). This coefficient constitutes one of the variables in the Beer-Lambert Law, which is the linear relationship between absorbance and the concentration of a given species.

The second approach to molecular decomposition covered in this thesis concerned the possibility of using low-power generated plasma discharges to control chemical active gas processes with much higher energy throughput. New technologies to solve environmental problems are more and more in demand nowadays. Existing methods cannot always be used because they are too expensive, have unwanted by-products or simply don't work. A new approach is to create active species in situ so transport losses can be avoided. Pulsed corona and silent discharges are such methods. Its principle is that high energy electrons are created during the propagation phase of the streamer. These electrons dissociate molecules and create radicals such as O, OH, $N_2(A)$ and indirectly HO_2, O_3 and others. All these radicals initiate chemical reactions which mainly cause oxidation of impurities present in the gas or liquid. This makes it possible to convert e.g. NO and/or SO_2 into acids and hydrocarbons into CO_2 and H_2O. The applicability of the method is demonstrated in many laboratories. The research now is aimed at obtaining more detailed information in order to understand, optimize and scale-up the process.

The theoretical part presented here concerning non-thermal plasma processing, have focused on the physics describing different discharge processes together with previous work where changes in the characteristic properties of reaction kinetics in combustion processes under influence of different discharge configurations has been observed. Earlier experiments have indicated various effects depending on the discharge type, cathode/anode configuration, field strength and orientation, the geometrical relation with the flame zone, flame and fuel type. Earlier experiments have been concerned with the influence of gas discharges both on unreacted gas mixtures of fuel-air, directly in the flame zone and in the flue gas.

Pollution control and decomposition of pollutants (NO_x, SO_x, CO_x), hydrocarbon reforming, production of chemical species (ozone), incineration/control of volatile organic compounds (VOC) and other hazardous emissions, toxic gas destruction are also among several processes being investigated for non-thermal plasma processing. In plasma

processing two different types of plasmas are in use; Hot plasmas generally in thermodynamic equilibrium created by electric arcs and cold plasmas, which thermodynamically are in a non-equilibrium state, and normally produced by luminescent discharges.

Electric arc permits the use of high effects, up to 10 *MW* and more. The process is in thermodynamic equilibrium at high temperatures and the supplied electric energy is distributed among all the degrees of freedom. Cold plasmas in non-equilibrium created by luminescent discharges offers good chemical selectivity combined with the possibility to canalize the energy in selected directions. Products can be extracted directly with no special means of cooling. Unfortunately many non-equilibrium discharge devices are limited in effect and operate at sub-atmospheric pressures. A conventional luminescent discharge device normally operates at effects lower than 3 *kW* and at pressures around 20 *torr*. Radio- and super frequency discharges however makes it possible to operate at both higher pressure (200 *torr*) and with considerable higher effects (1 *MW*). These processes are also characterized by high electron densities ($N \cong 10^{13}\ cm^{-3}$) and strong electric fields. Newer applications for plasma processing has been developed over the last decade, which allows atmospheric operating pressure and effects up to 40 *kW* per pair of electrodes.

Cold or non-thermal plasmas are plasmas in which the electron mean energies are considerably higher than those of the molecules and atoms of the ambient gas. The major part of the discharge supplied electrical energy goes into the production of energetic electrons, rather than into ambient gas heating. The energy in the plasma is thus directed preferentially to the electron impact dissociation and ionization of the background gas to produce radicals. The nature of the discharge and the composition of the background gas determine which kind of, and how much radicals that will be created. Since radicals have a selective nature, only specific background gas components will be affected. This is what gives non-thermal plasmas its selective nature.

The purpose of the first experimental approach on non-thermal plasma processing was to gain knowledge of the gliding arc concept and its operation in general. Besides this, two different aspects with the gliding arc were investigated. The first one was to measure the amount of NO_x formed in pure air during normal operating conditions equivalent to the size of the reactor e.g. flow rate. The second aspect was to investigate the ability of the

gliding arc to decompose methane in lean to stoichiometric air-methane mixtures with the purpose of achieving complete decomposition to final products.

The second experimental approach on non-thermal plasma processing for hydrocarbon decomposition can be seen as a continuation of the latter experiments performed with the gliding arc discharge reactor, where the idea investigated being basically the same but with a different technical approach. The subject originated from discussions between me, my tutors and The Norwegian Defence Construction Service. The main initial idea was that plasma processing could have a potential as a method to deal with the threat from FAE weapons to defence blockhouse constructions by cold rapid oxidation of air-carried gaseous fuels. Another applicable area was to use plasma as a method for destruction of e.g. toxic military gases or other gaseous contaminants in centralized destruction plants. The technology can e.g. be applied as a part of a larger air treatment system for destruction of environmental air contaminants in advanced life support (ALS) systems. In this part, techniques for hydrocarbon (CH_4 and C_3H_8) decomposition/conversion, known as the non-thermal discharge was considered. With this technique an electric field was applied to produce high energy electrons in the gas stream while leaving the bulk temperature of the gas unchanged. The high energy electrons served to generate reactive species such as O, OH, and HO_2 that attack the species in question through subsequent reactions. The specific device configurations investigated were all of the dielectric barrier discharge type either as simple or double barrier type, meaning the discharge is sustained between one or two dielectric surfaces respectively. I also would like to emphasize that the use of the Tesla coil principle to generate the high frequency low current (and high voltage) which powers the electrodes, is rather unique when compared to earlier reported work.

1.2 SCOPE OF THE WORK

The objective of these investigations on molecular decomposition was to study experimentally, by shock tube and non-thermal plasma, the decomposition of nitromethane and two selected hydrocarbons, respectively. The investigations were mainly of an experimental nature.

The decomposition and oxidation of nitromethane in a shock tube was studied. The results were analysed and compared with kinetic calculations based on several reaction mechanisms. The aim of the present experiments on NM was to verify and establish a representative reaction mechanism for the simulation of thermal high-temperature

decomposition and oxidation of NM in gas phase, close to detonation conditions.

The subject which concerned the use of non-thermal plasma to generated and initiate reactions to decompose/oxidize selected hydrocarbons (methane and propane) in air was composed of one theoretical and two experimental parts.

The aim of the first experimental approach was to gain knowledge of the gliding arc concept, to measure the amount of NO_x formed in pure air during normal operating conditions and to investigate the ability of the gliding arc to decompose methane in lean to stoichiometric air-methane mixtures with the purpose of achieving complete decomposition to final products.

The aim of the second experimental approach was to apply non-thermal plasma to stoichiometric air/hydrocarbon mixtures (methane and propane in air) to investigate how fast these hydrocarbons could be decomposed.

It is the author's firm believe that substantial advances in the cleanup of low-concentration (below several percent) undesirable compounds from "contaminated" air streams can be achieved by exploiting non-thermal plasma treatment.

1.3 OUTLINE OF THE THESIS

The results obtained through different experiments performed on molecular decomposition of hydrocarbons in gaseous mixtures during the current studies have been tied together and are presented as a whole. Chapter 2 is a general overview of basic gas-phase chemical and plasma kinetics, intended to lead into the two experimental approaches, shock tube and non-thermal plasma. Chapter 3 and 4 deals with the theoretical and experimental report of the nitromethane decomposition studies, were Chapter 4 contains the theoretical part and Chapter 5 the experimental part. The same structure applies to the following Chapter 5 and 6, with one theoretical and two experimental parts, dealing with the generation and application of non-thermal plasma. Chapters that reports experimental activities includes a short summary and conclusion. Chapter 7 then summarize and conclude the achievements from all the investigations.

CHAPTER 2.

BASIC THEORY ON GAS-PHASE CHEMICAL AND PLASMA KINETICS

2.1 INTRODUCTION

The idea that the world around us is made up of large numbers of identical very small particles called molecules, and that the myriads of different kinds of molecules are simply differently arranged groups of atoms, is only a little over 150 years old. The properties of both compounds and elements, especially the relative masses of the different elements which made up a compound, were studied extensively in the eighteenth century. Correspondence between chemists, formalized by publication of experimental results in the journals of scientific societies, led to the compilation of tables of composition and properties of pure compounds. The understanding of the nature of matter as molecules was first set down by John Dalton (1766-1844). This led to his formulation of the atomic theory of matter in 1805. In 1911, Ernest Rutherford showed, by bombardment of atoms with the nuclei of helium atoms (alpha particles), that the mass of an atom is concentrated in a very small central portion of the atom which is called the atomic nucleus. The atomic nucleus is made up of nucleons, of which there are two important fundamental types: electrically positive protons and electrically neutral neutrons. Surrounding the atomic nucleus are the electrically negative electrons. The masses and charges of these three fundamental constituents of atoms are listed in table 2-1.

Table 2-1: Characteristics of the fundamental particles

Particle	**Electrical Charge**	**Rest Mass**	**Molar Mass**
	C	**kg**	**g/mol**
electron	-1.60217733×10-19	0.91093897×10-30	0.0005486
proton	+1.60217733×10-19	1672.6231×10-30	1.0072697
neutron	0.0	1674.9543×10-30	1.0086650

The electrons are the portion of the atom which engages in chemical reactions. The properties of the electrons of an atom are determined mainly by the number of protons present in the nucleus of the atom. The number of neutrons generally has a negligible effect upon the properties of the electrons which are of chemical significance. Thus the chemical nature of an atom, which is to say the chemical properties of an element, is determined by the number of protons in the nucleus. This number of protons is called the atomic number. The mass of the atom, its atomic mass, depends significantly upon both the number of protons and upon the number of neutrons present in the nucleus.

Chemical reactions are reactions between chemical species in which bonds holding atoms together are broken and formed. Atoms are conserved and rearranged. Chemical reactions, if fully balanced or full reactions, are also balanced with respect to electrical charge. When studying electrochemical reactions, it is therefore often useful to write half-reactions in which electrical charge is balanced by electrons.

The very high speed of gas molecules under normal room conditions would indicate that a gas molecule would travel across a room almost instantly. However, the slow diffusion of gas molecules which are moving very quickly occurs because the gas molecules travel only short distances, called the mean free path, in straight lines before they are deflected in a new direction by collision with other gas molecules. This mean free path of the molecules increases as the temperature increases; as the pressure decreases; and as the size of the molecules decreases.

When an atom loses one electron it forms an ion and the process is known as ionization. The enthalpy difference between the gaseous atom and the gaseous ion formed from it by the loss of an electron can be measured in terms of the electrical potential required to emit electrons from the atom and is called the ionization potential.

2.2 ELEMENTARY GAS-PHASE CHEMICAL AND PLASMA KINETICS

Both chemical and plasma- or electrochemical reactions take place at a given rate which depends on a set of specific system conditions, such as pressure and temperature.

Systems in thermal equilibrium are systems where all species share the same gas temperature. An extension to such a system are the plasma systems, which are not in thermal equilibrium and are characterized by more than one temperature, in which

reactions may depend on temperatures associated with different species; i.e. reactions may be driven by collisions with electrons, ions, or charge-neutral species. These two systems or conditions are often denoted as the third and fourth state of matter. The difference is that the plasma system has been supplied with an additional specific amount of energy which separates some of the gas component molecules into a collection of ions, electrons, charge-neutral gas molecules, and other species in varying degrees of excitation. Depending on the amount of energy added, the resulting plasma can be characterized as thermal or non-thermal.

Investigating systems that include plasma kinetics, which most reactive systems (e.g. energy conversion) do, requires additional information such as tabular data for collision cross sectional areas and ion-ion, ion-electron, molecule-electron reactions and ion and neutral transport coefficients. Collision cross sectional areas is proportional to and transformable to standard rate coefficients which are needed for solving reaction mechanisms by kinetic modelling. Most of the plasma reactions require some auxiliary information beyond the Arrhenius coefficients to distinguish these reactions from the default thermal reactions, such as temperature dependence and energy-loss per collision. Plasma reactions are also most often irreversible reactions and in the case of electron kinetics, the interactions between electrons and neutral species can be intrinsically irreversible. As for the neutral systems, information on thermodynamic properties for both the ions and electrons must be known.

2.2.1 Oxidation

In the presence of free O_2, all organic materials (living organisms, wood, coal, oil, synthetic polymers, solvents, etc.) are only metastable intermediates on the way to CO_2. Under normal conditions in the presence of O_2, CO_2 is the only thermodynamically stable carbon compound. The stability of all organic compounds in the presence of O_2 and hence the yield of desired products in oxidations therefore depends only on the kinetics of the reaction involved, i.e., on the prevailing conditions (temperature, effect of high-energy radiation, nature and concentration of catalysts or stabilizers (inhibitors) present, presence of other reaction partners, impurities, etc.).

Table 2-2 lists some estimated rates of typical reactions, and the linearly extrapolated time required for complete conversion.

Table 2-2: Various oxidation reactions.

Rates, u, of various oxidation reactions and linearly extrapolated time t required for complete formula conversion (Ullmann's Encyclopedia of Industrial Chemistry (1998))

u^a	u^b	time[c]	**Examples of reactions**
molecules $cm^{-3}s^{-1}$	$mol\ L^{-1}s^{-1}$		
10^3 - 10^{10}	10^{-18} - 10^{-11}	10^{10} - 10^3 *a*	initial rate of un-catalysed hydrocarbon oxidations
10^{13} - 10^{14}	10^{-8} - 10^{-7}	2 a - 10 *weeks*	degradation of un-stabilized plastics under irradiation
10^{16}	10^{-5}	ca. 20 *h*	industrial radical reactions (e.g., liquid phase oxidation and polymerization)
10^{18}	10^{-3}	ca. 10 *min*	heterolytic reactions
10^{20}	10^{-1}	ca. 6 *s*	heterolytic reactions
10^{22}	10	ca. 10^{-2} *s*	heterogeneously catalysed hydrocarbon oxidations
10^{24}	10^3	ca. 10^{-4} *s*	explosions; ion reactions

a. Pure hydrocarbons contain about 6×10^{21} molecules per cubic centimetre.
b. 1 mol/L corresponds to ca. 6×10^{20} molecules per cubic centimetre.
c. 1 *year* = 8760 *h* = 3.15×10^7 *s*.

The oxidation of organic materials can be roughly divided into homolytic oxidation and heterolytic oxidation reactions. Homolytic oxidation reactions are chain reactions of organic and inorganic compounds with oxygen involving radicals formed by homolytic cleavage of interatomic bonds (homolytic=decomposition of a compound into two neutral atoms or radicals). Explosions and combustion reactions, ageing of polymers and oils, and many industrial oxidation reactions in the homogeneous liquid and gas phases belong to this group. All types of organic compounds can be subjected to radical chain oxidation. Because many of these reactions proceed spontaneously even at low temperatures they are also called auto oxidations. In heterolytic oxidation reactions an active oxygen compound (e.g., a peroxyacid, hydroperoxide, or O_2) or a metal ion in its high valence state oxidizes the starting material in a two-electron transfer reaction.

Homolytic gas-phase oxidations are all combustion processes and gas explosions that

take place in free gas space without heterogeneous catalysts. Examples include the combustion of heating oil and natural gas for the production of heat and energy and the rapid combustion of gasoline and diesel in internal combustion engines. Thus the homolytic gas-phase oxidation is one of the most important chemical reactions with respect to the amounts of materials consumed.

2.2.2 Chemical reaction rate expressions

The law of mass action defines the reaction rate. It states that the rate of disappearance of a chemical species is proportional to the products of the concentrations of the reacting chemical species, each concentration being raised to the power equal to the corresponding stoichiometric coefficient. The proportionality constant in this expression is defined as the specific reaction-rate constant, k. For a given chemical reaction, k is independent of the concentration, c_i, and depends only on the temperature. The specific reaction-rate constant includes the effects of the collision frequency and the Boltzman factor, which is the fraction of collisions that have energy greater than the activation energy, E_a.

The reaction rate constant is an important factor, when studying decomposition. In a closed constant-volume system, the rate of a chemical reaction can be defined simply as the rate of change with time of the concentration of any of the reactants or products, including electron-molecule reactions. The rate will be defined as a positive quantity, regardless of the component whose concentration change is measured. As an example, consider the generalised chemical reaction:

$$aA + bB \quad \rightarrow \quad cC + dD \tag{2-1}$$

The rate can be expressed as -dA/dt, -dB/dt, -dC/dt, -dD/dt, were A, B, C and D designate the concentration of reactants or products in arbitrary units. A unique rate of reaction, consistent with the specified stoichiometry, can be readily defined for the above reaction as:

$$\nu = -\frac{1}{a}\frac{dA}{dt} = -\frac{1}{b}\frac{dB}{dt} = \frac{1}{c}\frac{dC}{dt} = \frac{1}{d}\frac{dD}{dt} \qquad \textbf{Eq. 2-1}$$

which is equal to:

$$\nu = k \cdot A^{n_1} \cdot B^{n_2} \cdot \ldots \cdot C^{n_i} \qquad \textbf{Eq. 2-2}$$

where n_1, n_2 and n_i are the partial orders of the reaction and $n = n_1 + n_2 + \ldots + n_i$, the global reaction order.

The rates of most chemical reactions are very sensitive to temperature changes. The well known Arrhenius formulation gives a relationship between the specific rate constant k, and the absolute temperature T:

$$k = A \cdot e^{-E_a/(RT)} \qquad \textbf{Eq. 2-3}$$

where A is assumed to take account for the collision effects, the orientation of the colliding molecules and a small temperature dependence (most often neglected) of the pre-exponential factor.

First-order reactions

The rate equation for a first-order reaction implying one reactant, that is C → products, can be written as:

$$-\frac{dc}{dt} = k \cdot c \qquad \textbf{Eq. 2-4}$$

where c represents the concentration of the reactant C. This equation can be integrated between $c_{t=0} = c_0$ and $c(t) = c_t$:

$$\int_{c_0}^{c_t} \frac{1}{c} dc = \int_0^t k\,du \qquad \textbf{Eq. 2-5}$$

$$\Rightarrow$$

$$\ln c_t - \ln c_0 = -kt \Rightarrow \ln\left[\frac{c_0}{c_t}\right] = k \cdot t \qquad \textbf{Eq. 2-6}$$

solving for c_t gives the integrated rate expression for the reaction:

$$c_t(t, k, c_0) = c_0 \exp(-kt) \qquad \textbf{Eq. 2-7}$$

A plot of ln(c) versus time should then give straight line with slope, - k, if the actual reaction is of first order. If the chosen dependent variable is the quantity of decomposed reactant, designated as x, and c_0 is the initial concentration. Then $c = c_0 - x$ and:

$$-\frac{dc}{dt} = -\frac{d}{dt}(c_0 - x) = \frac{dx}{dt} = k \cdot (c_0 - x) \qquad \textbf{Eq. 2-8}$$

When integrated between t=0 to t and $c=c_0$ to c the equation becomes:

$$\ln\left[\frac{c_0}{c_0 - x}\right] = k \cdot t \qquad \textbf{Eq. 2-9}$$

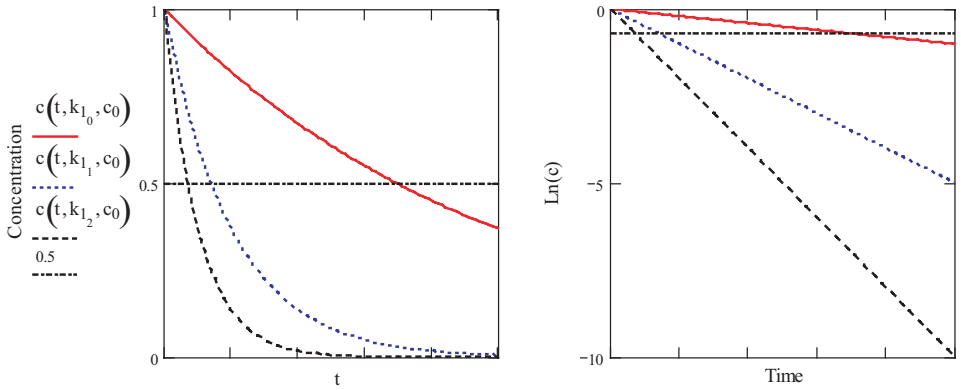

Figure 2-1: Example of first-order kinetics.

Behavior of a first-order reaction given $c_0 = 1$ as initial concentration for three selected values of the rate constant, k = 0.01, 0.05 and 0.1

Equation 2-9 has been plotted in figure 2-1 for three different values of the reaction rate constant. A plot of the natural logarithm to the apparent concentration versus time will produce a straight line.

Second-Order Reactions

For a reaction of second order with respect to one reactant, the rate equation becomes:

$$-\frac{dc}{dt} = k \cdot c^2 = \frac{dx}{dt} = k \cdot (c_0 - x)^2 \qquad \textbf{Eq. 2-10}$$

When integrated between t = 0 to t and c = c to c_0, one obtains:

$$\frac{1}{c} - \frac{1}{c_0} = k \cdot t = \frac{1}{c_0 - x} - \frac{1}{c_0} \qquad \textbf{Eq. 2-11}$$

As exampled in figure 2-2, a plot of the inverse of the apparent concentration vs. time will be linear for a second-order reaction.

N'th-Order Reactions

For a reaction of n'th-order ($n \neq 1$) with respect to a single reactant the rate equation can be expressed as:

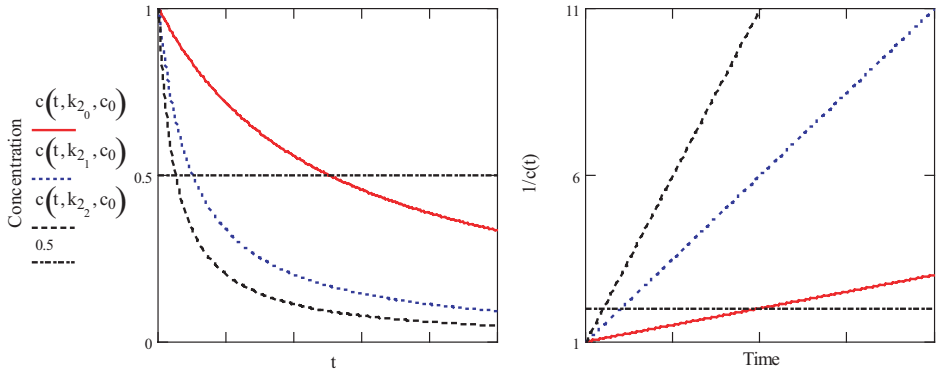

Figure 2-2: Example of second-order kinetics.

Behavior of a second-order reaction given $c_0 = 1$ as initial concentration for three selected values of the rate constant, k = 0.01, 0.05 and 0.1

$$\frac{dx}{dt} = k \cdot (c_0 - x)^n \qquad \textbf{Eq. 2-12}$$

which integrates to:

$$\frac{1}{n-1} \cdot \left[\frac{1}{(c_0 - x)^{n-1}} - \frac{1}{c_0^{n-1}} \right] = k \cdot t \qquad \textbf{Eq. 2-13}$$

Half-lifetime, $t_{1/2}$

An alternative method of determining the reaction order is to measure the half-life, $t_{1/2}$, as a function of initial concentration. The half-lifetime is simply the time necessary for the concentration to decrease to one half of the initial concentration:

$$\frac{c_t(t = \tau, k, c_0)}{c_0} = \frac{1}{2} \qquad \textbf{Eq. 2-14}$$

From the integrated rate equation for a first-order reaction:

$$\frac{1}{2} = \exp(-k\tau) \Rightarrow \tau = \frac{\ln 2}{k} = t_{1/2} \qquad \textbf{Eq. 2-15}$$

and for reactions of n'th order:

$$t_{1/2} = \frac{1}{k(n-1)} \cdot \frac{2^{n-1} - 1}{c_0^{n-1}} \qquad \textbf{Eq. 2-16}$$

Thus the dependence of $t_{1/2}$ on the initial concentration determines the reaction order

directly. It is also important to notice that the half-lifetime for reactions of orders higher than one, is dependent on the initial concentration.

2.3 SHOCK TUBE INDUCED CHEMICAL DECOMPOSITION

The realization of the fist shock tube in 1899 to study the process of pressure equalization was done by a Frenchman by the name of Vieille. The first experiments on dynamics, physics and chemistry in shock tubes had its early start in the 1950's. Today the shock tube experiments are still considered as an important method when it comes to bring gases rapidly to high pressure and temperature. In the domain of combustion/incineration this method offers a way to study chemical reactions at high temperatures within a confined boundary and thereby deduce reaction parameters for well defined pressure and temperature domains.

A shock tube is a device in which a gas at high pressure (the driver gas) is initially separated from a gas at lower pressure (the test gas) by a diaphragm. The controlled breaking of the diaphragm will then produce a plane shock wave which propagates through the test gas raising it to higher temperature and pressure levels, initiating reactions which decompose the mixture. As the shock wave moves through the test gas, a rarefaction wave moves back into the high-pressure gas at the speed of sound. The test gas and the driver gas make contact at the "contact surface" which moves along the tube behind the shock front. Conventional notation represents the conditions in the unperturbed, low-pressure test gas by the subscript 1, so that the initial pressure and temperature in this region are denoted as P_1 and T_1, respectively. The region between the shock front and contact surface is denoted by 2; that between the contact surface and rarefaction wave by 3. The initial conditions on the high-pressure side are given the subscript 4. If the shock wave is allowed to undergo reflection at the end of the tube, the pressure conditions in this region are given the subscript 5.

Figure 2-3A shows the ideal movements of the shock front, the contact surface, the rarefaction wave and the reflected shock wave in a distance-time diagram. The set of equations which describe the concentration, velocity and temperature distributions downstream of the shock are derived from the well-established conservation laws of mass, momentum and energy transfer. The flow is assumed to be adiabatic; transport phenomena associated with mass diffusion, thermal conduction and viscous effects are assumed to be negligible.

Test times behind shock waves are typically in the order of a few hundred microseconds and hence, neglecting of these transport processes is of little consequence. Initial conditions for the governing equations are derived from the Rankine-Hugoniot relations for flow across a normal shock.

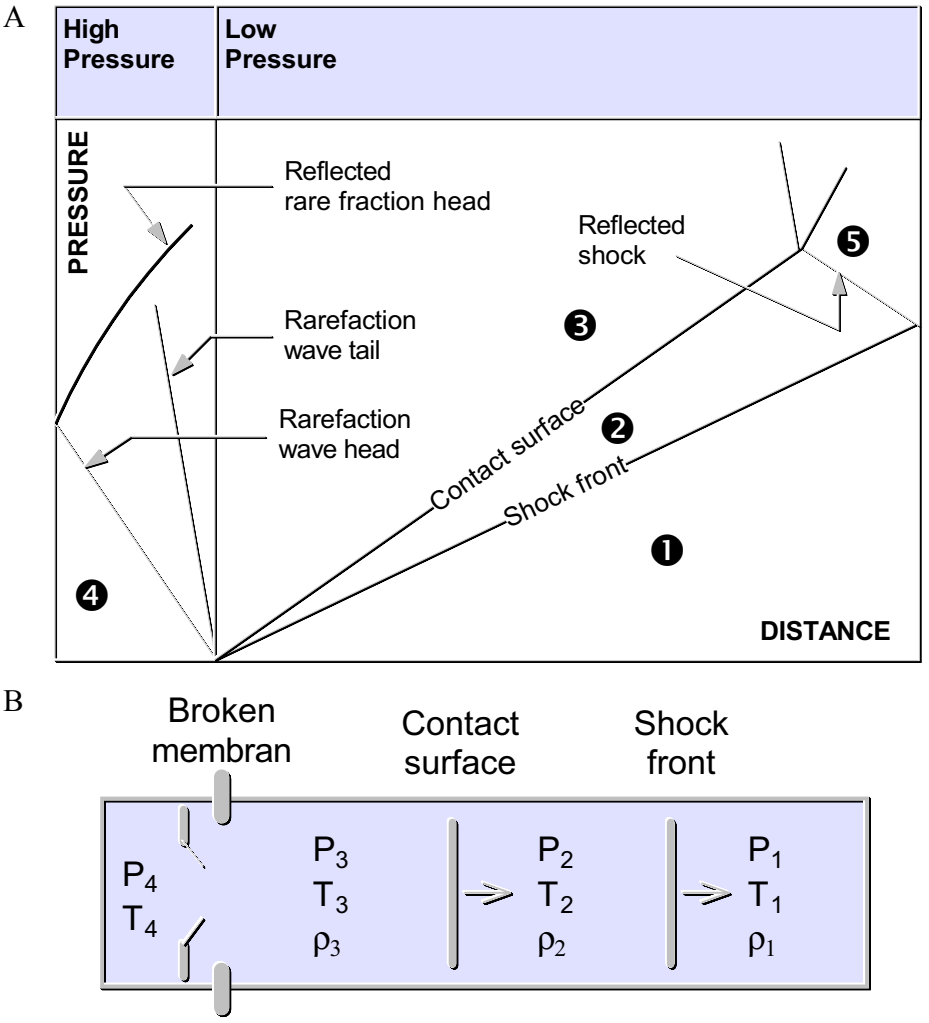

Figure 2-3: Distance-time diagram and membrane rupture.

A: Diagram showing the movements of the shock front, contact surface, rarefaction wave, and reflected shock wave and B: Gas condition for the driver and the working gas an instant after the rupture of the membrane ($T_3 < T_4$ and $P_2 = P_3$)

A shock tube consists generally of a cylindrical tube which is closed at the extremities and separated in two parts by a membrane. The first section is called the high-pressure

section and the second is called the low-pressure or experimental section, as indicated in figure 2-4. The low-pressure section is again divided into two sub-sections referred to as the intermediate- and the working section.

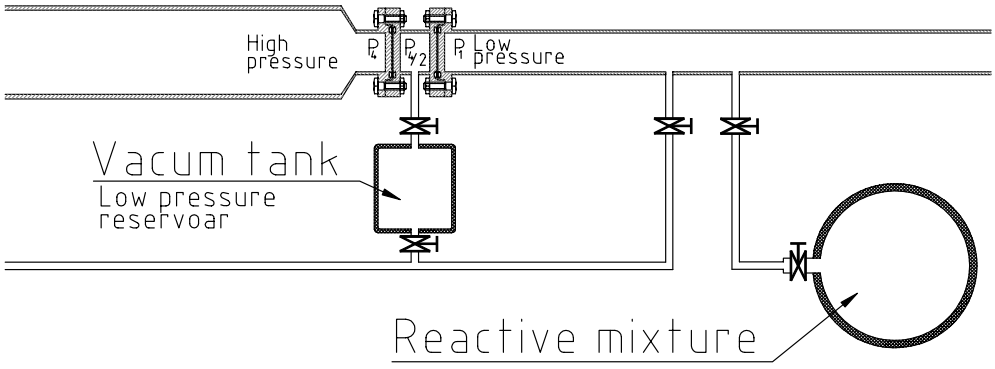

Figure 2-4: Schematic shock tube.

The driver section is filled with an inert gas under high pressure, with pressures ranging from one to several bars. Examples of inert gasses are He, Ar, N_2 etc. The low pressure section is filled with the gas which is to be studied. Normally the pressure in this section is between a few torr and atmospheric pressure. When the membrane between the two sections breaks, the working gas is simultaneously compressed and heated by the physical force released in the shock wave. Figure 2-3B shows the gas condition in the shock tube a given time after the rupture of the membrane, where subscripts refers to:

1. The working gas initial state.
2. The shocked working gas.
3. The driver gas in the region situated between the shock front and the contact surface.
4. The driver gas initial state.

After the rupture of the membrane, a series of shock compression waves propagates through the gas in the low-pressure section. The gas is compressed adiabatically and the process is close to irreversible. These shock waves join rapidly to form a plane shock wave which propagates at supersonic speed (V_1). The incident shock wave is successively followed by the so-called contact surface which separates the driver and the working gas.

The shock front separates the unshocked (state 1) and the shocked gas (state 2). After the passage of the shock, the working gas initially at P_1 and T_1, is instantaneously brought to P_2 and T_2. When the shock wave hits the opposite end of the working section, the shock is reflected back through the already shocked gas. The working gas at state (2) is now brought up to a new pressure and temperature of P_5 and T_5 (state 5, not illustrated in figure 2-3B).

In shock tube experiments, normally only one or two compounds are measured at a time. Varying degrees of dilution are achieved by using inert gases which do not take place in the reactions other than acting as third bodies. The shock tube principle offers the possibility of achieving high temperatures and pressures rapidly. The rise in temperature is caused by the passage of a shock wave travelling at supersonic speed and may be sufficient to excite both molecular oscillation and electronic state and thereby provoke dissociation, ionization and third body decomposition reactions.

Ionization: $e + A_2 \rightarrow A_2^+ + 2e$ (2-2)

Dissociation: $e + O_2 \rightarrow 2O + e$ (2-3)

Third body: $AB + M \rightarrow A + B + M$ (2-4)

At this high temperature the absorption of energy plays an important role. By using an UV-absorption technique where light emission on selected wavelengths is measured, the concentration evolution of a reactant behind the incident or reflected shock wave can be followed. This quantitative method is based on the law of Beer-Lambert, which is the linear relationship between absorbance and concentration of an absorbing species (see APPENDIX A). The law defines the absorbance, D, as:

$$D = \varepsilon(\lambda) \cdot l \cdot c \qquad \textbf{Eq. 2-17}$$

where:

c : reactant concentration [mol/m^3]

l : optical distance (tube diameter) [m]

$\varepsilon(\lambda)$: wavelength-dependent absorption coefficient [m^2/mol]

Figure 2-5 shows an often used device setup for measuring light absorbance for the exposed compound or molecule. Modern absorption instruments can usually display the

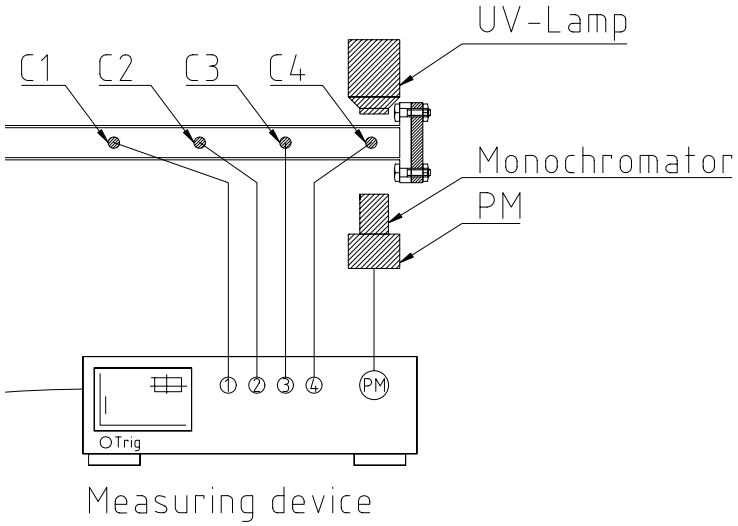

Figure 2-5: Measuring light emission at selected wavelengths

data as transmittance, %-transmittance or absorbance. An unknown concentration of a gaseous compound can be determined by measuring the amount of light that a sample absorbs and applying Beer's law.

2.4 NON-THERMAL PLASMA INDUCED CHEMICAL DECOM-POSITION

Pollution control and decomposition of pollutants (NO_x, SO_x, CO_x), hydrocarbon reforming, production of chemical species (ozone), incineration/control of volatile organic compounds (VOC) and other hazardous emissions, toxic gas destruction are among several processes being investigated for non-thermal plasma processing.

The purpose of an electrical discharge produced non-thermal plasma is to provide a large range of species, excited and ionized atoms/molecules and radicals, which may either have a catalytic effect (initiate reactions) or be consumed (take part in ongoing reactions) in chemical reactions. A continuous supply of discharge induced species, depending on the background gas composition and pressure, will have two main effects on the processed gas; charging macro particles (aerosols, dust) and launching chemical reactions. The plasma technology may be compared to the chemistry of combustion, but instead of using heat to break up contaminants, the plasma device destroy molecules by producing highly reactive free radicals - atoms or molecules that have impaired electrons.

Historically the field of advanced decomposition/oxidation technologies (AOT) has involved processes in which organic compounds were decomposed via the hydroxyl radical OH. This technology was first used in the treatment of water using OH radicals generated from the photolysis of ozone (O_3) or hydrogen peroxide (H_2O_2) or a combination of both processes. In the past several years, the field has been expanded to include processes which involve other free radicals, some of which are reductive rather than oxidative. The AOT process today includes treatment of gaseous as well as aqueous-based effluents. The interest in the AOT process has grown considerably because of their applications to pollution control and waste treatment. They show particular promise for the treatment of hazardous and toxic pollutants because the reaction rates of free radicals can be orders of magnitude larger than those of a strong oxidizes like O_3.

The decomposition of gas by electrical discharge depends on electrical discharging characteristics, such as pulse rise time, pulse peak voltage, pulse frequency, etc. Therefore, it is important to find the best conditions for the decomposition. In these devices a discharge is maintained in which most of the electrical energy goes into production of high temperature electrons, typically 5 to 10 *eV*. At the same time, the bulk of the gas remains at (approximately) ambient temperature. These high-energy electrons cause different processes during the collision with molecules of the carrier gas. The primary active species formed are ions, radicals and excited species. The radicals react very slowly with the carrier gas and are available for the degradation of the trace components. The most important radicals for removal are O and OH. Furthermore, the so called “secondary cleaning radicals” (HO_2, O_3), which are generated in the later phase of the process are also important.

Pollution of air, water, and soil by a large number of very different organic and inorganic chemical species is a continuing problem arising from human society. No single solution is possible for destroying all types of wastes due to the diversity of the chemical properties of the waste components. Some of the waste treatment methods only transfer the toxic component from one phase to another. While this may serve to concentrate the waste in a more readily disposable form, it does not alter the chemistry of the pollutant. Other processes use chemical reactions to transform the waste into less toxic by products. Chemical transformations can be induced by a number of very different processes, where the basic chemical pathways can be of a limited number of types. Oxidative and reductive pathways are the major ways for the transformation of many organic compounds into less

toxic by-products. Biological processes use the metabolism of entire cells to degrade contaminants. These metabolic pathways are in turn catalysed by specific biochemical catalysts, namely individual enzymes. Biological processes have the advantage of being highly specific; however they are generally very slow and require a fairly narrow range of operating conditions. Non-biological processes may use inorganic catalysts or high temperatures in various environments to speed up various chemical reactions. Incineration is an example of a high temperature oxidation process where most organic compounds are oxidized to carbon dioxide and water. Another class of waste treatment methods are the advanced oxidation processes. Advanced oxidation processes use different energy sources such as electrical discharges, ultrasonic pulses, electron beams, and UV light to produce highly reactive species such as hydroxyl radicals, ozone, hydrogen peroxide, hydroperoxyl radicals, and energetic electrons to initiate degenerative reactions leading to the removal of various organic and inorganic waste species. The key distinguishing feature is the input of energy in the form of chemical, electrical, or radiation (or combinations of these) to a gas or liquid containing the waste components to be degraded.

The hydroxyl radical is one of the most reactive species known with an oxidizing potential of 2.80 *V*. It can be made through a variety of processes including the electron impact dissociation of water. Ozone follows at 2.07 *V*, and it has been extensively used in Europe to disinfect water for close to 100 *years*. More recently, many applications of ozone to destroy to hazardous waste have been pursued. Hydrogen peroxide at 1.78 *V*, is also a highly oxidizing species. Other important oxidizing species include the hydroperoxyl radical at 1.70 *V*, and chlorine at 1.36 *V*. Combinations of UV light with ozone and hydrogen peroxide have been found to be particularly effective at degrading a wide range of hazardous organic species. The problem with the development of advanced oxidation processes include development of low cost and robust methods to produce the reactive species and detailed consideration of the formation of intermediate or by-products which may occasionally be more toxic than the precursor compounds. Many challenges in the areas of reactor design, chemical kinetics, mass transfer, analytical chemistry, and process optimization remain to be addressed in order to bring these methods to their full potential.

Physical and chemical processes in electric discharges

Electrical discharges have been known to initiate chemical reaction in gases and gas mixtures for over 400 *years*. As a result of the deeper knowledge of the discharge physics

and the ever increasing demand for more efficient (economy, energy and pollution control) chemical processing, the use of such discharges as a chemical tool to alter conditions of specific gas mixtures has showed an increasing tendency for industrial applications in the last tertiary. A discharge can exhibit changes by decomposition and/or by the creation of new chemical bindings, e.g. dissociation of di-atomic molecules to atoms and creation of components from elements or molecules. When used for surface treatment and critical cleaning applications, ions and electrons in the plasma react with the surface of materials placed within the plasma chamber. The result is a complete removal of organic contamination, and on polymers, a permanent chemical modification of the surface. Reactive chemical functionalities may be imparted to the surface resulting in a dramatic increase in bond strength and other properties, without affecting the bulk properties of the material.

A fundamental question has been if the chemistry related to such discharges follow the law of equilibrium, which relates the concentration between reactants and products to a constant which depends on temperature and activation energy for the actual reaction. Experiments indicates that electrochemical changes due to a discharge at moderate temperatures does not follow this law, neither the classical law of thermodynamics, and that there are other processes which control such reactions. The difference is that thermo-chemical equilibrium is related to thermodynamics while electrochemistry at moderate temperature is related to the reaction kinetics itself, which is affected by reverse reactions and excited species (due to high energy electrons, von Engel (1983)). We can explain these processes by the production of free electrons and positively charged particles (sometimes also negative) caused by electron collisions. Because of the electric field, the electrons are forced to move relatively fast against the anode while the ions slowly drifts in the direction of the cathode. When free electrons collide with neutral gas molecules, they are dispersed in all directions, but lose little energy. The speed of the electrons (= energy) can be described by a form close to the Maxwell-Boltzman distribution.

It should be noted that while both electrons and molecules have velocity distributions very close to the Maxwell-Boltzman distribution, there is a large difference between the temperatures which characterize these two groups (Blaustein (1969)). A given amount of all the electrons contained in a given electric field will have energy high enough to excite and ionize surrounding gas molecules. The excited molecules can then either emit photons, react chemically with other particles to form components or radicals or dissociate

into neutral atoms. The products created in such processes are often neutral, but can for a short period of time be excited to a level beyond that of the surrounding gas.

Electrochemical induced reactions are often separated into a physical and a chemical part. The electric breakdown in the gas is described by the physical part while the chemical part is related to the resulting chemical reactions. Both processes are mutual dependent and can not be examined separately. Figure 2-6, from Eliasson and Kogelschatz (1991a), illustrates how a silent discharge process can be separated into discharge physics and plasma chemistry.

Another example is the chemical equilibrium for the $2CO + O_2 \rightarrow 2CO_2$ system. Here it has been found that the equilibrium concentration for the three components at a gas temperature of 2600 *K* corresponds to the concentrations that can be found in a corona discharge at 300 *K*.

By using mass spectrometry, it has been shown that both the electrons and the molecules in a hydrogen discharge have a temperature close to the surroundings when the dissociation corresponds to what is expected for thermal and chemical equilibrium at temperatures close to 4000 *K* (Blaustein (1969)).

The reason why two such well mixed “gases” can have such a high temperature difference can be explained by the fact that the flow of energy at stationary conditions from an energy source through a magnetic field can be transferred practically without losses to the electrons under given conditions. The neutral gas molecules absorb no energy from the electric field while the ions only absorb a small part. As a result of the collisions, energy distributions are formed. The electron energy distribution is characterized by high average energy compared with the molecule distribution, often as much as by a factor of 100. The reason is that, because of the much lower electron mass ($2x10^3$ - $2x10^5$ electron masses per atom mass), only little energy is lost when an electron collides with a molecule. The total amount of energy that the molecules can absorb from collision with electrons is proportional with the electron concentration and the collision frequency. In a discharge process it is the electrons that constitutes the link between the physics and the chemistry and simultaneously acts as the most important particles in the initial phase of a chemical reaction. The electrons transport the energy between the electric power supply to the gas, where ions and excited species are produced. These will further dissociate to free

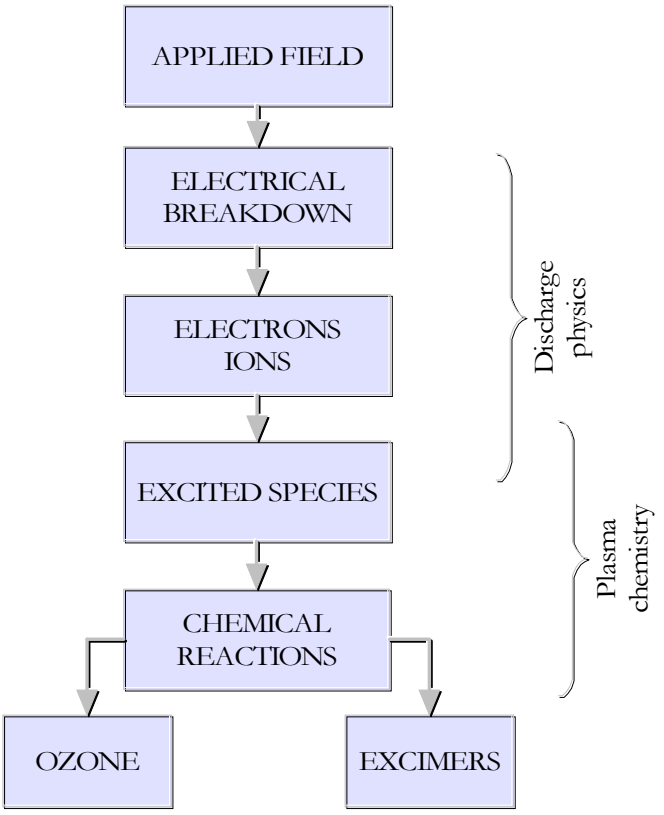

Figure 2-6: The electrochemical process.

The figure illustrates how we can separate the electrochemical process into a physical and a chemical part.

radicals, which in turn can react with each other or with other gas molecules and produce new active species.

Most of these important processes in a gas discharge take place mainly in the discharge gap. In the discharge gap, between the electrodes, is where we find the highest field strengths, the highest concentration of ions and most of the electron energy and therefore, indirectly, the highest concentration of free radicals and highly excited molecules. The discharge volume is always given by the specific discharge configuration.

Initiation of chemical reactions

In plasma chemistry, it is the electrical discharge that supplies the energy which again initiates the chemical reactions and in cases of non-equilibrium plasmas, practically all the energy is transported by the electrons (Elisaaon and Kogelschatz (1991b)). In a glow

discharge, the electrons continuously receive energy from the applied electric field. Because of the low pressure, the electrons do not undergo enough collisions to come to equilibrium with the surrounding gas molecules. Under stationary discharge conditions, the energy loss is dominated by recombination of electrons and ions on the surrounding surfaces.

In a corona and in the silent discharge, the situation is completely different. The higher pressure causes the electrons to lose almost all their energy to the surrounding atoms and molecules. Sparks can usually be avoided by using specially designed electrode geometries. In the case of corona, it is the rapidly diminishing field which decelerate the electrons on their way to the anode. In comparison to the corona discharge, the electron current in a silent discharge is limited by the di-electrical barrier.

In the case of streamer spark-over, which is often used in volume plasma chemistry, the streamer head creates an almost homogenous plasma filament surrounded by a low self-induced electric field, filled with charged and excited particles. Because of the high electron energy ($\approx 5\ eV$) and the short lifetime, the electrons lose very little energy through elastic collision with surrounding neutrals.

The energy of the electrons is determined by two parameters:

1. The total field to which the electrons are exposed, that is the imposed field and the (possibly much higher) self-induced field.
2. Interaction with the surroundings.

The equation which describes these parameters is given by the Boltzman equation, in its simplest form expressed as:

$$\frac{\partial f}{\partial t} + \nu \cdot \frac{\partial f}{\partial x} + a \cdot \frac{\partial f}{\partial \nu} = \left.\frac{\partial f}{\partial t}\right|_e \qquad \textbf{Eq. 2-18}$$

This equation expresses the change in the electron energy distribution function (EEDF) as a function of distance, x, velocity, v, and time, t, caused by binary collision with particles. The acceleration, a, is proportional with the force acting on the electron and given by a=(e×E)/m in a field E where m is the mass of the electron having a charge *e*. The right side term describes the change in EEDF caused by collisions with other particles and is the term connecting the physics of the electrons to the chemistry of the atoms or molecules. Each process has an optimal set of parameters, where the mean energy of

electrons colliding with molecules is one of the most important. If we need to dissociate a molecule, the energy transferred from the electrons must exceed the energy necessary to break the specific bindings.

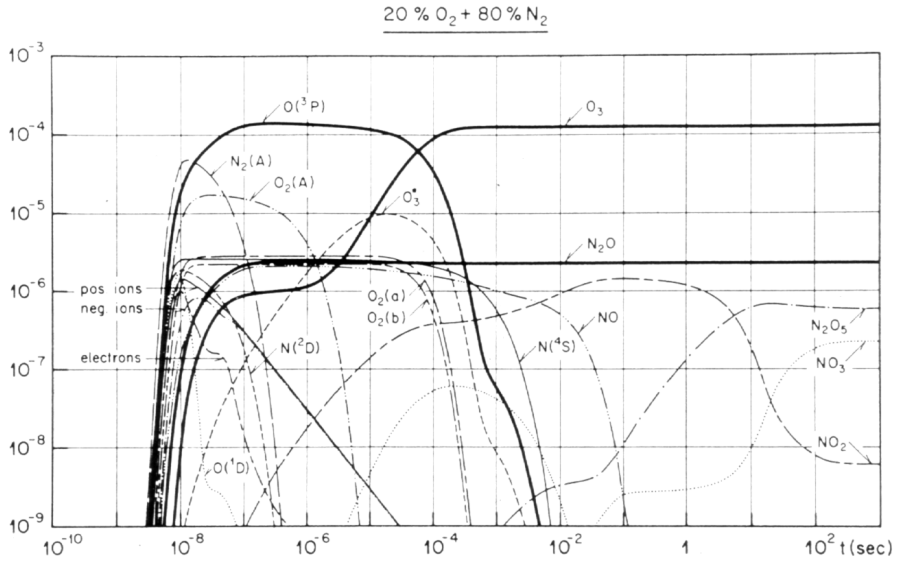

Figure 2-7: Micro discharge in air.

The main species produced from a single micro discharge in air (Eliasson and Kogelschatz (1991a)).

Figure 2-7 shows the computed simulation (143 reactions between 30 different reactants) for the formation of different species initiated by a single micro discharge in air (80% N_2 and 20% O_2). The short electron pulse (~10 *ns*) liberate energy through electrons to different excited levels of N_2 and O_2. Some of this energy leads to dissociation and finally to the creation of O_3 and various nitrous oxides. After approximately 50 *ns* most of the charge carriers have disappeared and the chemical reactions continue.

In non-equilibrium plasmas it is mainly the high energy electrons produced by the discharge mechanism that initiates the chemical reactions. The fast electrons collide with gas molecules and excite them to higher energy levels, thereby losing some of their energy which again has to be renewed by the electrical field.

In a corona discharge only little can be done to affect the electron energy (the radius of curvature and the polarity of the active electrode). Another approach is to apply rapid voltage pulses (pulsed corona) across the discharge gap. In the case of a silent discharge

the electron energy is controlled by the product *nd* (*n*: gas density, *d*: distance between electrodes). According to Paschen the initiation of a discharge in an electrical field is purely a function of this product. The smallest voltage necessary to initiate electrical breakdown in a given discharge gap is given by the law of Paschen (1889) (Sigmond (1996)). If we assume that all the electron impacts within the gas are applicable with (two-particle-) equivalence we have the relation:

$$\alpha/n = f(E/n) \qquad \text{or} \qquad \alpha/p_0 = f(E/p_0) \qquad \textbf{Eq. 2-19}$$

, where α/n is proportional to the number of ionizations per mean free path and α is the number of new electrons produced by the first electron. Then the law of Paschen states that: If all discharge processes are applicable with equivalence, the breakdown voltage between two plane parallel electrodes is just a function of the product.

For initiation of plasma chemical reactions it is very important that the energy transfer between the electrons and the surrounding atoms/molecules is as effective as possible. This is best achieved using short electron pulses, which is exactly what occurs within the micro discharges in a silent discharge.

Chemistry in non-equilibrium discharges

In previous chapters, we have seen that chemical reactions in a plasma, primarily is caused by the electrons. The electrons (e) collide with the gas molecules (B, M) and bring these to higher energy levels by supplying the corresponding part of their kinetic energy. The excited species can now, because of their higher internal energy, initiate reactions as shown by a simple example:

$$e + M \rightarrow M^* + e \qquad (2\text{-}5)$$

$$A + M^* \rightarrow C + D \qquad (2\text{-}6)$$

Because the reaction $A + M^* \rightarrow C + D$ only can take place at very high temperatures, it is in reality reaction (2-5) which initiates the formation of the products C + D. Each chemical reaction is characterised by a few main parameters; reactants (e.g. A, B, M^*), products (e.g. C, D), temperature, pressure, the enthalpy and the rate coefficient *k*. A rate coefficient for electron reactions can be calculated if we know the electron energy distribution (EEDF) and the collision area (σ) for the actual process.

Figure 2-8 (left figure) illustrates how the reaction between A and B must be supplied

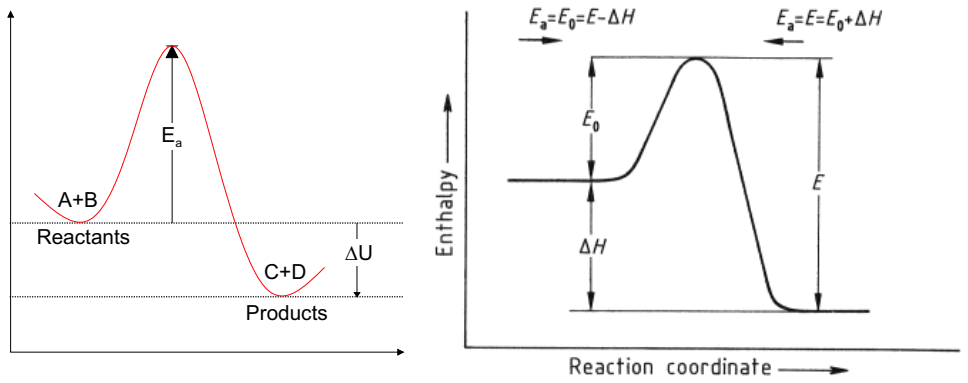

Figure 2-8: Activation energy.

Activation energy and relationship between E_a, E, E_o and H for exothermic (→) and endother--mic (←) reactions.

by an activation energy of E_a to be able to initiate. On the other hand, if one of the reactants is excited to a higher energy level, e.g. $B=M^*$, this activation energy can be overcome and the reaction will go as in (2-6). When the collision cross-section σ is given as a function of either energy or velocity, and the distribution function is solved by solving the Boltzman equation, the reaction coefficient, k, can be calculated by solving the integral:

$$k = \langle \nu\sigma \rangle_f = \int_0^\infty \nu\sigma f(\varepsilon)d\varepsilon \quad \text{where} \quad \int_0^\infty f(\varepsilon)d\varepsilon = 1 \qquad \textbf{Eq. 2-20}$$

If there is a reaction between two atoms or molecules, the procedure becomes fairly the same, except that one has to take account for the movement of both A and B, that is to take the average of two distribution functions, f_a and f_b.

The main type of reactions that may occur in volume plasma chemistry is given in figure 2-9, from which we see that the electron concentration in a non-equilibrium volume discharge is mainly determined by four reactions (Eliasson and Kogelschatz (1991a)). In a stationary case, the electron consumption by interception and recombination must balance with those electrons produced by ionisation and detachment. The free electrons in a gas discharge must transfer the energy gained from the electrical field through elastic and inelastic collisions with neutral gas molecules. In an elastic collision only translational energy is transferred while in an inelastic collision, an exchange occurs, between the internal energy of the electron and the internal energy of the molecule, in the form of

excitation or ionisation (which further may lead to dissociation). These type of collisions are sources to different molecular fragments. Some examples are different electron-oxygen molecule reactions, as given by Mukkavilli et al. (1988):

Ionization:
$e + O_2 \rightarrow O_2^+ + 2e$

Dissociative attachment:
$e + O_2 \rightarrow O^- + O$

Dissociation:
$e + O_2 \rightarrow 2O + e$

Vibrational excitement:
$e + O_2 \rightarrow O_2(a^*\Delta g) + e$

Dissociative ionization:
$e + O_2 \rightarrow O^+ + O^- + e$

The kinetic rate coefficient may theoretically be calculated for any electron- molecule reaction from the knowledge of the electron energy distribution function and the collision area for the actual process. Mukkavilli et al. (1988) have performed modelling of the chemical reactions resulting from a DC corona discharge in dry and moist air.

In a continuous discharge we have to encounter for both the production and the consumption of the free electrons. Here, an important loss factor is the ambipolar diffusion of electrons to the surrounding walls. The other important electron loss process is the recombination between electrons and ions which, depending on the electron density, may occur by the following reactions (Blaustein (1969)):

$e + AB^+ \rightarrow A + B$ $\quad A^+ + e + e \rightarrow A + e$ $\quad e + A + B \rightarrow A + B^-$

$A + e \rightarrow A + h_v$ $\quad e + AB \rightarrow A + B^-$

The important electron production process mainly takes place at the electrode surface (or close to the surface in respect to the distance between the electrodes). The large amount of bulk electrons are secondary electrons produced in the discharge volume by ionisation by collision:

$$e + A \quad \rightarrow \quad 2e + A^+ \tag{2-7}$$

High temperature electrons in a plasma can excite as well as ionize neutral atoms and molecules in the discharge, however the limit for excitation is lower than for the ionization (because of the electron energy distribution). The excitation process is the main cause for light emitted during the discharge and at the same time a process which produces active neutral species. A simple excitation is for instance the reaction:

Electron/Molecular Reactions			
Excitation:	$e + A_2$	$\rightarrow$	$A_2^* + e$
Dissociation	$e + A_2$	$\rightarrow$	$2A + e$
Attachment	$e + A_2$	$\rightarrow$	A_2^-
Dissociative attachment	$e + A_2$	$\rightarrow$	$A^- + A$
Ionization	$e + A_2$	$\rightarrow$	$A_2^+ + 2e$
Dissociative ionization	$e + A_2$	$\rightarrow$	$A^+ + A + e$
Recombination	$e + A_2^+$	$\rightarrow$	A_2
Detachment	$e + A_2^-$	$\rightarrow$	$A_2 + 2e$
Atomic/Molecular Reactions			
Pennning Dissociation	$M^* + A_2$	$\rightarrow$	$2A + M$
Pennning Ionization	$M^* + A_2$	$\rightarrow$	$A_2^+ + M + e$
Charge Transfer	$A^\pm + B$	$\rightarrow$	$B^\pm + A$
Ion Recombination	$A^- + B^+$	$\rightarrow$	AB
Neutral Recombination	$A + B + M$	$\rightarrow$	$AB + M$
Decomposition			
Electronic	$e + AB$	$\rightarrow$	$A + B + e$
Atomic	$A^* + B_2$	$\rightarrow$	$AB + B$
Synthesis			
Electronic	$e + A$	$\rightarrow$	$A^* + e$
	$A^* + B$	$\rightarrow$	AB
Atomic	$A + B$	$\rightarrow$	AB

The main types of reactions occurring in volume plasmas.

Where:

A, B= atoms;

A_2, B_2= molecules;

e = electrons,

$\pm$ = ions;

* = excited species.

Figure 2-9: Volume plasma reactions.

$$e + A \rightarrow e + A^* \quad (2\text{-}8)$$

Of additional interest to the discharge chemistry is that excited neutrals may engage reactions which is only subjected to neutrals in their ground state. If a molecule is being excited a possible dissociation may occur:

$$e + AB \rightarrow e + (AB)^* \rightarrow e + A + B \quad (2\text{-}9)$$

For this to occur, the energy of excitation must exceed the energy of dissociation. Not only is this an effective mechanism for the production of free radicals, the products also

hold a kinetic energy which exceeds that of the surrounding neutrals.

One of the most important elementary gas phase processes, from a plasma chemical point of view is therefore, the excitation of neutral atoms and molecules, which in turn will produce free radicals and active neutrals. Both radicals and active neutrals are initiators for neutral chain reactions within the plasma.

* * *

CHAPTER 3.

THEORY ON NITROMETHANE DECOMPOSITION

3.1 INTRODUCTION

Nitro is an abbreviation for nitromethane, CH_3NO_2, which is used as an additive in 2-stroke model engine fuel. Common percentages of nitromethane in model fuel range from 0 % up to 40 %, for high performance marine engines. Marine engines typically can run higher nitro percentages because they are water cooled, which allows them to run hotter burning fuel. (i.e. higher nitro percentages.) Other additives that are commonly found in RC fuel are oil, petroleum and/or synthetic, rust inhibitors, wetting agents and anti-foaming agents. These are all added to improve the performance and life of the engine. Nitromethane is an interesting explosive, both for civil and military purposes. Nitromethane has a high energy output, and is also the nitro paraffin for which most data is available (in liquid form). Nitro paraffins are any of a group of organic compounds formed by replacing one or more of the hydrogen atoms of a paraffin hydrocarbon with the univalent group, NO_2, as in nitromethane. It was first prepared in 1872 by Kolbe, and was for many years considered as a very stable compound. It was not until 1938 that McKittrick and co-workers reported that nitromethane could be detonated under conditions of strong confinement. This versatile chemical is used in a wide range of industrial applications including stabilizer for chlorinated hydrocarbons (1,1,1-trichloromethane), component for special fuels in internal combustion engines, solvent for many chemical reactions such as polymerization, corrosion inhibitor and raw material in the synthesis of many useful chemicals. It also has bactericidal properties and therefore, sometimes used in the coating industry. Some uses are:

- Raw material and stabilizer in the synthesis of many useful chemicals as for chlorinated hydrocarbons (1,1,1 -trichloromethane). Stabilizer for halogenated alkanes, in aerosol formations, in paste formulations for inks, in model aircraft

fuel and in the production of the fumigant chloropicrin.

- Fuel for rockets and specialized internal combustion engines.
- Solvent in many chemical reactions such as polymerizations; reaction-media fluid for Friedel-Crafts reactions; re-crystallization solvent; polar solvent in synthesis; solvent for zein.
- Corrosion inhibitor.
- Intermediate in synthesis of organic dyes, textiles, surfactants, insecticides, pharmaceuticals and explosives.

Nitromethane is an oxygen-donating fuel, not reliant completely upon atmospheric oxygen for combustion. It is liquid under normal conditions and classified as a toxic substance N°210 by INRS. NM is further classified as a flammable liquid, and can be combined with certain (amongst other) amines to form a cap-sensitive high explosive. This would make an example of a true binary explosive in which neither of the components is by itself an explosive. Such a blend of nitro paraffins would make an ideal compromise for purposes where the explosive must be relatively safe in liquid form, but highly detonable once dispersed into a droplet-air cloud. NM is relatively sensitive to shock initiated detonation, which may be regarded as both an advantage and a disadvantage depending on which purpose it is intended for.

Nitromethane is a useful explosive for studying detonation phenomena. It is particularly attractive in laboratory experiments because it is:

- A small molecule and so lends to theoretical as well as experimental studies
- Liquid at ambient conditions, and therefore homogeneous
- Transparent
- The simplest explosive containing the nitro functional group
- Relatively safe to handle
- Stable under normal temperature conditions
- Relatively low toxicity

This simplicity coupled with the fact that nitromethane can be strongly sensitized by small quantities of amines or by some other ways, makes it of interest for further studies. Because nitromethane is being used in industrial fine chemistry, it is interesting to study

its detonation properties in order to avoid any industrial hazards. The subset of its gas phase kinetics derived from CH_3 radical is related to the well-studied methane (CH_4) kinetics something which makes this molecule suitable for numerical modelling.

3.2 NITROMETHANE PROPERTIES

3.2.1 Physical and chemical data

Nitromethane is, under normal temperature and pressure conditions, a transparent liquid with a characteristic odour. The chemical raw structure is H_3CNO_2. It is not easily dissolved in water, only 9.5 *ml* per 100 *ml* water at 298 *K*. The principal physical and chemical characteristics for nitromethane are listed in table 3-1

Table 3-1: Principal physical and chemical characteristics for NM.

Parameters	Reference	Value	Denomination
Molecular Mass		61.04	*kg/kmol*
The C-N bond in NM has an energy of:	(Melius (1988)) (Cook (1987))	246.44 266.52	*kcal/mol* *kcal/mol*
Critical Point:	P_c T_c	62.30 587.95	*atm* *K*
Boiling Point		373.95	*K*
Melting Point		256.15	*K*
Density		1.1322	kg/m^3
Vapour Density (Air=1)		2.11	
Vapour Tension (At 298 K)		3.60	*kPa*
Refractive Index		1.3817	
Ionisation Potential		11.1	*eV*

The explosive properties of nitromethane are listed in table 3-2.

Table 3-2: Nitromethane explosive properties.

Parameters	Remarks	Value	Denomination
Chapman-Jouguet pressure		14	*GPa*
Detonation velocity	(at 298 *K*)	6247	*m/s*

Table 3-2: Nitromethane explosive properties.

Parameters	Remarks	Value	Denomination
Temperature of auto inflammation		418	^oC
Flame point	closed confinement	35	^oC
	open confinement	43	^oC
Explosion limits in air:	lower	7.1	*vol%*
	upper	63	*vol%*
Reaction-zone length	(at 298 *K*)	30	*mm*
Reaction-zone time	(at 298 *K*)	6	*ns*
Failure diameter in pyrex	(at 298 *K*)	16	*mm*
Failure diameter in brass	(at 298 *K*)	2.3	*mm*

The vapour pressure can be calculated with the commonly used formula:

$$\log P = -\left(0.215 \cdot \frac{A}{T}\right) + B \qquad \textbf{Eq. 3-1}$$

with P in *torr* and T in *Kelvin* where $P = P_{CH_3NO_2} = 33.75$ *torr* (at 298 *K*).

3.2.2 Thermodynamic data

The BURCAT (Burcat and Mc Bride (1994)) tables allow us to calculate the specific heat, the heat of formation and the entropy of nitromethane, as functions of temperature, according to the following polynomials:

$$C_p^0 = R \cdot (a_1 + a_2 T + a_3 T^2 + a_4 T^3 + a_5 T^4) \qquad \textbf{Eq. 3-2}$$

$$H_T^0 = RT \cdot \left(a_1 + \frac{a_2}{2} T + \frac{a_3}{3} T^2 + \frac{a_4}{4} T^3 + \frac{a_5}{5} T^4 + \frac{a_6}{T}\right) \qquad \textbf{Eq. 3-3}$$

$$S_T^0 = R \cdot \left(a_1 \ln T + a_2 T + \frac{a_3}{2} T^2 + \frac{a_4}{3} T^3 + \frac{a_5}{4} T^4 + a_7\right) \qquad \textbf{Eq. 3-4}$$

The coefficients a_1 to a_7 are given in table 3-3, for two temperature ranges and atmospheric pressure (1 *atm* = 101325 *Pa*).

Table 3-3: Tabulated coefficients.

Tabulated values taken from "1994 Ideal Gas Thermodynamic Data for Combustion and Air Pollution Use" (Burcat and Mc Bride (1994)).

T (K)\a_i	a_1	a_2	a_3	a_4	a_5	a_6	a_7
T > 1000 *K*	0.7257E+1	0.9742E-2	-0.3299E-5	0.4975E-9	-0.2730E-13	-0.1227E+5	-0.1265E+2
T < 1000 *K*	0.1665E+1	0.1813E-1	0.1201E-5	-0.1243E-7	0.5600E-11	-0.1027E+5	0.1823E+2

When calculated at T = 298.15 *K* one obtains:

$$C^0_{p(g)} = 57.33 \quad J/(mol\ K)$$

$$\Delta H^0_f = -74.41 \quad kJ/mol$$

$$S^0 = 275.98 \quad J/(mol\ K)$$

with $C^0_{l(g)} = 106.17 \quad J/(mol\ K)$

and $\Delta H^0_f = -75.0 \quad kJ/mol$ (experimental)

The (C-N) bond breaking energy, denoted EC-N, and the heat of formation have been investigated by several investigators and are listed in table 3-4. The values found by Glänzer and Troe (1972), are the activation energies for nitromethane decomposition for high and low pressures. The C-N bond breaking energy (EC-N) is the energy needed to break the bond between a carbon atom and a nitrogen atom. Numerous scientists have shown that C-N bonds are weaker than C-H and H-N bonds in nitromethane molecules.

Table 3-4: Bond dissociation energy and heat of formation.

Values for bond dissociation energy and heat of formation obtained from several authors.

E_{C-N} [*kJ/mol*]	ΔH_{289} [*kcal/mol*]	Code	Calculation	Experimental	Low pressure	High Pressure	Reference
241.997	-16.48 (-69 *kJ/mol*)	X	X				Melius, C.F.,1986
	-17.91 (-75 *kJ/mol*)			X			Melius, C.F., 1986
266.699		X	X				Cook, M.D., Haskins, P.J.,1987

Table 3-4: Bond dissociation energy and heat of formation.
Values for bond dissociation energy and heat of formation obtained from several authors.

E_{C-N} [*kJ/mol*]	ΔH_{289} [*kcal/mol*]	Code	Calculation	Experimental	Low pressure	High Pressure	Reference
244.927 ± 2.0934	Activation energy					X	Glänzer, K., Troe, J., 1972
175.846	Activation energy				X		Glänzer, K., Troe, J., 1972
250.371			X				Seely, L.B, Tegg, D., Shaw, R., Berke, J.G., 1967
247.021			X				Benson, S.W., O'Neal, H.E.,1970
230.693			X				Dubikhin, V.V., Nazin, G.M., Manelis, G.B., 1971
192.593		X	X				Cook, M.D., Haskins, P.J., 1989
274.654		X	X				Cook, M.D., Haskins, P.JR,1989
252.464				X			Cook, M.D., Haskins, P.J.,1989
280.934		X	X				Zaslonko, I.S., Kogarko, S.M., Mozzhukhin, E.B., Petrov, Yu.P.,1972
201.385				X			Zaslonko, I.S., Kogarko, S.M., Mozzhukhin, E.B., Petrov, Yu.P.,1972

3.2.3 Solid nitromethane

The crystal structure of solid NM was determined by Trevino *et al*.. They found the structure to be ortho-rhombic with four molecules per cell. The structure is made of columns of molecules with the molecule's C-N bonds nearly parallel to each other and perpendicular to the axes which are in the crystallographic e-direction.

3.3 THERMAL DECOMPOSITION OF GASEOUS NM

There have been numerous earlier studies on the thermal decomposition of nitromethane, where the majority of the experiments have been carried out below 1000 K using pure (mostly) liquid CH_3NO_2. Because of the complexity of the reactions involved, it has been rather difficult to accurately determine the rate for the initial dissociation process and the mechanism for the overall reaction mechanism.

3.3.1 The reaction scheme of gaseous NM decomposition

The initial step for the decomposition of nitromethane is the one suggested by Glänzer and Troe (1972) for low pressure:

$$CH_3NO_2 + M \quad \rightarrow \quad CH_3 + NO_2 + M \tag{3-1}$$

Numerous workers have agreed that the initial step may be visualized as shown in figure 3-1. After the C-N bond splits, the reaction mainly proceeds in two parallel pathways (Guirguis et al. (1983)). The first pathway starts with CH_3NO_2 attacked by radicals to form CH_2NO_2, which unimolecularly decomposes to form formaldehyde. The second pathway starts with the methyl and nitrogen dioxide reacting to form methoxy radicals, which decompose almost instantaneously to give formaldehyde. The CH_2O from both pathways is then attacked to produce formyl radicals (HCO). These radicals react later with NO_2 to yield the products NO, CO, and CO_2. A third and minor pathway is included at the end of the figure. It begins with the methyl radicals recombining to form ethane, ethyl radicals and ethylene. Ethane and ethyl radicals are then reduced to ethylene which when attacked by OH radicals gives CH_2O and CH_3 (Guirguis et al. (1983)).

It is believed that the radical reactions do not release enough energy to compensate for that energy consumed by the decomposition of nitromethane. As a result, although the concentration of the radicals reaches its maximum steady state level early in the reaction process, ignition does not occur until all the nitromethane is consumed. The energy released then by the radical reactions increases the temperature, and rapid ignition occurs (Guirguis et al. (1985)).

3.3.2 Thermal decomposition of nitromethane in shock tubes

There have been few studies on thermal decomposition of nitromethane in shock tubes. One of the first experiments where the values for this unimolecular dissociation reaction at

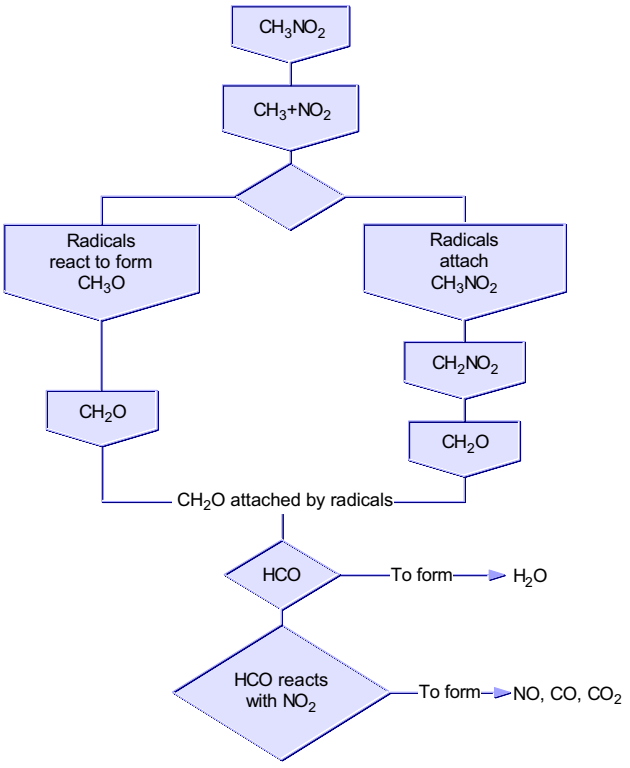

Figure 3-1: NM decomposition.

Schematic representation of the NM decomposition (Guirguis et al. (1983), Guirguis et al. (1985).

the high and low pressure limits were determined was realized in Switzerland by Glänzer and Troe (1972). They studied the decomposition of gaseous nitromethane highly diluted in argon ($1.5*E^{-6} < C_{Ar} < 3.5*E^{-4}$ mol/cm^3) at temperatures between 900 and 1500 *K*. Concentration profiles of CH_3NO_2 and NO_2 were recorded. It was observed that the unimolecular reaction was in its fall-off range (between high- and low pressure conditions). However by choosing a wide enough pressure range, they managed to separate the high- and low pressure dependency on the global decomposition rate.

at low pressure:

$$k_0 = 10^{17.1} \exp\left(-\frac{21.13}{T}\right) \cdot [Ar] \qquad \left[\frac{cm^3}{Mol \cdot s}\right] \qquad \textbf{Eq. 3-5}$$

and at high pressure:

$$k_0 = 10^{16.25}\exp\left(-\frac{29.44}{T}\right) \qquad \left[\frac{1}{s}\right] \qquad \textbf{Eq. 3-6}$$

Recently Perche, Tricot and Lucquin (1979a) confirmed this pressure dependency. They studied the decomposition reaction at low pressure and temperature conditions in an attempt to establish the mechanism for the overall decomposition reaction. A mechanism consisting of some 30 reactions was employed to simulate the formation of various products such as: CH_2O, HCN, CH_3OH, CH_4, H_2O, NO_x, CO_x, N_2O and N_2. The measurements were made by GC analysis and/or UV absorption. Reasonable, semi quantitative agreement between observed and calculated profiles could be achieved by judicious choice of rate constants for the selected reactions.

Hsu and Lin (1985) used a stabilized CW CO laser to study the kinetics of the production of NO and CO, which are two of the key products in CH_3NO_2 decomposition at high temperature. Their objective was to establish a reasonable mechanism for the simulation of these two chemically active intermediates, which undoubtedly play an important role in the energy release in ignition or detonation of nitromethane at high pressure and temperature conditions. Highly diluted CH_3NO_2/Ar mixtures (0.15-0.75 *vol%* CH_3NO_2) were used in incident shock tube experiments over the temperature range from 940 to 1520 *K* and pressure range between 0.4-1.0 *bar*. A mechanism consisting of 37 chemical reactions was used to model the formation of NO and CO over the entire range of the experimental conditions. The model used for the reaction rate constants for the pyrolysis of nitromethane was the one developed by Perche, Tricot and Lucquin (1979a). For the elementary reactions and the rate constants of the global reactions, the values found by Glänzer and Troe (1972), were used. The exploration of the experimental results and those found from the model showed that:

- NO_2 is formed by the rupture of the nitromethane C-N bond (which is a result already stated by other authors).
- The main part of the NO formed is a result of the reaction:

$$CH_3 + NO_2 \rightarrow CH_3O + NO \qquad (3\text{-}2)$$

- The main paths for the CH_2O (formaldehyde) formation (which are the precursor of CO) are the following:

$$CH_3O + M \rightarrow CH_2O + H + M \qquad (3\text{-}3)$$

$$CH_3NO_2 + H \rightarrow CH_2NO_2 + H_2 \quad (3\text{-}4)$$

$$CH_3NO_2 + OH \rightarrow CH_2NO_2 + H_2O \quad (3\text{-}5)$$

$$CH_2NO_2 \rightarrow CH_2O + NO \quad (3\text{-}6)$$

- The formation of C_2H_6 and other C_2's slows down the formation of CO.

Reaction (3-4) and (3-5) gives CH_2NO_2, which by unimolecular decomposition produces CH_2O. Hsu and Lin (1985) also showed that NO is a product formed early in the pyrolysis and that CO is formed later in the process. In the same year as Hsu and Lin (1985), Guirguis et al. (1985) performed shock tube experiments on the decomposition of pure nitromethane in an attempt to improve the registration of the pressure signals. The temperature conditions (1000-1600 *K*) were close to those employed by Glänzer and Troe (1972). The authors where able to show the very important role of NO_2 on the flame acceleration. They also observed that the inflammation did not occur before all of the nitromethane had been consumed. According to earlier studies on the decomposition of nitromethane (measured by UV absorption on 239 ±2 *nm*) by Zaslonko et al. (1972), using temperatures ranging between 1030-1580 *K* and a pressure range between 1-2.8 *atm*, the three first steps of the decomposition are:

$$CH_3NO_2 \rightarrow CH_3 + NO_2 \quad (3\text{-}7)$$

$$CH_3 + NO_2 \rightarrow CH_3O + NO \quad (3\text{-}8)$$

$$CH_3 + NO_2 \rightarrow CH_3ONO \quad (3\text{-}9)$$

They also found that the reaction rate constant, k, should be on the form:

$$k = 10^{12.8} \exp\left(-\frac{201.25}{RT}\right) \quad \left[\frac{1}{s}\right] \quad \textbf{Eq. 3-7}$$

This means that the activation energy for this reaction is lower than the expected value for a unimolecular decomposition. In fact the activation energy for the C-N bond is somewhere between 217.56 and 220.5 *kJ/Mol*. Zaslonko et al. (1972) explained this by saying that the probability of having a chain reaction was low in this case, due to the observation that the methyl radical formed is rapidly transformed to CH_2NO_2, which is only slightly activated by the following reaction:

$$CH_3 + CH_3NO_2 \rightarrow CH_4 + CH_2NO_2 \quad (3\text{-}10)$$

3.3.3 Numerical methods

The first studies of NM pyrolysis were reported by Taylor and Vesselovsky (1935). Considerably later, plausible initiation steps were deduced by Cotrell, Graham and Reid (1951). The first reliable measurements of the rate of unimolecular decomposition of NM and the effects of pressure was done by Glänzer and Troe (1972) using a shock tube. More recently an attempt was made (Perche, Tricot and Lucquin (1979a), Perche, Tricot and Lucquin (1979b)) to construct a detailed chemical reaction mechanism based on static experiments operating at extremely low pressure and temperature. Based on some of this work, Guirguis et al. (1983) continued the development of the reaction mechanism for the NM decomposition.

Guirguis et al. (1985) later presented a mechanism for ignition of high-temperature gaseous NM. The temperatures and pressures behind the reflected shock were in the range 1000-1600 *K* and 1-10 *atm*. Measurements were made of the time evolution of the pressure at the end wall, as well as of the simultaneous pressure and NO absorption at a given position in the tube. In the proposed reaction mechanism, initiation starts with the C-N bond breaking yielding CH_3 and NO_2. The Methoxy and CH_2NO_2 radical then propagate the reaction through two parallel pathways, both producing CH_2O, which when attacked by OH and H radicals, yields HCO radicals, carrying the reaction to completion.

In the same year, Hsu and Lin (1985) studied the decomposition of NM in a shock tube using a frequency stabilized CW CO laser to measure the real time production of NO and CO. They used highly diluted NM/Ar mixtures (0.15-0.75 *vol%*) in incident shock experiments over the temperature range from 940-1520 *K* and pressure range from 0.4-1.0 *atm*. Based on a mechanism consisting of 37 chemical reactions, they were able to model quantitatively the NO profile over the entire temperature range.

One study (Cook and Haskins (1987)) was aimed to prove that the first step of the nitromethane decomposition is the rupture of the C-N bond, that is:

$$CH_3NO_2 \quad \rightarrow \quad CH_3 + NO_2 \tag{3-11}$$

It was found that the energy necessary to break the C-N bond (266.27 *kJ/mol*) was much smaller than the energy necessary to break the C-H bond. The authors therefore concluded that the initial step in the nitromethane decomposition must be the suggested reaction (3-11).

3.4 OXIDATION OF GASEOUS NM

The understanding of the reaction between nitromethane and oxygen is important, because it is relevant for chemical processes which may play a role in the nitration or oxynitration of hydrocarbons, or in the formation of photochemical smog. In fact, the oxidation of nitromethane may occur via numerous radical reactions which are equally likely to occur during the course of both these processes (Tricot, Perche and Lucquin (1981)). Only few studies have been carried out on the oxidation of nitromethane. The latest works have been done by Tricot, Perche and Lucquin (1981), Dechaux and Perche (1983) and Kang et al. (1991).

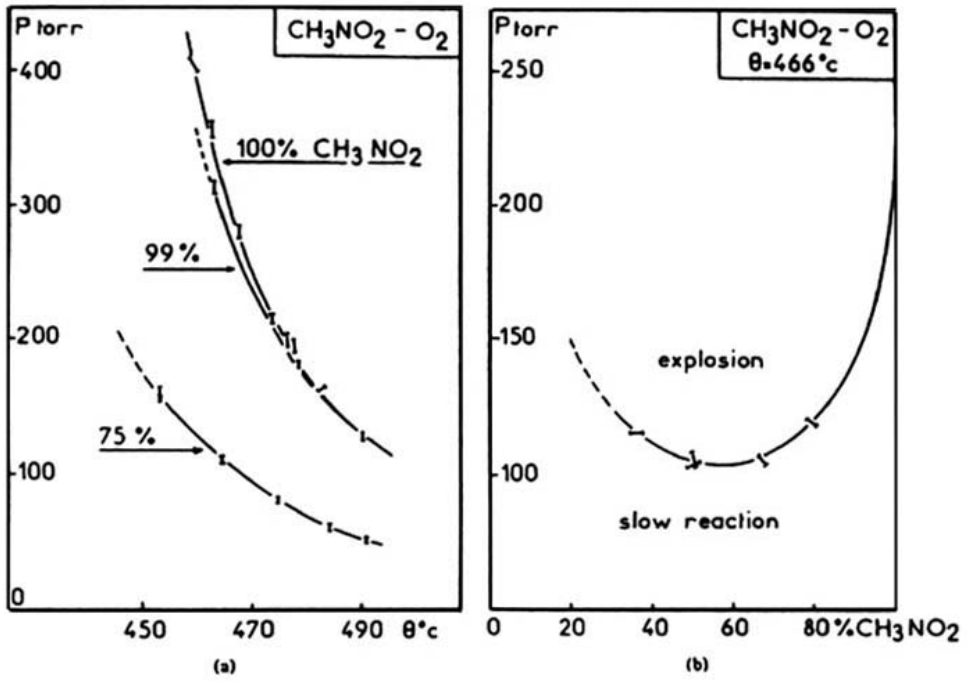

Figure 3-2: NM Explosion limits

Explosion limits for mixtures of NM-O_2 from Tricot, Perche and Lucquin (1981).

Taylor and Vesselovsky (1935), Hillenbrandt and Kirkpatrick (1953) and Frejacques (1953) showed that oxygen has a prompting effect accompanied by a reduction in the overall stoichiometry of the transformation when compared with nitromethane alone.

The explosive reaction of nitromethane with oxygen has been studied by several

authors; Choen (1963), Borisov, Kogarko and Skachkov (1966) and Tricot, Perche and Lucquin (1981). Dechaux and Perche (1983) determined the explosion limits as a function of temperature and oxygen concentration.

Tricot, Perche and Lucquin (1981) found the explosion limits for NM-O_2 mixtures to be remarkably lower than compared to pure NM (see plot in figure 3-2). In addition to the oxidative behaviour of NM, slow- and explosive reactions were investigated. It was found that the explosion limit was reduced significantly when oxygen was added (figure 3-2a), and that the overall activation energy found from these explosions limits decreased when the oxygen concentration increased. When the initial temperature was held constant and the reactant mole fraction was varied, the explosion limit curve showed a maximum at approximately 50 % NM/ 50 % O_2 (figure 3-2b). During the course of the slow reaction, increasing the amount of NM or oxygen, the main difference was that the global rate only seemed to be slightly sensitive to oxygen concentration, but markedly sensitive to the NM concentration.

3.4.1 Theories on the ignition process

Ignition is a transition from a non-reactive to a reactive state in which external stimuli lead to thermo-chemical runaway followed by a rapid transition to self-sustained combustion. Spontaneous ignition may occur when a reactive mixture is formed, raised to a definite temperature and pressure, and then left alone. It may burst into flame after a certain time. At the onset of a spontaneous ignition there is usually a rapid rise in temperature, emission of visible radiation and rapid chemical reactions.

The usual conditions for ignition are given by the three parameters; temperature, time and turbulence. The ignition temperature is defined as the lowest temperature at which explosion may occur under given conditions in a given mixture.

Ignition of High-Temperature Gaseous NM

A detailed chemical mechanism describing ignition of pure gaseous nitromethane at high-temperature was compiled and tested by Guirguis et al. (1985), using shock tube experiments. The temperatures and pressures behind the reflected shock were in the range 1000-1600 K and 1-10 atm, respectively. The proposed initiation mechanism, as visualized in figure 3-1, starts with the breaking of the C-N bond, which yields CH_3 and

NO_2. Methoxy and CH_2NO_2 radicals then propagate the reaction through two parallel pathways.

Both pathways produce CH_2O which, when attacked by OH and H radicals, yields HCO radicals which carry the reaction towards completion. As long as unreacted nitromethane is present, its unimolecular (C-N bond rupture) reaction serves as an energy sink, preventing ignition. As a result, although the radical concentrations reach their maximum level early in the overall process, ignition does not occur until all NM is consumed. Then, the energy released by the radical reactions causes rapid ignition. The computations show that the reaction $NO_2 + H \rightarrow OH + NO$, plays a key role in accelerating ignition in NM because it controls the OH-concentration, due to the absence of other efficient routes to OH. This effect is also expected in other explosives containing C, H, and the nitro or the nitrate groups, because other efficient OH formation routes do not exist. Comparison with experiments shows that the proposed mechanism predicts correct induction times within the pressure and temperature range of the experiments.

Ignition of Shocked Condensed Nitromethane

Bardo (1985) has proposed another reaction mechanism whose reaction pathways are calculated with semi empirical electronic structure methods. Ten steps are needed to obtain the known detonation products. All steps are pressure accelerated (negative volume of activation) so that they have the high rates necessary to satisfy the temporal constraints imposed by strong initiating shocks.

In contrast to reactions occurring at high temperatures in gas, liquid or solid phases at ambient pressure, high compression greatly accelerates some reactions and greatly reduces the probability of others. The mechanism is based on the formation of a dimer from the head-to-tail reaction of CH_3NO_2 monomers. This first step is highly exothermic (-48 *kcal/mol*) and is the fastest possible bimolecular reaction for nitromethane. Nevertheless for any pressure under 50 *kbar* this step is slow. But the half-life $t_{1/2}$ of this reaction reaches the value of 5.1^{-12} *s* at P= 80 *kbar* and T = 850 *K*. Because there is a change in rate determining step around P= 50 *kbar*, the interesting possibility exists that the ability of NM to achieve a stable high-velocity detonation may be determined by this change in rate determining steps in the neighbourhood of 50 *kbar*. Indeed, the half-life for C-N bond scission, or for any unimolecular bond breaking process in CH_3NO_2, is much larger than the times associated with shock initiation which are often less than a

microsecond. As shock pressures higher than 70 *kbar* is needed to achieve initiation of detonation in homogeneous solid and liquid NM (Hardesty (1976)), the bimolecular reaction is the overwhelmingly dominant reaction at all high pressures of interest for ignition of condensed nitromethane.

3.4.2 Ignition delay time

When a mixture of a fuel and oxidizer is subjected to shock heating, it ignites after an induction period known as the ignition delay time. This delay is due to the exponential behaviour of the overall oxidation rate and originates from chain branching reactions and/or adiabatic temperature increase during the course of the reaction. An analysis of the phenomenon can be found in a review by Lifshitz (1984). Ignition delay times are determined by a complex set of chemical reactions and depend on initial temperature, pressure, and gas composition. A useful format for presenting the data is on the basis of the Arrhenius rate relation, and the ignition delay time can be written as:

$$\tau = K \cdot \exp\frac{E}{RT} \cdot [NM]^l[O_2]^m[Ar]^n \qquad [sec] \qquad \textbf{Eq. 3-8}$$

When some kinetic data are available, ignition delay times are very useful in modelling, to verify if the proposed model is complete and reasonably correct. While these data are probably the most complex shock tube data to understand, they are substantially simpler than comparable data in flames. Generally, the ignition delay time increases when the temperature decreases.

Kang et al. (1991) are the only workers who have studied ignition delay times of nitromethane. They have investigated ignition delay times of $NM/O_2/Ar$ mixtures behind reflected shocks. The ignition delay time was defined as the time interval between the arrival of the reflected shock and a following strong pressure spike. The experiments were carried out over the temperature range 1250-1900 *K*, behind reflected shocks. From the experimental results, an empirical correlation was derived,

$$\tau = 10^{-1.11}\exp\left(\frac{1075}{T}\right) \cdot [CH_3NO_2]^{0.59}[O_2]^{-0.72}[Ar]^0 \quad [sec] \qquad \textbf{Eq. 3-9}$$

which can be verified by plotting all the experimental kinetic data as shown in figure 3-3. Dorko et al. (1975) found a similar correlation over the temperature range 1200-1800 *K*, studying ignition delay times of $CH_4/NO_2/O_2/Ar$ mixtures:

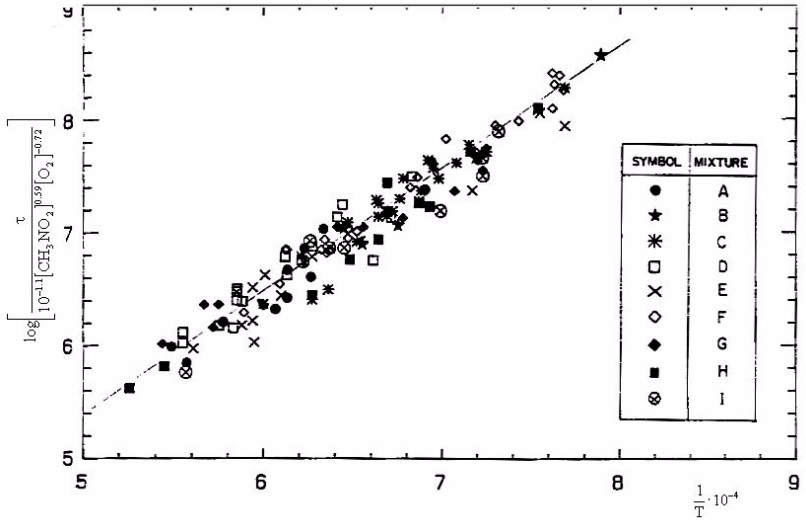

Figure 3-3: Plot of log(y) vs. 1/T.

Plot of log(y) vs. 1/T for the nine mixtures. All the experimental points coincide to a single line (Kang et al. (1991)).

$$\tau = 6.45 \cdot 10^{-5} \exp\left(\frac{14453}{T}\right) \cdot [CH_4]^{-0.32}[NO_2]^{-1.3}[O_2]^{-0.2}[Ar]^{1} \quad [\text{sec}] \qquad \textbf{Eq. 3-10}$$

In table 3-5 the exponent and activation energies for some selected explosive gaseous mixtures have been extracted from various sources. As with alkane mixtures, the argon content in the NM/O_2/Ar mixture has no influence on the ignition delay time. The concentration of NM, however, increasingly inhibits detonation, having a reaction order almost equal to that of propane. It can be seen that the role of O_2 as a detonation promoter is reduced in the case of NM mixtures when compared to other alkane mixtures. A possible explanation for this, might be the substituted NO_2 -group.

Table 3-5: Comparison of different explosive fuel (gas)/O_2/Ar mixtures.

Comparison of exponents and activation energies from different correlations for ignition delay times.

Fuel	**Fuel exponent**	**O_2 exponent**	**Ar exponent**	**E_a [kJ/mol]**
CH_4	0.33	-1.03	0.0	193.891
C_2H_6	0.46	-1.26	0.0	143.189

Table 3-5: Comparison of different explosive fuel (gas)/O_2/Ar mixtures.

Comparison of exponents and activation energies from different correlations for ignition delay times.

Fuel	Fuel exponent	O_2 exponent	Ar exponent	E_a [kJ/mol]
C_3H_8	0.57	-1.22	0.0	176.683
CH_3NO_2	0.59	-0.72	0.0	89.43
CH_4 NO_2	-0.32 -1.3	-0.2	1.0	120.161
C_2N_2	-1.01	-0.21	0.22	145.701

The activation energy is markedly decreased compared to methane, which could be due to one of two factors; the C-N bond energy or the reactivity of the NO_2 radical giving rise to additional chain branching processes for the detonation reaction. We can see from the correlation for the ignition delay time that it has a much higher sensitivity towards the activation energy rather than the concentration of the reactants.

3.5 NM DETONATION STRUCTURE

For a number of years it has been known that most gas phase detonations propagate in an oscillatory manner and contain shock waves which propagate back and forth across the detonation reaction zone, perpendicular to the direction of motion of the detonation. The transverse shock waves intersect with the main shock to form a mach-stem configuration and the point of intersection is known as a triple point. The motion of the triple points inscribes a complex pattern on the walls of a properly prepared detonation tube.

Experimental results have shown that the pattern quite often is rectangular, and the size of the pattern is a function of the particular chemical system. Each of the diamond shaped regions is called a detonation cell and the corners of each cell are places where oppositely travelling transverse waves have collided. Within each cell, the detonation has a maximum velocity immediately after the collision of two triple points, as a result of very high local pressures generated by the reflection of the transverse waves. The pressure, the velocity of the main detonation wave, and the velocities of the transverse waves all decay to a minimum value which is reached just prior to the next collision process. It should be noticed that only the average velocity is equal to the Chapman-Jouguet velocity and that

the main wave decays from an overdriven state to an under driven state over the distance of the cell.

Shchelkin (1959) suggested that processes involved in condensed-explosive detonation should be very similar to those found in gaseous mixtures. The detonation wave should be an unstable shock wave initiated combustion process, locally intensified by collisions of oblique waves.

Presles, Desbordes and Guerraud (1995) examined the detonation structure in NM and NM/O_2 mixtures and found that its structure presents some remarkable specific features in comparison with classical gaseous explosive mixtures.

Comparison between gaseous and liquid NM detonation structure

Numerous experiments have been performed to study the nitromethane detonation structure. However these studies have mostly been performed on nitromethane in liquid or solid phase. Dremin, Rozanov, and Trofinov (1963) did one of the fist studies on the structure of nitromethane detonations in condensed phase. They made simultaneous butt-end and lateral smoked-foil records of liquid nitromethane detonation. These records clearly showed dark zones and also a backward progress of detonation over these zones which led the authors to define them as zones of undetonated nitromethane.

Apparently, nitromethane loses its transparency under the action of shocks travelling from detonating zones of the charge. The detonation front does not spread over the whole cross section of the charge, and zones of unreacted substance remain, capable of subsequent detonation. The formation of these unreacted zones seems to be accounted for by the inner structure of the detonation front. As the reaction occurs only in individual centres, in regions with collision between oblique waves, the luminosity of the detonation front should involve microscopic inhomogenities. The addition of as little as 15 to 16 *vol%* of acetone (miscible with NM in any proportion) permitted recording of inhomogenities in the luminosity of the detonation front (that was not possible in pure NM because of the limited resolution of the high-speed smear camera).

In this case the detonation record represents a system of intersecting bright and dark bands of a similar slope. This slope represents the propagation velocity inhomogenities in the detonation front. The butt-end records show that the leading front luminosity is inhomogeneous at any time.

This may indicate that the reaction is not present throughout the cross section, but at various centres, and this shows, in turn, that the detonation front is not smooth. The average inhomogenity dimensions were estimated from butt-end records. The number n of bright (or dark) bands over the charge diameter d was counted by means of a micro photometer. In accordance with the theory worked out by Shchelkin (1959), the inhomogenity scale increases with increasing time of reaction, i.e. with increasing percentage of acetone in the mixture. Experiments carried out with tubes of a length ten times their diameter showed that the dimensions of inhomogenities in the detonation front do not change with time. This means that this mode of detonation is stationary.

Later Urtiew, Kusubov, and Duff (1970) performed a study similar in nature to that of Dremin, Rozanov, and Trofinov (1963). However, because of differences in the experimental conditions the results are not directly comparable. These results showed that the detonation front in nitromethane is non-uniform and unstable, and that the cell pattern showed a similar structure as for the cell structure in gaseous nitromethane detonations. A wall-tracing recording device was used to study the detonation in homogeneous nitromethane/acetone mixtures. The authors observed that for a 80 *vol%* nitromethane and 20 *vol%* acetone mixture a non-uniform but very regular pattern quite similar to that observed on the carbon-soot records (smoked-foil) of gaseous detonations. They observed a multiheaded detonation front with cellular structure in some nitromethane-acetone mixtures, intrinsically unstable and travelling as a whole at a constant detonation velocity near its theoretical C-J value. For instance, after 2 *ms* and only 9 *cm* of travel in a 2x2 cm^2 tube, the wave had reached an apparent steady state (5.65 *mm/μsec* for 80/20 mixture or 5.46 *mm/μsec* for 75/25 mixture). These high values indicate that the observed processes are full-scale detonations.

Surface indentations found along the wall traces provide additional evidence that the traces were produced by localised peaks of pressure such as those associated with triple wave intersections. At any time each individual cell (size of 1 *mm* for 80/20 mixture in a 1.5x1.5 cm^2 tube; the cell size being the distance between the two parallel lines measured perpendicular to the tube axis, and correspondingly for the multiheaded detonation to Dremin's definition, d/n, which is the ratio of the tube diameter to the number of bright or dark bands appearing on the film) is bounded by wave discontinuities that are in continuous transverse motion and collision. As the initial conditions are varied by decreasing the tube cross section or increasing the amount of acetone diluent, the cell size

grows bigger. But a critical case of steady-state single mode detonation has not been reached. However, marginal detonation was observed in a transient state when the initial conditions and the confinement were such that the process decayed to extinction. In all such cases, just before the extinction occurred, the cell size became comparable to the tube width. Assuming that the extinction of pure nitromethane also occurred when the cell size became comparable to the tube size and that there were no special effects related to the two-dimensional nature of this experiment or to confinement, they found a size of the non-uniformity in pure nitromethane of the order of 0.6-0.7 *mm*. Other experiments have been carried out to study the behaviour of the detonation process as it propagates through a tube and encounters a change in the cross sectional area.

Further Dremin, Rozanov, and Trofinov (1963) realised butt-end records showing that under certain conditions detonation properties can be strongly altered when detonation passes from a narrow into a broad tube. Indeed, if the progress of detonation in nitromethane is accounted for by inhomogenity collisions in the detonation front, and if in some part of the front the oblique waves meet nothing to interact with (because of the tube enlargement), then inhomogenities cease to initiate reactions in this site of the front, and this results in the formation of an unreacted zone. This decrease of the detonation front can lead to the termination of the detonation. The butt-end records of such a process show that the lines corresponding to termination of the reaction are seen to be parallel to those for propagation of inhomogenities, i.e. the rate of diminution of the detonation front is equal to the velocity of propagation of inhomogenities over its surface. They found a critical diameter of 17 to 18 *mm* at 18 ^{o}C for pure nitromethane, and with rise in acetone content this value rapidly increases.

The tube enlargement effects have also been observed by Urtiew, Kusubov, and Duff (1970). They explained it on the basis of a complex triple wave structure in which the process is carried on behind the transverse moving waves and sustained by continuous interactions and head-on collisions of such. During the transition into sudden enlargement of the area, the normal and steady detonation suffers a momentary lack of reflection which locally attenuates the process to such an extent that it goes to extinction. This extinct region, where no reaction takes place, propagates toward the centre of the tube with the velocity of sound corresponding to that behind the detonation wave, and as a result forms a triangular dome in the direction of the motion. If a wall of the larger tube is encountered before a certain state of attenuation is reached, the reflection off that wall re-ignites the

mixture; but revival of the process over the whole cross section additionally depends on the width of the non reactive zone, and also on whether the two reflected waves produce a sufficiently strong explosion centre upon their collision. Urtiew, Kusubov, and Duff (1970) also made records of the cell structure which confirmed those found by Dremin, Rozanov, and Trofinov (1963), showing that the cell structure in nitromethane condensed and gaseous phase detonations have a similar pattern. Howe, Frey and Melani 1976) made similar records of the cell structure in solid nitromethane detonations. Guirguis, Oran and Kailasanath (1986) used a numerical model to study the nitromethane cell structure. These results showed that the detonation front became more and more curved as the temperature of the induction period increased or when the energy of activation was decreased, both resulting in a more regular cell pattern.

3.6 EFFECTS OF ADDITIVES

Studying the effects of additives is of interest because of their ability to either enhance or inhibit shock initiation, and thereby alter the properties of nitromethane based gaseous or liquid mixtures.

Nitromethane sensitisation by Amines

It has been known for a long time that the sensitivity of nitromethane to shock initiation can be enhanced by addition of quite small quantities of various amines. Engelke, Earl and Rohlfing (1986) observed that the addition of diethylenetriamine (DETA) induced a large effect on NM detonation behaviour. For instance, by adding 0.030 *%* (weight) of DETA to NM the pyrex failure diameter originally of 16.2 *mm* becomes 9.6 *mm*, and the detonation reaction zone length is shorten by 20 *%*. This sensitisation was confirmed by Cook and Haskins (1987), using a NOL Large Scale Gap Test device. He also observed a gap value increase by NaOH addition (5 *%*). Russians workers (Kondrikov et al. (1977)) found similar effects with the organic bases di- and tri-ethylamine, thus the effect is not specific to a particular organic base.

Nitromethane sensitisation by UV-radiation

Engelke, Earl and Rohlfing (1986) and Kondrikov et al. (1977), discovered that exposure of NM to intense UV irradiation over several hours sensitised the detonation by causing a reduced failure diameter.

Effects of glass micro balloons

Micro balloons are principally used to make explosive emulsions more sensitive to shock initiation. Presles et al. (1989) performed experiments with an homogenous NM/MB suspension, the MB's having a size between 5 and 30 μm, where they managed to detonate the mixture at very low pressures. Adding a MB mass fraction of 20 % made it possible to initiate a detonation with a pressure of 15 *kbar* instead of 110 *kbar* as for pure nitromethane. Because of the large discrepancy between the NM density (1.135) and MB density (0.132), the addition of PMMA (3 %) as gelling agent was required to obtain an homogeneous mixture. Experimental measurements of the detonation velocity and pressure in NM-PMMA/GMB mixtures show that it is possible to change the NM detonation characteristics over a large scale, reaching very low values when high GMB concentrations are involved. Lee, Frost and Lee (1993) have made recent experiments using MB of much lager size (66 *mm*-2.4 *mm*). They managed to show that a brutal change in the detonation mechanism occurred depending on the size of the MB's, due to effects inside and between the MB's.

Effects of aluminium particles

Kato and Brochet (1976) have investigated NM/Al mixtures in order to bring experimental support to the postulate (Urtiew, Kusubov, and Duff (1970)) that failure process and cellular structure are strongly connected. The observation through the side wall of the tube has shown the regular repetition of failure and reignition processes which may be due to aluminium combustion. The butt-end record has demonstrated the origin and the mechanism of these processes. The failure and the reignition processes have been interpreted on the basis of the cellular structure. A sensitisation of the explosive mixtures by the increase of aluminium concentration has also been observed.

Sensitisation by Hydrazine

A study of the detonability of binary and ternary mixtures of nitromethane, hydrazine and methanol revealed that hydrazine strongly sensitises nitromethane and nitromethane/methanol mixtures. According to Forshey, Cooper and Doyak (1969), this is caused by the formation of the so-called aci-ion form.

Nitromethane-Oxygen-Argon gaseous mixtures

The expression as given by eq. 3-11 for the ignition delay time of $NM/O_2/Ar$ mixtures, was proposed by Kang et al. (1991), with E = 21.36 ±0.51 *kcal/mol*. It appears that argon has no influence on the ignition delay time. The concentration of NM, however, increasingly inhibits detonation, and its reaction order is almost equal to that of propane. The concentration dependence of the oxygen in these mixtures is anomalous, compared with the relative concentration dependence of fuel and oxidant in the hydrocarbon mixtures. The role of oxygen as a detonation promoter is reduced in the reaction of the NM mixtures. This could be due to the substituted nitrogroup. The experimental results (as visualized in figure 3-3) leading to the expression is given by (see chap. 3.4.2 on page 47):

$$\tau = 10^{-1.1} \exp\frac{E}{RT} \cdot [CH_3NO_2]^{0.59}[O_2]^{-0.72}[Ar]^0 \qquad \textbf{Eq. 3-11}$$

* * *

CHAPTER 4.

EXPERIMENTAL AND THEORETICAL STUDY OF NITROMETHANE SHOCK TUBE DECOMPOSITION

4.1 INTRODUCTION

Thermal decomposition (pyrolysis) and oxidation experiments of highly diluted gaseous nitromethane (NM = CH_3NO_2) behind a reflected shock was performed in a shock tube. A kinetic model is proposed to predict the nitromethane decomposition profiles and the ignition delays which are compared to the measured ones.

Based on results from earlier studies, the purpose of the present experiments was to verify and establish a representative reaction mechanism for the simulation of thermal high-temperature decomposition and oxidation of NM for gas phase, close to detonation conditions.

Thermal decomposition of NM

The experimental measurements have been performed on the thermal decomposition (pyrolysis) of highly diluted gaseous nitromethane (CH_3NO_2) behind a reflected shock. From before only few experiments on the pyrolysis behavior of gaseous NM have been performed. These kinds of experiments are usually done to collect information on the decomposition behavior of a selected component at different temperatures, pressures and concentrations. The most important information usually deduced from thermal decomposition, is the rate constant, k ($cm^3/mol \times s$), given by the evolution of the species concentration behind the reflected shock. From the form of the concentration evolution vs. time, calculated from the absorption signals registered by the monochromator, the reaction order may be deduced (zero, first, second or third order).

Such knowledge gives valuable information for computer modeling reaction schemes. Measured overall decomposition rates can be used to justify the global rate derived from

the modeling. Thermal decomposition experiments also gives valuable information on the molecular extinction coefficient, ε, which is a wavelength-dependent molar absorptivity coefficient with units of 1/(*Mole*×*cm*). This coefficient constitutes one of the variables in the Beer-Lambert Law, which is the linear relationship between absorbance and the concentration of a given species (see APPENDIX A).

The nitromethane used was an ALDRICH product, having a purity of at least 99.8 *%*. Two experimental series were done, the first one with NM diluted in nitrogen (0.3-1.0 *vol%* NM) and the second with NM diluted in argon (0.2-1.5 *vol%* NM). The experiments were performed in a 4.8 *m* long double membrane shock tube with an internal diameter of 52.5 *mm*. Pressure registrations were taken at four different locations close to the tube-end wall and UV spectroscopy was used to follow the dissociation of NM as a function of time during the passage of the reflected shock. For the measurement of the NM concentration profile a wavelength of 220 *nm* was selected based on the measured UV spectra of NM taken at the CNRS laboratory. For some experiments at higher pressure levels some of the experiments had to be performed at higher wavelengths chosen at 225 and 230 *nm*. In the first series the initial pressure in the high (p_4) and low (p_1) pressure section ranged between 1.1-4.0 *bar* and 30.2-131 *torr* respectively. In the second series these pressures ranged between 0.9-4.6 *bar* and 50-354.1 *torr*. The highest and lowest shock wave velocity was calculated to be 1.02 and 0.64 *km/s*, respectively. The strength of the shock was controlled by inserting membranes of different thickness and varying the initial pressure in the driver section.

According to the measurements of the thermal decomposition of NM an expression for the half-live time and the decomposition rate constant was found as a function of the inverse of the temperature of the reflected shock. The results showed that the decomposition reaction was of first order with respect to NM.

Decomposition experiments are often the precursor to auto-inflammation (ignition) experiments, in which oxygen is mixed with the component of current interest (oxidation). The purpose of these experiments is to study the time-lag before inflammation at given compositions. The delay time is defined as the time interval between the instant that the mixture was raised to the temperature and pressure of the reflected shock, and the time when we observe the start of the reaction between oxygen and the given species. If the pressure and the temperature are high enough, an inflammation will occur. Extending the experiments by introducing a third component in the mixture, a so-called sensitizer or

additive, may significantly alter the sensitivity to explosion. Some additives promote the sensitivity, while others will give the opposite effect.

NM Oxidation experiments

As a complement to and in parallel with the experiments on NM thermal decomposition, experiments where performed on decomposition of nitromethane/oxygen mixtures. The reactions of NM/O_2/Ar-mixtures behind the reflected shock were studied in the temperature range 995-1378 *K*, within the pressure range 44.3-599.5 *kPa* and with equivalence ratios between 0.5-3.5. The purpose of these experiments was to deduce the so-called ignition delay time, which is defined as the time span from the arrival of the reflected shock until emission is observed. The monochromator was set to register light emission at a wavelength of 235 *nm*.

4.2 EXPERIMENT

The experimental apparatus for composing the mixture necessary for the shock tube experiments consisted of a number of glass tubes connected to form a closed system as shown in figure 4-1. The system had connections to a vacuum pump, a manometer and the glass bulb in which the mixture was to be stored..

Liquid NM was injected into the evacuated system under ambient temperature conditions through a septum by a needle and vaporized into the 10 dm^3 glass bulb. The diluent (and eventually oxygen/additive) could then be supplied through a system of valves into the same glass bulb. The exact mixture composition was calculated by the law of partial pressures. To avoid impurities and condensed matter to enter the glass bulb, a liquid nitrogen trap was installed between the pump and the mixture rig. After each mixture had been made, the trap was emptied and the system cleaned thoroughly with alcohol to minimize the risk of collecting impurities which again once in the mixture, could influence the NM behavior. The necessary liquid volume could be calculated as a function of the desired vapour pressure measured by the manometer, depending on the ambient temperature. Assuming all the injected liquid vaporised, the necessary liquid volume is given by the relation:

$$V_l = \frac{P_g V_g M}{RT\rho} \qquad \textbf{Eq. 4-1}$$

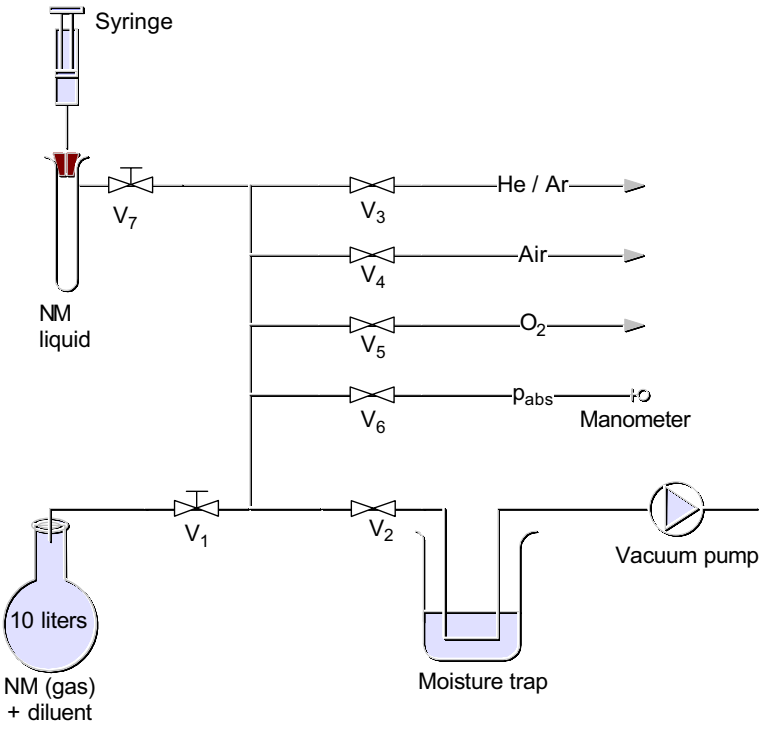

Figure 4-1: Experimental apparatus for preparing the mixtures.

P_g, M and ρ, represents the vapour pressure measured by the manometer, the molecular mass and the density of the injected liquid. R, T et V_g represent the gas constant, the ambient temperature and the total volume of the system, respectively.

4.2.1 Description and function of the current shock tube

The shock tube used for the experiments on the thermal NM-decomposition was of a double membrane type, which means that there is no need for a mechanical rupture system. A correct combination of membrane thickness and pressure ratio between the driver and intermediate section will insure a controlled rupture of the membrane. The LCSR-laboratory at CNRS Orléans has four shock tubes at their disposal of which three are in all in stainless steel but the fourth which has a low pressure section in pyrex glass for visualization purposes. The tubes are of different sizes and their use depends on the nature of the experiment. The principle of the double membrane system consists of separating the driver section and the working section by a intermediary section having a volume being negligible compared to the total volume of the two tubes. The pressure

between the two membranes is usually between P_4 and $P_4/2$, as shown in figure 4-2. Before each experiment the inert gas is introduced to both the intermediate and the driver section, up to a pressure of about half the final pressure in the driver section. A low pressure reservoir is connected to the intermediate section separated by a fast opening manual valve. The opening of this valve will cause the membrane to rupture. Altogether the tube consisted of five separable sections with a total length of 4,802 *m*. All the parts were made of stainless steel type Z2CN 18-10. The inner surface had been polished to avoid perturbation by wall-effects. Figure 4-3 visualizes the experimental setup.

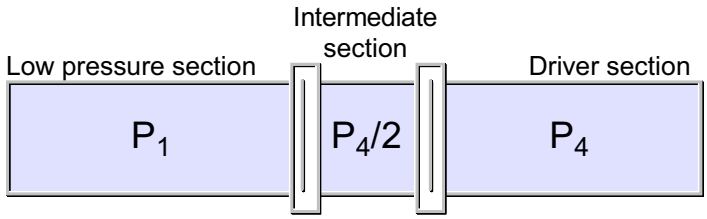

Figure 4-2: The Pressure filling.

The High Pressure Section

Some characteristics of the high pressure section (figure 4-4) where:

- Internal diameter, d_i = 114.2 *mm*
- Thickness, t = 6.02 *mm*
- Length, l = 1.0 *m*
- Volume, V = 10.0 dm^3
- Max total pressure, p_{max} = 40.0 *bar*

The Intermediary Section

The closed tube end had two external connections, one for the filling of the piston gas and another for the evacuation. The open end had joints for bolting to the next section. This section consisted of two flanges bolted on a short tube element. Between each flange and the tube element, a Mylar polyester membrane with a specific thickness (depending on the specific pressure in the driver section) was fastened and forced to stretch between two rubber gaskets being compressed against each other. The intermediate section had an internal diameter of 52.5 *mm* (as for the low pressure section), was 52 *mm* long and had a

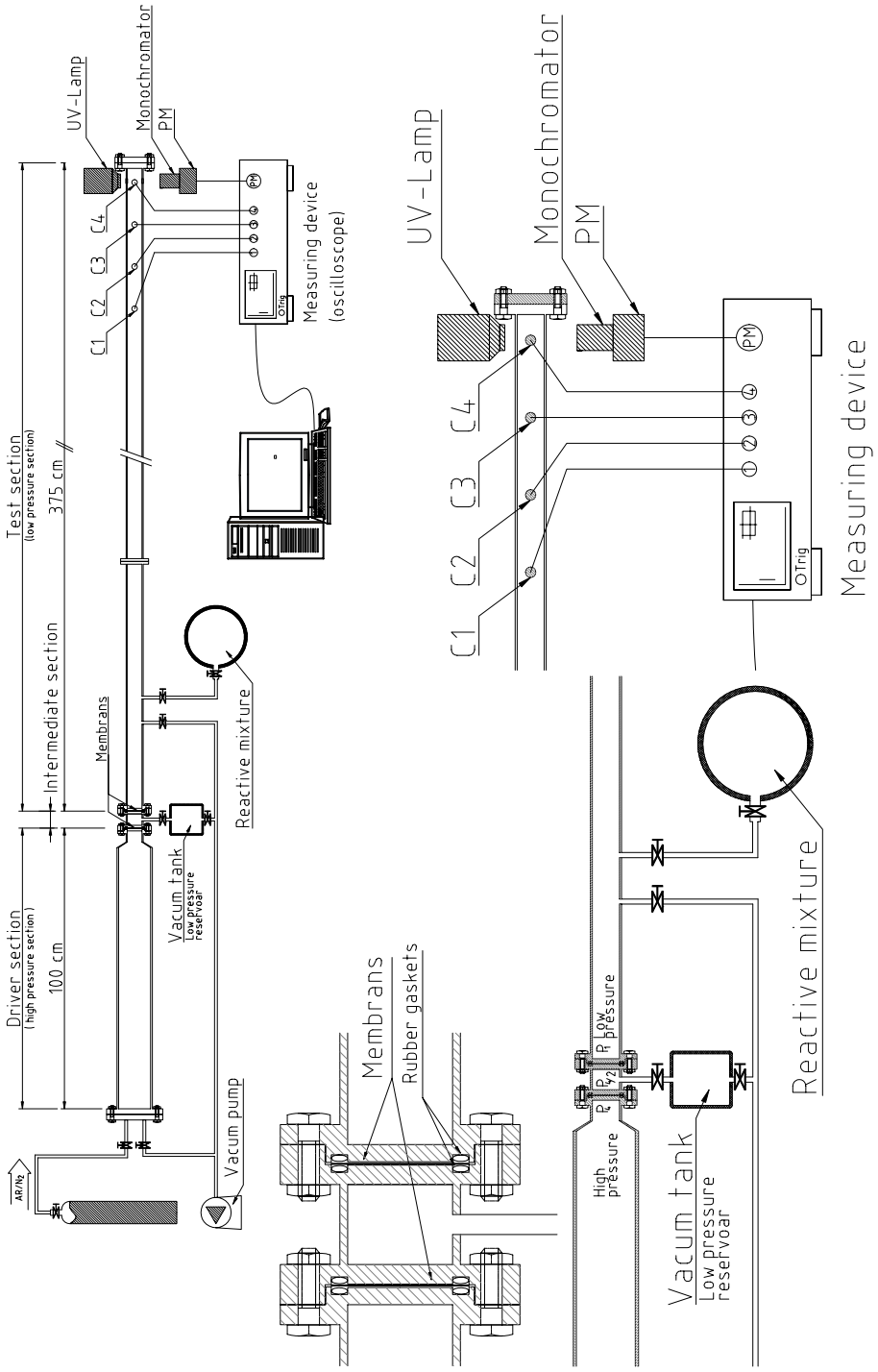

Figure 4-3: Experimental setup.

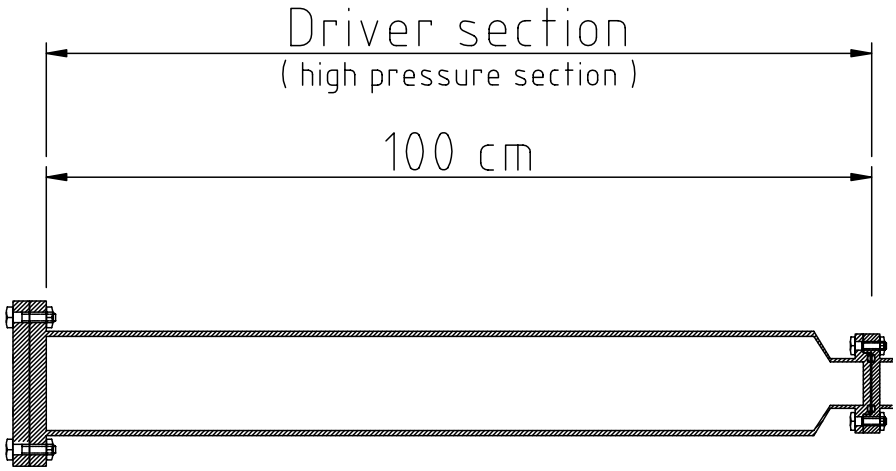

Figure 4-4: Shock tube high pressure section.

volume of 0.112 dm^3. The section had the same external connections as the driver section for the pumping and filling. The double membrane system is illustrated in figure 4-5.

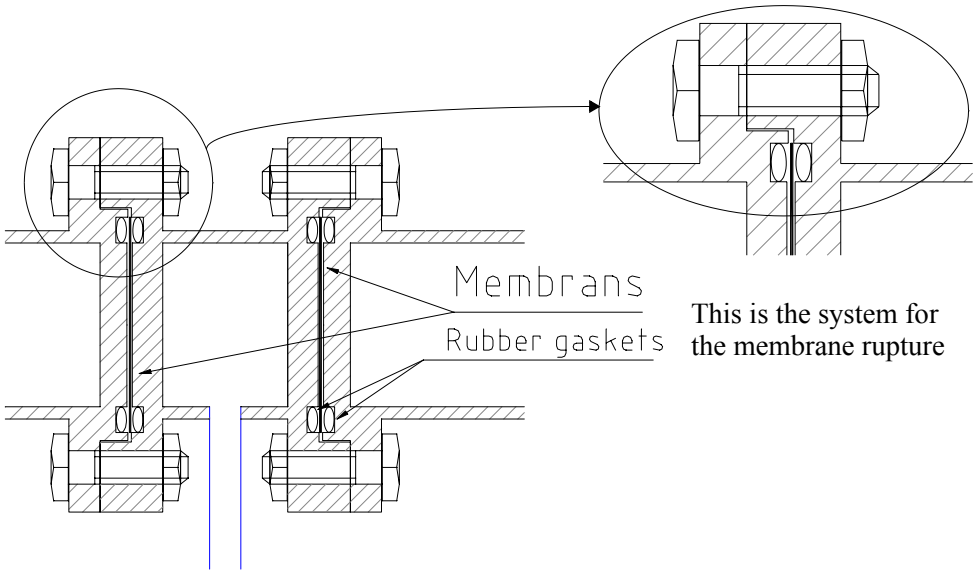

Figure 4-5: Double membrane system.

The Low-Pressure Section

The low pressure section (figure 4-6) had the same internal diameter as the intermediate section, which is 52.5 *mm*. It had a thickness of 3.91 *mm*, and was made up of three separable tube elements having a total length of 3.75 *m* (35, 200 and 140 cm). The first element was 0.35 *m* long and had external connections for gas filling and pumping as well as temperature measurements. The second element had a length of 2.0 *m* and did not have any external connections. The third had nine external connections (of which four were in use during the experiments) designed for pressure captor emplacement.

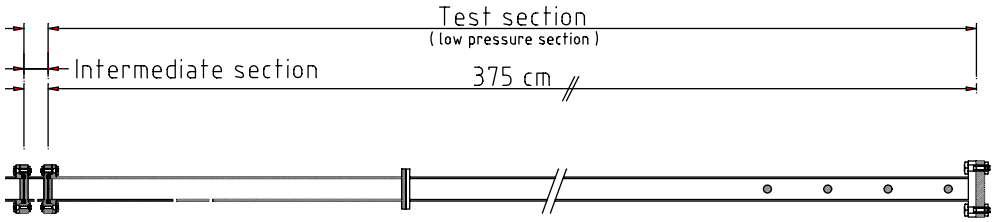

Figure 4-6: The shock tube low pressure (or test) section.

For the optical measurements (ex. UV) the tube was equipped with special glass windows made from calcium fluoride (CaF_2), situated 12 *mm* from the tube end, one on each side perpendicular to the tube axis.

UV Spectrometry Diagnostics

All the instruments for the optical measurements were situated on a moving bracket to insure the same position for each experiment. The apparatus for the absorption measurements was situated 12 *mm* from the end of the low pressure section with the source (deuterium lamp HAMAMATSU C1518) and the captor (monochromator JOBIN-YVON HR250M) situated opposite to each other on each side and perpendicular to the tube axis. The monochromator, which is a wave length selector, can be set to the desired wave length. The Photomultiplicator (HAMAMATSU R977, with operating range between 200 and 900 *nm*) was connected after the monochromator. A pair of CaF_2 optical windows (absorption/emission range 200 *nm* to 13 *mm*, 8 *mm* i.d. and 4 *mm* thick) was mounted in the tube wall on the axis between the source and the captor. The signals from the Photomultiplicator were registered by a digital oscilloscope (PHILIPS PM 3384-100 MHz, 200MS/s) and then into a computer for further treatment. The signals obtained for

the absorption intensity over time are proportional to the concentration evolution in time for the reactive in the tube based on the law of Beer-Lambert (see APPENDIX A). Figure 4-3 and figure 4-7 illustrates the layout for measuring the light emission caused by the NM decomposition reactions after the passage of the reflected shock.

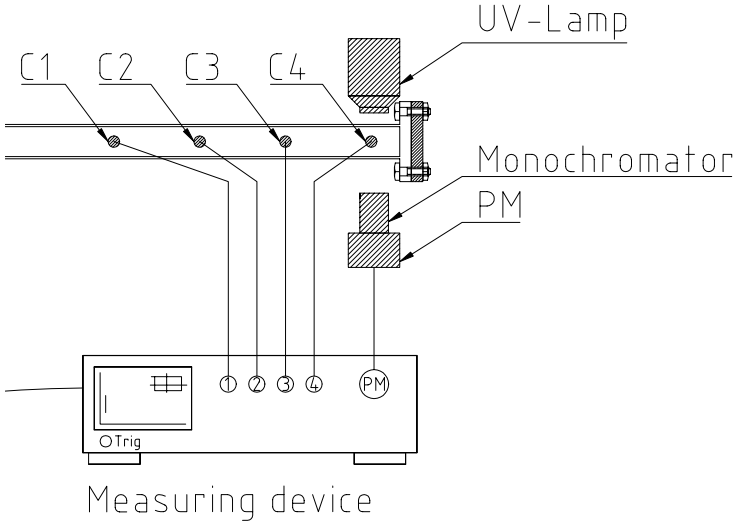

Figure 4-7: Measuring light emission at selected wavelengths

4.2.2 Calculating the state of the incident and reflected shock

When the pressure, temperature and density behind the shock wave was calculated, the following was assumed:

- Molecular transport processes and turbulence is neglected
- The gas is treated as a perfect gas
- Wall-effects are considered negligible

A computer program realized (see APPENDIX A for details) at the laboratory of CNRS/LCSR was used for predicting the state of the gas behind the incident and the reflected shock. The shock front is considered to have an infinitely small thickness and to behave like a discontinuity for all the state variables relative to the experimental gas. The gas is assumed to be non-viscous and non-conductive and the wall-effects are assumed to be neglectable. The variation of $\gamma = C_p/C_v$ with temperature was taken into account. The formulas used are the equations describing the conservation of mass, momentum and energy. By combining these equations, the well-known Hugoniot relation can be found.

The equations describing the pressure and the temperature behind the reflected shock are given as:

$$\frac{p_5}{p_1} = \left(\frac{\gamma+1}{\gamma-1} - \frac{p_1}{p_2} + 2\right)\left(\frac{1+(\gamma+1)p_1}{(\gamma+1)p_2}\right) \qquad \textbf{Eq. 4-2}$$

$$\frac{T_5}{T_1} = \frac{p_5}{p_2}\left(\frac{\gamma+1}{\gamma-1} + \frac{p_5}{p_2}\right)\left(1 + \frac{(\gamma+1)p_5}{(\gamma-1)p_2}\right) \qquad \textbf{Eq. 4-3}$$

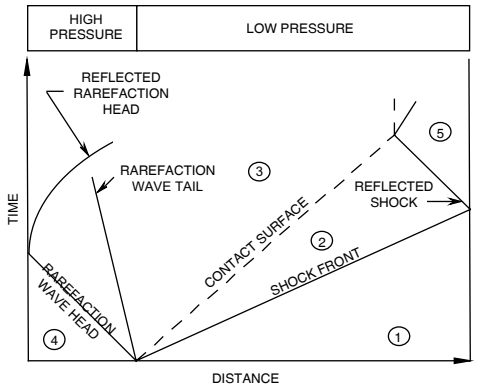

,where the subscript corresponds to the states as given by figure 2-3 and repeated here for convenience.

These equations are derived from the set of equations in APPENDIX A, under the incident and reflected shock parameter calculations. Also in the same appendix, is the Pascal coded equations used for the calculations.

Assuming the validity of the law of Beer-Lambert, the concentration profile as a function of time may be calculated from the absorption signals. The normalized concentration as a function of time can then be written as (derived in APPENDIX A):

$$\frac{C(t)}{C_{t=0}} = \frac{\log\left[\frac{V_f - V_0}{V_f - V(t)}\right] - \log\left[\frac{V_f - V_0}{V_f - V_\infty}\right]}{\log\left[\frac{V_f - V_0}{V_f - V_{t=0}}\right] - \log\left[\frac{V_f - V_0}{V_f - V_\infty}\right]} \qquad \textbf{Eq. 4-4}$$

where

V_0 : voltage signal for 100 % transmission

V_f : voltage signal for 0 % transmission

$V(t)$: voltage signal as a function of time

V_∞ : voltage signal for products when the decomposition has gone to completion

If we assume that $V \to V_0$ when $t \to \infty$, as illustrated in figure 4-8, then $V_\infty = V_0$ and eq. 4-4 reduces to:

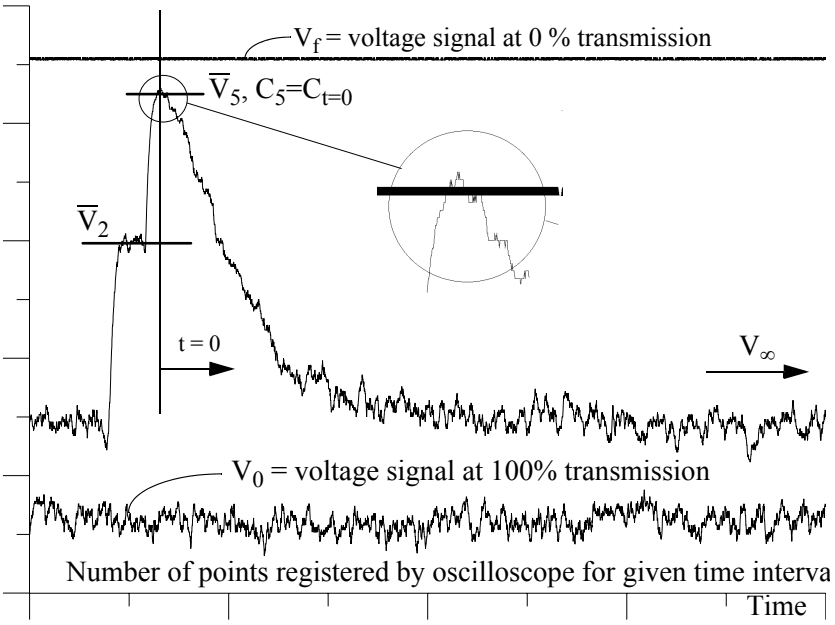

Figure 4-8: Values extracted from illustrative absorption signals.

A Pascal code was written to extract mean values for incident and reflected shock conditions needed to calculate values for density, D, and the molecular extinction coefficient, ε.

$$\frac{C(t)}{C_{t=0}} = \frac{\log\left[\frac{V_f - V_0}{V_f - V(t)}\right]}{\log\left[\frac{V_f - V_0}{V_f - V_{t=0}}\right]} \qquad \textbf{Eq. 4-5}$$

If we further assume that the molecular extinction coefficient, ε in m^2/mol, is independent with respect to temperature, that is $\varepsilon_5 \cong \varepsilon_2 = \varepsilon$, we can simplify to:

$$\frac{C(t)}{C_5} = \frac{\log\left[\frac{V_f - V_0}{V_f - V(t)}\right]}{D_5} \qquad \textbf{Eq. 4-6}$$

taking $C_{t=0}$ as C_5, corresponding to the state of the reflected shock (see APPENDIX A).

The density of the incident and the reflected shock can be found by:

$$D_5 = \log\left[\frac{V_f - V_0}{V_f - \overline{V}_5}\right] \quad , D_2 = \log\left[\frac{V_f - V_0}{V_f - \overline{V}_2}\right] \qquad \textbf{Eq. 4-7}$$

where $\overline{V}_5$ and $\overline{V}_2$ are found as the mean values of the absorption signals within the reflected and incident shock, respectively, as illustrated in figure 4-8 (for additional decomposition examples see figure 4-11).

From the law of Beer-Lambert we can then calculate the molecular extinction coefficient (as shown in APPENDIX A), ε, in m^2/mol, as:

$$\varepsilon_2 = \frac{D_2}{C_2 \cdot l} \quad , \quad \varepsilon_5 = \frac{D_5}{C_5 \cdot l} \qquad \textbf{Eq. 4-8}$$

where l is the optical distance (in *m*) and C_i the concentration of NM in mol/m^3 given by:

$$C_{NM} = X_{NM} \cdot \frac{p}{RT} \qquad \textbf{Eq. 4-9}$$

4.2.3 Measurements

Besides the registration by oscilloscope of the decomposition profile, different variables were registered and calculated for each experiment. A sample registration sheet is given in figure 4-9, here shown for experiment 18.

Nitromethane decomposition

Experimental measurements were performed on the thermal decomposition (pyrolysis) of highly diluted gaseous nitromethane (also referred to as NM or its chemical composition, CH_3NO_2) with mixtures of 0.2 to 1.5 *vol %* NM in nitrogen or argon, over the temperature range 850-1550 *K* and pressure range 190-900 *kPa*. 46 experiments were diluted with nitrogen and 44 diluted with argon. Out of these there were 9 experiments with no reaction. During the experiments the NM concentration, the membrane thickness, the wavelength of observation and diluent was increasingly varied to achieve a spectrum of decomposition profiles (see table 4-1). For the thermal decomposition, the absorption of NM was followed at 220 nm (for highly diluted mixtures) and 225-230 nm (for less diluted mixtures).

To be able to derive the rate constant for the global decomposition of NM, both the concentration as a function of time (absorption signals) and the pressure had to be measured. The apparatus for this has been described in previous sections. During all the experiments, the decomposition reaction time was less than 1 *ms*. Besides the time

Measurements | Man #18 | MANIP MED UK MAKRO.XLS

ManNo	18	Date Man	14.10.1994

P1	83.12	[Torr]	Date Mélange	13.10.1994	
P4	2.3	[Bar]	CH3NO2	0.50	[vol%]
T1	20	[°C]	O2		[vol%]
Lambda	220	[nm]	Diluante		[vol%]
Epmem	18	[µm]	N2	99.50	
Temps 1	160	[ηs/div]	Temps 2	0.2	[ms/div]
CH 1/4	50	[mv/div]	CH 1/2	50	[mv/div]
CH 2/4	50	[mv/div]	CH 2/2	50	[mv/div]
CH 3/4	50	[mv/div]			
CH 4/4	50	[mv/div]	Hauttension	710	[V]
Dist. entre capt.	150	[mm]			
t 12	163.6	[ηs]			
t 23	163.8	[ηs]	Nom Fichiers	m182z	
t 34	165.1	[ηs]		m182	
t moyenne	164.17	[ηs]		m184	

Commentarire :

Calculs :

	Pressure [kPa]	Temp. [K]	Density	Conc. [Mol/m3]	ε [m2/Mole]
2 : Incident	86.69	655.98	0.507	***0.079***	***121.519***
5 : Reflected	387.65	1056.34	2.081	***0.221***	***179.590***

ε5/ε2 =	***1.478***	
v moyenne	913.71	[m/s]

Figure 4-9: Variables & parameters registered for each run.

dependent decomposition signals and pressure, values for initial pressure, temperature and mixture composition were registered for each experiment. All registered variables are shown in figure 4-9, with experiment 18 taken as an example.

Nitromethane oxidation

In parallel to and following the decomposition experiments, oxidative experiments on the ignition delay times of NM/O_2/Ar mixtures were investigated over high temperature and low to high pressure ranges. These experiments were carried out with eight different mixtures of gaseous NM and oxygen diluted in argon as tabulated in table 4-2, with pressures ranging between 44.3-600 *kPa*, and temperatures ranging between 842-1378 *K*.

Table 4-1: Number of reactive experiments by categories.
The number of experiments with reaction, divided into categories of diluent, *vol%* NM, wavelength and membrane thickness.

Variable	No. of exp. nitrogen	No. of exp. argon
NM <vol% >		
0.2	-	17
0.3	10	13
0.33	14	-
0.5	8	7
1.0	6	-
1.5	-	6
Wavelength <nm>		
220	38	26
225	-	11
227	-	1
230	-	5
Membrane thickness <μm>		
8	9	15
12	16	4
18	13	17
23	-	7

Some experiments were carried out with highly diluted mixtures (mixture 5 at 98.65 *%* argon). The other experiments were carried out with mixtures diluted in 84 to 94 *%* argon at 235 *nm*. The equivalence ratio in table 4-2, Φ, was calculated as the mass ratio of fuel/oxidizer over stoichiometric fuel/oxidizer, $(F/O)/(F/O)_{st}$. In the case of mixtures with 84 to 94 *%* dilution, there were no pressure spikes observed when ignition occurred, but emission was observed in most of the signals. Some signals occurred without any emission or pressure spikes. The absorption signals for mixtures highly diluted were very little informative on the same wavelength, 235 *nm*, referred to the other experiments. These experiments showed that highly diluted mixtures should be studied at lower wavelengths around 220 *nm*. Highly diluted mixtures do not absorb enough at the

wavelength of 235 *nm*. This can be seen from the UV spectrum of nitromethane (figure 4-10). This was the reason why only few highly diluted mixtures of NM/O_2/Ar were studied.

Table 4-2: Mixture for ignition delay time experiments.

The oxidative experiments for the ignition delay time were carried out with eight different mixtures of NM/O2/Ar. Here x, y and z are the molar fractions of nitromethane, oxygen and argon, respectively. Molecular weights are: W_{NM}=61, W_{O2}=32 and W_{Ar}=40.

Mixture Number	x	y	z	Number of experiments	Eq. ratio Φ	W_{mix} [kg/mol]
1	0.04	0.03	0.93	4	2.33	40.6
2a	0.04	0.0408	0.9192	4	1.72	40.51
2b	0.039	0.0413	0.9197	7	1.65	40.19
3a	0.05	0.08	0.87	3	1.09	40.41
3b	0.05	0.0856	0.8644	2	1.02	40.37
4	0.0204	0.0407	0.9389	6	0.877	40.1
5	0.003	0.0105	0.9865	4	0.525	39.98
6	0.064	0.0568	0.8792	11	1.97	40.89
7	0.0356	0.1244	0.84	19	0.5	39.75
8	0.064	0.032	0.904	16	3.5	41.09

Optical measurements

The NM spectrum, as illustrated in figure 4-10, was taken at the CNRS laboratory facilities. From this one can observe that NM does not absorb significantly at wavelengths above 350 *nm*, which is why NM is transparent in the visible domain. The absorption minimum is located at approximately 242 *nm*, as shown by point 3 in figure 4-10. This spectrum was used to select a proper wavelength for the monochromator. If we select a wavelength for which there is very little absorption, the signal to the oscilloscope may be to weak and concentration differences difficult to observe. If we select a wavelength for which the absorption is too high, the signals to the oscilloscope will be saturated, that is we only observe a portion of the concentration range. If experiments are to be compared, each series of experiments should be performed using the same wavelength.

The wavelength in the experiments with pure decomposition was set to 220 *nm*, which after a series of preliminary tests showed to give a correct picture of the concentration evolution for our initial concentration range (0.2-1.5 *vol%* NM), taking account for the

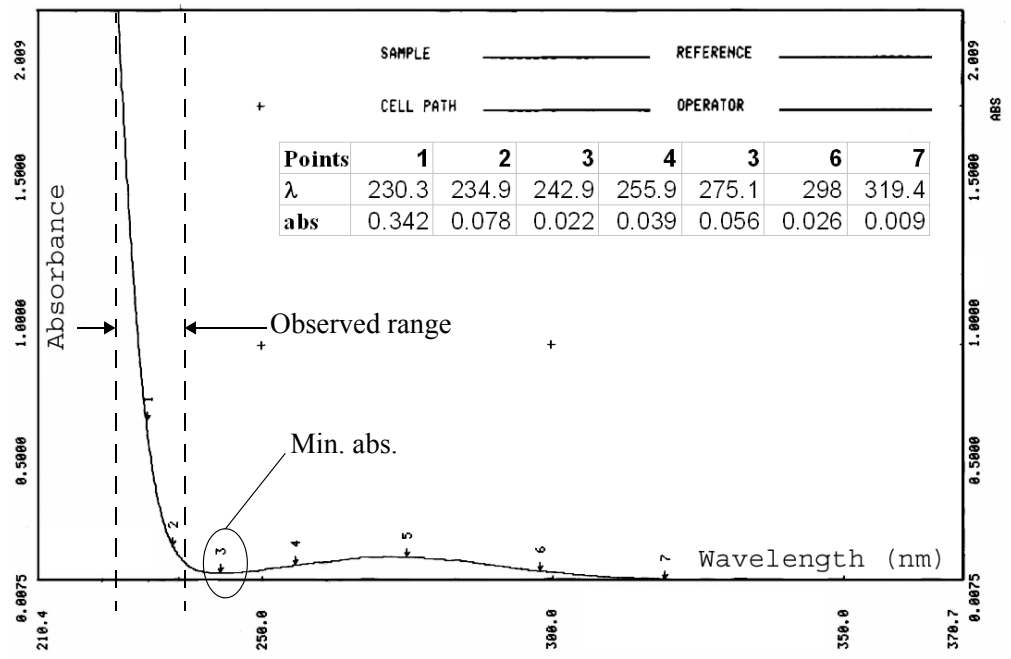

Figure 4-10: UV spectra of pure nitromethane taken at the LCSR.

variation of the concentration with temperature and pressure behind the reflected shock. Some of the experiments performed in the highest pressure and temperature domain demanded higher wavelengths (225-230 *nm*).

The values for the incident and reflected pressure and temperature were calculated using the computer code discussed in Chapter 4.2.2 and in APPENDIX A. It is also important to have in mind that the absorption signal observed by the oscilloscope is the global decomposition of NM. It is solely a measure of the instant concentration of NM. The magnitude of this concentration depends on both pressure, temperature and the different molecules that interacts on NM through one single or several reactions. The importance of each reaction depends on the associated specific reaction rate and can be found through simulation of reaction kinetics and sensitivity analysis. Figure 4-11 shows the absorption signals for some experiments (exp. 18, 46, 66 and 88) as registered by the oscilloscope. These signals are further converted to give the normalized concentration profile and to determine the density, D, and the molecular extinction coefficient, ε.

For the experiments with oxidation of $NM/N_2/O_2$ mixtures, the wavelength was initially set to 235 *nm*. The absorption signals were divided into three types of signals,

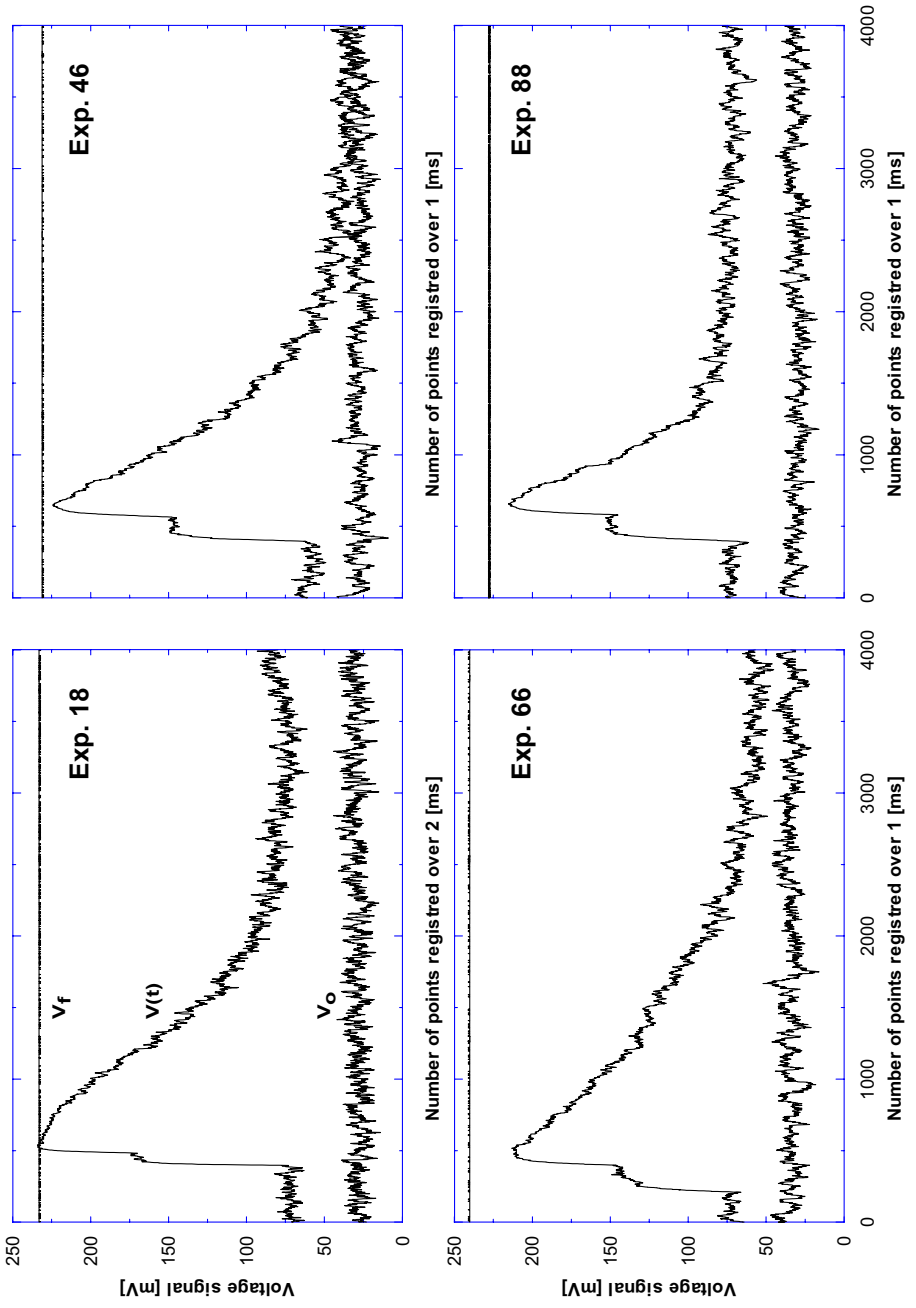

Figure 4-11: Absorption signals (exp. 18, 46, 66, 88).

Signals logged by the computer. V_f = tension at 0 % transmission, V_0 = tension at 100 % transmission. V(t) = tension as a function of time during the decomposition.

signals of type 1, 2 and 3. The type 1 and 2 signals were recorded at 235 *nm* while the type 3 signal was recorded at 306 *nm*. Figure 4-12 and figure 4-13 show the characteristic form for each of these signal types. The letters x, y and z are the molar fractions of nitromethane, oxygen and argon respectively.

Specific examples representing each signal type:

- Type 1: x=0.064, y=0.0568, z=0.8792,p_5=76.5 kPa and T_5=1143.3 K
- Type 2: x=0.0356, y=0.1244, z=0.84, P_5=68.53 kPa and T_5=1145 K
- Type 3: x=0.0356, y=0.1244, z=0.84, P_5=63.55 kPa and T_5=1089 K

Signals of type 1 were characterised by the appearance of emission when all or most of the nitromethane had been consumed, which means that an emission signal is superimposed on the light source signal, because of an ignition. Figure 4-12 shows a signal of this type.

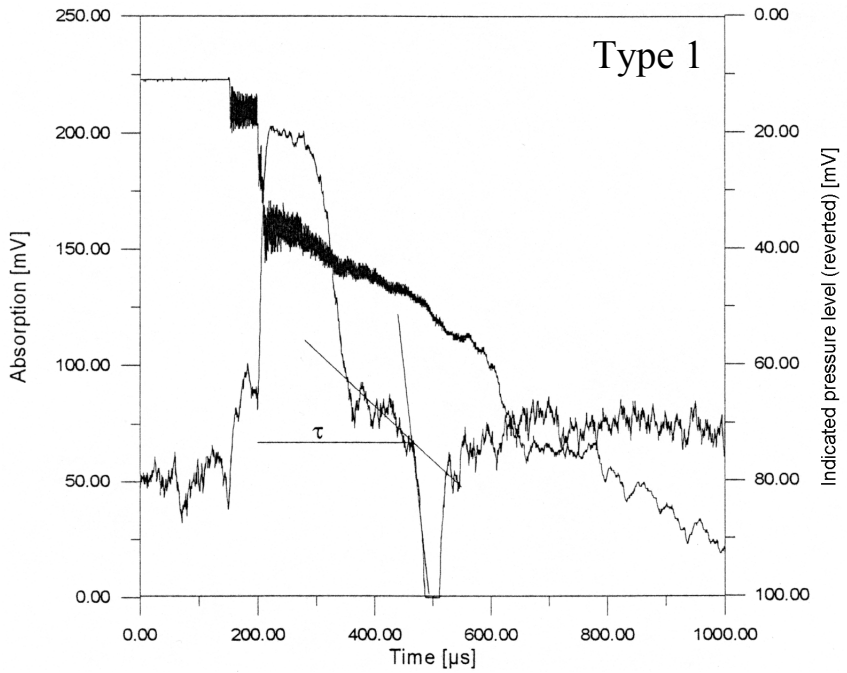

Figure 4-12: Signal type 1 - $NM/O_2/Ar$ mixtures.

Type 1: x = 0.064, y = 0.0568, z = 0.8792, p_5 = 76.5 *kPa* and T_5 = 1143.3 *K*

The first stable period shows the nitromethane absorption before the arrival of the incident shock front. Then an increase in absorption is observed because of gas compression in the incident shock, which is followed by a short stable period before the reflected shock arrives. In the reflected shock, the absorption attains its maximum value. For temperatures lower than 1200 *K* an incubation time is observed. One can see, from figure 4-12, that the absorption decreases relatively fast, which means that nitromethane is consumed. Then the signal has a small stable period, followed by an inverted absorption spike (emission) that drops below 0 % absorption level. This means that there are radicals, produced from the oxidation, that emit at this wavelength.

In some cases, when the inverted absorption spike does not drop below 0 % absorption, it is difficult to decide if there is an emission. An explanation can be that some products absorb at this wavelength and then decompose or oxidise.

Thirty seven signals of type 1 were recorded over large temperature and pressure ranges, mostly for rich mixtures. Emission occurred in lean mixtures when temperatures were higher than 1300 *K*. Only one signal of this type (mixture 7, which was lean) was recorded.

Signals of type 2 (figure 4-13) showed an incubation time followed, either, by simultaneous decomposition and oxidation, or only oxidation. The phenomenon should, however be further studied in order to understand the reaction mechanism in more detail. Only a small increase in pressure and no emission was recorded when ignition occurred.

Signals of type 3 (figure 4-13) was characterized by emission occurring a certain time after the arrival of the reflected shock. Among the 13 signals recorded with mixture 7, only one of these revealed an emission signal. Emission occurred when temperatures were higher than 1300 *K*. Therefore, the last 8 experiments with mixture 7 were carried out without a light source in order to check if emission occurred. The signals were recorded on a wavelength equal to 306 *nm*, characteristic for OH^-, which is an important radical in the ignition process.

Pressure measurements

Four piezo-electric pressure captors of type CHIMIE METAL (series A25L05B) were mounted on line starting 12 *mm* from the end wall of the low pressure section, each having an exposed area of 0.75 cm^2 and a response time of 0.4 *ms*. The distance between each of the captors was 150 ± 1 *mm*. The shock wave speed was determined by the

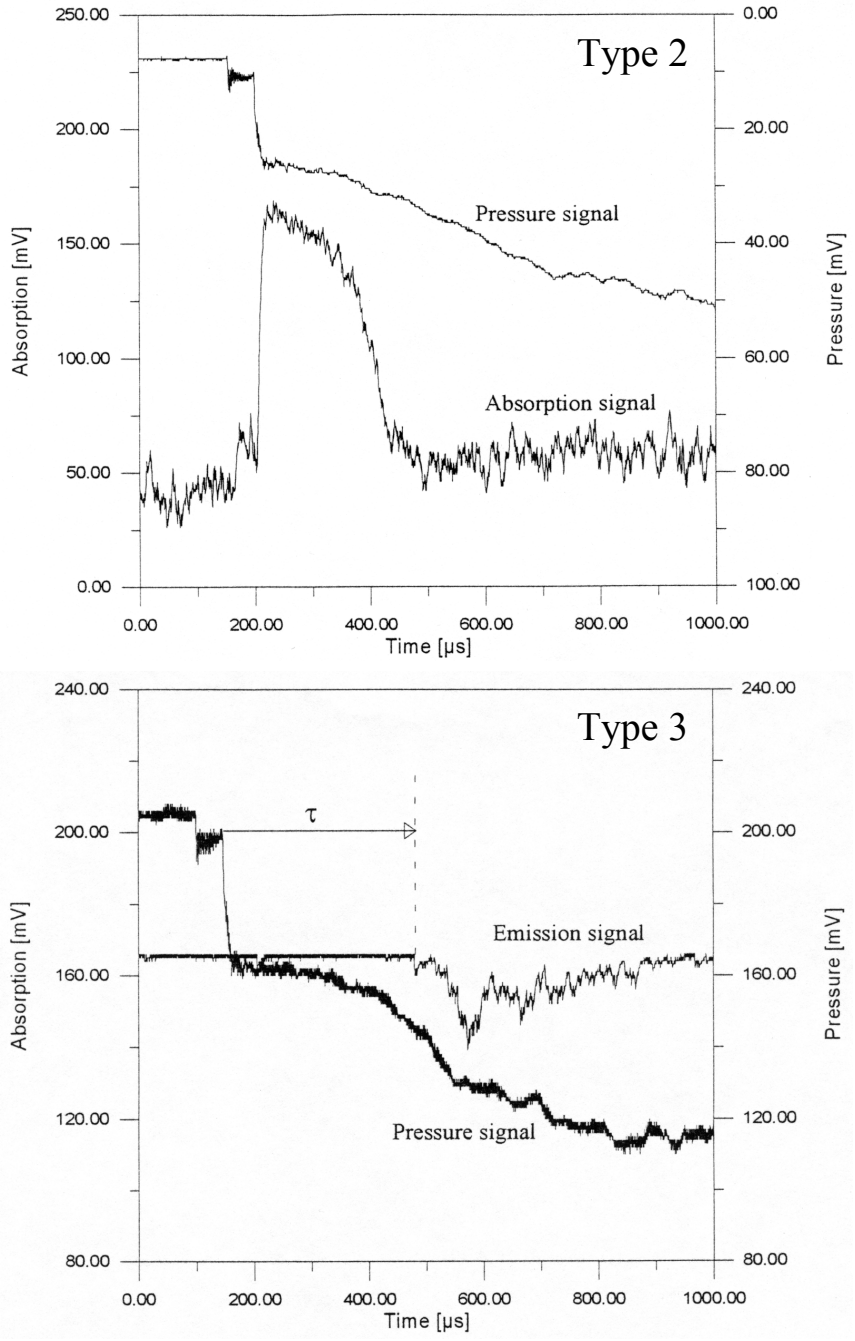

Figure 4-13: Signal type 2 and 3 - NM/O_2/Ar mixtures.

Type 2: x=0.0356, y=0.1244, z=0.84, P_5=68.53 kPa and T_5=1145 *K*
Type 3: x=0.0356, y=0.1244, z=0.84, P_5=63.55 kPa and T_5=1089 *K*

pressure signals delivered from the four piezo-electric captors, signals being registered on a numerical oscilloscope.

Readings for some selected experiments can be seen in figure 4-15 (reflected shock inverted and absorption) and figure 4-16 (for all four captors). Data for these experiments are tabulated in figure 4-14.

Exp.	P_1	P_4	Epmem	Diluante	% NM	WL
Man #18	83.12	2.30	18	N_2	0.50	220
Man #46	131.00	4.00	18	N_2	0.33	220
Man #66	245.50	3.20	18	Ar	0.20	220
Man #88	340.00	4.40	23	Ar	0.20	225

Exp.	P_2	T_2	D_2	C_2	ε_2	P_5	T_5	D_5	C_5	ε_5	$\varepsilon_2/\varepsilon_5$	$V_{moyenne}$
Man #18	86.690	655.980	1.168	0.079	279.807	387.650	1056.340	4.791	0.221	413.521	1.478	913.71
Man #46	142.400	672.600	0.876	0.084	198.558	647.900	1091.000	3.324	0.236	268.605	1.353	933.61
Man #66	174.950	657.300	0.720	0.064	214.043	585.760	1118.900	1.933	0.126	292.334	1.366	677.71
Man #88	254.960	678.410	0.923	0.090	194.529	873.520	1168.820	2.656	0.180	281.410	1.447	694.44

Figure 4-14: Data acquired decomposition experiments taken as examples.

The extended data set for decomposition experiments taken as examples, exp. 18, 46, 66 and 88. Data for remaining experiments can be found in APPENDIX B.

By using more than just two pressure captors the speed of the shock wave at different positions could be calculated to verify whether the speed was constant or not. The mean velocity was then used in the calculations of the conditions behind the reflected shock (T_5 and p_5).

The passage of the shock front results in a very rapid rise in pressure in the shock plane. As the shock wave passed the fist captor (C_1) two numerical oscilloscopes (PHILIPS PM 3384 -100 *MHz*, 200 MS/s) were triggered, one for the pressure signals and one for the absorption signals. For convenience the inverse of pressure (C_4) in the reflected shock was registered together with the absorption signals, as for the examples in figure 4-15.

Figure 4-16 clearly illustrates the arrival and the corresponding reflection of the imposed shock wave. The reflected shock which was measured by captor 4, can be seen to origin from the opposite direction. During the observation time, no pressure jump was observed as the emission occurred, but a continuous and smooth pressure increase was observed in some experiments. If a small pressure increase was observed, it can be explained by the fact that piezoelectric pressure transducers are sensitive to temperature. An increase in temperature near the shock tube wall may therefore give an increase in the pressure signals.

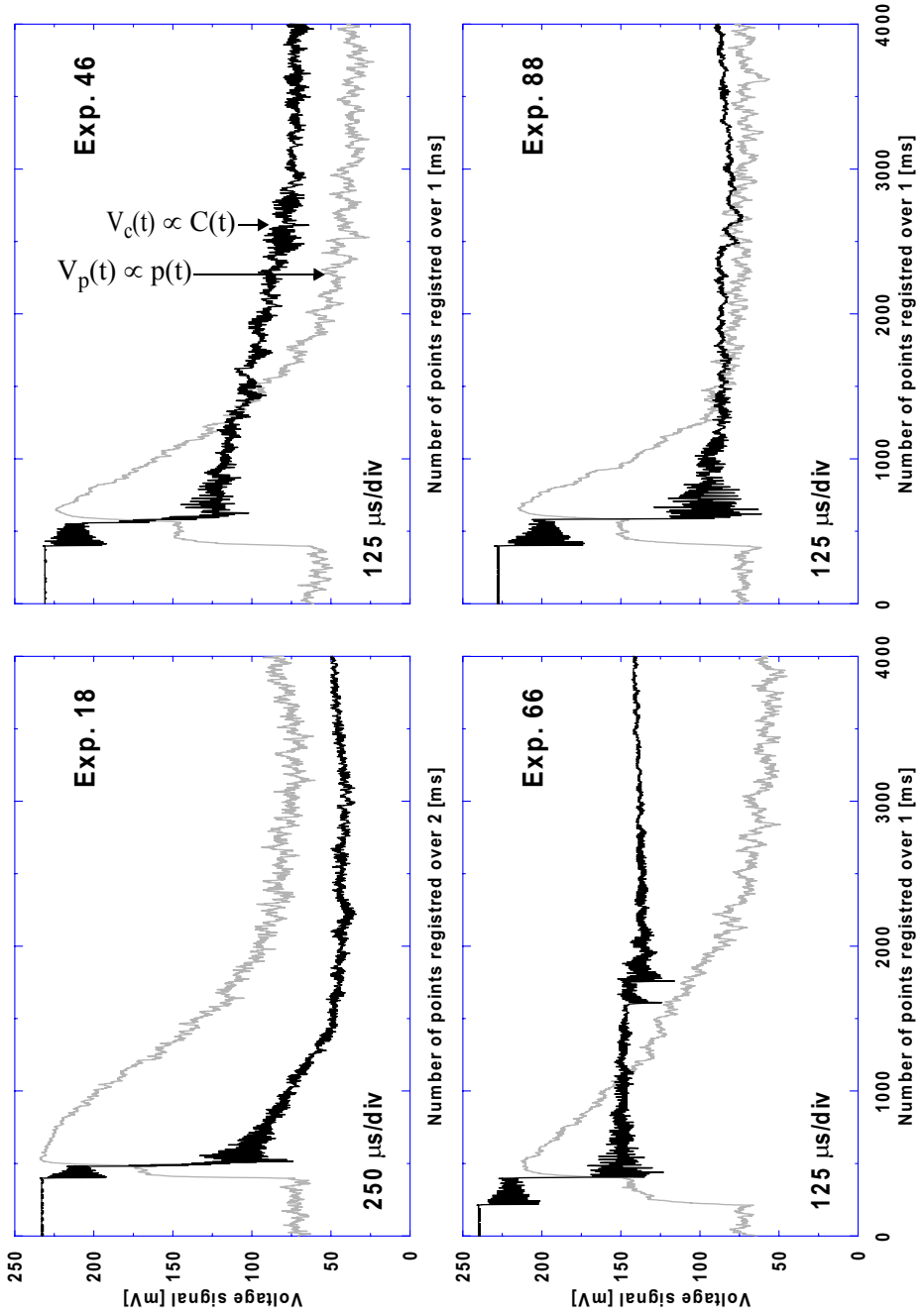

Figure 4-15: Examples of pressure signals logged.

Examples of pressure signals logged for experiment 18, 46, 66 and 88 (channel 4, incident and reflected shock). The pressure signals are inverted and shown in the same time scale as the corresponding NM decomposition signals.

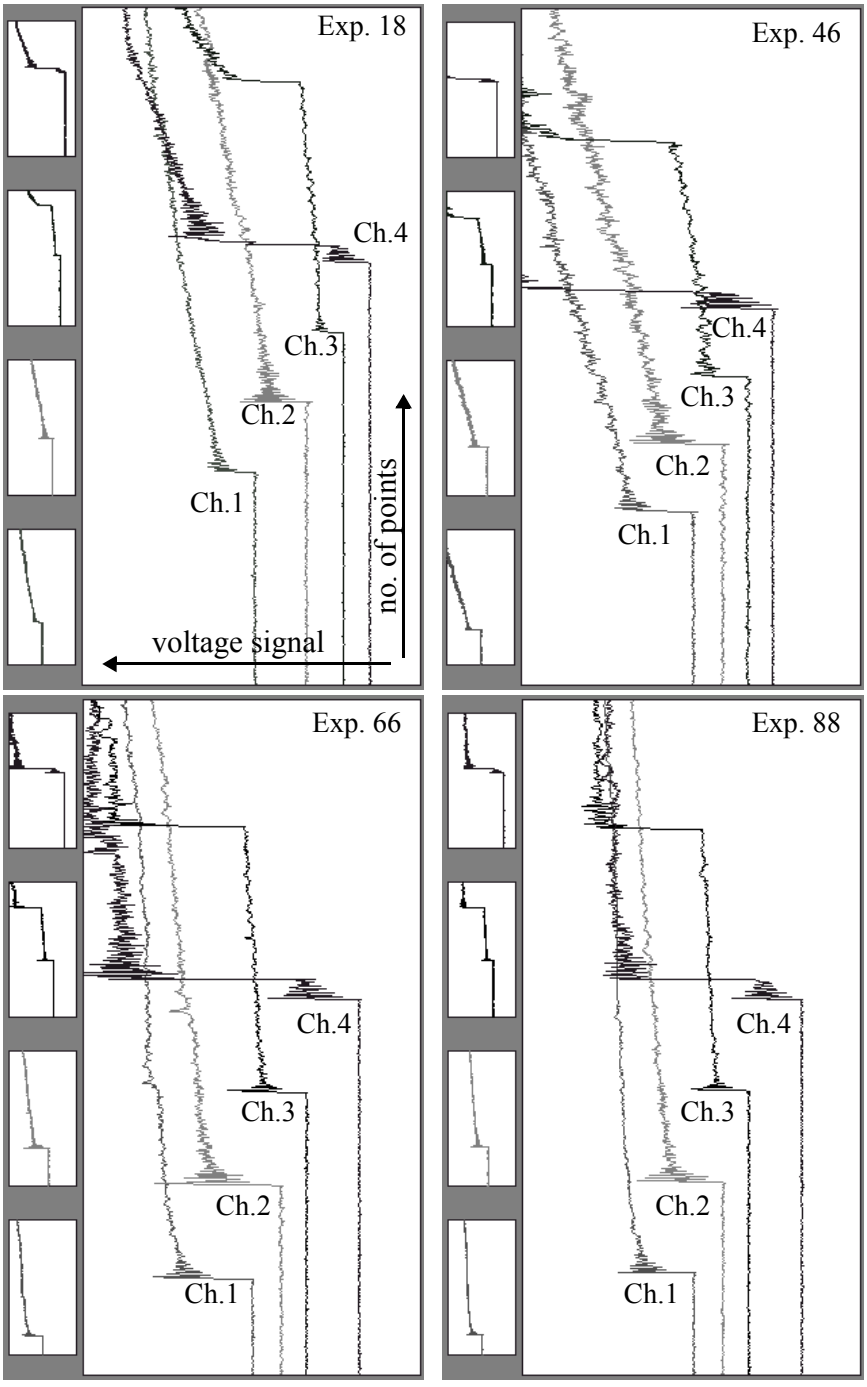

Figure 4-16: Pressure signals.

Signals registered by oscilloscope for all four channels for experiment 18, 46 (NM/N_2) and 66, 88 (NM/Ar). The signals are on a scale from 0 to 250 mV.

4.3 RESULTS AND DISCUSSION

In order to minimize complications due to secondary and tertiary reactions, most of the decomposition experiments were carried out using CH_3NO_2 highly diluted in either nitrogen or argon. Reflected shock experiments using mixtures of 0.2 to 1.5 *vol%* NM in nitrogen or argon were performed over the temperature range 850-1550 *K* and pressure range 190-900 *kPa*, with 46 experiments diluted in nitrogen and 44 diluted in argon. Out of these there were 9 experiments with no reaction. 54 (N_2/18, Ar/36) experiments were considered useful in the sense that they had been performed with no observable errors caused by external events and were within the range of measurability of the oscilloscope (results are tabulated in APPENDIX B).

In parallel to, and following the decomposition experiments, oxidative experiments on the ignition delay times of NM/O_2/Ar mixtures were investigated over high temperature and low to high pressure ranges. These experiments were carried out with eight different mixtures of gaseous NM and oxygen diluted in argon as tabulated in table 4-2, with pressures ranging between 44.3-600 *kPa*, and temperatures ranging between 842-1378 *K*. Some experiments were carried out with highly diluted mixtures (mixture 5 at 98.65 *%* argon). The other experiments were carried out with mixtures diluted in 84 to 94 *%* argon at 235 *nm*. 76 experiments on nitromethane oxidation were carried out (see APPENDIX B).

The shock temperatures and pressures of the current experiments was estimated to an accuracy of 1-2 *%*, calculated from the discrepancy in the measurements of the shock speed (U), from $\Delta U/U=\Delta s/s+\Delta t/t$. The speed was calculated from the distance between the four pressure captors and the time interval of shock passage as registered by the oscilloscope.

4.3.1 NM/Ar and NM/N_2 - decomposition experiments

The absorption coefficient

The absorption coefficient is a measure of the concentration of gas molecules momentarily present in the volume slit-space as observed by the monochromator. This is further discussed in APPENDIX A under the Beer-Lambert section. The molecular extinction or absorption coefficient, ε, is measured in units of m^2/mol. Knowing the pressure and the

temperature in the different states, the molecular extinction coefficient, ε_i, is determined from the following expression (from eq. 4-8):

$$\varepsilon_i = \frac{D_i}{C_i \cdot l} = \frac{D_i \cdot R \cdot T_i}{X_i \cdot p_i \cdot l} \qquad \textbf{Eq. 4-10}$$

The variation of the ratio of the absorption coefficient in the incident vs. the reflected shock with reflected shock temperature is plotted in figure 4-17. In figure 4-18 the absorption coefficient for each diluent, and the wavelength have been plotted for both the incident and the reflected shock. The reason why we want to visualize the temperature dependence of the extinction coefficient is to get an idea of the error we are introducing when assuming absorption coefficient temperature independence, that is, when ε_i is considered constant during the decomposition.

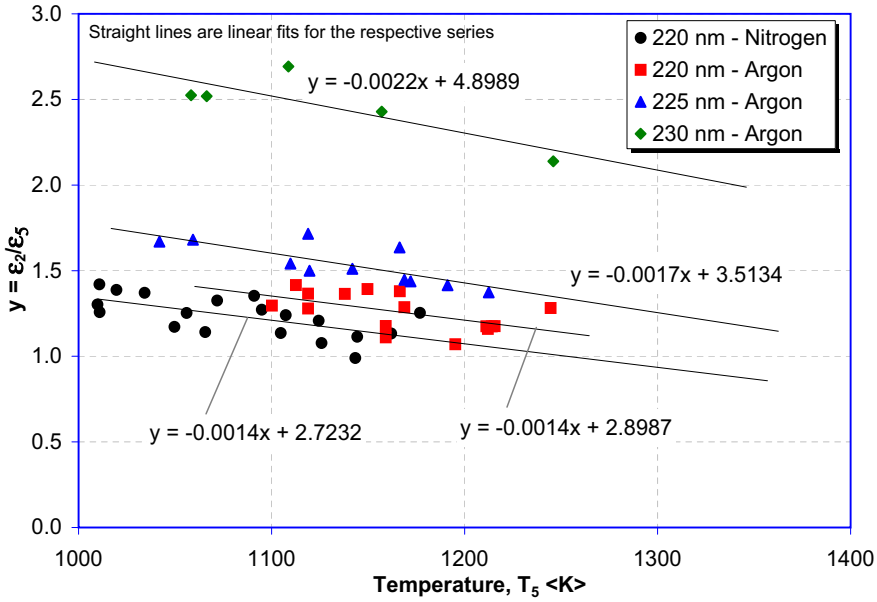

Figure 4-17: Absorption ratio coefficients

Variation of the absorption coefficient ratio (epsilon incident/reflected shock) as a function of the temperature of the reflected shock.

Figure 4-17 and figure 4-18 shows that the wavelength and choice of diluent have a substantial influence on the absorption coefficient. The linear variation with temperature is insignificant within the temperature domain of the present experiments. The simulated

cases for each experiment showed variations in temperature in the range of 2-4 ^{o}C during the short period of decomposition (< 300 μs).

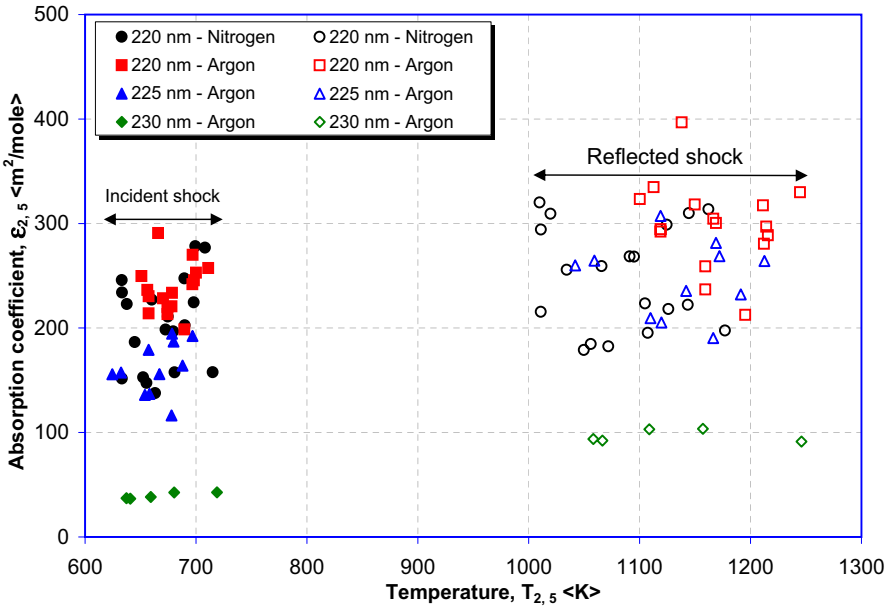

Figure 4-18: Absorption coefficients vs. temperature.

Variation of the absorption coefficients in the incident and the reflected shock as a function of their inherent temperatures.

Shock speed versus initial pressure ratios

Analysing the experiments by looking at the incident shock speed vs. the initial pressure ratio for the driver- and working gas section, shows a clear difference for the two different cases of diluents, as illustrated by the plot in figure 4-19. This relates to the molecular differences, such as weight (M_{N2}=28, M_{Ar}=39.95) and size, between nitrogen and argon. The less heavy nitrogen molecules are easier to accelerate and we obtain a higher shock velocity for a given amount of energy (p_4/p_1).

Non-reactive experiments

Typical signals registered (experiment 35 taken as example) for pressure and absorption at 220 *nm* diluted with nitrogen observed for non-reactive conditions during 1 *ms*, are illustrated in figure 4-20. The pressure behind the reflected shock can be seen to be close to constant. The slight increase in pressure is due to the temperature increase affecting the

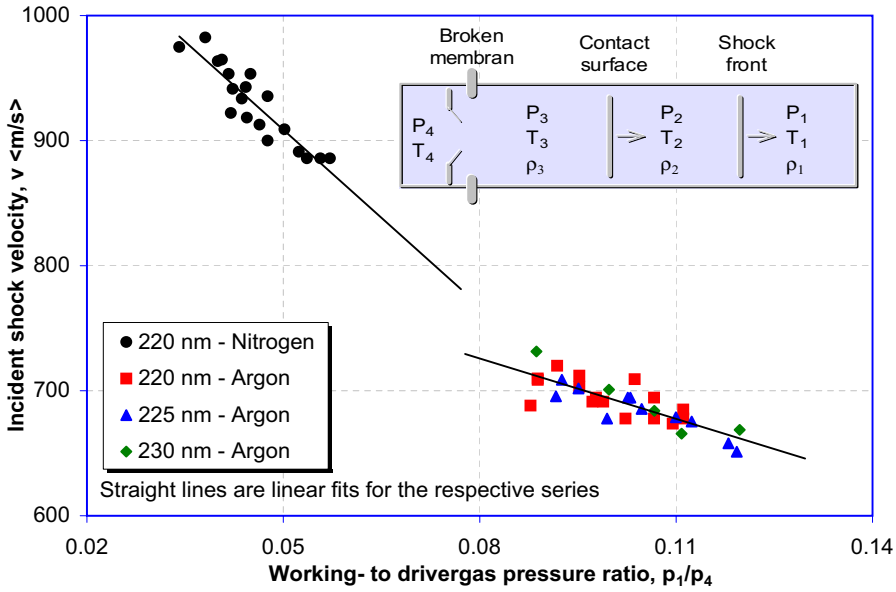

Figure 4-19: Shock velocity vs. driver to working gas pressure ratio.

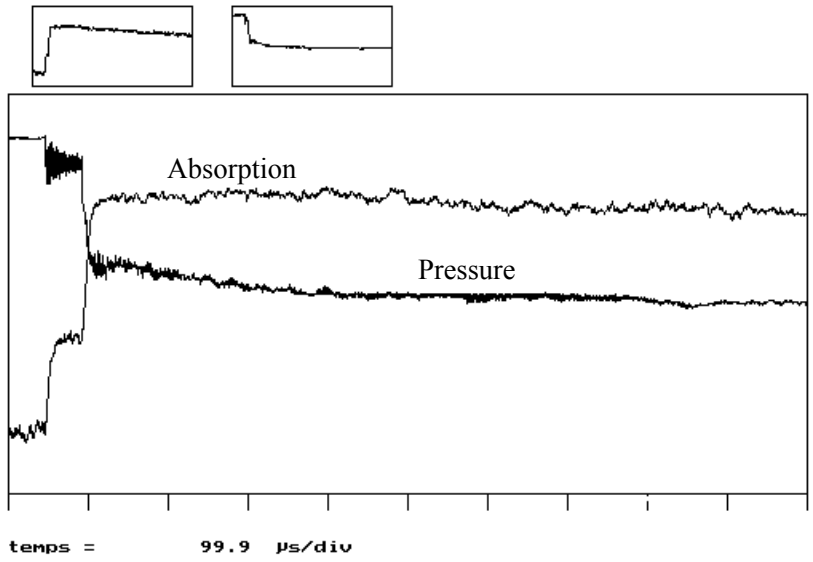

Figure 4-20: Pressure and absorption signals for exp. 35.

During 1 *ms* after the passage of the reflected shock for a wave-length of 220 *nm* in a mixture of 0.0033 NM + 0,9967 N_2 (exp. No. 35).

pressure captors. The absorption first increased over the incident and then over the reflected shock, appears to be approximately constant, indicating no decomposition. Table 4-3 shows the calculated thermodynamic parameters for the same experiment.

Table 4-3: Reflected shock conditions for experiment 35

Calculated conditions behind the reflected shock for experiment 35, diluted with nitrogen and having a molar ratio of NM(0.0033)/N_2(0.9967)

```
 Mardi 7/10/1997    Némuro de la manipulation  :  35
     0%  CH3NO2   +    100%  N2
Masse molaire moyenne du mélange=   28.12
```

Distance (en mm) = 150.00	Temps (en µs) = 190.30
Vitesse du son (en m/s) = 348.08	Nombre de MACH = 2.26

T1 = 293.15 K	P1= 11.84 kPa	RO1=0.1366 Kg/m3	U1= 788.2 m/s
T2 = 557.49 K	P2= 69.04 kPa	RO2= 0.42 Kg/m3	U2= 257.1 m/s
T5 = 854.99 K	P5= 265.54 kPa	RO5= 1.05 Kg/m3	U5= 352.2 m/s
T2/T1 = 1.9100	P2/P1= 5.8298	RO2/RO1= 3.07	P4/P1= 11.8
T5/T2 = 1.5336	P5/P2= 3.8462	RO5/RO2= 2.508	P5/P2= 22.4

The conditions for which no reaction was observed during 1 *ms*, from all the present experiments, are listed in table 4-4. From studying the decomposition profiles it was found that no decomposition occurred during 1 *ms* of registration when the temperature was less than approximately 990 *K* and within the present pressure range. As with decomposition experiments non-reactivity in NM/Ar/O_2-mixtures was also observed for the lower temperature and pressure conditions. When the temperature in the reflected shock was lower than approximately 1000 *K* (at any pressure), no decomposition nor oxidation was observed.

Table 4-4: Conditions for non-reactivity

Non-reactive experiments during 1 *ms* of registration for mixtures of NM/N_2 and NM/Ar.

Exp.	% NM	P5 [kPa]	T5 [^{0}C]	D5	C5	ε_5	$\varepsilon_2/\varepsilon_5$	V_{mean} [m/s]
Man #10	1.00	247.900	989.300	3.810	0.301	240.784	1.137	874.81
Man #11	1.00	202.740	899.280	2.245	0.271	157.718	1.396	818.18
Man #16	0.50	395.360	980.960	4.252	0.242	334.120	1.308	868.22
Man #24	0.30	221.610	883.260	0.914	0.091	192.235	1.622	806.45

Table 4-4: Conditions for non-reactivity

Non-reactive experiments during 1 *ms* of registration for mixtures of NM/N_2 and NM/Ar.

Exp.	% NM	P5 [kPa]	T5 [^{o}C]	D5	C5	ε_5	$\varepsilon_2/\varepsilon_5$	V_{mean} [m/s]
Man #26	0.30	208.620	961.410	0.840	0.078	204.344	1.525	855.68
Man #30	0.30	385.810	968.810	1.475	0.144	195.465	1.196	859.43
Man #31	0.30	368.540	948.160	1.439	0.140	195.442	1.293	847.46
Man #34	0.33	252.970	938.130	1.664	0.107	296.131	1.364	841.12
Man #35	0.33	265.540	854.990	1.796	0.123	277.507	1.339	788.09

Reactive experiments - The reaction order

From the absorption signals, take experiment 84 as an example. Then by the law of Beer-Lambert, the normalized concentration profile for NM can be determined as a function of time. As observed in figure 4-21, there is no delay in decomposition, as sometimes observed for certain species. This can be verified by examining each of the decomposition profiles, given in APPENDIX B. As soon as the NM reaches the required combination of pressure and temperature, the decomposition starts immediately. From this figure we can estimate the time for complete decomposition to approximately 0.3 *ms*.

Already from the curve of the raw-data, the negative exponential form of the curve suggests a fist order reaction with respect to NM. Figure 4-22 shows the normalized concentration profile in linear and logarithmic scale for experiment 84. The shape of the curve takes an exponential form (negative exponent), which indicates that the reaction is of first order. The profiles were calculated down to $C(t)/C_0 = 0.4$, which is reasonable beyond the reaction half-life time, giving a representative interval for the derivation of the reaction rate.

A comparison of the concentration versus time for a general first- and second-order reaction, given equal parameters, is shown in figure 4-23. We note that the dimension of the two reaction rate constants is different. The comparison is only valid if $k_1=k_2\times B$ and $A_0=B_0$. To determine whether a deduced reaction rate is of first or second order, the residual errors of the corresponding fits must be examined. Doing this, one should also have in mind that the first points measured of a decomposition profile often are less accurate, for several reasons. Invalid or bad points should therefore first be eliminated

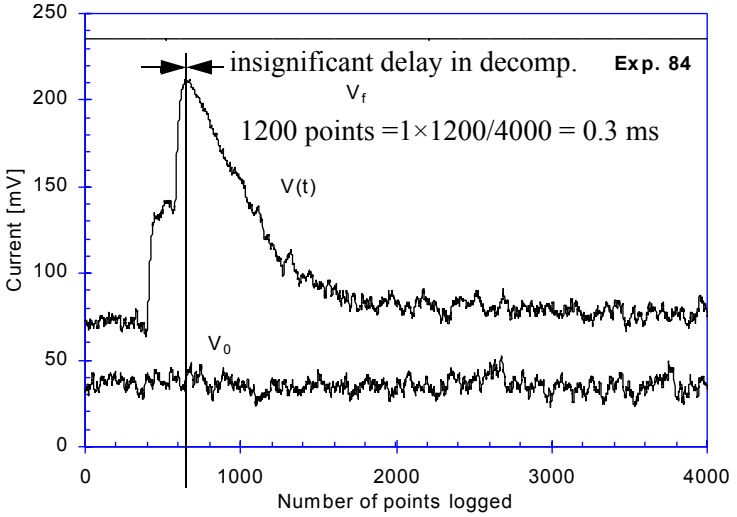

Figure 4-21: Absorption signals for exp. 84.

Absorption signals registered by the oscilloscope (exp. 84) as voltage vs. the total number of registered points (4000 *points* = 1 *ms*).

before doing the residual analysis on the first- and second-order fits. Although a second-order fit of a first-order reaction may fit very well, a plot of the residuals may unveil that the second-order fit has significant systematic errors.

$$\sigma_{fit} = \sqrt{\frac{\sum_i (residuals_i)^2}{N-2}} \qquad \textbf{Eq. 4-11}$$

The reaction order can be deduced from the experimental data by analysing the residual errors. In figure 4-24, the residual error has been plotted for some selected experiments (46, 66 and 88). All three plots more or less confirm that the global decomposition of NM is a first-order reaction. From the plot of the natural logarithm to the normalized concentration profile, the reaction rate can be found directly as the slope to the linear fit. From the Arrhenius expression:

$$k = A \cdot e^{-E_a/R \cdot T} \qquad \textbf{Eq. 4-12}$$

which can be written as:

$$\ln k(T, \ldots) = \ln(A) - \frac{E_a}{RT} = C - T_a \cdot \frac{1}{T} \qquad \textbf{Eq. 4-13}$$

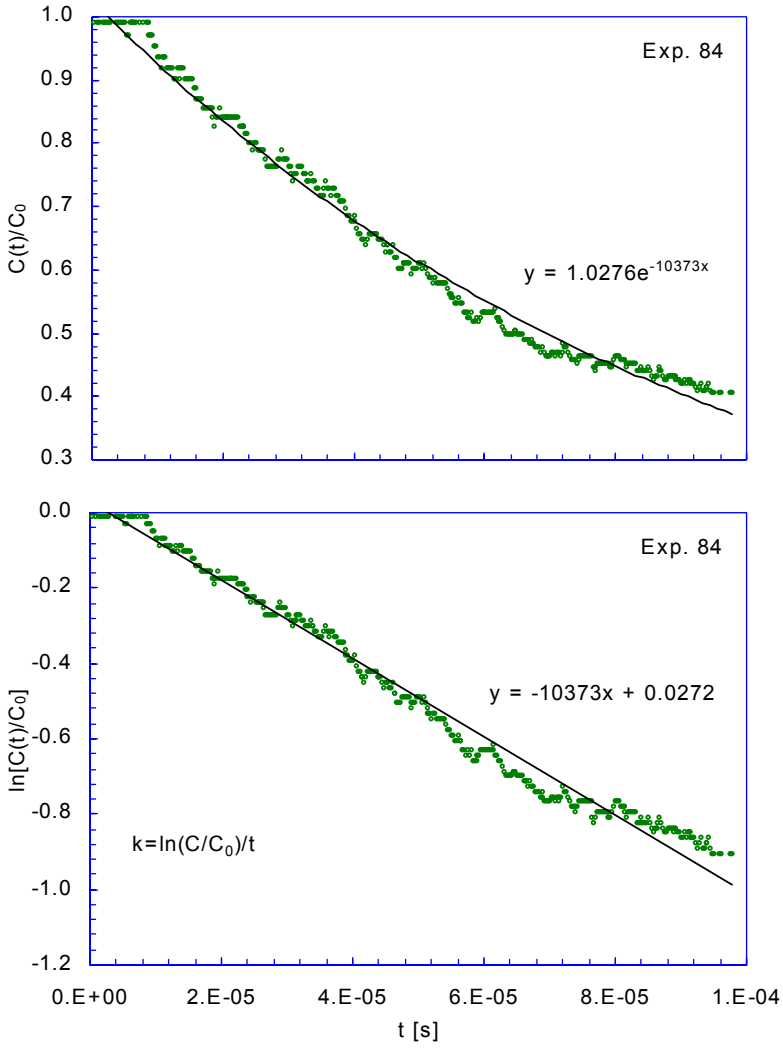

Figure 4-22: Concentration profiles for experiment 84.

Normalized concentration profile $C(t)/C_0$, and logarithmic profile $\ln[C(t)/C_0]$, as a function of time calculated from the absorption signals for exp. 84. The plots were used to extract the reaction rate constants for the corresponding temperatures, $k_i(T_i)$ in (s^{-1}).

For each category of wavelength and diluent one can then find the pre-exponential constant and the apparent activation temperature (also denoted as E_T). This leads to a set of data describing $k_i(T_i)$ in s^{-1}. Under certain conditions, some reaction rate expressions depend on pressure as well as temperature as illustrated in figure 4-25 from the Chemkin III manual (1999). Plotting the rate constant versus the pressure or concentration of

Reaction rates: $\frac{d}{dt}A = -k_1 \cdot A$ $\quad A_0 = 1$ $\quad k_1 = \begin{bmatrix} 0.01 \\ 0.05 \\ 0.1 \end{bmatrix}$

$\frac{d}{dt}B = -k_2 \cdot B^2$ $\quad B_0 = 1$

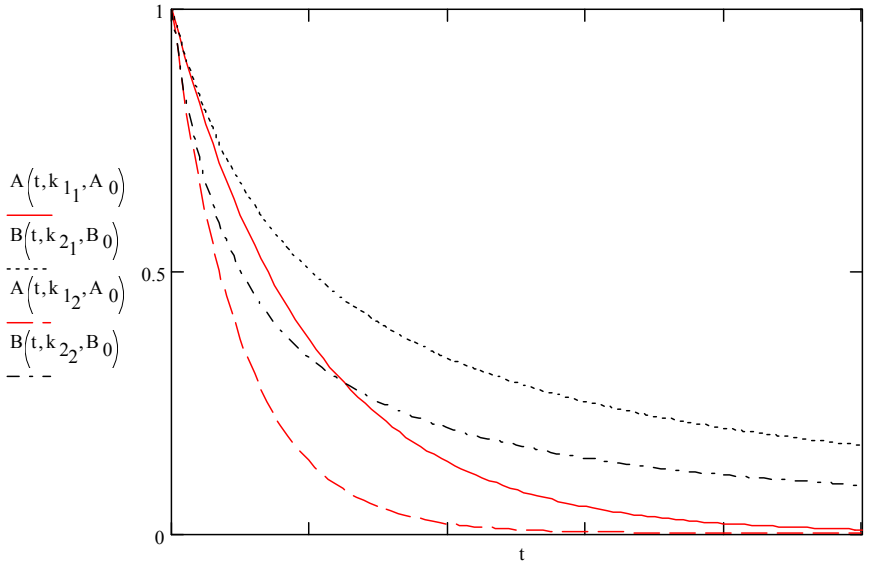

Figure 4-23: Comparing first- and second-order kinetics.

diluent for constant temperatures, makes it possible to distinguish between a low- and high pressure region. When the pressure exceeds a certain transition domain, k is no longer a function the pressure ($\propto$ [diluent]). Sometimes experiments are performed with this analysis in mind, which is to try to keep the temperature in the reflected shock as constant as possible while varying the pressure. The current experiments, however, were not planned with this particular analysis in mind, as can be seen from figure 4-26. The diluent (or pressure range) is not wide enough, and the temperatures are heavily scattered. By analysing the fall-off regime, it is possible to calculate by extrapolation, the asymptotic limits for the reaction rate constant. This will result in a rate expression for a high and a low pressure regime, given on the Arrhenius form as:

High pressure: $k_\infty = A \cdot \exp\left(-\frac{E_a}{RT}\right) \quad [s^{-1}]$ **Eq. 4-14**

Low pressure: $k_0 = [\text{Diluent}] \cdot A \cdot \exp\left(-\frac{E_a}{RT}\right) \quad [cm^3 mole^{-1} s^{-1}]$ **Eq. 4-15**

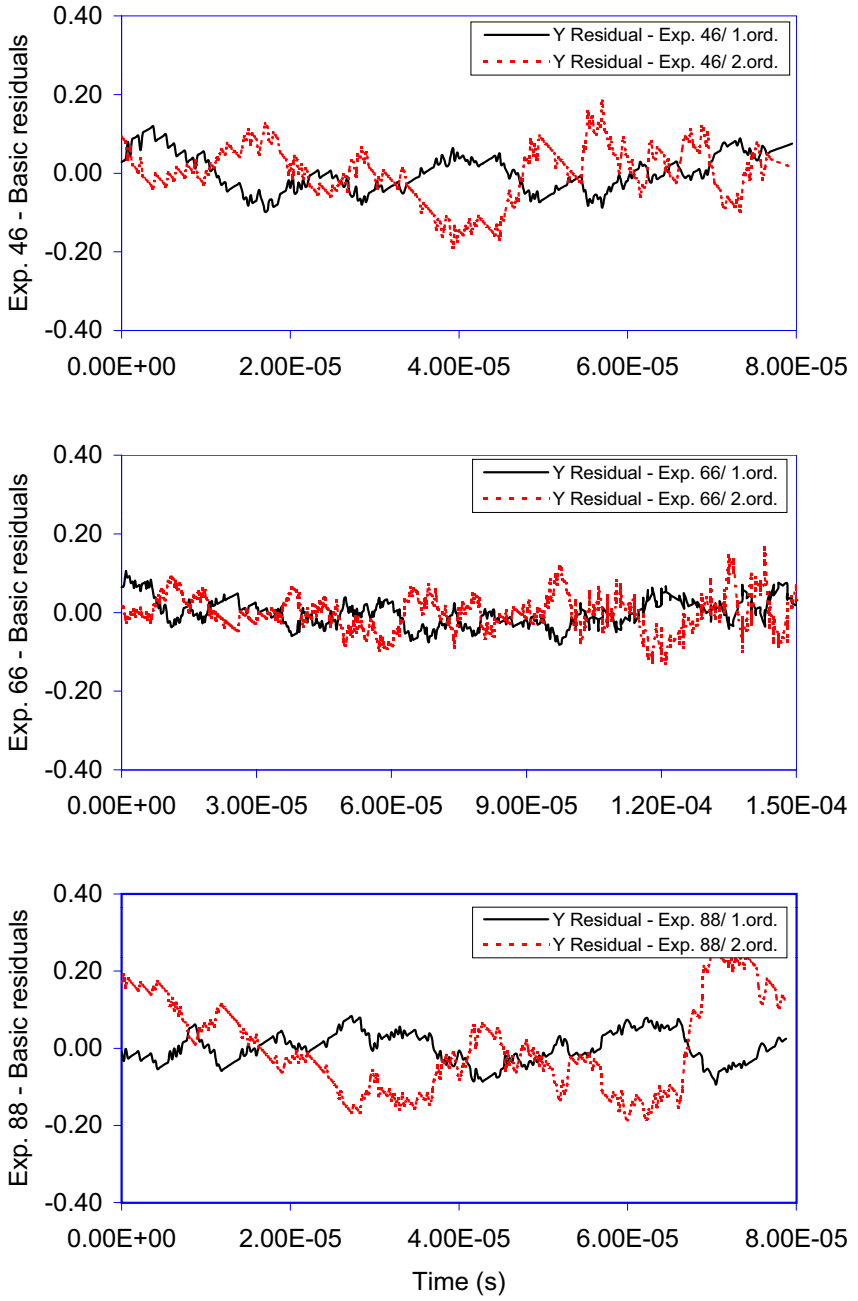

Figure 4-24: Residual errors - reaction order

Plots of the residual errors for first- and second order decomposition profile assumptions for three selected experiments (46, 66 and 88).

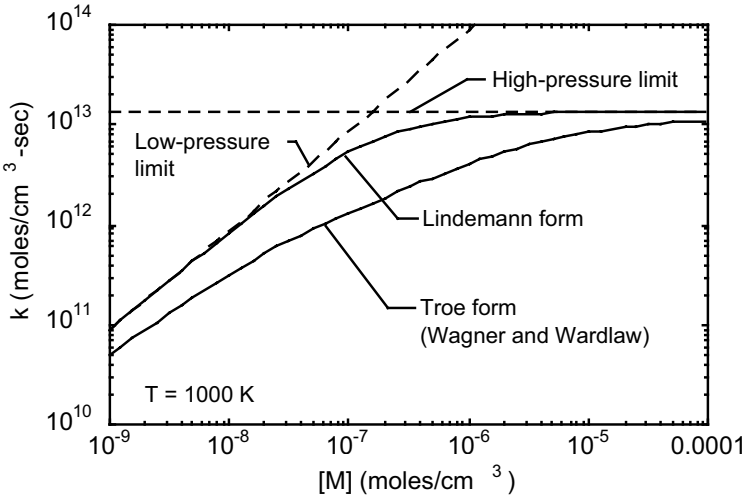

Figure 4-25: Rate constant vs. pressure at fixed temperature

Rate constant vs. pressure at fixed temperature for an unimolecular fall-off reaction. The Troe and Lindemann forms are illustrated as are the low- and high-pressure limiting forms (Chemkin III manual (1999)).

In this work, no attempt was done to derive separate expressions for the high- and low pressure domain. From the plot of the current experiments (figure 4-26) together with the transition curves derived by Glänzer and Troe (1972), we observe that we are mainly in the transition-, towards the high-pressure domain. The heavy scattering is caused by both temperature and pressure variations in the present experiments.

Half-life times

When an incubation time is observed, it is difficult to define a reaction order. As the temperature increases the incubation time gets smaller and tends to zero above approximately 1200 *K*. The half-life time, $t_{1/2}$,is defined as the time needed to consume 50 % of the initial concentration from the arrival of the reflected shock, and is a function of the temperature and pressure corresponding to the state of the reflected shock. A value for the half-life time can be obtained directly from the absorption signals since the absorption signals are directly proportional to the concentration. If concentration is preferred, the absorption signals can be converted to concentration by the law of Beer-Lambert (APPENDIX A). An expression for the half-time, $t_{1/2}$, is given on an Arrhenius equivalent form as:

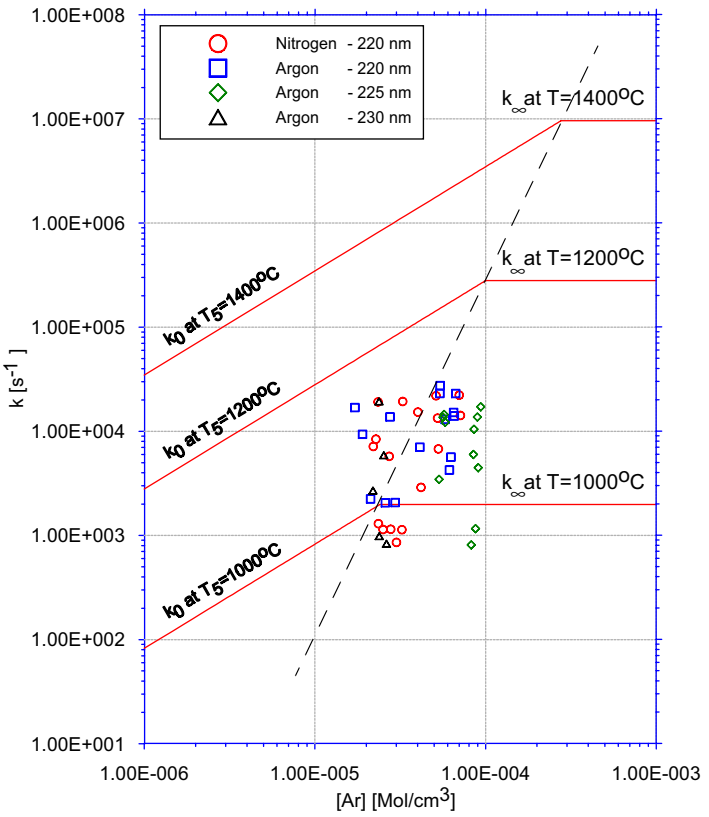

Figure 4-26: Fall-off curves for current experiments.

Straight lines are high- and low pressure asymptotic limits deduced by Glänzer and Troe (1972).

High pressure domain: $k_\infty \cong 10^{16.2} \cdot \exp\left(-\frac{247\ \text{kJ/mole}}{RT}\right) \quad [s^{-1}]$

Low pressure domain: $k_0 \cong 10^{17.1} \cdot \exp\left(-\frac{205\ \text{kJ/mole}}{RT}\right) \quad [cm^3 mole^{-1} s^{-1}]$

$$t_{1/2} = A \cdot e^{E/(RT)} \qquad \textbf{Eq. 4-16}$$

Defining Y as:

$$Y = \ln(t_{1/2}) = \ln(A) + E/(RT) = \ln(A) + E_T \cdot \frac{1}{T} \qquad \textbf{Eq. 4-17}$$

Then A and E_T are deduced from the best linear correlation for the obtained curve Y=f(1/T) from all experiments and their corresponding values for $t_{1/2}$.

The rate constant and the half-life time is related by:

$$k = \frac{\ln(2)}{t_{1/2}} \quad (s^{-1}) \qquad \textbf{Eq. 4-18}$$

If the processing of the data has been done correctly, the rate constant from the slope of the concentration vs. time and the rate constant from the half-life time value, should give approximately the same values. Some values from the decomposition experiments are tabulated for comparison in table 4-5. Both figure 4-27, figure 4-28 and table 4-5 show that there are no significant differences between the experimental and calculated half-life times.

Table 4-5: Comparison of half-life times

Comparison between the experimental and calculated half-life time of NM in NM/Ar and NM/N_2 mixtures.

Experiment	$t_{1/2, exp.}$	$t_{1/2, calc.}$	Experiment	$t_{1/2, exp.}$	$t_{1/2, calc.}$	Experiment	$t_{1/2, exp.}$	$t_{1/2, calc.}$
220 nm - nitrogen			220 nm - argon			225 nm - argon		
Man #28	1.01E-04	1.30E-04	Man #73	4.02E-05	5.70E-05	Man #89	2.05E-04	1.55E-04
Man #13	7.88E-05	9.00E-05	Man #72	8.09E-05	8.50E-05	Man #87	5.19E-05	3.00E-05
Man #42	4.00E-05	3.50E-05	Man #71			Man #85	5.05E-05	4.10E-05
Man #27	5.30E-04	3.80E-04	Man #49	7.24E-05	3.90E-04	Man #90	6.07E-05	5.50E-05
Man #23	6.29E-04	9.70E-04	Man #74		1.70E-05			
Man #41	2.91E-04	5.45E-04	Man #54	2.56E-05	1.90E-05	Man #86		5.15E-04
			Man #47	2.53E-05	2.00E-05	Man #83	1.23E-04	1.00E-04
Man #33	1.25E-04	1.40E-04	Man #53	2.28E-05	2.20E-05	Man #84	6.44E-05	6.40E-05
Man #40	5.92E-04					Man #82	5.35E-04	3.40E-04
Man #39			Man #55	1.54E-04	2.10E-04	Man #88	4.86E-05	4.00E-05
Man #12			Man #48	3.08E-04	3.30E-04	Man #81	1.63E-04	1.19E-04
Man #22	3.30E-05	3.50E-05	Man #50	5.46E-05	5.60E-05	Man #80	4.42E-05	4.00E-05
Man #32	9.37E-05	1.75E-04	Man #52	3.27E-04	3.60E-04			
Man #21	4.50E-05	4.00E-05						
Man #29	2.37E-04	2.40E-04	Man #62	1.08E-04	1.10E-04			
			Man #59	1.87E-04	6.60E-04			
Man #38	3.25E-05	3.50E-05	Man #57	3.06E-05	3.10E-05			
Man #43	5.60E-05	7.10E-05	Man #58	2.65E-05	2.80E-05			
Man #36	1.02E-04	1.65E-04				Experiment	$t_{1/2, exp.}$	$t_{1/2, calc.}$
			Man #61	5.71E-05	5.90E-05	230 nm - argon		
Man #45	3.16E-05		Man #60	1.61E-04	1.37E-04	Man #79	2.59E-04	3.90E-04
Man #46	4.65E-05		Man #66	1.26E-04	1.36E-04	Man #76	3.95E-05	4.10E-05
			Man #64	4.77E-05	6.10E-05	Man #78	7.20E-04	8.65E-04
			Man #65	5.60E-05	6.10E-05	Man #77	1.21E-04	1.60E-04
			Man #63	3.31E-05	3.50E-05	Man #75		9.35E-04

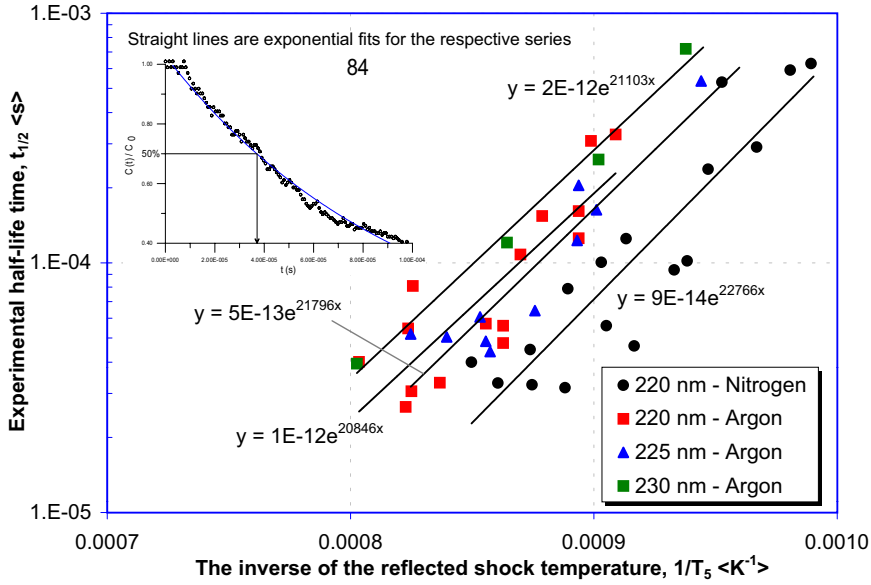

Figure 4-27: Half-life time signals for decomposition experiments.

The reaction rate constant

The evolution of the NM concentration behind reflected shock waves was deduced from the analysis of the absorption signals. It was found that the NM concentration profile corresponded well to the law for a first order reaction. In the temperature and pressure range, the initial step is likely the bimolecular reaction, as several authors have reported it:

$$CH_3NO_2 + M \quad \rightarrow \quad CH_3 + NO_2 + M \qquad (4\text{-}1)$$

,where M is a third body (e.g. N_2 or Ar). To derive the Arrhenius expression for eq. 4-1, the experimental pressure independent reaction rate values, k_∞ in s^{-1}, derived from analysing the decomposition signals as in figure 4-22, was plotted against the inverse of the temperature in the reflected shock, T_5. From figure 4-29 (bottom) the reaction rate expression, $k_\infty(T_5)$ in s^{-1}, can be extracted from the best exponential fit of k_∞ vs. $1/T_5$. Pressure dependent reaction rates k_0, in $cm^3/(mole \times s)$, are found by reducing the extracted k_∞ values with diluent concentration. An expression for $k_0(T_5)$, in $cm^3/(mole \times s)$, can then be derived again from the best exponential fit of k_0 vs. $1/T_5$ (figure 4-29, topmost). The equation for the resulting best exponential fits and the values of the Arrhenius parameters extracted from these plots are tabulated in table 4-6 and table 4-7.

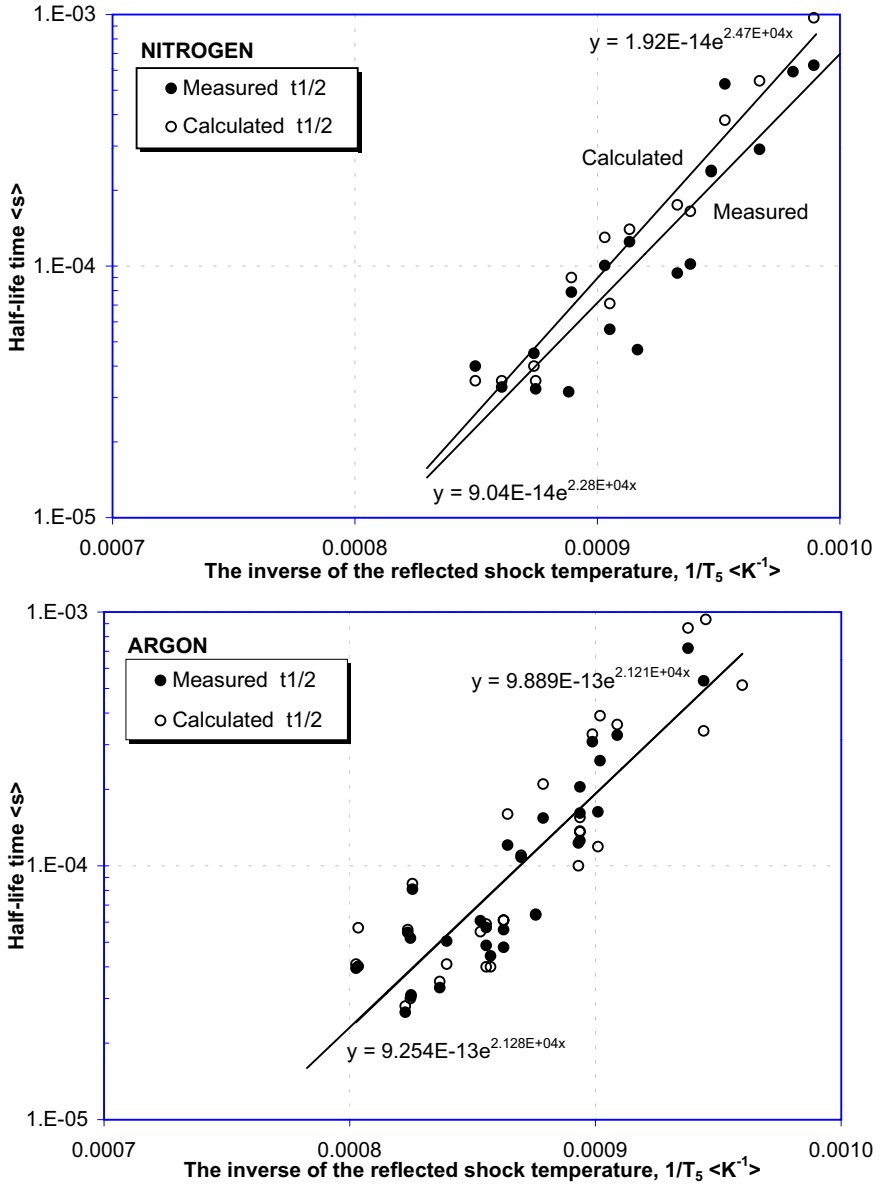

Figure 4-28: Half-life times versus the inverse of the reflected shock.

Comparison between the experimental and calculated half-life time of NM in NM/Ar and NM/N_2 mixtures. Straight lines are exponential fits for experimental and calculated data. The equation describing the respective fitted data are indicated.

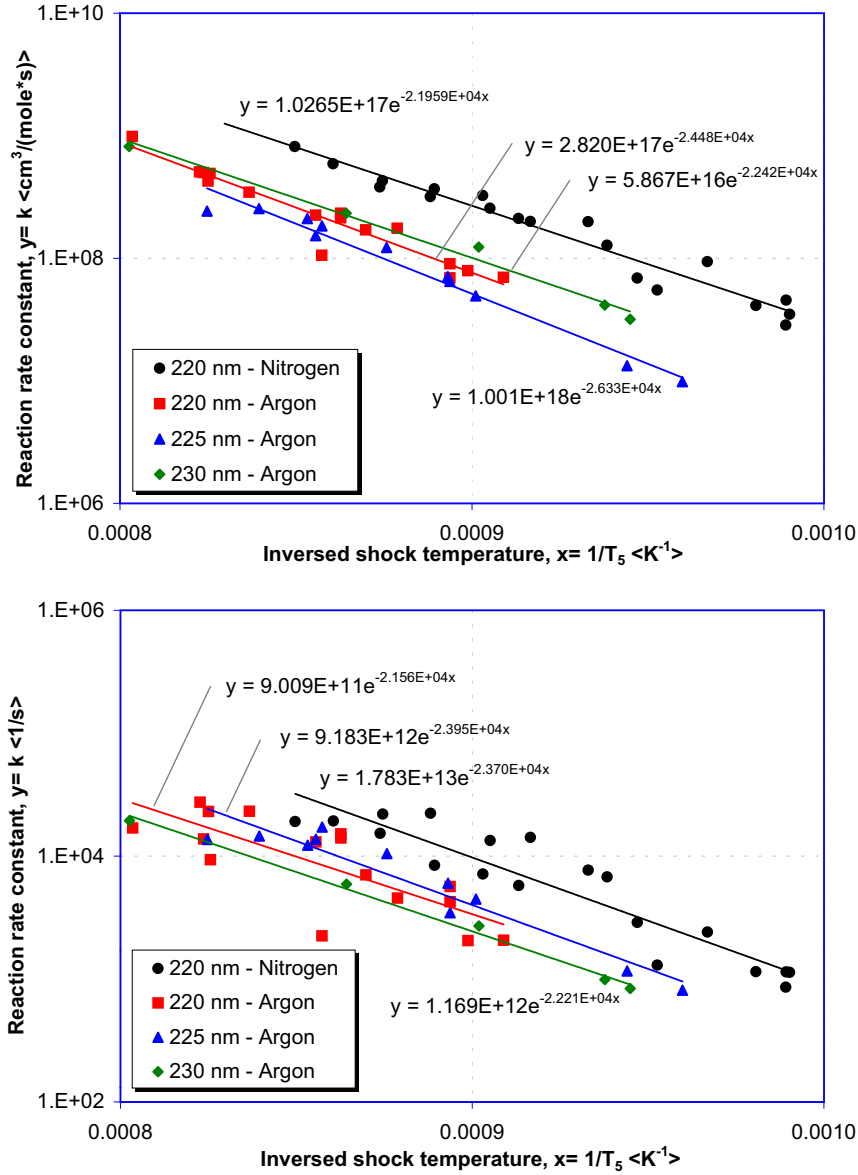

Figure 4-29: The reaction constant

The temperature dependence of the reaction rate constant with (topmost) and without diluent concentration <*mol/cm*^{3}> as parameter.

Table 4-6: Rate equations

Rate equations derived from experimental data with units in *cm^3/(mole s)* in the Arrhenius form of $k = A \times \exp(-E_T/T)$ and $k = A \times \exp(-E_a/RT)$ with k in *cm^3/(mole×s)*.

Diluent	**Wavelength** λ **[nm]**	**The reaction rate constant, k** $k = A \times \exp(-E_T/T(K))$ **[cm^3/(mole×s)]**
N_2	220	$k = 1.026 \times 10^{17} \exp(-21960 / T(K))$
Ar[a]	220-230	$k = 3.738 \times 10^{17} \exp(-24900 / T(K))$
For argon in separate wavelength domains		
Ar	220	$k = 2.820 \times 10^{17} \exp(-24480 / T(K))$
Ar	225	$k = 1.001 \times 10^{18} \exp(-26330 / T(K))$
Ar	230	$k = 5.867 \times 10^{16} \exp(-22420 / T(K))$

a. Resulting from a single fit for argon, through all data points regardless of wavelength (extracted from figure 4-30).

Table 4-7: Parameters derived from the Arrhenius expression.

Parameters of the Arrhenius expression derived from the best fit equation for each wavelength domain and different diluents given R = 1.986 kcal/(kmole×K) = 8.315 kJ/(kmole×K).

Diluent	**Wavelength** λ **[nm]**	**A**	**E_T** **[K]**	**$E_a = E_T \times R$** $E_T \times R$ **(kcal/mole×K)** **[kcal/mole]**	$E_T \times R$ **(kJ/mole×K)** **[kJ/mole]**
N_2	220	$10^{17.011}$	21960	43.6	182.6
Ar	220-230	$10^{17.574}$	24900	49.5	207.0
For argon in separate wavelength domains					
Ar	220	$10^{17.45}$	24480	48.6	203.6
Ar	225	10^{18}	26330	52.3	218.9
Ar	230	$10^{16.768}$	22420	44.5	186.4

The tabulated results give two expressions for the rate constant as a function of temperature, one with nitrogen as diluent and the second with argon as diluent. These expressions for the rate constant can then be directly incorporated into any desired reaction mechanism:

Diluted with nitrogen:

$$k = 10^{17.011} \cdot \exp\left(-\frac{182.6\ \text{kJ/mole}}{RT}\right)\ [\text{cm}^3/(\text{mole} \cdot \text{s})] \qquad \textbf{Eq. 4-19}$$

Diluted with argon (over all observed wavelengths):

$$k = 10^{17.574} \cdot \exp\left(-\frac{207\ \text{kJ/mole}}{RT}\right)\ [\text{cm}^3/(\text{mole} \cdot \text{s})] \qquad \textbf{Eq. 4-20}$$

In figure 4-30 and figure 4-31, results from previous authors have been incorporated for comparison (Glänzer and Troe (1972); Hsu and Lin (1985); Cotrell, Graham and Reid (1951); Zaslonko et al. (1972)). From the figures we can observe that the current results tend to fall somewhere halfway between earlier results from Glänzer and Troe and Cotrell et al. The results obtained both by Zaslonko et al. and Hsu and Lin, correspond very well with the current results. From figure 4-30 it is interesting to observe the increased NM decomposition when diluting with nitrogen, compared to that of argon, which is due to the higher activation energy. In table 3-4 several values for the activation energy, E_a, are listed for comparison.

The difference in reaction rate when comparing for argon at different wavelengths, is somewhat inconsistent in that the rate constant at 225 *nm* is a little lower than at 230 *nm* (figure 4-29). This inconsistency is possibly a result of inaccuracy in the measurements.

A plot of the reaction rate constant, k (s^{-1}), versus the temperature of the reflected shock with argon as parameter, will unveil the pressure dependency of the NM decomposition in the low-pressure area. Increasing the pressure above the high-pressure transition domain, should only give one straight line in such a plot, because of the pressure independency here. From figure 4-26 we can see that the current experiments are all within the transition domain. This is also reflected in figure 4-32, when observing the pressure dependent separation. The possible pressure dependence for the current results indicates that we really are in the transition domain.

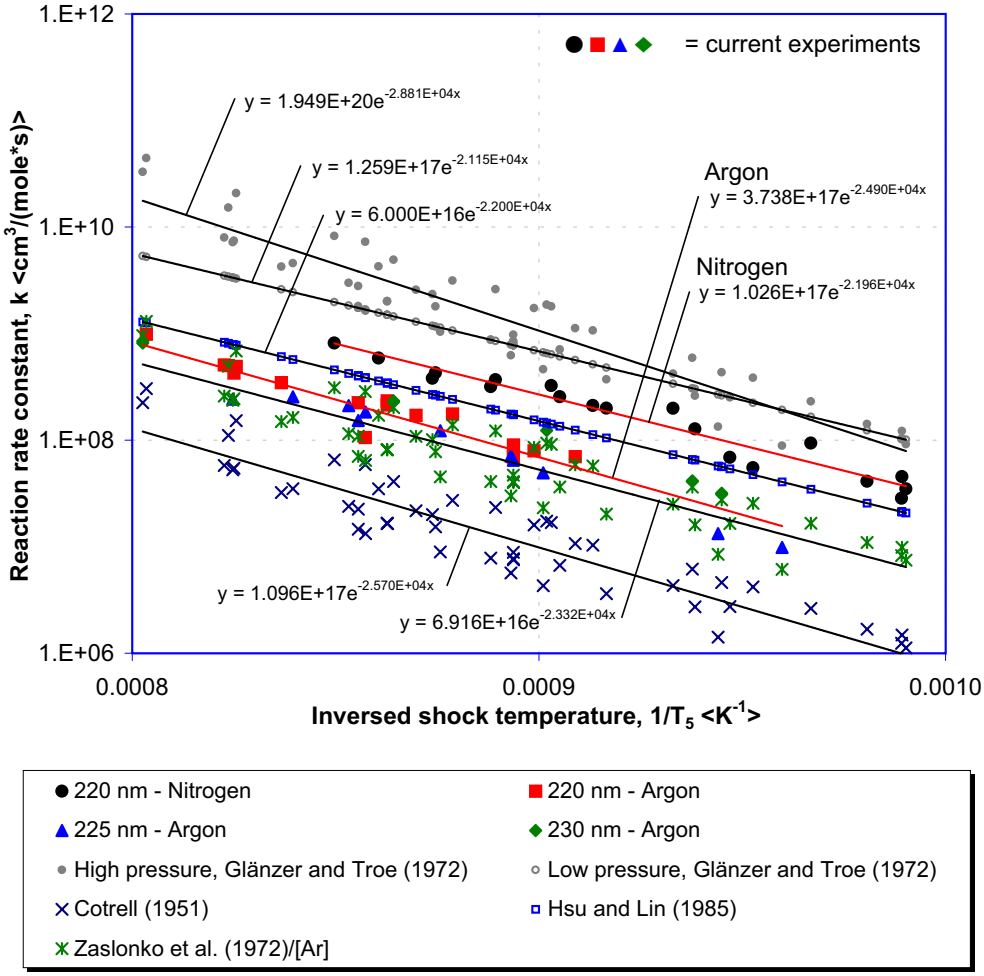

Figure 4-30: The reaction rate constant, k $<cm^3/(mol \times s)>$.

The logarithmic evolution of the reaction rate constant, k, versus time. Comparison of previous work (Glänzer and Troe (1972); Cotrell, Graham and Reid (1951); Hsu and Lin (1985); Zaslonko et al. (1972)) with current experiments.

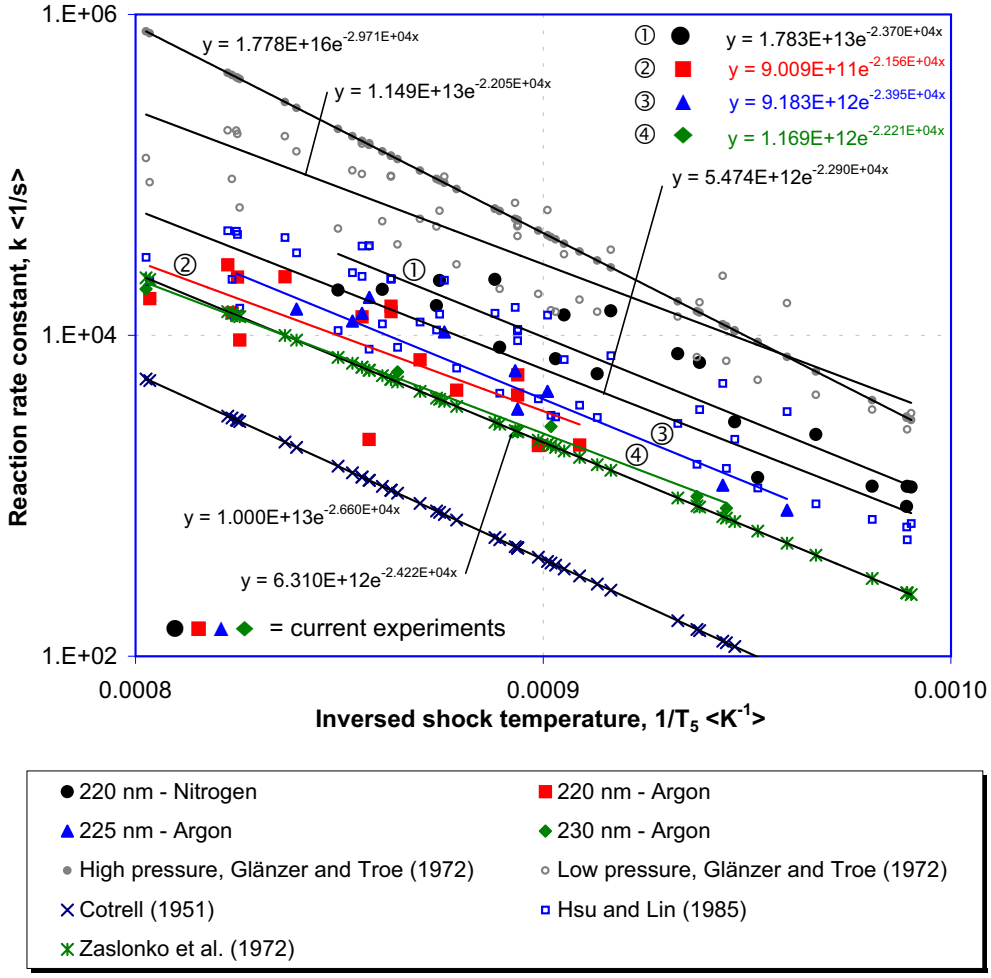

Figure 4-31: The reaction rate constant k <*1/s*> versus $1/T_5$ <*K*>.

The logarithmic evolution of the reaction rate constant, k, versus time. Comparison of previous work (Glänzer and Troe (1972); Cotrell, Graham and Reid (1951); Hsu and Lin (1985); Zaslonko et al. (1972)) with current experiments.

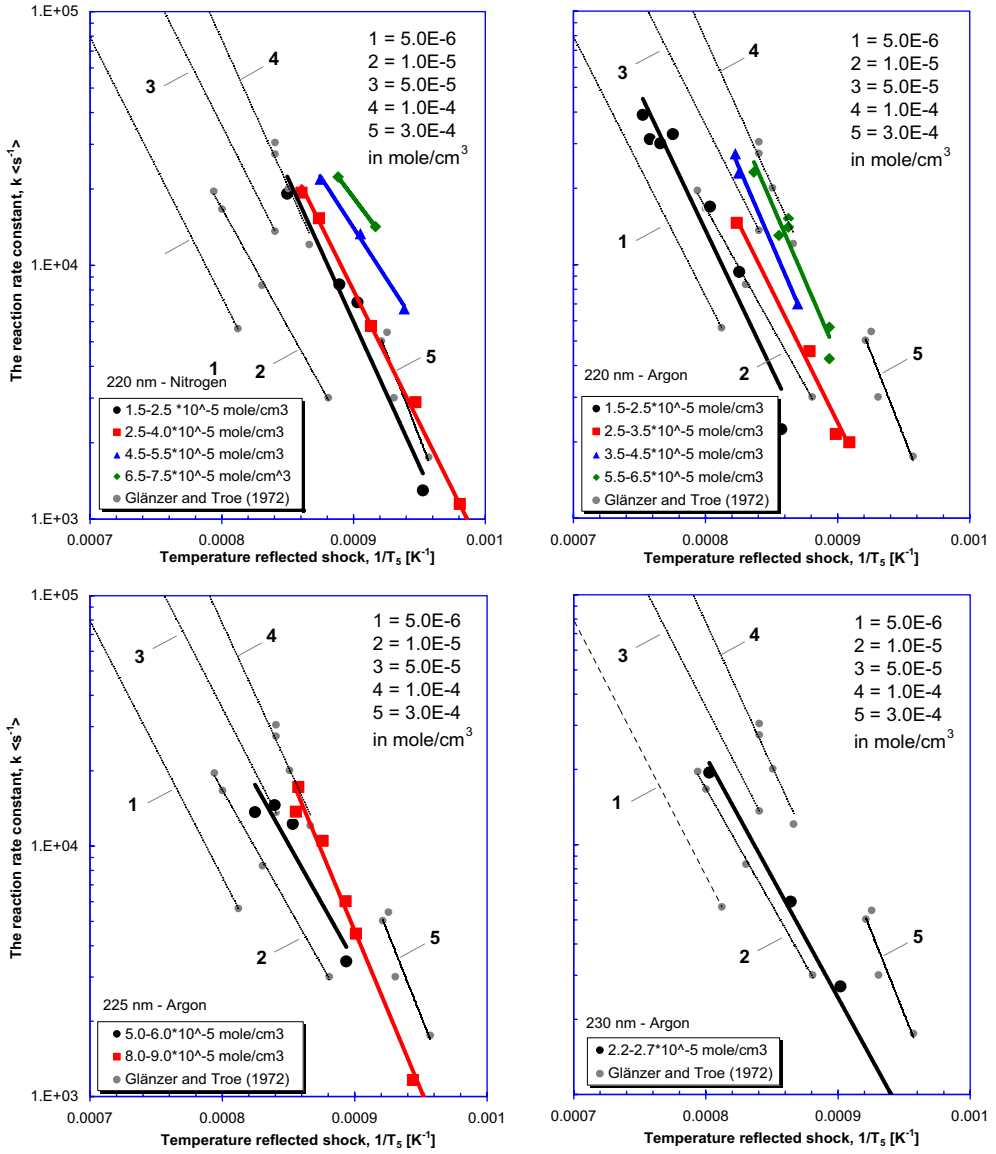

Figure 4-32: The reaction rate temperature dependency.

Comparison of the results obtained in current experiments with results (thin dotted lines) obtained by Glänzer and Troe (1972), where the abscissa is the reaction rate constant, k in s^{-1}, and the ordinate axis is the inverse of the temperature of the reflected shock, T_5 in K^{-1}. The straight lines indicates points with constant pressure (equivalent to argon concentration)

4.3.2 NM/Ar/O_2 - oxidation experiments

Half-life time correlations

Half-life time correlations are useful to obtain a rate constant for the decomposition of pure nitromethane. However, when oxygen is added, the half-life time measured can be compared to investigate the influence of additives on the nitromethane decomposition rate. From the behavior of the signal measured during the experiments, the NM absorption signals were divided into three types:

1. Absorption signals with emission
2. Absorption signals (observed emission)
3. Emission signals

Figure 4-33 shows a plot of the natural logarithm to the half-life times obtained for type 1 and 2 signals vs. the inverse of the temperature of the reflected shock. As defined in earlier chapters, type 1 signals were characterised by the appearance of emission when all or most of the nitromethane had been consumed, which means that an emission signal is superimposed on the light source signal because of an ignition. Type 2 signals showed an incubation time followed either by simultaneous decomposition and oxidation or only oxidation.

Figure 4-33 shows the equations describing the linear correlations for each signal type. The resulting correlation for both type 1 and 2 are illustrated on the same plot. The reason that the points are scattered can be explained by the fact that the experiments have been performed in the fall-off range. When the experiments fall within the low-pressure range, it means the reactions are pressure dependent and should be found on the pressure dependent form:

$$k_0 = [\text{Diluent}] \cdot A \cdot \exp\left(-\frac{E_a}{RT}\right) \quad [\text{cm}^3\text{mole}^{-1}\text{s}^{-1}] \qquad \textbf{Eq. 4-21}$$

The correlations for the half-life time can be expressed on an Arrhenius type of form, similar to the expression for the rate constant.

Signal of type 1:

$$t_{1/2} = 2.71 \cdot 10^{-9} \cdot \exp\left(\frac{12180.6}{T}\right) \qquad \textbf{Eq. 4-22}$$

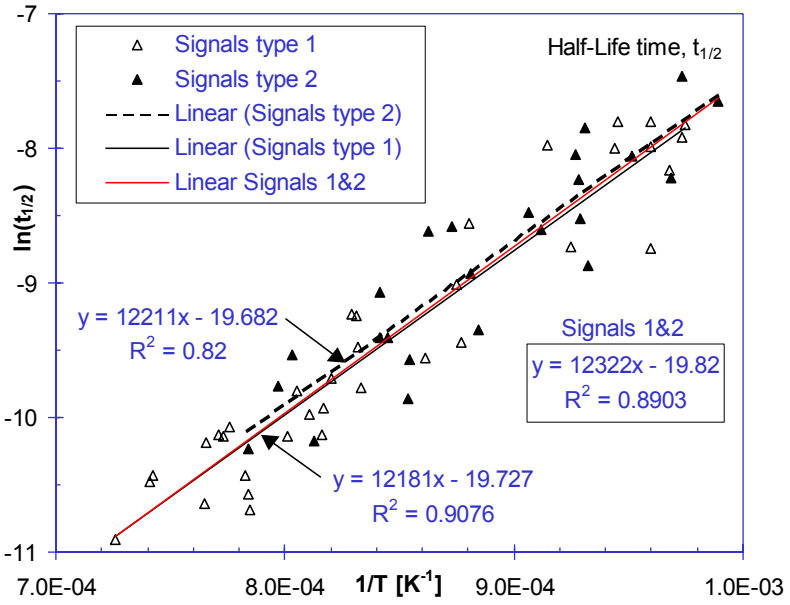

Figure 4-33: Half-life times for signals of type 1 and 2.

A linear correlation for the half-life time vs. the inverse of the temperature of the reflected shock can be found for the experimental results for the NM/O_2/Ar mixtures.

Signal of type 2:

$$t_{1/2} = 2.83 \cdot 10^{-9} \cdot \exp\left(\frac{12210.6}{T}\right) \qquad \textbf{Eq. 4-23}$$

Signal of type 1 and 2:

$$t_{1/2} = 2.47 \cdot 10^{-9} \cdot \exp\left(\frac{12321.7}{T}\right) \qquad \textbf{Eq. 4-24}$$

Ignition delay times

In the present study on nitromethane oxidation the ignition delay time has been defined as the time interval between the arrival of the reflected shock and the beginning of light emission at 235 *nm*, for signals of type 1 and 3. Here the type 3 signals were signals characterized by emission occurring a certain time after the arrival of the reflected shock. Because there were neither emission nor pressure increase from signals of type 2, it was not possible to apply the same definition. It was decided to define a characteristic time, as

the time needed to decompose 10 % of the nitromethane from the arrival of the reflected shock. The characteristics of each signal type are illustrated in figure 4-12 and figure 4-13.

Two correlations were sought, one to express the ignition delay times for signals of type 1 and 3, and another for the defined characteristic time for signals of type 2. It is desirable to develop a model for the ignition delay times in terms of both the reflected shock temperatures and the initial gas concentrations. On the basis of the Arrhenius rate relation, the correlation for ignition delay time can be formulated as follows:

$$\tau = K \cdot \exp\frac{E}{RT} \cdot [NM]^{l}[O_2]^{m}[Ar]^{n} \qquad [\text{sec}] \qquad \textbf{Eq. 4-25}$$

or written as:

$$\tau = K \cdot x^{l} \cdot y^{m} \cdot z^{n} \cdot \left(\frac{P}{RT}\right)^{l+m+n} \exp\left(\frac{E}{RT}\right) \qquad \textbf{Eq. 4-26}$$

when [...] = zP/(RT). This form is very often used when comparing data for ignition delay times. We then reformulate eq. 4-26:

$$\ln\tau = \ln(K) + l \cdot \ln[NM] + m \cdot \ln[O_2] + n \cdot \ln[Ar] + \frac{E}{RT} \qquad \textbf{Eq. 4-27}$$

Y can be defined as:

$$Y = \ln(K) + \frac{E}{RT} = \ln\tau - (l \cdot \ln[NM] + m \cdot \ln[O_2] + n \cdot \ln[Ar]) \qquad \textbf{Eq. 4-28}$$

A correlation for the ignition delay time, obtained by least-square linear regression, can then be elaborated and the reliability of the correlations proven by plotting the experimental data as Y versus 1/T.

Ignition delay time correlation for signals of type 1 and 3
The correlation was found to be:

$$\tau = 0.3669 \cdot 10^{-2} \cdot [NM]^{-1.02}[O_2]^{-1.08}[Ar]^{1.42} \cdot \exp\left(\frac{7767}{T}\right) \qquad \textbf{Eq. 4-29}$$

which is valid under conditions as follows:

$$1 < \Phi < 3.5$$
$$0.039 < x < 0.064$$
$$0.032 < y < 0.08$$
$$0.864 < z < 0.92$$
$$44.3 < P < 277.94\ kPa$$
$$1026 < T < 1378\ K$$

,with an accuracy of 18.5 *%* (figure 4-34A). When the molar fraction of argon tends to unity ($z^{1.42} = 1$), as with highly diluted mixtures, a different correlation may be derived with an accuracy of 25 *%*.

$$\tau = 0.3696 \cdot [NM]^{0.11}[O_2]^{-0.67}[Ar]^{0.0} \cdot \exp\left(\frac{7126}{T}\right) \qquad \textbf{Eq. 4-30}$$

This expression, in which the molar fraction of argon does not appear, can then be applied to slightly or non-diluted mixtures. It should be noted that the pressure dependency for both correlations is not significantly different.

A quasi-constant activation energy can be deduced from the correlations as:

- $E_{Tq} = 64.574\ kJ/mol$ (from eq. 4-29)
- $E_{Tq} = 59.246\ kJ/mol$ (from eq. 4-30)

Ignition delay time correlation for signals of type 2

A correlation similar to the ignition delay time was found as:

$$\tau_{10\%} = 0.3005 \cdot 10^{-2} \cdot [NM]^{-0.28}[O_2]^{0.12}[Ar]^{-0.59} \cdot \exp\left(\frac{13657}{T}\right) \qquad \textbf{Eq. 4-31}$$

, with an accuracy of 19.4 *%* (figure 4-34B) and valid under following conditions:

$$0.5 < \Phi < 2.33$$
$$0.0204 < x < 0.064$$
$$0.0105 < y < 0.1244$$
$$0.84 < z < 0.9865$$
$$52.48 < P < 483.29\ kPa$$
$$1001 < T < 1275\ K$$

From eq. 4-31, the oxygen component can be seen as positive; in most correlations for ignition delay time, this exponent is however, found to be negative. This means that increasing the oxygen content will reduce the ignition delay time. However, because of the

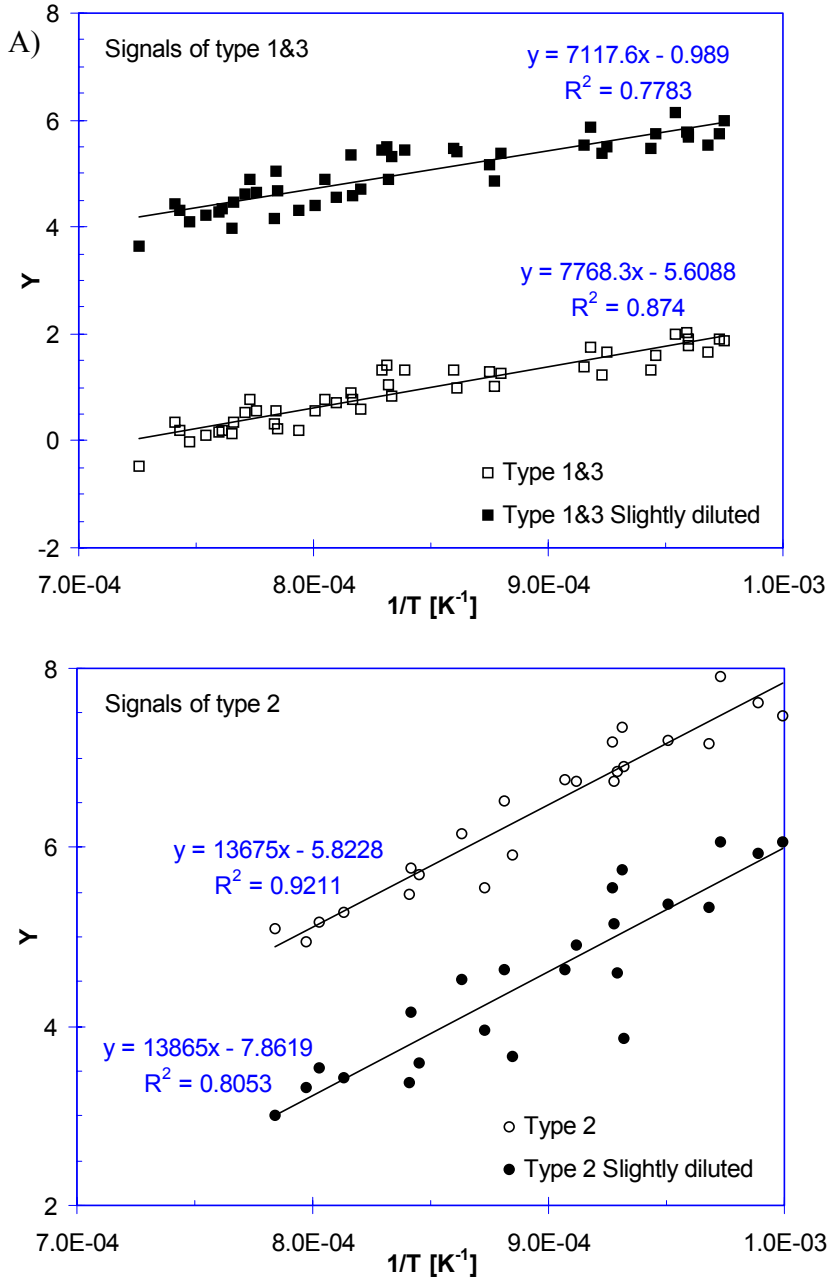

Figure 4-34: Ignition delay time and characteristic time correlations.

Ignition delay time and characteristic time correlations for signals of type 1 and 3 (A) and type 2 (B), where the ordinate axis is defined from eq. 4-28. Correlations for slightly diluted mixtures are also shown.

definition used here, this correlation is not directly comparable to correlations found in literature. As with the signals of type 1 and 3, we can deduce a correlation for slightly diluted mixtures, when the molar fraction of argon equals unity:

$$\tau_{10\%} = 0.3844 \cdot 10^{-3} \cdot [NM]^{-0.12}[O_2]^{0.10}[Ar]^{0.0} \cdot \exp\left(\frac{13866}{T}\right) \qquad \textbf{Eq. 4-32}$$

, with an accuracy of 26.9 *%* (figure 4-34A). A quasi-constant activation energy can be deduced from the correlations as:

- E_{Tq} = 113.544 *kJ/mol* (from eq. 4-31)
- E_{Tq} = 115.282 *kJ/mol* (from eq. 4-32)

An ignition delay time was derived for the signal of type 1 and 3, defined as the time interval between the arrival of the reflected shock and the detection of emission. For signals of type 2, the Arrhenius correlation was defined as the time interval between the arrival of the reflected shock and the time where 10 *%* of the nitromethane had been consumed.

Table 4-8: Ignition delay times

Comparison of ignition delay times deduced from experiments with those found by Kang et al. (1991).

	Delay time	Constant	Exponential factor NM	O_2	Ar	E_a [kJ/mol]	Remarks
1	$\tau_{10\,\%}$	0.003005	0.28	0.12	-0.59	113.5	Signal of type 2
2	$\tau'_{10\,\%}$	0.0003844	-0.12	0.10	0.00	115.3	
3	τ	0.003669	-1.02	-1.08	1.42	64.56	Signal of type 1 and 3
4	τ'	0.3696	0.11	-0.67	0.00	59.24	
5	τ_{Kang}	0.0776	0.59	-0.72	0.00	89.43	Kang et al. (1991)

4.4 COMPUTER SIMULATIONS

Introduction

In the area of chemical decomposition of explosives, nitromethane (CH_3NO_2) was chosen for an in-depth study partly because of its relatively simple chemical structure. In a modeling point of view it is advantageous because of the subset of its gas phase kinetics derived from CH_3 radicals which is related to the "well-known" methane (CH_4) kinetics.

The present study presents the different elementary reactions and their rate constants, thermodynamical data for species involved and the mechanisms pertinent to the thermal decomposition of nitromethane collected from various sources and authors. Thermo chemical data for some of the species expected to be involved in the reaction were missing from the reaction mechanisms found in the literature and had to be estimated by using group additivity theory.

Different reaction mechanisms have been collected from various authors (Guirguis et al. (1983), Guirguis et al. (1985), Hsu and Lin (1985), Perche, Tricot and Lucquin (1979a) and Perche, Tricot and Lucquin (1979b)) and compared

The reaction mechanism

The present experimental study on the thermal decomposition of gaseous NM in a shock tube was performed using NM-mixtures (0.2-1.5 *vol%*) highly diluted in either nitrogen or argon, in the pressure range 1.8-9.0 *atm* and temperature range 850-1550 *K*. High dilution has the advantage of minimising effects due to secondary and tertiary reactions. Measurements were done in the reflected shock. During most of the experiments, the NM concentration evolution over time was registered by UV spectroscopy at 220 *nm*. However, experiments performed in the highest concentration (1.5 *vol%*) and pressure range (9 *atm*.) required UV absorption at higher wavelengths (225 and 230 *nm*).

Reaction mechanisms from different authors

For the kinetic modeling, three different decomposition mechanisms were found to apply to our experimental conditions (Hsu and Lin (1985); Guirguis et al. (1983), 1985). The reaction mechanisms are tabulated in table 4-9 (more information in APPENDIX C). The reaction mechanisms were adapted to the computer code CHEMKIN (SHOCK and SENKIN). Thermodynamical data for the species were taken from the BURCAT (Burcat and Mc Bride (1994)) database.

Table 4-9: Species considered for each of the three reaction mechanisms.

Mechsenk 010-011 Guirguis et al. (1983)	**Mechsenk 020-021** Guirguis et al. (1985)	**Mechsenk 030-031** Hsu and Lin (1985)	**Mechanism used in the present study**
AR	AR	AR	N_2 / Ar
	C_2H_2		
	C_2H_3		
C_2H_4	C_2H_4	C_2H_4	C_2H_4
C_2H_5	C_2H_5	C_2H_5	C_2H_5
C_2H_6	C_2H_6	C_2H_6	C_2H_6
	CH_2NO		
CH_2NO_2	CH_2NO_2	CH_2NO_2	CH_2NO_2
CH_2O	CH_2O	CH_2O	CH_2O
	CH_2OH		
CH_3	CH_3	CH_3	CH_3
CH_3NO	CH_3NO	CH_3NO	CH_3NO
CH_3NO_2	CH_3NO_2	CH_3NO_2	CH_3NO_2
CH_3O	CH_3O	CH_3O	CH_3O
CH_3OH	CH_3OH	CH_3OH	CH_3OH
CH_3ONO			CH_3ONO
CH_4	CH_4	CH_4	CH_4
CO	CO	CO	CO
CO_2	CO_2	CO_2	CO_2
H	H	H	H
H_2	H_2	H_2	H_2
H_2O	H_2O	H_2O	H_2O
	HCN	HCN	
HCO	HCO	HCO	HCO
HNO	HNO	HNO	HNO
HNO_2	HNO_2	HNO_2	HNO_2
NO	NO	NO	NO
NO_2	NO_2	NO_2	NO_2
O	O		O
OH	OH	OH	OH

Data for missing species

Data for the missing species was furnished by using group additives theory or by relating the species to similar ones in chemical structure and getting reasonable values for the vibrational frequencies of the missing or extra bonds to form the species in question. The thermodynamic data for the CH_2NO_2 was calculated by using group additivity theory (Ritter and Bozzeli (1987)). Figure 4-35 gives the calculated results. Later, thermodynamical data for the missing compound was found in the Chemkin III thermodynamic database and used in all the current simulations.

The database form includes the species name, the elemental composition of the species, and the temperature ranges over which the polynomial fits to thermodynamic data are valid. The fits to C_P^0/R, H_0/RT, S_0/R consist of seven coefficients for each of two temperature ranges. Further information about the fitting procedure and data for many species can be found in a report on the CHEMKIN Thermodynamic Database (Chemkin III manual (1999)).

Calculated thermodynamic values

```
THERMO
   300.000  1500.000  5000.000
CH2NO2    yy            C   1H   2O   2N   1G   300.000  5000.000 1392.000    01
 9.05455173E+00 6.12929579E-03-2.16895133E-06 3.44548621E-10-2.03138597E-14    2
 1.00753133E+04-2.27713594E+01 2.21085613E-03 2.88069222E-02-2.41476202E-05    3
 1.01115879E-08-1.69070685E-12 1.30441706E+04 2.52669417E+01                   4
END
```

Values from the Chemkin III database

```
THERMO
   300.000  1000.000  5000.000
CH2NO2       RAD  T04/98C  1.H  2.N  1.O  2.G   200.000  6000.000              1
 7.67214886E+00 7.04674142E-03-2.55301211E-06 4.14646979E-10-2.49316782E-14    2
 1.52307521E+04-1.22510821E+01 2.46754293E+00 1.56130407E-02 4.71686464E-06    3
-2.05123642E-08 1.02705094E-11 1.69015807E+04 1.59016345E+01 1.83372153E+04    4
```

Figure 4-35: Calculated thermodynamic data.

Comparison of values taken from the Chemkin III thermodynamic database (Chemkin III database (1997)) and calculated thermodynamic data for the CH_2NO_2-radical based on group theory and known values for CH_3NO_2 (Ritter and Bozzeli (1987)).

Reaction mechanism applied in simulations

Based on the three most comprehensive reaction mechanisms found in literature, a reaction mechanism was assembled, containing only the most significant chemical reactions (APPENDIX C).

For each of the diluents, the reaction constant and the activation energy (A and E for

						A	b	E
nitrogen:	CH3NO2 + M	=	CH3	+ NO2 + M		**1.03E17**	0.00	**43.60**
argon:	CH3NO2 + M	=	CH3	+ NO2 + M		**3.75E17**	0.00	**49.50**

SPECIES CONSIDERED:
AR/N2 CH3NO2 CH3 NO2 NO CO CO2 CH2O HCO CH4 CH2NO2 H H2 H2O OH HNO CH3OH
C2H6 C2H5 C2H4 CH3O CH3NO HNO2 O CH3ONO

	REACTIONS CONSIDERED	(k = A T^b exp(-E/RT)) A	b	E
1.	CH3NO2+M=CH3+NO2+M	**1.03E+17/3.75E+17**	0.0	**43.6/49.5**
2.	CH3+NO2=CH3O+NO	1.30E+13	0.0	0.0
3.	CH3O+M=CH2O+H+M	4.00E+40	-7.5	22.6
4.	NO2+H=NO+OH	2.90E+14	0.0	0.8
5.	CH3O+NO=CH2O+HNO	3.20E+12	0.0	0.0
6.	H+NO+M=HNO+M	5.40E+15	0.0	-0.6
7.	CH3O+NO2=CH2O+HNO2	4.00E+11	0.0	0.0
8.	HNO2+M=NO+OH+M	3.00E+18	0.0	46.7
9.	CH3+NO=CH3NO	4.00E+12	0.0	0.0
10.	CH3O+NO=CH3ONO	6.30E+13	0.0	0.0
11.	CH3O+H=CH2O+H2	1.00E+14	0.0	0.0
12.	CH3O+H=CH3+OH	9.09E+17	0.0	15.2
13.	CH3+OH=CH2O+H2	8.00E+12	0.0	0.0
14.	CH3O+OH=CH2O+H2O	3.20E+13	0.0	0.0
15.	H2+OH=H2O+H	5.20E+13	0.0	6.5
16.	CH3O+CH3O=CH3OH+CH2O	1.10E+13	0.0	0.0
17.	CH3NO2+CH3=CH2NO2+CH4	2.40E+11	0.0	9.0
18.	CH3NO2+NO2=CH2NO2+HNO2	3.07E+12	0.0	18.3
19.	CH3NO2+H=CH2NO2+H2	2.50E+09	1.3	2.6
20.	CH3NO2+OH=CH2NO2+H2O	6.90E+04	2.6	-1.9
21.	CH2NO2=CH2O+NO	1.00E+13	0.0	36.0
22.	CH2O+H=HCO+H2	2.50E+09	1.3	2.6
23.	CH2O+OH=HCO+H2O	6.90E+04	2.6	-1.9
24.	CH2O+NO=HCO+HNO	2.86E+14	0.0	42.0
25.	CH2O+CH2NO2=HCO+CH3NO2	2.50E+13	0.0	10.0
26.	HCO+NO2=HNO2+CO	1.00E+14	0.0	0.0
27.	HCO+NO2=H+CO2+NO	1.00E+14	0.0	0.0
28.	HCO+NO2=OH+CO+NO	1.00E+14	0.0	0.0
29.	HCO+M=H+CO+M	1.00E+15	0.0	14.7
30.	HCO+NO=HNO+CO	2.00E+11	0.5	2.0
31.	CO+OH=CO2+H	1.50E+07	1.3	-0.8
32.	CO+O+M=CO2+M	2.80E+13	0.0	-4.5
33.	CH3+CH3=C2H6	2.50E+12	0.0	0.0
34.	CH3+CH3=C2H5+H	8.00E+14	0.0	26.6
35.	CH3+CH3=C2H4+H2	1.00E+16	0.0	32.0
36.	C2H6+CH3=C2H5+CH4	5.50E+14	0.0	21.5
37.	C2H6+OH=C2H5+H2O	6.30E+13	0.0	3.6
38.	C2H6+H=C2H5+H2	1.30E+14	0.0	9.4
39.	C2H5+M=C2H4+H+M	4.70E+14	0.0	26.6
40.	C2H5+OH=C2H4+H2O	2.00E+13	0.0	0.0
41.	C2H4+OH=CH2O+CH3	5.00E+12	0.0	0.0
42.	CH4+OH=CH3+H2O	3.20E+13	0.0	5.0

NOTE: E units Kcal/mole, A units mole-cm-sec-K

Figure 4-36: Reaction mechanism used in current simulations.

reaction no. 1 in the Arrhenius expression as in figure 4-36) for NM, was derived directly by optimizing curve fits over all the decomposition experiments and by comparing results found in previous studies. Changing the reaction constant according to the previous

experimental results on NM decomposition can be justified by analysing the rate of production for each reaction. This analysis showed that the consumption of nitromethane is due mainly to the third body reaction, $CH_3NO_2 + M \rightarrow CH_3 + NO_2$, over the experimental temperature and pressure ranges of the present experiments. These results are further justified by the findings of Glänzer and Troe (1972), which claimed that the decomposition on nitromethane could be explained solely by this third body reaction.

The solution of the set of ordinary differential equations describing the collected elementary reactions to get the evolution of the species, temperature and pressure used the two modules SHOCK and SENKIN, which are contained in the CHEMKIN collection. This package allows information for the chemical reactions to be input in the standard form of writing chemical reactions. The thermodynamic data used were those from the BURCAT database (Burcat and Mc Bride (1994)).

Results and discussion

Shock tube experiments and extensive numerical simulations were used to provide information required to construct and modify existent reaction schemes for a detailed chemical mechanism for the decomposition of gaseous nitromethane diluted in either nitrogen or argon. Measurements were made of the transient NM concentration at a fixed location in the tube by using infrared spectroscopy at given wavelengths.

Three existing reaction schemes suitable for our experiments were taken as a basis to assemble a reaction mechanism suitable for the present conditions. In all three reaction schemes, the initiating reaction was the breaking of the C-N bond to yield CH_3 and NO_2. Methoxy and CH_2NO_2 radicals then propagate the reaction through two major parallel pathways both producing CH_2O. Formaldehyde is then reduced to HCO which react with NO_2 to yield the products. The calculated results from the different reaction schemes were compared to experiments and found to give good predictions of the decomposition of NM over the temperature and pressure range considered.

NM decomposition experiments

In figure 4-37, four selected experiments (exp. 13 and 38 diluted in nitrogen, and exp. 66 and 88 diluted in Ar) have been reproduced using the present reaction mechanism. The main products from decomposing NM over the given time interval are illustrated in figure 4-37, and given as: NO, CH_2O, CO, H_20, H_2, N_2

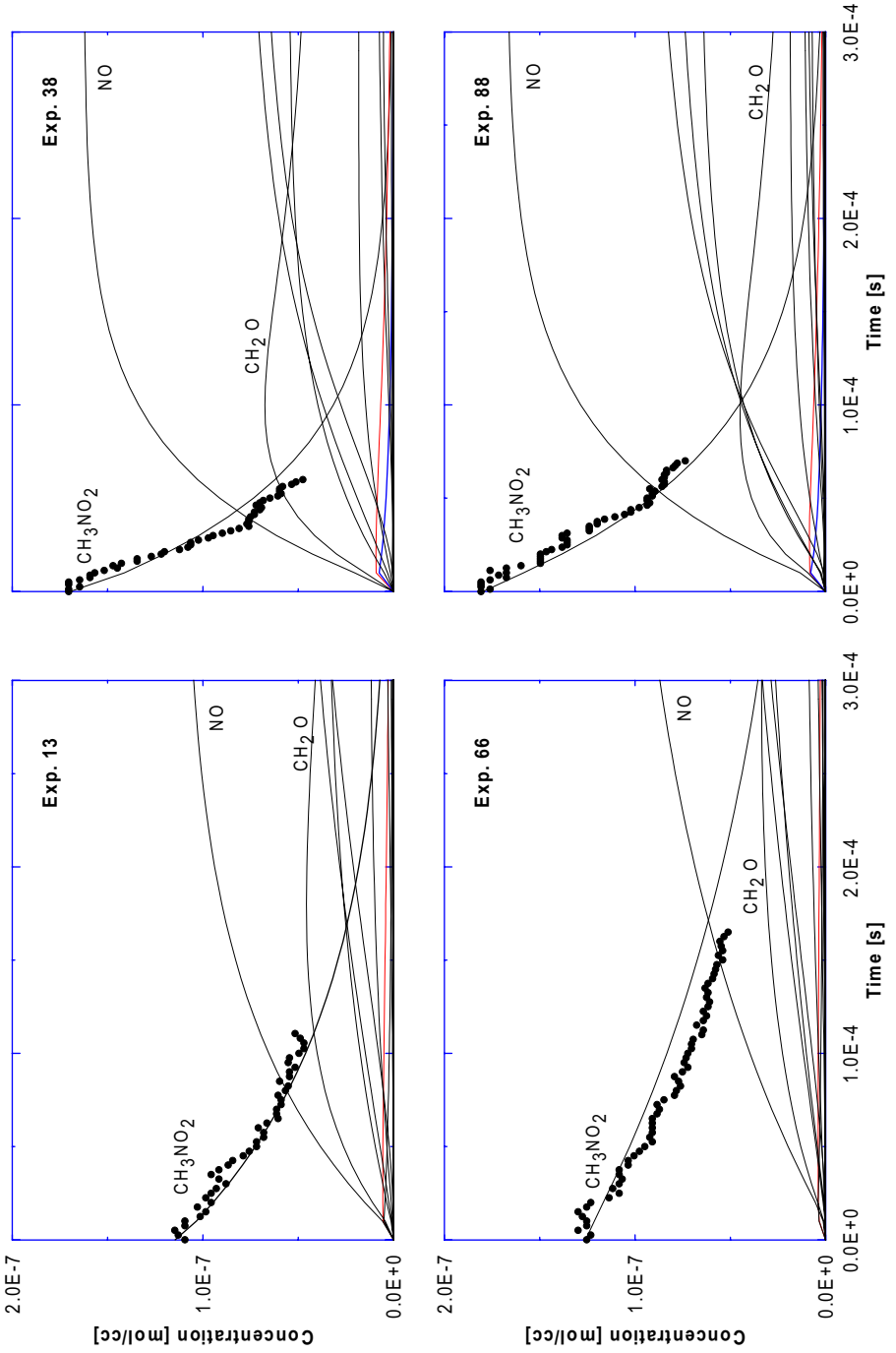

Figure 4-37: NM decomposition - simulations.

Comparison between experiments and simulated results for exp. 13 and 38 (diluted in N_2), 66 and 88 (diluted in Ar).

As we can see, the selected reaction mechanism is capable of reproducing the main course of the global NM decomposition. The final products are found as:

$$H_3CNO_2 \quad \rightarrow \quad CO + H_2O + 0.5N_2 + 0.5H_2 \qquad (4\text{-}2)$$

Further simulation examples are shown in figure 4-38 and in figure 4-39, both for NM diluted in argon and in nitrogen. It can be seen that there is good agreement both for different diluents and under various conditions of pressure and temperature. All the simulations are found in APPENDIX D.

Comparison with results from previous authors

Glänzer and Troe (1972) used mass spectrometry to measure the overall products from NM decomposition. At 1400 *K*, the composition was measured as:

$$CH_3NO_2 \quad \rightarrow \quad \tfrac{1}{2}CH_4 + \tfrac{1}{2}CO + \tfrac{1}{2}H_2O + NO \qquad (4\text{-}3)$$

The authors suggested that the thermal decomposition of highly diluted CH_3NO_2 in a shock tube resulting from high temperature conditions could be explained solely by the unimolecular dissociation given by the third body reaction as given by the first reaction in figure 4-36. Through shock tube experiments, they derived rate expressions for both high- and low pressure given as:

High pressure $k_\infty \cong 10^{16.2} \cdot \exp\left(-\frac{247\ kJ/mole}{RT}\right)\ [1/s]$ **Eq. 4-33**

Low pressure $k_0 \cong [Ar]10^{17.1} \cdot \exp\left(-\frac{175.8\ kJ/mole}{RT}\right)\ [cm^3/mole \cdot s]$ **Eq. 4-34**

In figure 4-40 we have used these expressions to create so-called fall-off curves for some selected temperatures. The rate constants derived from the present experiments have then been plotted on the graph. From the different plots of the experimental data, it can be seen that the experiments have been performed in the transient region, which is in the region between pressure dependent and independent rate constant. From figure 4-40 it can be seen that the experimental data for NM diluted in either nitrogen or argon at 220 *nm* are heavily scattered in a plot of ln(k) versus the inverse of the reflected shock temperature. The reason for this scattering is that almost all the current experiments had different temperatures. The present experiments were not however, initially performed for the specific deduction of fall-off curves. However, the present results can be used to simulate fall-off curves by keeping a constant temperature and increasing the pressure (diluent

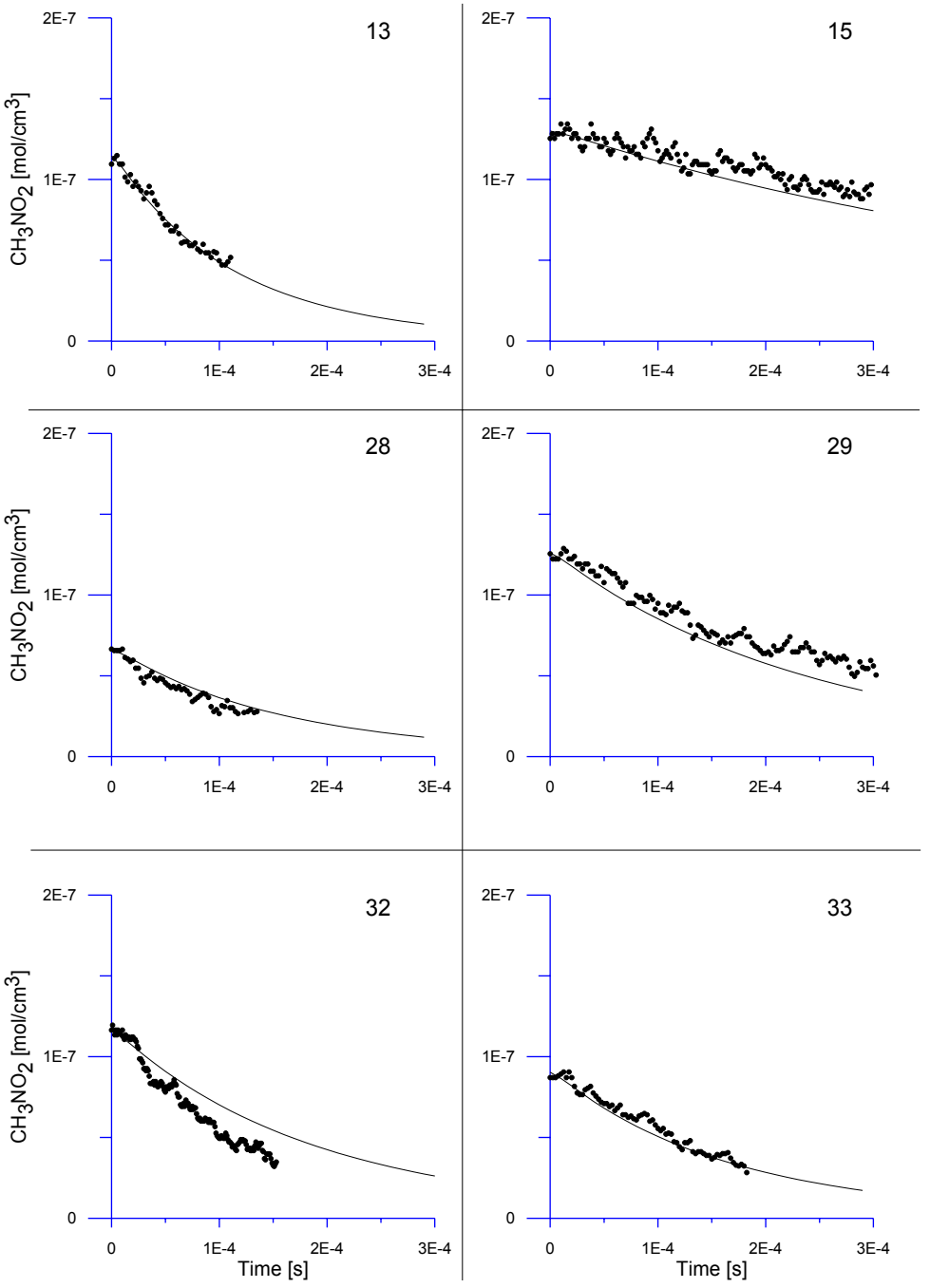

Figure 4-38: Examples from simulations with N_2.

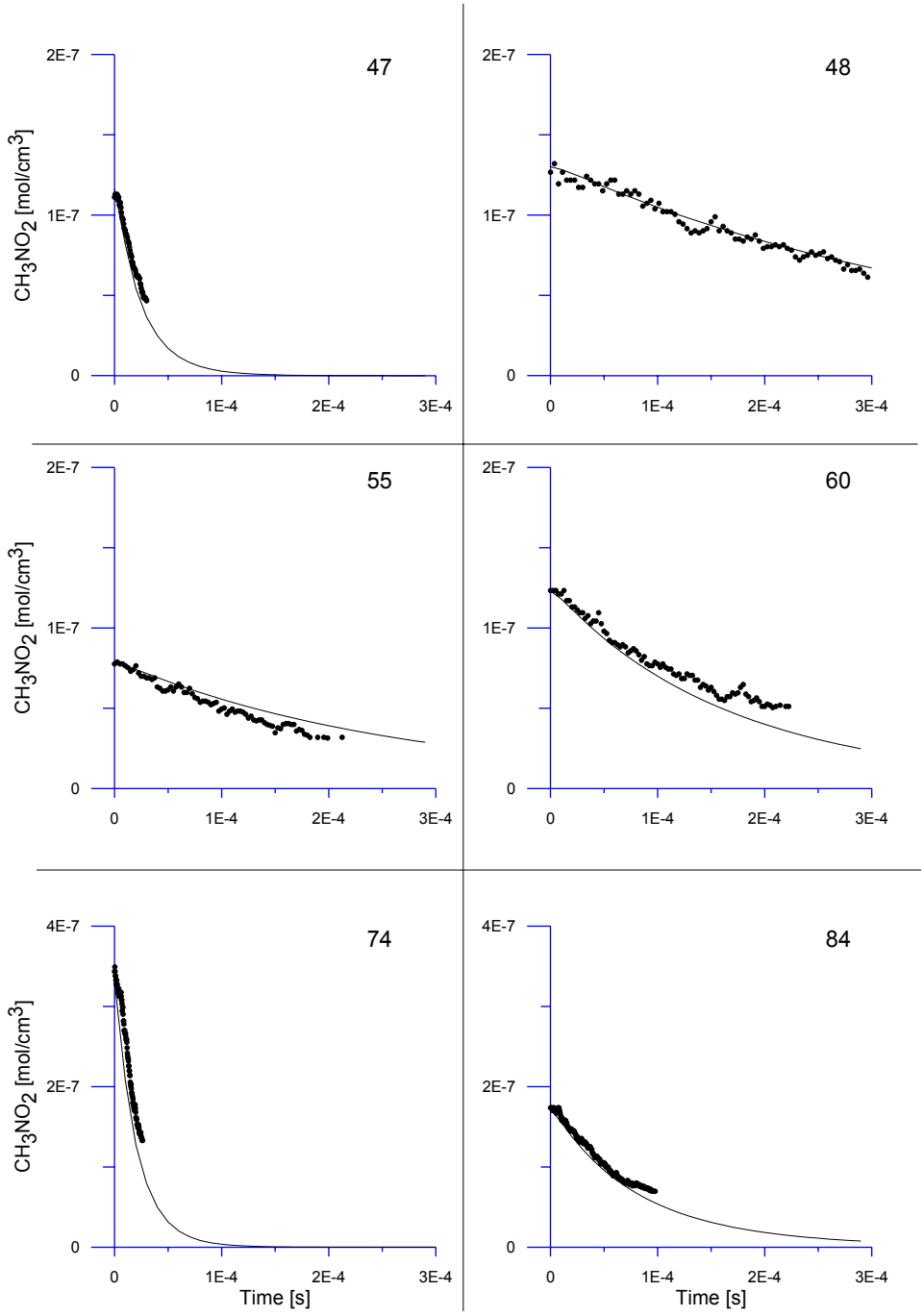

Figure 4-39: Examples from simulations with Ar.

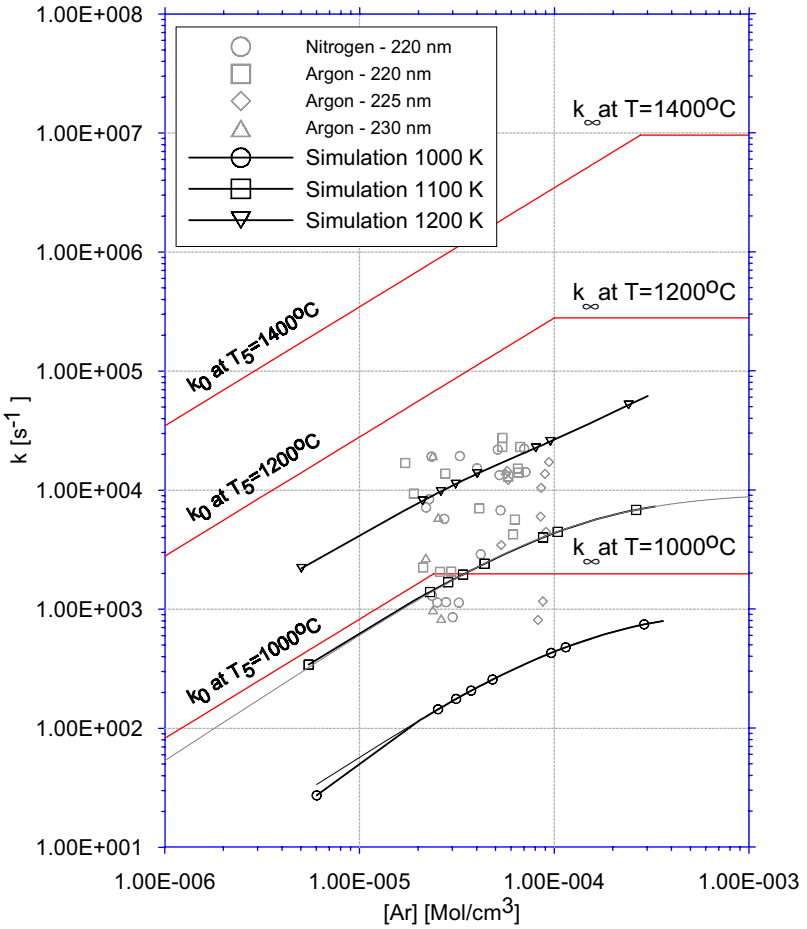

Figure 4-40: Fall-off curves for the NM decomposition.

Simulations compared to data obtained by Glänzer and Troe (1972). The results were obtained by running simulations at fixed temperatures (1000, 1100, 1200, 1300 K) while increasing the pressure ($\propto$ to diluent concentration) and extracting the reaction rate constants from the NM decomposition profiles. The straight lines (in log-log figure) are the asymptotic limits for low pressure NM decomposition as deduced by Glänzer and Troe (1972).

concentration) in small intervals. The simulated curves are plotted in figure 4-40. It can be seen that these simulations predict lower reaction rates for a given temperature, than the results from Glänzer and Troe (1972). Above 1200 ^{o}K, in the high-pressure domain, the present simulations produced increasingly erratic results. The present results predict lower reaction rates compared to those achieved by Glänzer and Troe (1972), by a order of between 7.5 to 10 times. This is most probably due to the fact that the present experiments

were not initially performed for the specific deduction of fall-off curves and therefore predicts less accurate results, although they do predict very well the global decomposition of NM for all the experiments performed. Also for the case given in figure 4-41, the present results tend to be somewhat under predictive.

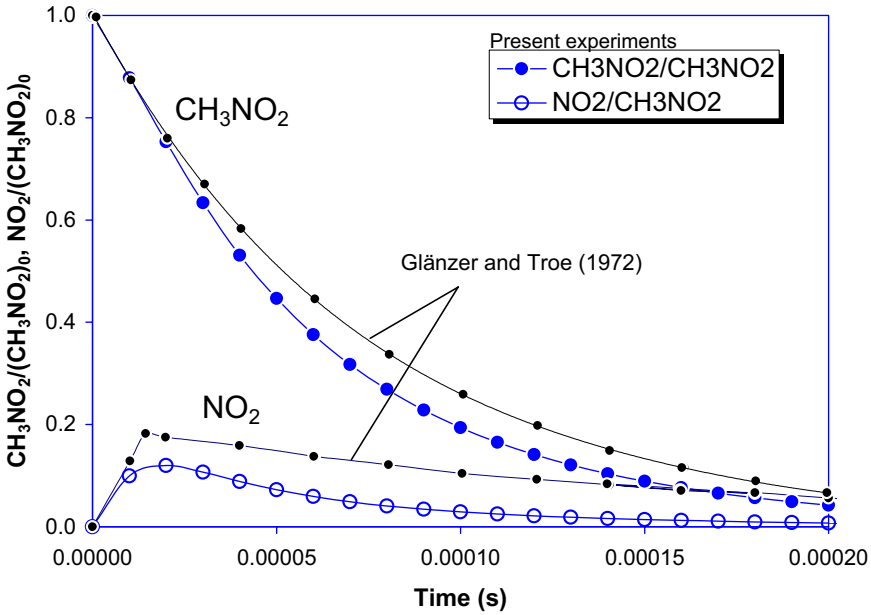

Figure 4-41: NM decomposition profile.

Calculated CH_3NO_2- and NO_2-profiles compared to experimental values. ($[CH_3NO_2]$ = 2.27E-8 *mol/cm*^{3} at t=0, [Ar]=6.14E-5 *mol/cm*^{3}, T_5=1180 *K* (Glänzer and Troe (1972)).

Own mechanism used for comparison, with Arrhenius parameters; A = 1.01E+18 (*mole-cm-sec-K*), b=0 and E_a=52.3 (*kcal/mole*) for the reaction CH_3NO_2+M = CH_3+NO_2+M as deduced from experiments at 225 *nm* (see table 4-6 and table 4-7).

Rate-of-production analysis

Another useful tool for understanding reaction mechanisms is the rate-of-production analysis. Rate-of-production analysis can determine the contribution of each reaction to the net production or destruction rate of each species in a given reaction mechanism. Such an analysis was carried out in CHEMKIN for the transient conversion of CH_3NO_2 over a time scale comparable to the decomposition experiments (≅ 0.3 *ms*) using the current reaction mechanism as given in figure 4-36.

The rate-of-production analysis was carried out for selected experiments (as given in table 4-10) for both types of diluents (N_2 and Ar) at representative temperatures, pressures

and mixture compositions. From the simulations, only data for the most significant reactions were extracted before being normalized. The three most significant reactions are referred to by a number which corresponds to the number given in the reaction mechanism in figure 4-36, and was found to be reaction 1, 19 and 20 (extracted to table 4-11).

Table 4-10: Selected experiments for the rate-of-production analysis

	Memb. [μm]	Dilutent	NM [vol %]	Wavel. [nm]	P_5 [kPa]	T_5 [K]	D_5	C_5 [mol/m^3]	ε_5 [m^2/mol]	$\varepsilon_2/\varepsilon_5$	$V_{incident}$ [m/s]
Man #22	12	N2	0.50	220	318.02	1162	1.18	0.16	136.23	1.13	974.9
Man #23	8	N2	0.30	220	211.79	1011	0.37	0.08	93.57	1.42	885.8
Man #27	8	N2	0.30	220	206.32	1050	0.29	0.07	77.73	1.17	909.1
Man #43	18	N2	0.33	220	482.52	1105	0.88	0.17	97.06	1.14	941.4
Man #47	8	Ar	0.50	220	252.30	1306	0.75	0.12	122.45	1.06	741.4
Man #52	12	Ar	0.50	220	271.90	1100	1.10	0.15	140.48	1.30	673.7
Man #59	18	Ar	0.20	220	389.94	1053	0.72	0.09	153.91	1.46	655.0
Man #62	18	Ar	0.20	220	394.80	1150	0.60	0.08	138.19	1.39	688.1
Man #63	18	Ar	0.20	220	666.79	1195	0.65	0.13	92.32	1.07	703.1

Table 4-11: Main reactions for NM derived from rate-of-production analysis

The Arrhenius form for the reactions is given as: $k = A\,T^b \exp(-E/RT)$

Reaction number	Reaction	A (N_2/Ar) mole-cm-sec-K	b	E (N_2/Ar) Kcal/mole
1.	CH3NO2+M=CH3+NO2+M	**1.03E+17/3.75E+17**	0.0	**43.6/49.5**
19.	CH3NO2+H=CH2NO2+H2	2.50E+09	1.3	2.6
20.	CH3NO2+OH=CH2NO2+H2O	6.90E+04	2.6	-1.9

Figure 4-42 and figure 4-43 illustrates the substantial effect that reaction no. 1 (from table 4-11) has on the NM decomposition, both as an initiating step and throughout the whole decomposition progress. We also notice that increasing the temperature of the system increases the contribution of reaction no. 1 and overall decreases the contribution from reaction no. 19 and 20. This clearly substantiate the conclusion drawn by several previous workers (Glänzer and Troe (1972), Guirguis et al. (1983), Guirguis et al. (1985), Perche, Tricot and Lucquin (1979a), Perche, Tricot and Lucquin (1979b), Hsu and Lin (1985)), that the initial step in the NM decomposition must be the suggested reaction no. 1.

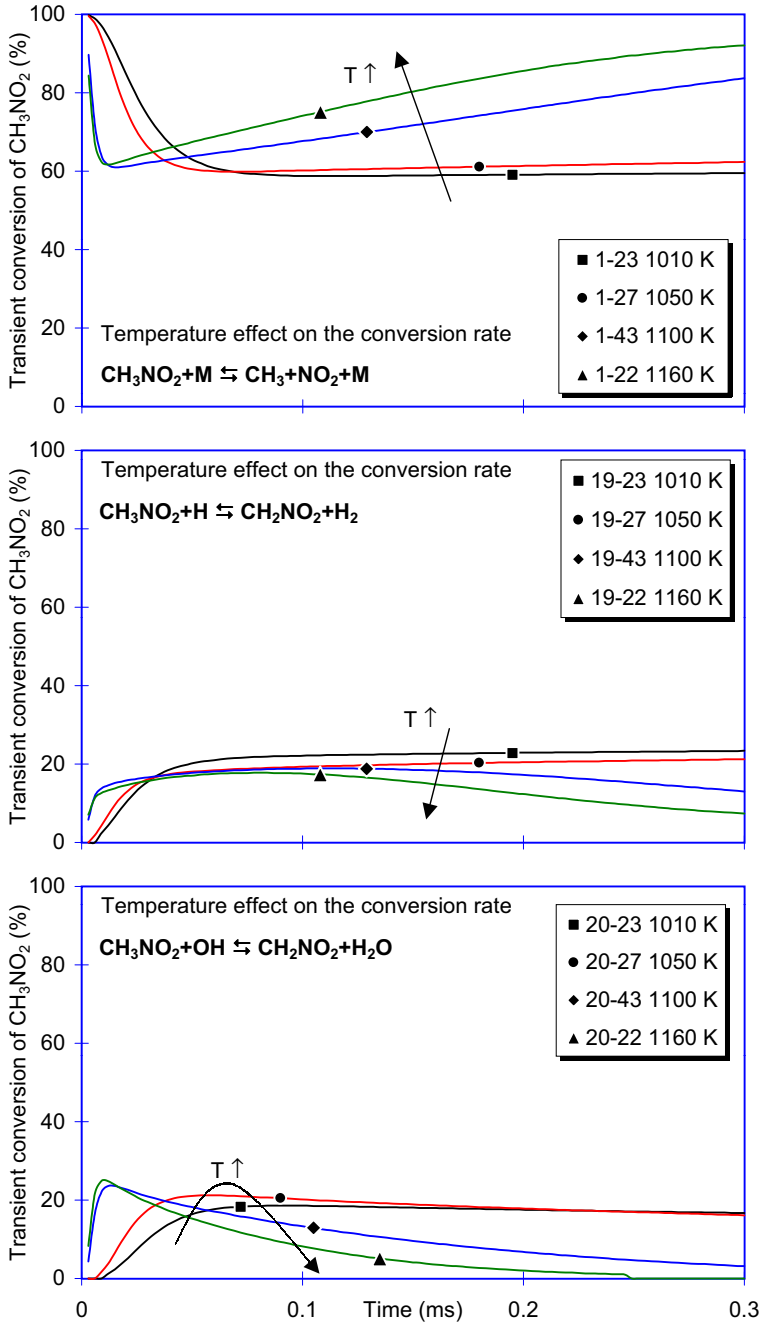

Figure 4-42: Rate-of-production analysis - nitrogen diluted.

The temperature effect on the normalized net rate-of-production profiles for each significant reaction (for NM: reaction 1, 19 and 20) in the mechanism (see reaction mechanism in figure 4-36) describing the CH_3NO_2 decomposition diluted in N_2.

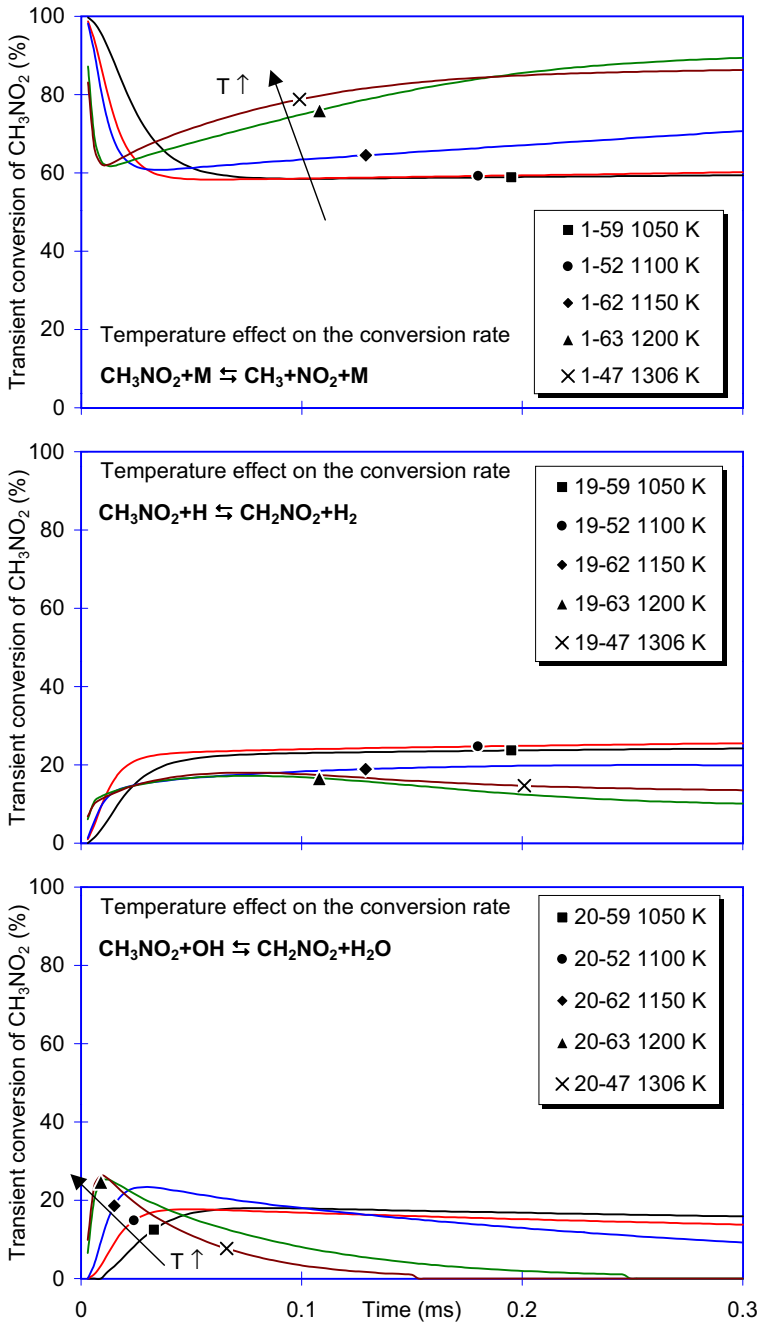

Figure 4-43: Rate-of-production analysis - argon diluted.

The temperature effect on the normalized net rate-of-production profiles for each significant reaction (for NM: reaction 1, 19 and 20) in the mechanism (see reaction mechanism in figure 4-36) describing the CH_3NO_2 decomposition when diluent is Ar.

4.5 CONCLUSION AND RECOMMENDATIONS FOR FURTHER WORK

The nitromethane spectrum was taken and analysed, showing that nitromethane do not absorb significantly at wavelengths above 350 *nm*, which is why nitromethane is transparent in the visible domain. The absorption minimum was located at approximately 242 *nm*. The spectrum was used when proper wavelengths was selected for the monochromator mounted on the shock tube, used for measuring nitromethane absorption during the course of decomposition.

By comparing the experimental against the calculated results it was verified that decomposition of highly diluted nitromethane at high-temperature conditions could be explained by the unimolecular dissociation reaction alone, given by the third body reaction as:

$$CH_3NO_2 + M \quad \rightarrow \quad CH_3NO_2 + M$$

Depending on the speed of the decomposition as calculated from the intensity profiles versus time, the decomposition experiments were separated into two groups: non-reactive and reactive. Experiments was found to be non-reactive when no decomposition was measured during 1 *ms* of registration for any given pressure and temperature. This was observed for reflected shock temperatures less than 990 *K*. Some experiments were lost because the decomposition was too fast to be registered by the preset oscilloscope time resolution.

Reflected shock experiments on NM decomposition, using mixtures of 0.2 to 1.5 *vol%* NM in nitrogen or argon were performed over the temperature range 850-1550 *K* and pressure range 190-900 *kPa*, with 46 experiments diluted in nitrogen and 44 diluted in argon. Out of these there were 9 experiments with no reaction. 54 (N_2/18, Ar/36) experiments were considered useful in the sense that they had been performed with no observable errors caused by external events and were within the range of measurability of the oscilloscope. From the different plots of the experimental data, it can be seen that the experiments was performed in the transient region, which is in the region between pressure dependent and independent rate constant. Heavy scattering was observed when the data were plotted over the entire pressure domain, both for NM decomposition and oxidation. By residual error analysis of the measured decomposition profiles it was found that NM decomposition ($CH_3NO_2 + M \rightarrow CH_3 + NO_2 + M$) corresponds well enough to a

law of first order, verified down to the reaction half-life time. Arrhenius expressions were derived for the NM decomposition at different wavelengths and diluents from the plot of the best exponential fit of the experimental k-values versus the inverse of the temperature in the reflected shock, T_5. Rate equations derived from experimental data with units in *cm^3/(mole s)* in the Arrhenius form of $k = A \times \exp(-E_T/T)$ and $k = A \times \exp(-E_a/RT)$ with k in *cm^3/(mole×s)* were found as:

Diluent	**Wavelength**	**The reaction rate constant, k**
	λ [nm]	**$k = A \times \exp(-E_T/T(K))$ [cm^3/(mole×s)]**
N_2	220	$k = 1.026 \times 10^{17} \exp(-21960 / T(K))$
Ar	220-230	$k = 3.738 \times 10^{17} \exp(-24900 / T(K))$
For argon in separate wavelength domains		
Ar	220	$k = 2.820 \times 10^{17} \exp(-24480 / T(K))$
Ar	225	$k = 1.001 \times 10^{18} \exp(-26330 / T(K))$
Ar	230	$k = 5.867 \times 10^{16} \exp(-22420 / T(K))$

Parameters derived from the above Arrhenius expressions have further been extracted:

Diluent	**Wavelength**	**A**	**E_T**	**$E_a = E_T \times R$**	
	λ [nm]		**[K]**	**$E_T \times R$ (kcal/mole×K) [kcal/mole]**	**$E_T \times R$ (kJ/mole×K) [kJ/mole]**
N_2	220	$10^{17.011}$	21960	43.6	182.6
Ar	220-230	$10^{17.574}$	24900	49.5	207.0
For argon in separate wavelength domains					
Ar	220	$10^{17.45}$	24480	48.6	203.6
Ar	225	10^{18}	26330	52.3	218.9
Ar	230	$10^{16.768}$	22420	44.5	186.4

In parallel to, and following the decomposition experiments, oxidative experiments on the ignition delay times of NM/O_2/Ar mixtures were investigated over high temperature and low to high pressure ranges. These experiments were carried out with eight different mixtures of gaseous NM and oxygen diluted in argon, with pressures ranging between 44.3-600 *kPa*, and temperatures ranging between 842-1378 *K*. Some experiments were carried out with highly diluted mixtures (mixture 5 at 98.65 *%* argon). The other experiments were carried out with mixtures diluted in 84 to 94 *%* argon at 235 *nm*. 76 experiments on nitromethane oxidation were carried out

The oxidation experiments were divided into three different types according to the type of decomposition signals achieved. For signals with emission (Type1: absorption signals with emission, Type 3: emission signals without light source) and for slightly or non-diluted mixtures the apparent quasi-constant activation energy was found from the correlations, to be 64.574 *kJ/mol* and 59.246 *kJ/mol*, respectively. For signals of type 1 and 3, the correlation for the ignition delay time was deduced as:

$$\tau = 0.3669 \cdot 10^{-2} \cdot [NM]^{-1.02}[O_2]^{-1.08}[Ar]^{1.42} \cdot \exp\left(\frac{7767}{T}\right)$$

,with an accuracy of 18.5 *%* and valid in the temperature and pressure domain between 44.3 <P< 277.94 *kPa* and 1026 <T< 1378 *K*, respectively. When the molar fraction of argon tends to unity ($z^{1.42} = 1$), and for slightly diluted mixtures, a different correlation may be derived as:

$$\tau = 0.3696 \cdot [NM]^{0.11}[O_2]^{-0.67}[Ar]^{0.0} \cdot \exp\left(\frac{7126}{T}\right)$$

, with an accuracy of 25 *%*.

For the absorption signals (Type 2: emission observed) a characteristic time was defined as the time interval between the arrival of the reflected shock and the instant when 10 *%* of the nitromethane had decomposed. By this definition the following correlation for the ignition delay time was found to be:

$$\tau_{10\%} = 0.3005 \cdot 10^{-2} \cdot [NM]^{-0.28}[O_2]^{0.12}[Ar]^{-0.59} \cdot \exp\left(\frac{13657}{T}\right)$$

, with an accuracy of 19.4 *%* and valid in the limited pressure and temperature domain between 52.48 <P< 483.29 *kPa* and 1001 <T< 1275 *K*, respectively. For slightly or non-diluted mixtures the correlation was found as:

$$\tau_{10\%} = 0.3844 \cdot 10^{-3} \cdot [NM]^{-0.12}[O_2]^{0.10}[Ar]^{0.0} \cdot \exp\left(\frac{13866}{T}\right)$$

, with an accuracy of 26.9 *%*.

A quasi-constant activation energy (ΔE) was deduced from the latter correlations to 113.544 *kJ/mol* and 115.282 *kJ/mol*, respectively.

Through computer simulations of the thermal NM decomposition it has been verified that the reaction mechanism indeed initiates through the third body decomposition of the nitromethane molecule as stated by previous authors. After the decomposition of the NM molecule, the reactions proceeds by two major and parallel pathways, both including radical reactions, to produce CH_2O. The latter acting as a source for further radicals when attacked by existing OH and H radicals, producing HCO radicals that will carry the reactions to completion. The simulated profiles correspond well to those obtained experimentally.

Further work

The experiments should be expanded to investigate the influence of different additives to study the nitromethane sensitivity, the additives being either proptors or inhibitors to the nitromethane reaction mechanism. It would also be of interest to compare the oxidation experiments with data computed by reduced and/or detailed kinetic modeling.

CHAPTER 5.

THEORY ON NON-THERMAL PLASMA INDUCED DECOMPOSITION

5.1 INTRODUCTION

The second subject considered in this thesis subdivides into a common theoretical part and two experimental parts. This chapter gives an introduction to plasma physics and plasma reactors with applications. The main question investigated in this work was the possibility of using low-power generated plasma discharges to control chemical active gas processes with much higher energy throughput. Through times many phenomenons connected to different forms of electrical discharges have been observed. For over 200 years ago Benjamin Franklin in USA and d'Alibar in France conducted the first serious experiments on electrified clouds. In 1752 B. Franklin flew a dragon into a thunder cloud, an observed sparks between the metal wire connected to this one, and the ground. Lightning has through all times been surrounded by myths and is until today still partly an unexplained phenomenon. Today the physicians characterize lightning as an electric gas discharge in air. In the area which concerns this report, one such discharge is of special interest. This is the so-called corona discharge, which is a low-power gas discharge configuration characterized by high tension and low current. The word origins from the French word “couronne”, which means crown. A corona discharge is a space charge dominated gas discharge between electrode surfaces were one or both have such a small curvature radius and thereby such a high geometrical field concentration, that all of the primary ionization takes place close to this one.

The following theoretical part gives a brief overview of different cold plasma devices and applications of such and will hopefully clarify some of the reasons for the current experimental investigation. A detailed description of the gliding arc device is given, which will be applied in one of the experimental parts.

5.2 PLASMA BASICS

Compared with the gaseous state, plasma is characterized by more complicated particle interactions: (electrons, ions, atoms and molecules) elastic and inelastic collisions (excitation, dissociation and ionization), radiative processes, interaction with electromagnetic fields, etc. The concept of this state was first introduced by Langmuir and Tonks in 1929. When energy is supplied to a solid it becomes a liquid. Apply more energy to a liquid and it becomes a gas. If further energy is applied to a gas, it then becomes a plasma. It is well known that a limited number of parameters, e.g. temperature and pressure is sufficient for the description of equilibrium plasma properties. By using the term "temperature" (1 eV=11600 K) one is able to give a quantitative description of the distribution of the particles in the plasma both where the internal degrees of freedom - electronic, vibrational and rotational - and where the velocities of translational movement are concerned. The equilibrium temperature is the only parameter in the law of mass action describing the relationship between the concentrations of initial and final products of chemical reactions. Depending on the plasma interaction with the external medium and on the duration of the occurring processes analysed, boundary conditions, etc., plasma can be non-equilibrium, partial non-equilibrium and equilibrium.

Plasma at thermodynamic equilibrium is the limited, somewhat idealized case of a state of plasma where all gradients and flows are absent and plasma parameters remain unchanged in time and space. At the thermodynamic equilibrium the state of the plasma (all its elementary processes e.g. dissociation, association, ionization and recombination as well as the general properties, e.g. radiation, thermal capacity, density, etc.) is entirely determined by its chemical composition and two thermodynamic parameters, for example temperature and pressure. For non-equilibrium plasma systems these parameters are insufficient for the description of its properties. A simplified description often used in plasma models can be implemented when the rate of energy exchange between particles of the same kind considerably exceeds the exchange between different particles. Plasma consists of several specific groups of particles to each of which the term "temperature" can be applied. In non-equilibrium plasmas a situation often arises in which the "temperature" differs substantially between the various groups, something which again simplifies the procedure of making non-equilibrium models.

In order to define various kinds of plasmas it is useful to characterize them in terms of important plasma parameters. This is usually done in terms of electron density, n_e, and

electron temperature, T_e. The fist quantity is the most important one because the electrons play a dominant role in both excitation and transport processes. The second parameter varies between 1 *eV* (~11600 *K*) for high density thermal plasmas to a few *eV* for low pressure plasmas. The ratio of electron density and neutral density (ionization degree) is also an important parameter. Lelevkin, Otorbaev and Schram (1992) have reported that for different plasmas this ratio may vary by more than six orders of magnitude.

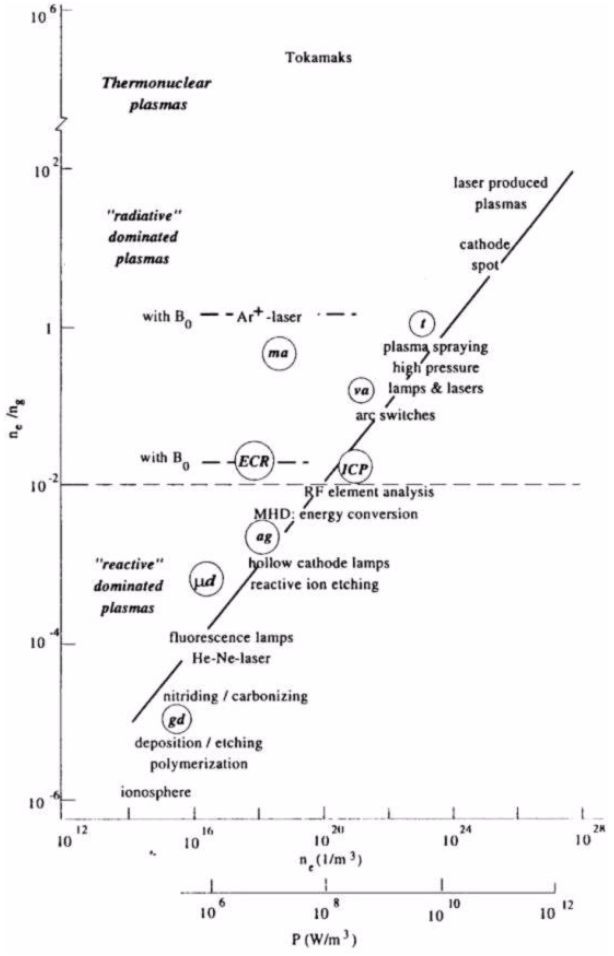

Figure 5-1: Plasma characteristics

Plasma characteristics in terms of electron density and ionization degree for several plasma applications and plasma types. (**gd**: glow discharge, (**d**: microwave discharge, **ag**: anomalous glow, **ECR**: electron cyclotron resonance discharge, **ICP**: inductively coupled plasma, **va**: vacum arc, **t**: thermal plasma, **ma**: magnetized arc (Lelevkin, Otorbaev and Schram (1992)).

In figure 5-1 various plasma processes are shown in terms of the electron density n_e and the density ratio n_e/n_a. The dashed line separates plasmas with a high ionization degree from plasmas with low ionization degree.

The main difference between a plasma and a gas is the presence of charged particles in the plasma. At temperatures below ~ 10 *eV* one refers to plasma as low-temperature or cold. At T > 10 *eV* full ionization of neutral particles has occurred and the plasma is called high-temperature or hot (Granovsky (1971)). In thermal plasma at temperatures under 5000 *K* the concentration of charged particles is very small in comparison with the concentration of neutral particles (atom and molecules). As temperature increases, T>5000 *K*, so does the number of charged particles, and specific properties for plasma appear. Plasma is electrically conductive; it interacts with electromagnetic fields, radiates and absorbs electromagnetic waves, etc. The density of the electrical charges in plasma is determined by the electron and ion concentrations. Some important differences between equilibrium and non-equilibrium plasmas are listed in table 5-1.

Table 5-1: Hot and cold plasmas.
Some important differences between equilibrium and non-equilibrium plasmas.

Equilibrium PLASMAS	**Non-equilibrium plasmas**
High power consumption, up to 50 *MW* and more	Low power consumption, generally less than 3-10 *kW* though we do find exceptions at 1 *MW*.
High pressure, 1 *atm* and more	Low operating pressure, less than 20 *torr*. Some exceptions with higher power consumption, are operated up to 1 *atm*.
High temperature, up to 20000 *K*	
Relaxation time relatively fast, meaning that $T_e=T_v=T_o=T_r$. Often approximated by the assumption of partially local thermodynamic equilibrium (PLTE)	Fast relaxation time, meaning that $T_e>>T_v>>T_o$
They are non-selective	Are selective plasmas which means that specific reactions can be optimised.
Low efficiency, e.g. regular arc discharge	High efficiency, e.g. conventional glow discharge

The operation of a generic non-thermal plasma discharge can be described in terms of the four processes shown in figure 5-2.

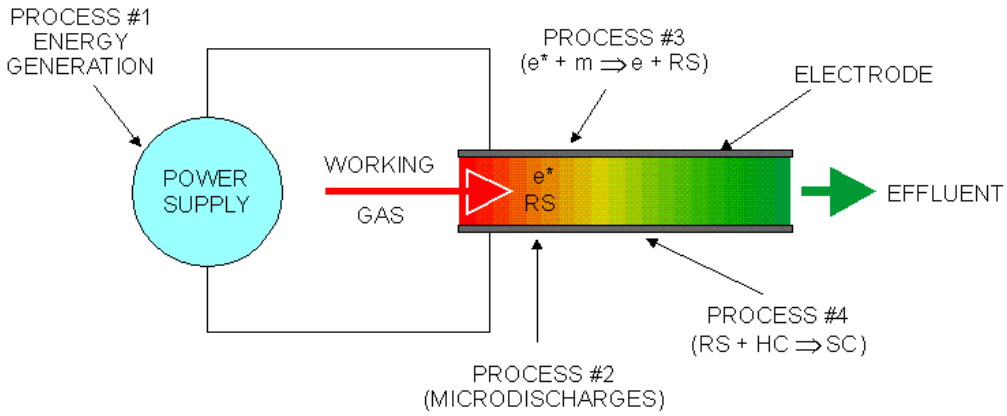

Figure 5-2: Typical non-thermal barrier plasma discharge (NTPD).

The required energy is provided by a high-voltage power supply. This high voltage, and the corresponding high electric field, is applied to the electrodes. As the working gas flows between the electrodes, the applied field breaks down the gas, creating a partially ionized plasma. At atmospheric pressures, this breakdown results in a multitude of current filaments, or breakdown channels, called micro discharges. Within the micro discharges the input energy is efficiently transferred to the electrons. The diameter of each of these discharge channels has been found to be on the order of 100 μm and the lifetime ranges from 1-100 ns. Because of the short time duration of the discharges, the electrons and heavy particles do not thermally equilibrate, and while the temperature of the electrons, e*, is on the order of 3-8 eV (40 000-100 000 K), the bulk gas (heavy particles) temperature remains approximately constant. The relatively large collisional cross-section between 3-8 eV electrons and most molecules, leads to collisions between these energetic electrons and atoms/molecules, resulting in the formation of excited atomic/molecular states and other highly reactive species (RS). The reactive species are a result of energetic-electron/molecule collisions, and hence, they are formed only within the micro discharges. After a discharge extinguishes, the created reactive species collide with other molecules, causing chemical reactions that alter hazardous compounds (HC) into more controllable, or simpler compounds (SC).

The latter non-thermal barrier process was found to probably be the most effective process for decomposing the hydrocarbons selected for the decomposition studies in the

second experimental approach. It was the theory and pervious work found on this kind of discharge systems that led to the development of several discharge reactors and power systems during the current investigations. The discharge process generated by the gliding arc device applied during the first experimental approach, provided much of the same plasma conditions as would a barrier discharge, but was more a mix of hot and cold plasma processes. Nor did is have the pulsating effect obtained by the barrier discharge when the micro discharges initiates and extinguishes.

5.3 DISCHARGE GENERATED PLASMA

5.3.1 Discharge classifications

When electric discharges occurs in gases, only a very short time (nano to milliseconds) is necessary to transform the gas from a very good isolator to an efficient conductor, even for voltages just exceeding the breakdown voltage by a few percent. Table 5-2 classifies basic gas discharges by three commonly agreed criteria.

Table 5-2: Classification of gas discharges (Sigmond (1996)).

A. **By the dependency of externally generated electron current**	**B.** **By discharge current- and voltage**	**C.** **By discharge mechanism**
1. Dependent discharge	**1.** Static and kvasistatic	**1.** Townsend discharge
2. Independent discharge	**2.** Pulsed	**2.** “Glimm” discharge
	3. High frequency	**a.** Normal “Glimm” discharge **b.** Abnormal “Glimm” discharge
		3. Arc discharge
		4. Corona discharge

Breakdown mechanisms

Two distinct discharge mechanisms are defined in the literature. There have been, and still are, disagreements on the mechanism of initiation for both of these:

1. The Townsend mechanism
2. The channel- or “streamer” mechanism

The Townsend mechanism seems to be the active breakdown mechanism in most gases for the pressure × distance range up to a few thousand *torr* × *cm* and over-voltages up to a few hundred percent. After the exposure of the gas to a given voltage and when the first electron has detached from the cathode surface, the current will increase exponentially with time because of primary and secondary ionization processes. Repeated electron avalanches will further result in the build-up of space charge-fields, which again will accelerate the current from exponential to over-exponential.

The Townsend mechanism seems to be the active breakdown mechanism in most gases for the pressure × distance range up to a few thousand *torr* × *cm* and over-voltages up to a few hundred percent. After the exposure of the gas to a given voltage and when the first electron has detached from the cathode surface, the current will increase exponentially with time because of primary and secondary ionization processes. Repeated electron avalanches will further result in the build-up of space charge-fields, which again will accelerate the current from exponential to over-exponential.

The channel- or “streamer” mechanism comes to importance when the values of pressure times distance and over-voltage are so high that one electron from the cathode surface results in such a big avalanche that the space charge-fields from this equals the outer forced electrical field. The head of the avalanche is self-accelerated and leaves a near neutral plasma channel (electrons and positive ions) behind on its way to the anode. Even the first electron from the cathode will therefore produce a conducting residual plasma channel stretching from the anode and backwards towards the cathode. The time for the first electron to produce the plasma channels is in the order of the electron transit-time. Photons produced by the avalanches, will move towards the cathode and produce secondary avalanches. The most known example of such a multi stage discharge mechanism is probably the lightning produced by thunder clouds and the ground.

Characteristics and discharge subgroups

In plasma physics there are four main groups of discharges classified by their physical behaviour (and construction) under given conditions (see figure 5-3).

Glow discharge: The stationary form is a low-pressure discharge, usually between parallel plates confined in a depressurized tank. Because of the low pressure, the discharge is characterized by a strongly reduced field, low current and voltage and high electron energies.

Corona discharge: The biggest disadvantage of the glow-discharge is that one has to increase the voltage as the pressure increases. At higher pressure, this discharge configuration tends to be unstable and may produce arcs between the electrodes. One way of stabilizing the discharge, is to use in homogeneous electrodes that is point-to-plane electrode configurations. This change in configuration gives rise to a new and as well important kind of discharge, the corona discharge, either positive or negative. For both the positive and the negative, the active ionization volume at low voltages, will be much smaller than the total discharge volume (unipolar corona). Increasing the tension will result in so-called streamers, which are charge carrying filaments (bi-polar corona). Corona discharges will be discussed more extensively in following chapters.

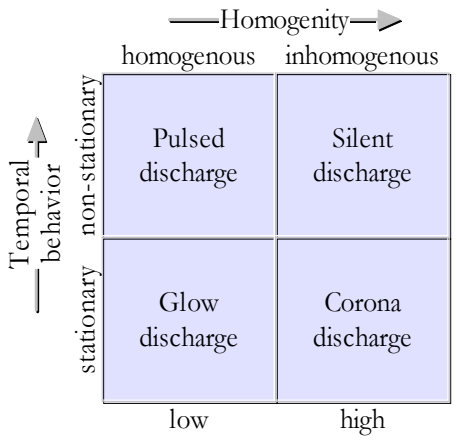

Figure 5-3 illustrates how different discharge types are arranged after temperature behaviour, pressure domain and visual appearance. Their characteristic appearance in terms of geometry can be seen in figure 5-4 with the most important corresponding characteristic parameters given in Table 5-3.

Figure 5-3: Different discharge types.
Different discharge types are arranged after temporal behavior, pressure and appearance.

Silent discharge: This discharge type, which will bee further elaborated in the following chapters, has been developed especially for use in volume plasma chemistry, which is for the treatment of larger gas volumes. It combined the high ionization potential in a glow discharge with the higher operative pressure in a corona discharge. The discharge configuration is a very good source for the production of plasma filaments containing high-energy electrons. In most gases, the electric breakdown field correspond to an electron energy around 1-10 ***eV***. This is the ideal electron energy for excitation and ionization of atoms and molecules, and thereby the breaking of chemical bindings.

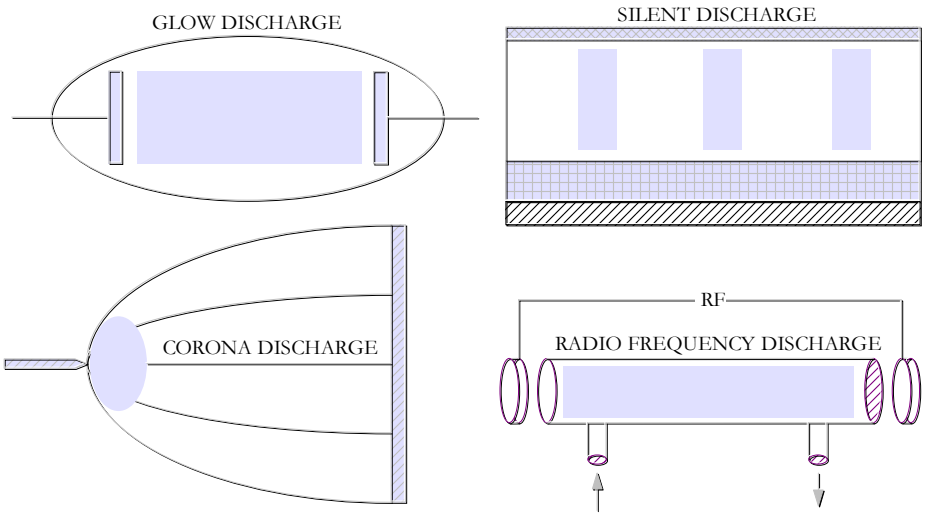

Figure 5-4: Characteristic visual appearance.

Characteristic visual appearance of four main discharge types; the silent-, glow-, corona and radio frequency discharge.

Table 5-3: Characteristic parameters for different discharge types.

	Glow	**Corona**	**Silent**
Pressure domain	< 10 *mbar*	1 *bar*	1 *bar*
Electric field	10 *V/cm*	0.5-50 *kV/cm* (varying)	0.1-100 *kV/cm*
Reduced field	50 *Td*	2-200 *Td* (varying)	1-500 *Td*
Electron energy	0.5-2 *eV* (5000- 20000 K)	5 *eV* (varying)	1-10 *eV*
Electron density	10^{8}-10^{11} cm^{-3}	10^{13} cm^{-3} (varying)	

Pulsed discharge: Pulsed DC discharges with puls duration shorter than 1 μ*s*, have the advantage that electrons can be generated and energized without affecting the much heavier ions. As a result, higher field strengths can be applied during the pulse duration without generating sparks over the discharge volume. By using pulsed discharges with puls duration of nanoseconds, the temperature associated by electron energy (T_e) may be separately affected without increasing the temperature of the surrounding molecules. This means that less energy is lost in the form of heat. Being able to apply higher voltages

across the electrodes, will result in a corresponding increase in electron concentration, which again, because of the space charge effects, will result in better dispersion of the electrons over the volume confined by the electrodes.

5.3.2 The corona discharge

The corona discharge is a blend of the Townsend, Glim and arc discharge. Based on the geometrical definition, a corona discharge is either a townsend or a Glim discharge but not an arc discharge, which is defined to be independent of the geometry. Corona is characterized by high field strength and low currents and may occur over a broad pressure domain. They are easy to establish and fairly stable. The cathode mechanism in a corona discharge is mainly the same as in a “glimm” and in a Townsend discharge, except that it “burns” in an extremely in homogenous field.

Corona arises when electrons are accelerated to an energy level high enough to ionize neutral molecules. This leads to an increase in the electron concentration which finally results in an electron avalanche. The discharge itself is composed from many short pulses, with frequencies up to 100 *kHz*, often referred to as “Trichel” pulses. The corona discharge, depending on the intended application, makes use of two specific aspects of the discharge mechanism; ions produced or the energetic ions produced by the plasma. Which ions that are produced depend on the polarity of the active electrode and the characteristics of the gas in which the discharge takes place. In general, for processes which require energetic ions, the discharge is configured such that the plasma region is confined to a smallest possible volume. On the contrary, if the process requires energetic electrons, the active plasma volume should preferably be dispersed over the largest volume possible. A corona discharge is, according to earlier definitions, a gas discharge where the geometry limits the gas-ionization process to a high tension area around the active electrode. Depending on the polarity of this electrode, the discharge can be positive, negative or bi-polar (symmetrical). The discharge can further be catheterized from the current supply type into either alternating current (AC), direct current (DC), pulsed or high frequency. What is unique to the corona discharge is that it has a low field drift area, connecting the ionization region with a low-field passive electrode. In this region, electrons and ions drifts and reacts with neutral atoms and molecules, but with to little energy to ionize and with too little density to react with other ionized particles.

Another feature of the corona discharge is the presence of what we call streamers. This

occurs when the electron avalanche produced exceeds 10^6 to 10^8 electrons. Both positive and negative streamers may occur with the positive streamer as the most unstable and least controllable. The largest electrochemical potential is found for a non-sparking repetitive streamer corona, in which ionizing regions very fast traverse the discharge gap. The volume which is traversed by these streamers will be exposed to short bursts of highly energetic electrons with energies between 12-16 *eV.* These electrons are then followed by "slower" electrons with energies between 1-2 *eV* in the streamer channel.

The conclusion is that if we want to take advantage of energetic electrons to initiate certain chemical reactions, the corona discharge should be fed with short pulses, not longer than the time for the streamers to cross the discharge gap including the time for the relaxation of the secondary electrons. Another advantage with this is that larger streamers can be utilized because the pulsed tension avoids the development of sparks. Because of the short pulse duration, most of the energy supplied goes to increase the electron temperature, without significant increase in the temperature of the surrounding molecules.

5.3.3 The silent discharge

The silent discharge dominates for applications in volume plasma chemistry because it combines the large volume excitation of the glow discharge with the high pressure of the corona discharge. Typical parameters of silent discharges are listed in Table 5-3. The main elements of a silent discharge configuration are shown in figure 5-4. A characteristic of the silent discharge is that a dielectric layer covers at least one of the electrodes or sometimes both, as illustrated in figure 5-5.For this reason the silent discharge is also referred to as the "dielectric-barrier discharge", or simply, "barrier discharge". The dielectric layer is the key for the proper functioning of the discharge. Once ionization occurs at a location in the discharge gap the transported charge accumulates on the dielectric. The field due to this charge reduces the field in the gap and interrupts the current flow after a few nanoseconds. The duration of the current pulse depends on the pressure and the effective ionization characteristics of the gas as well as on the dielectric properties. By applying a e.g. a waveform voltage of sufficient amplitude, a large number of such micro discharges is induced. They are randomly distributed in space and time. At the maximum and minimum of the applied voltage the displacement current is zero (dU/dt = 0) and the micro discharge activity stops, only to start again when the breakdown field is reached in the gap during the next half-wave. The dielectric serves two functions; it limits the amount of charge transported by a single micro discharge and distributes the micro

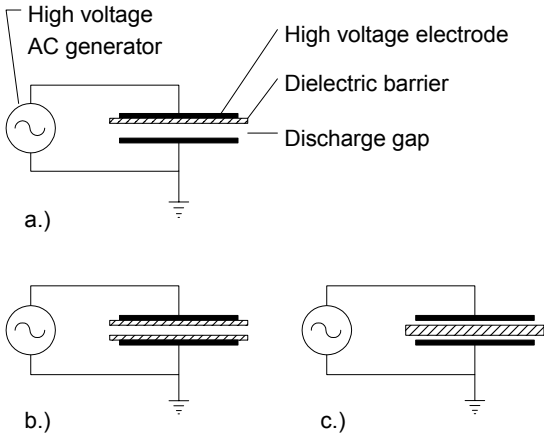

Figure 5-5: Silent discharge configurations.

discharges over the entire electrode area. Because the dielectrics do not emit or absorb a significant amount of free electrons, the charge transfer across the gap through the micro discharges eventually reduces the "net" electric field at the location of each discharge, causing them to extinguish. Consequently, the device does not rely on the imposed voltage pulse-width to limit the duration of the micro discharges, and these devices are usually driven by a simple high-voltage AC power supply.

The silent discharge is an excellent source of filaments containing energetic electrons. In most gases the reduced field at breakdown corresponds to electron energies of about 1-10 *eV*, which is the ideal energy range for the excitation of atomic and molecular species and the breaking of chemical bonds. As a result, almost all the electrons generated are sufficiently energetic to split molecules.

5.3.4 Plasma chemistry modelling

There are two main commercial products on the marked today:

- AURORA, by Reaction Design (part of the CHEMKIN package)
- KINEMA, by Kinema Research and Software

Reaction Design of San Diego, California, USA, was founded in 1995 to provide software simulation and modelling tools to help process engineers create more efficient and environmentally friendly manufacturing processes. In 1997, Sandia National Laboratories selected Reaction Design as the exclusive worldwide licensee for its

CHEMKIN Collection and other software, which it had developed to aid in the design of processes that utilize chemical reactions. Under this agreement, Reaction Design markets, supports, enhances and expands this set of software modelling tools.

Kinema Research & Software was founded in 1989 by Dr. Lowell Morgan. They have more than a century of combined experience in physics. Kinema performs contract research is plasma chemistry modelling, atomic and molecular physics, and data service as well as writes and markets computer software for modelling and simulation of partially ionized plasmas. Tabular data sources for collision cross sectional areas and ion-ion, ion-electron and molecule-electron reactions are scarce and not yet easily obtainable. Most laboratories today use in-house data for their modelling needs. Never the less, more and more data are today freely available. Table 5-4 lists some sources for publicly accessible data for plasma modelling.

The basic needs when doing plasma modelling

Data should be in as “unprocessed” a form as possible. (e.g., cross sections are preferred over Townsend coefficients). Databases for the different processes are vital, like for the:

- Ion and Neutral transport coefficients
- Electron-impact cross sections
- Heavy particle reaction coefficients
- Gas/plasma-surface reaction probabilities

Some sources of data for different species are tabulated in table 5-4.

Table 5-4: Publicly available data sources for some species

Source	Data available
Art Phelps (http://jilawww.colorado.edu/www/research/colldata.html)	O2, N2, CO, CO2, H2, H2O, NO, SF6, He, Ne, Ar, Xe, Na, and Mg
Skip Morgan/Kinema (http://www.sni.net/kinema/download.htm)	N2, O2, H2, Cl2, HCl, F2, CH4, CF4, SiH4, SF6, He, Ne, Ar, Kr, Xe
NIST Electronics and Electrical Engineering Laboratory (J. Olthoff) (http://www.eeel.nist.gov/eeel_pages/811.html)	CF4, CHF3, CCl2F2, C2F6, C3F8, Cl2, SF6

Table 5-4: Publicly available data sources for some species

Source	Data available
Art Phelps (http://jilawww.colorado.edu/www/research/colldata.html)	O2, N2, CO, CO2, H2, H2O, NO, SF6, He, Ne, Ar, Xe, Na, and Mg
University of Illinois (http://uigelz.ece.uiuc.edu)	He, He*, Ne, Ne*, Ar, Ar*, Kr, Kr*, Xe, Xe*,N2, N, O2, O, H2, H, Cl2, Cl, F2, F, SiH4, Si2H6, CH4, C2H6, CF4, C2F6, H2O, N2O, NH3, HCl, CCl4, CCl2F2, NF3, CO2, CO, SO2, BCl3, BF3,Hg, Hg*, HgBr, Cu, Cu*, Al, Al*, Ti, Ti*
C. Gorse, University of Bari, (cap@chimica.uniba.it)	H2(v),D2(v)
NIST Physics Division (Y.-K. Kim), Electron Impact Ionization (http://physics.nist.gov/PhysRefData/Ionization/Xsection.html)	H, He, SiFx, SF6, H2, N2, O2, H2O, CO, NO, CO2, NH3, CH, CH2, C2H2, CH3, CH4, C2H4, C2H6, C3H8, C6H6, SiF, SiF2, SiF3, SF6, CS, CS2, COS, H2S, NO2, N2O, O3, S2, SO2, SiH, SiH2, SiH3, SiH4, Si2H6, Si(CH3)4, GeH, GeH2, GeH3, GeH4, Ge2H6, CF4, C2F6, CF3
ORNL “RedBooks” (http://www-cfadc.phy.ornl.gov/redbooks/redbooks.html)	He, H2, D2

DataBase Processor

A method to convert raw database to model usable coefficients (e.g., cross sections to rate coefficients), a reaction mechanism and a basic plasma model is also required, i.e.:

- Boltzmann solver
- Maxwellian “integrator” of cross sections

Reaction Mechanisms:

- A collection of previously used (and hopefully validated) reaction mechanisms.
- Scaling laws or IYMG (If you must guess) procedures for generating unavailable data.

A “basic” global plasma model

(Normally available when using commercial products e.g. AURORA or KINEMA)

- Rapid (and error-less) method to convert a reaction mechanism into ODE's

or PDEs

- Method to convert “power” into “excitation” (Circuit model, electromagnetics solver)
- Robust integration technique
- Higher dimensionality (2D) as required

5.4 DISCHARGE CONFIGURATIONS AND REACTORS

This chapter will give a brief overview of some of the more commonly used electrical discharge reactors and their operation. Most of these reactors mentioned have yet to be commercialized although numerous types are in use in plasma research laboratories worldwide. There are many types of non-equilibrium plasma devices which has been developed for various applications. The potential of these devices for the destruction of pollutants or toxic molecules has already been demonstrated in many contexts, such as for nitrogen oxides (NO_x) and sulphur dioxide (SO_2) in flue gases, heavy metals and volatile organic compounds (VOC’s) in industrial effluents and also for chemical agents e.g. nerve gases.

There are two major methods of applying cold plasmas to the pollution control; electrical discharge technology in which energetic electrons are generated within the polluted gas, and electron beam technology in which electrons are externally generated. Some key aspects of these two methods towards practical applications are given in table 5-5. Other often used discharge technologies are dielectric barrier discharges, dielectric bed discharges and surface discharge induced plasma chemical process. Different removal mechanisms vary from oxidation, reduction/decomposition, scrubbing/absorption (in wet system), to aerosol formation followed by particle removal.

Table 5-5: Comparison of pulsed discharge and electron beam technologies

	Pulsed Discharge	**Electron Beam**
Operational pressure	atmosphere	vacuum
Electron generation	Internal (within polluted gas)	external
electron energy	10 eV*	$10^5 \sim 10^6$ eV
capital cost	Lower	Higher

Table 5-5: Comparison of pulsed discharge and electron beam technologies

operational cost	Higher	Lower
Disadvantage	Electrode corrosion	Dirty electron injection window; X-ray hazard

Electrical discharge techniques can be implemented in many ways, depending on the electrode configuration and electrical power supply. Different types of high-pressure discharges may be used as reactors for pollution control. The electrical and chemical properties of the plasma species produced in each reactor depend upon the mechanisms of discharge developments and ionization growth. Many electrical discharge devices achieve non-thermal conditions through the production of micro discharges called streamers. Streamers are plasma filaments produced by highly localized space-charge waves which enhance the applied field in front of the wave and propagate because of electron avalanching in this high field. Streamers yield good power efficiency within the short lifetime of the steamer because the ions do not experience significant movement and therefore do not contribute to the power consumption. The short lifetime of the streamer can be accomplished by using very short, high-voltage pulses (pulsed corona discharges) and/or with the use of a dielectric material between or coated on the electrodes (dielectric barrier discharge).

The energy consumption in a plasma reactor depends on both the chemical reaction efficiency of the plasma and the energy conversion efficiency from the main power source to the plasma. The electrical breakdown voltage is another important quantity in determining the performance of many pollution control devices.

Most of these devices operate on the same basic principle: *To produce a plasma in which the majority of the electrical energy goes into the production of energetic electrons*. Even though the electrons are short-lived under atmospheric conditions and rarely collide with specific molecules, they undergo many collisions with dominant background molecules, thus producing radicals that, in turn, inhibit specific reactions. The efficiency of these devices arises from the fact that radicals have relatively long lifetimes and react selectively.

The high capital cost of accelerators and x-ray hazards associated with the electron beam pollution control systems have motivated studies into alternate plasma based technologies such as those utilizing electrical discharges. Electrical discharges can be

produced in many different forms, depending on the geometry of the reactor and the electrical power supply.

The reason for reporting the numerous different approaches for constructing plasma reactors is that much time was spend during the current investigations, to construct different discharge reactors which were able to operate with the available power equipment.

5.4.1 Pulsed corona reactors

One type of discharge reactor that has shown very promising results is the pulsed corona reactor. The industrial implementation of this reactor has the advantage of low retrofit cost since it can use the same wire-plate electrode arrangement as in electrostatic precipitators. Precipitators are commonly used for collecting particle emissions from utility boilers, iron/steel industries, paper manufacturing, and cement industries. By driving the reactor with very short pulses of high voltage, short-lived discharge plasmas are created that consist of energetic electrons, which in turn produce the radical responsible for the decomposition of the toxic molecules. Pulsed corona discharge reactors have been shown, both in laboratory and industrial scale, to be effective in the removal of many types of gaseous pollutants.

A study was recently sponsored by the Japanese Ministry of International Trade and Industry to perform technical and economic assessments of the pulsed corona process for coal-burning utility boilers. The pulsed corona process was compared to the conventional calcium-gypsum process for deSO_x combined with the ammonia-catalytic process for deNO_x. A comparison was also made to the electron beam deSO_x/deNO_x process. The study committee concluded that the pulsed corona method deserves development as the next generation technology for the removal of SO_2 and NO_x in utility boiler plants.

In the past most studies of non-thermal deNO_x have been focused on the treatment of flue gases from power plants. For this application, the desired process involves the oxidation of NO_x to from nitric acid, which in turn is neutralized to ammonium nitrate and ammonium sulphate-nitrate solid by-products in the presence of SO_2 and ammonia. For internal combustion engine applications - in particular mobile sources, it not practical to collect solid or liquid by-products, and so the desired process is the reduction of NO_x to N_2, as in some conventional NO_x reduction techniques.

5.4.2 Dielectric-barrier reactors

In dielectric barrier discharge reactors, high voltages are applied between electrodes, one or both which are covered with a thin dielectric layer, such as glass. Dielectric-barrier discharge reactors are also referred to as silent discharge reactors. The geometry is commonly either planar (parallel plates) or cylindrical (coaxial tubes). Configurations like those used in corona discharges are also used in which one of the electrodes (e.g. a wire) is highly stressed, and the outer electrode is a metal foil wrapped around a glass tube. This is an old technique still in use, first used by Siemens in the 1850's for the production of ozone. Whereas in the pulsed corona method the transient behaviour of the plasma is controlled by the applied voltage pulse, the plasma that takes place in a dielectric discharge self-extinguishes when the charge built up on the dielectric layer reduces the local electric field. Therefore simpler electrical power supplies can be used. In some cases the efficiency of a silent discharge can be improved by applying high-repetition-rate voltage pulses in a manner similar to that of the pulsed corona discharge. Besides removal of NO_x, CO_x, SO_x, and soot in flue gases from combustion processes, the silent discharge have also been demonstrated to decompose many types of VOC's. In fact, any compound, organic or inorganic, which can be oxidized by oxygen atoms is a potential candidate for removal by plasma processing.

5.4.3 Surface discharge reactors

A surface discharge reactor consists of a planar or cylindrical aluminium ceramic having a series of strip-like electrodes attached to one of its surface and a film like counter electrode embedded inside the ceramic. A high-frequency AC high-voltage is applied to generate the discharge, starting from the side edges of the strip electrodes and uniformly covering the ceramic surface.

5.4.4 Ferroelectric bed reactors

The ferroelectric bed reactor employs a high-voltage AC power supply in conjunction with a tubular reactor packed with high-dielectric ceramic pellets. The pellets are held within the tube arrangement by to metal mesh electrodes. When external AC voltage is applied across the high dielectric layer, the pellets are polarized, and an intense electric field is formed around each pellet contact point. Many pulsed discharges take place around each contact point of the ferroelectric pellets, and the discharge energy can be controlled by changing the dielectric constant of the pellets, and by the voltage waveform.

The reactor has been demonstrated to decompose CH_4 and CO_2, as well as the destruction of a variety of hazardous organic compounds, including toluene, methylene chloride and CFC-113.

5.4.5 DC discharge reactors with fast gas flow

A discharge can be established by using a simple DC-high voltage power supply. The construction of the reactor is simple, typically consisting of an anode plate and a cathode containing a lot of sharp metallic pins. By pumping the gas through the discharge volume to produce fast flow at atmospheric or super atmospheric pressure (1-2 *atm*), a stationary discharge can be established without overheating the gas. The mode of operation resembles that of a gliding arc reactor.

5.4.6 The gliding arc reactor

In contrast to non-equilibrium plasma, equilibrium plasma tectonics make use of plasma furnaces or torches, in which the whole gas is heated in order to break up the desired molecules. Generally conventional electric arcs or plasma torches generating a so-called "thermal plasma" does not seem to bee well adapted for plasma chemistry. Most of the energy will be confined in narrow regions. Under atmospheric or higher pressure conditions, thermalization occurs and temperatures in the order of 10^3 *K* are observed. Under such conditions the processed gas goes through a complete thermal decomposition which is then followed by recombination in cooler regions to give the desired products. Though interesting laboratory results have been obtained by rapid cooling to quench the high temperature equilibrium, the only industrial process which has survived is he production of acetylene from light hydrocarbons (Hüls, Germany).

For many applications, particularly for the removal of very dilute concentrations of air pollutants, the non-thermal plasma approach would be most appropriate because of its energy selectivity and its capability of simultaneous removal of various compounds. For others, including many mixed waste streams, the best approach might be to use thermal plasma techniques to incinerate the complete waste, and to use a non-thermal reactor to clean the flue gases.

Electrical energy is commonly considered as a clean energy source and therefore well adapted to operate devices that can eliminate toxic vapours and gases without the disadvantage of classical fuel-operated devices which process supplies additional

green-house gases like CO_2. One advantage of electrical created plasma-assisted chemical methods lies in their ability to process large volumes.

The gliding arc is one amongst several other methods to generate plasma. At least two diverging electrodes must be placed in a fast gas flow injected in the centre of the electrodes. The electrodes can have different geometry's, either diverging, converging or straight. The most commonly used geometry is electrodes diverging in the flow direction, taking the shape of an ellipsis. The discharge will form between and along the electrodes. The length and shape of he discharges will depend on the applied voltage and current, the electrode geometry and the gas flow characteristics, were gas flow velocity is the far most important factor.

One of the characteristics of the gliding arc, is the displacement of the discharges along the electrodes in the flow direction. This displacement, together will the cooling gas flow prevents erosion of the electrode surface. The supplied electrical energy is directly and totally transferred to the gas. All gas or vapour, also dusty and/or misty, can bee directly processed at any inlet temperature and 0.1-5 *atm* pressure. The result is a voluminous plasma with relatively low energy density out of thermodynamic equilibrium. Some applications, mostly to engineering and environment control, were already tested in laboratory and trial scale reactors proposed for large ranges of gas flow and dissipated electric power.

The advantage of the gliding arc for gas purification lies in its low energetic cost for each atom or radical produced, compared with a normal cold discharge. The energetic cost is defined by:

$$A = \frac{H(T) - H(T_0)}{\alpha(T)} \qquad \textbf{Eq. 5-1}$$

where H(T) is the enthalpy of the mixture and $\alpha(T)$ is the fraction of activated species. The energetic cost for each species activated in a normal cold discharge (corona- or barrier discharge) is about 10 *eV* while in a gliding arc the cost is only 3-5 *eV*. The use of a gliding arc principle will therefore reduce the purification cost with around by a factor of two to three. *The principal inconvenience related to the gliding arc process in gas purification is the formation of non negligible quantities of nitric oxides (NO_x).*

Inexpensive gliding electrical discharges can considerably reduce the nuisances of classical gas processes. Some advantages of this “cold” catalytic plasma discharge is its

ability to supply controlled energy to the process. The same process can be operated at considerably lower temperature and thereby at lower energy cost.

During a first period the arc in thermodynamic equilibrium slides between the electrodes with a dissipated power per unit length that remains fairly constant. When the length of the arc attains a certain critical value the dissipated power is no longer sufficient to balance the heat losses. As a result, the gas temperature falls abruptly and the arc evolves towards a second mode far from equilibrium ($T_{surr.}$~ 2000 *K* and $T_{electron}$~ 10000 *K*). A physical model has been suggested by Fridman et al. (1994). The model makes it possible to show that a very important part (75-80 %) of the electrical energy involved in the arc is dissipated during the second period. The non-equilibrium plasma formed during the second period is particularly useful for inducing with high efficiency chemical reactions which involve vibrational excitation of molecules like for instance the decomposition of CO_2 and H_2S, the synthesis of NO_x, the production of H_2 form H_2O, conversion of CH_4 into C_2H_2, and the production of syngas ($CO + H_2$).

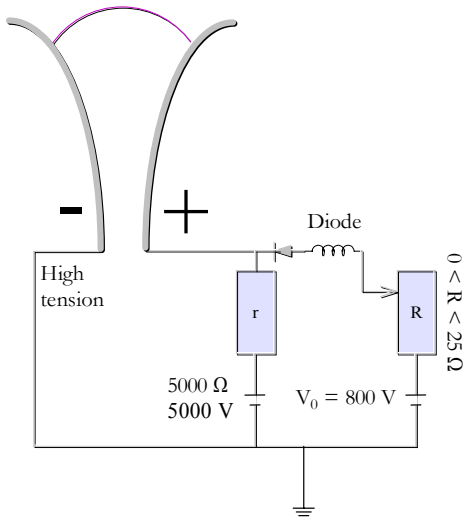

As showed by Lesuer, Czernichowski and Chapelle (1990), only a fairly simple disposal is necessary to realize a gliding arc (figure 5-6). To initiate an arc only a weak power source (5 *kW*) and high tension (5 *kV*, 5 *k*Ω) is required. The current may be in the order of 1 *A*.

Figure 5-6: A typical gliding arc apparatus.

To deliver a power which can be varied between 1 and 50 *kW*, a source capable of delivering a current, I_{max} = 60 *A*, with a tension of V_0 = 800 *V*, must be available and

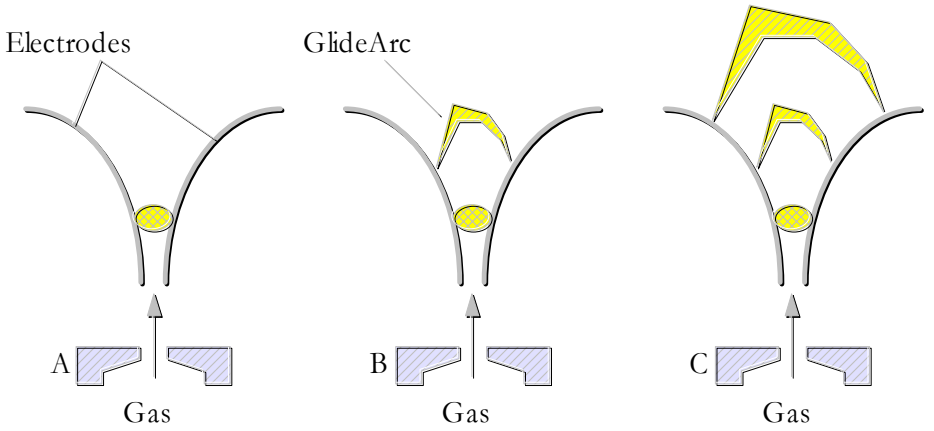

Figure 5-7: Onset, evolution and break-up of a gliding discharge.

protected from the high tension by a diode. The resistance R, in series with the power source, may vary between 1 and 25 Ω. To prolong the moment of the arc break-up, a self-inductance (L=25 *mH*) is implemented in the circuit in series with R. The development of an arc is illustrated in figure 5-7. The discharge initiates where the distance between the electrodes is smallest (1-2 *mm*).

After the *law of Pashen*, the electrical field necessary for break-down (in air) should be at least 3 *kV/m*. After an arc has been initiated, a weak low resistance plasma is formed, and the tension at the end of the electrodes falls rapidly to an order of some volts. At this moment, the diode opens and allows the current to increase, powered from the second source, to a value given by the ratio $V_0/R \approx 40$ *A*. During the increase of current, the plasma resistance is small compared to R. As reported by Fridman et al. (1994), the current is then given as:

$$I(t) = \frac{V_0}{R}(1 - e^{-t/\tau_L}) \qquad \textbf{Eq. 5-2}$$

were $\tau_L = L/R \approx 1$ *ms*.

The small plasma volume formed after the initiation of the arc is then forced to move with the imposed jet flow, giving it a speed of about 10 *m/s*. The arc is now in a regime of locally thermodynamical equilibrium, that is in each point along the arc the electron temperature is equal to the temperature of the surrounding gas molecules. The electrical effect per unit length of the arc is sufficient to compensate for the conductive losses from the arc to the surroundings. The current increases rapidly to its maximal value (V_0/R) and

the arc continues its displacement along the electrodes with increasing length, resistance and dispersed electrical effect, while the current slowly decreases. The temperature of the arc in equilibrium is now between 7000-10000 *K*.

The arc then reaches the instant when the resistance in the arc becomes equal to the resistance R (figure 5-6) and where the electrical effect dispersed in the plasma reaches a maximum. From this point on it is no longer possible to continue in equilibrium. The electric effect decreases but the conductive losses continue to increase. The arc now passes into a non-equilibrium state (see figure 5-8) characterized by an important drop in temperature ($T_o \sim 2000\ K$). As a result of the much lower temperature, the heat losses to the surroundings decreases, which again results in a rapid increase in arc length. Electron temperatures are estimated to about 10000 *K* (1 $eV \sim 11600\ K$).

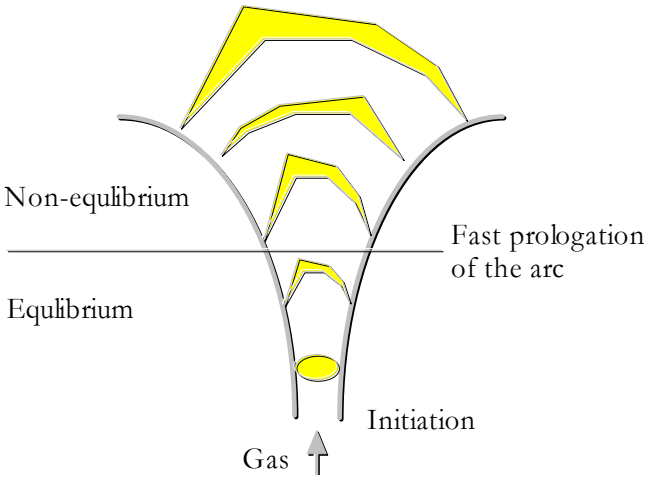

Figure 5-8: Characteristic evolution of a gliding arc.

The primary mechanism responsible for the production of electrons in this state, is assumed to be ionization in cascade. This non-equilibrium phase has been observed to be very dependent on the inductance, *L*. The arc extinguish when the heat losses overcomes the maximum electrical effect delivered by the power supply. The break in current then induces a new arc at the electrode roots, as in figure 5-9.

Although the arc motion is not well defined geometrically and there are no well developed quantitative models for the description of the relative velocities of the arc and gas flow, it is possible to state that the difference in arc and flow velocities increases with

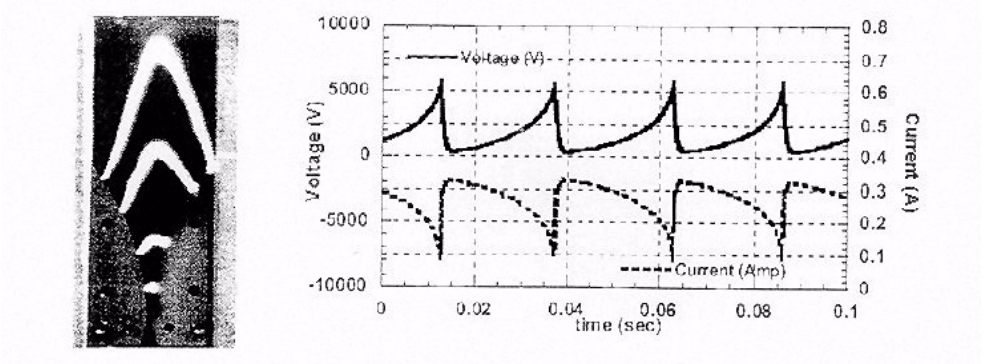

Figure 5-9: Current and voltage waveforms of the gliding arc discharge.

Typical current and voltage waveforms of the gliding arc discharge by high-speed imaging analysis. From Fridman et al. (1999)

the increase in the gliding arc power and absolute values of flow rates and, hence, flow velocities (Fridman et al. (1999)).

5.5 APPLIED NON-THERMAL PLASMA CHEMICAL PROCESSING

One of the technology advantages of most of the non-thermal plasma processing systems being developed today, are the modular architecture. This feature allows scaling to a wide range of system capacities; single-pass, short-residence time treatment systems. These systems also have the advantage of allowing:

- A high degree of hazardous compound removal
- Flexible modular architecture
- Simultaneous treatment of many different compounds
- Little or none chemical additives are required
- Almost instantaneous treatment feedback

Cold plasmas have been demonstrated to be very effective in treating air contaminant streams but they traditionally require high power consumption. This technology could be a viable candidate in a respirable atmosphere revitalization system or a contaminant source control system in advanced life support. The technology also can be applied in disinfection and biological and chemical decontamination of spacecraft surfaces.

Most of the non-thermal plasma systems can be considered safer than traditional

systems because no chemical additives are necessary and because they normally operate at ambient temperature and pressure. Preliminary cost studies show favourable economics but more study still needed in this area. Cost estimates show that this technology has the potential to become a cheaper alternative than traditional systems, i.e. SO_x and NO_x removal, if the technology is developed at full industrial scale and commercialized. The major technical challenges associated with different plasma systems today are to understand the reaction pathways and optimal process chemistry for system scaling economics.

The by-products from non-thermal plasma systems depends on a number of factors e.g. the particular compound to be treated, its concentration, the medium in which it is entrained, and others. For VOC treatment, chlorocarbons and chloro-fluorocarbons yield mineralized end products (i.e., water of combustion, carbon dioxide, and hydrochloric acid) and other by products (e.g., unstable chlorocarbons). A wet scrubber is normally used to neutralize acids and carbon dioxide as well as to further mineralize by-products and then neutralize acids to common salts. The volume of hazardous gas flow can be reduced by going from a large volume gaseous stream to solid salts in the scrubber.

Much of non-thermal plasma systems emerging today however, are based on the technology of the commercial ozone generation industry, where large megawatt plants are processing hundreds of tons per day of oxygen gas. Non-thermal plasma systems are versatile because they can be used with a variety of vapours and gases extracted from soils and ground water as well as stack and flue gases. Mobile treatment units can also be constructed. In a combined mode, where these systems are used in a secondary stage, even greater flexibility and effectiveness could be possible.

International results to date indicate that the technology shows promise for treating a variety of gaseous hazardous wastes (VOC's, SO_x, NO_x). Thermal treatment units, activated carbon, and selective catalytic reduction (SCR) are the most significant competitors at present.

Plasmas are sources of abundant free radicals (Bouios (1990); Flinn (1971); Akshi (1985); Junl-Dam and Brockmeier (1970); Baddour and Timmius (1967); Venugopalan (1983); McCarthy (1954)). Control and manipulation of the subsequent free-radical reactions are essential to the success of using plasmas for complete decomposition or in organic syntheses (Boenig (1988); Suib and Zhang (1991) and

(1992); Zerger, Suib, and Zhang (1992); Huang and Suib (1992)). Such control and manipulation are possible by appropriate design of plasma reactors.

Take partial oxidation of methane to methanol as an example. Methanol is an important industrial chemical, especially in view of its use as a gasoline additive and its potential use as an automobile fuel (Chang (1983)). Today methanol is manufactured from methane by steam reforming of methane to synthesis gas, which is then converted to methanol over copper-based catalysts (Danner (1970)). The steam reforming step is a capital and energy intensive process. The direct partial oxidation of methane to methanol is more desirable if high selectivity to methanol (>70%) and reasonable conversion rates are achieved (Edwards and Foster (1986)). Active research efforts are being carried out to find processes that can selectively oxidize methane to methanol (Shilov (1984); Foster (1985); Pitchai and Klier (1986); Kharas and Lunsford (1989), Brown and Parkyns 1991); Cesser and Hunter (1992).

Huang et al. (1994) explored the use of microwave plasmas to selectively convert methane to useful products. In a methane plasma, methane was dimerized to C_2 hydrocarbons at a selectivity higher than 95 % and conversions ranging from 30 % to 90 %. The energy efficiency to drive this thermodynamically unfavourable reaction varied from 0.2 to 3.3 %. In this study, oxygen, in addition to methane, was introduced to the plasma reactor in order to partially oxidize methane to methanol. The key objective was to control the reactions involving radicals and other reactive species generated by the plasma so that methane dimerization was minimized and the methane oxidization process stopped at the methanol stage. Partial success was realized by introducing methane immediately downstream of the plasma zone so that the critical radical reactions occur outside of the plasma zone to reduce total oxidation products. By introducing methane downstream from the plasma zone, the methane dimerization reaction was essentially eliminated.

In the absence of any initiator, methane may be directly oxidized to formaldehyde under mild conditions of non-equilibrium plasma. The reaction selectivity can be achieved up to 80 % at the best condition. Methane oxidation to formaldehyde has been studied widespread since 1960s. In general, previous works were carried out in the presence of initiator or at high temperature or at high pressure, were formaldehyde selectivity is low. Other explorations for possible new paths on methane oxidation to formaldehyde under mild conditions in the absence of any initiator have also been investigated (ISPC-7 Eindhoven, (1985)). While chemical reaction is beginning, high energy electron and other

activated species losing their energy, the chemical reaction is stopped. This means that realization of high selectivity and yield is entirely possible, if the products are disengaged from plasma region or are captured rapidly at the instant when reaction begins.

Thomas et al. (1993) studied the corona-induced oxidation of stoichiometric mixtures of ethylene, methane and acetylene in oxygen. They used a relatively low voltage system with a very simple electrode geometry to produce the discharges. The discharges were able to run fairly well because of the low reactor pressure being used (0.0395-0.0987 atm). Lowering the system pressure is well known to promote the efficiency of the discharge. Total oxidation of the hydrocarbons in question was achieved, within a time interval in the order of many minutes.

Gogolides et al. (1994) applied radio-frequency glow discharges in methane gas. The aim with these investigations was to develop a simplified gas-phase kinetic model that could confirm the experimental results. As Thomas et al. (1993) they used a low pressure system (80 *mTorr* - 1 *Torr*). The electrode spacing was between 2-6 *cm* and the power input between 0.06-0.15 W/cm_2. They proposed a mechanism where methane directly dissociated by electron attack to form CH_2 and CH_3 radicals, which further would contribute to the methane decomposition.

The applications of non-thermal plasmas for automotive exhaust and flue gas cleaning (SAE (1998); SAE (1999); Delphi Automotive Systems (2000); Hammer (2000)), toxic gas remediation (Xu and Kushner (1999); Coogan et al. (1993); Rosocha (1996)), have also widely been investigated.

Chernova et al. (2001) investigated the destruction of ethane in a corona discharge both experimentally and by modelling. This investigation was done to clarify whether a detailed elementary free radical reaction model could explain the kinetics, energy efficiency and the products of the destruction of a simple hydrocarbon molecule in a corona discharge. The experiments were performed at ambient temperature (298 ±3 *K*) and pressure (1.00 ± 0.05 *bar*). Mixtures of ethane and zero air were passed through the reactor with the flow rates of 0.17-4.8 cm^3/s. The active discharge power was varied in the range 0.01-4.0 *W*. The degree of the destruction was then measured at different ethane concentrations, flow rates, and discharge powers. Using both the electron impact MS as well as the GC/MS method to monitor the products, methyl nitrate (CH_3ONO_2), ethyl nitrate ($C_2H_5ONO_2$) and acetic acid (CH_3COOH) were identified among the destruction

products. The final products of the destruction, water and carbon dioxide, were observed using the MS detection method. Fairly good agreement between the experiments and the results from kinetic modelling was achieved. The results indicated a complete failure of the free-radical mechanism to account for the experimental observations.

These results could also be confirmed by Krasnoperov and Krishtopa (2001). These authors have published a review of the experimental results on the kinetics of the "destruction" of a number of organic and inorganic compounds in a dielectric barrier discharge obtained by the NJIT (New Jersey Institute of Technology) group during the last seven years. The types of the destruction kinetics, the kinetic laws, the effects of the concentration, power and the flow rate on the removal efficiency have been summarized. The products of the corona discharge processing were also discussed, when these were available. Experimental data for destruction of methane, ethane and some other selected species in air, extracted from the original table, are shown in table 5-6 with corresponding G-values.

Table 5-6: Extracted G-values for the destruction in corona discharge in air
A review of the experimental results on the kinetics of the "destruction" of a number of organic and inorganic compounds in a dielectric barrier discharge by Krasnoperov and Krishtopa (2001).

Molecule	**Formula**	**Concentration Range, ppm**	**G-value molecule/ 100 eV**	**"Ion Efficiency"** G / G_{ion}[a]
Methane	CH_4	61 – 1890	2.2×10^{-4} at 61 ppm 1.3×10^{-2} at 1890 ppm	1.3×10^{-3} at 61 ppm 7.6×10^{-2} at 1890 ppm
Ethane	C_2H_6	12 – 10000	0.18 ± 0.08	1.0
Heptane	C_7H_{16}	256 – 1062	0.27 ± 0.10	1.6
Octane	C_8H_{18}	252 – 966	0.29 ± 0.12	1.7
Nitric Oxide	NO	340 – 570	0.32 ± 0.21	1.9
Nitrogen Dioxide	NO_2	850 – 9800	0.62 ± 0.29	3.6
Sulfur Dioxide	SO_2	66 – 970	6.2×10^{-3} at 66 ppm 4.1×10^{-2} at 970 ppm	3.6×10^{-2} at 66 ppm 0.24 at 970 ppm

a. G_{ion} = 0.17 eV/100 eV was used

The G-value says how many molecules of a given species that have been created or destroyed per 100 *eV* of energy. The original table can be found in the full article and consisted of data for 18 different species. One of the conclusions that could be drawn was that methane (and sulphur dioxide) stood out from the rest of the species. These molecules have ionization energy larger than the ionization energy of molecular oxygen. Therefore, the charge transfer from molecular oxygen cation is impossible, and the mechanism outlined before does not work. These molecules must be activated either by the direct electron impact ionization or via the free-radical processes. This explains much lower efficiencies of the destruction as well as the concentration dependence of the G-values for these molecules.

The following chapters, 5.5.1-5.5.5, will give further insight on some of the current development on applied non-thermal plasma chemical processing. Each chapter is dedicated to a specific discharge method. Corona discharge, pulsed- and silent discharge and gliding arc are all based on technology in which energetic electrons are generated within the polluted gas. In contrast to this, the electron beam is based on externally generated electrons, which again are supplied to the polluted gas. The chapters that are of most interest for the current investigations are those covering the barrier discharges (5.5.3) and the gliding arc device (5.5.5).

5.5.1 Corona discharge chemical decomposition

A corona discharge is produced when the gas is exposed to an intense electric field, as defined previously in chapter 5.3.2. As in most non-thermal plasma systems, the energy supplied to the corona discharge reactor causes the molecules to break apart, thus forming ions and radicals which again initiate further reactions.

At the chemical engineering department at the University of New Hampshire, R. Worthen (1996) studied a corona discharge technique to remove NO from a stream of nitrogen (N_2). The reactor consisted of two cylindrical stainless steel electrodes, one inside the other. The outer electrode enclosed a quartz tube, and the inner electrode was enclosed by another quartz tube. Glass wool was then placed between the quartz tubes. The inner electrode was connected to an AC voltage source, the other was grounded. The reactor operated at room temperature and pressure. They found that with 22 *W* of power, a gas residence time of one second, an NO concentration of 250 *ppm*, and an 8 *mm* distance between the electrodes, 99 % conversion of NO to N_2 and O_2 was achieved. Changing the

frequency of the ac power source from 400 to 1000 *Hz* or the amount of glass wool packing did not significantly affect the efficiency for NO conversion.

A company named Litex, Inc. (Litex (1999)), plan to start (September 2000) volume production of their Litex CDD unit. The unit is a new product which is supposed to significantly reduce hazardous emissions generated by gasoline-powered automobile engines. The CDD is inserted into the exhaust system of a gasoline engine upstream from the three-way catalytic converter. The product has been undergoing extensive testing since 1997 and according to Litex, the unit is capable of reducing carbon monoxide (CO) emissions more than 80 %, and hydrocarbon (HC) and oxides of nitrogen (NO_x) emissions by more than 50 %, depending upon the sulfur contents of the fuels involved, which may range from 0 to more than 300 *ppm*. The operating power of the unit is approximately 25 *Watts*. The CDD is based on a technology initiated and patented by the Lockheed Martin Corp. The reduction is believed to occur as a result of a chemical process in which constituents found in the exhaust stream are altered by a non-thermal plasma (NTP) created by the CDD. This reaction creates active species that flow into the catalytic converter and increase catalytic activity while mitigating the effects of sulfur. shows the placement of the CDD unit in the cars exhaust system, upstream of the catalytic converter.

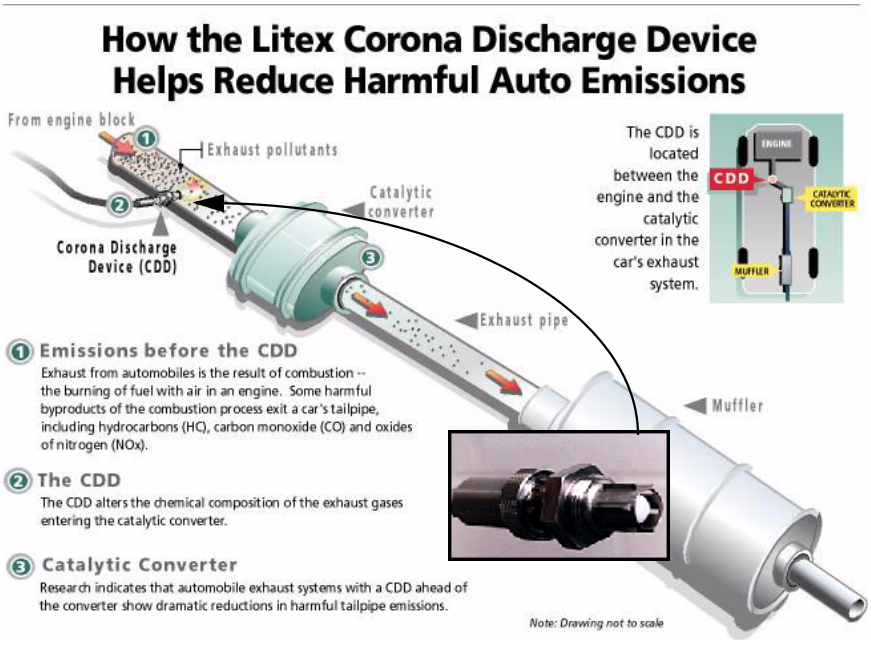

Figure 5-10: The Litex corona discharge device.

From figure 5-11 we can see how a fraction of the exhaust flow (between 5 % to 20 % depending on flow conditions) passes through the electric discharge region. The discharge produces radicals, such as hydroxyl (OH) and other oxidizing species, such as O_3 and NO_2 in the exhaust gas.

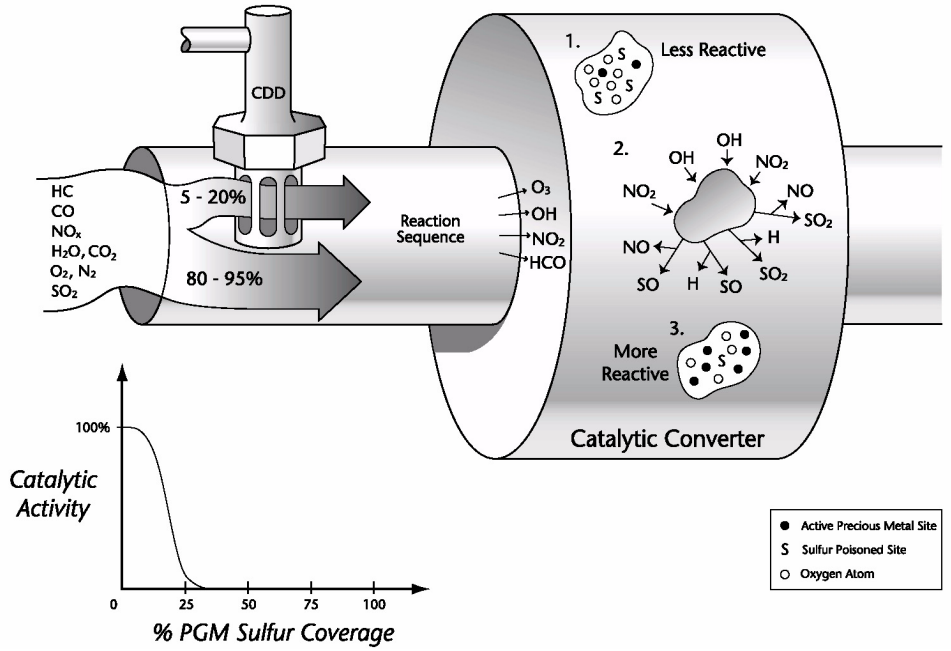

Figure 5-11: A model of the Litex process.

Downstream, various radicals such as OH, generated by the discharge device, initiate gas phase reactions that further generate oxidized hydrocarbon species (HCO), convert NO to NO_2, and subsequently regenerate OH radicals. This reaction mechanism enables short-lived radicals generated at the discharge device, to reach the catalyst surface.

A similar process has recently been realized by multi-national Delphi Automotive Systems (2000), a world leader in mobile electronics and transportation components and systems technology. They use what they call a NTP-device, which reduces NO_x and particulate emissions in direct injection gasoline and diesel engines. NTP devices produce high energetic electrons that collide with the background gas molecules, producing radicals that promote selective partial oxidation of NO to NO_2. The NO_2 generated through the NTP is reduced by an appropriate catalyst technology to non-harmful gasses. In steady-state testing of a diesel vehicle, the

non-thermal plasma exhaust aftertreatment system has demonstrated greater than 65 % reduction of oxides of nitrogen emissions without additional hydrocarbons to the exhaust stream, greater than 85 % with additional hydrocarbons, as well as demonstrating a significant reduction in particulates.

Figure 5-12: The Delphi Automotive Systems NTP process.

At the "Mondial de l'Automobile", PSA Peugeot Citroen and Delphi Automotive Systems announced they have signed an innovation agreement to apply non-thermal plasma exhaust aftertreatment (NTP) to future Peugeot Citroen vehicles. The agreement commits PSA Peugeot Citroen and Delphi to developments of technology for future vehicle applications.

PLASMACAT is a new, high energy-saving technology for the treatment of gaseous pollutants marketed by Up-To-Date Environmental Engineering AG (1999). The standard process consists of 2 stages, as shown in figure 5-13.

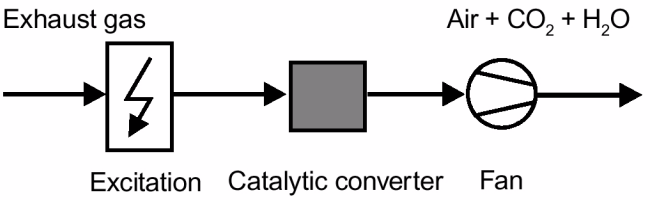

Figure 5-13: The PLASMACAT standard process.

In the excitation stage, the molecules of the waste gas are excited by an alternating electrical field of several thousand volts. The gas molecules at departure from the

excitation stage are in a condition of vibration which is theoretically equivalent to heating to several thousand degrees centigrade, without the gas itself changing in temperature to any significant degree (so-called cold plasma). Next the gas is fed over a contact catalyst, which also operates at ambient temperature, where the contaminant molecules are completely oxidised. The contaminants are then converted into harmless compounds (e.g. hydrocarbons into CO_2 and H_2O), without the creation of any by-products. The process consumes in the excitation stage about 0.5-2.5 *kWh* of energy per hour for a volumetric flow of 1000 m^3/h. The exact value depends on the type of contaminant, its concentration, and the air humidity. PLASMACAT is a combination process which may best be compared with catalytic incineration. The biggest difference lies in the manner by which the contaminant molecules are made reactive. The heating of the entire gas flow to higher temperatures is now replaced by an excitation in the alternating electrical field.

5.5.2 Pulsed plasma chemical decomposition

Non-thermal conditions mean that the electrons are heated, not the gas molecules. These micro discharges yield a large improvement in the power efficiency because, within the short lifetime of each micro discharge, the ions do not experience significant movement and therefore do not contribute to the power consumption. The short lifetime of these micro discharges is accomplished with the use of very short high-voltage pulses (pulsed corona discharge) and/or with the use of dielectric coatings on the electrodes (dielectric barrier discharge).

In collaboration with industry and the military, Southwest Research Institute (SwRI) engineers have developed a new technology that transforms environmentally harmful air pollutants into less harmful constituents (Grothaus and Fanick (1996)). The so-called corona reactor consists of a non-thermal plasma reaction process under atmospheric pressure. Tests conducted at SwRI showed that the reactor potential to neutralize a wide variety of pollutants in an energy-efficient manner. The reactor used in these tests consisted of 10 one-inch diameter, three-foot long reaction chambers operating in parallel. With input power between 100-300 *watts*, process-stream flow rates of 5-10 litres per minute in air or nitrogen, pollutant concentrations of a few hundred *ppm*, and with hydrogen or oxygen as additives (a few hundred *ppm*), significant removal levels of certain VOC's and PFC's were achieved. Typical energy densities applied to the reactor were less than 1000 *J/l*. The results showed that VOC's, C7H8, CH2Cl2, and CH3CCl3,

as well as NF3, were effectively removed from the gas stream, with destruction levels exceeding 99.9 percent. Eighty five percent of the CCl2F2 was destroyed.

Vogtlin (1994) at Electronics Engineering department at the Defence Sciences Engineering Division has been exploring the efficiency of pulsed plasma processing in the removal of nitrogen dioxide, nitrogen oxide, and other pollutants. His process used an electrical discharge to create chemical radicals from air molecules, radicals that can react with pollutants and form harmless compounds. Different additives such as hydrocarbons were also used to improve the efficiency of the removal. They found that the most efficient removal of NO_x was achieved by adding small amounts of a dilute aqueous solution of ammonia. The discharge reactor consisted of a stainless steel tube enclosing a high voltage wire, to which high voltage was applied in pulses shorter than 200 *ns*, resulting in non-thermal conditions through the production of short-lived micro discharges. For the experimental apparatus these workers used a closed-loop gas system with mixtures of bottled gas to simulate the flue gas. The processing chamber had been designed with a 5 *cm* diameter outer tube having a length of 15.24 *cm*.

At the Eindhoven Power Engineering Laboratory at Eindhoven University of Technology they have acquired many years of experience during the development of the pulsed corona technique (Eindhoven (1999)). They develop applications designed for odour removal from air flows, VOC destruction such as the removal of styrene and toluene from off gases, NO-oxidation, tar removal from biogas and inactivation of micro-organisms in air and in liquids. The high-voltage pulse source generates steep 50 *MW* power pulses of 100 *kV*. The unit operates at a repetition rate of 1000 *pulses per second*. In this way 2 *kW* of average power is continuously transferred to the gas in the form of corona discharge energy. Several years of experience have given some rough estimates of the energy needed per treated litre of waste flow. For 70 *%* removal from gases these energy densities have been found roughly to vary between 5 and 100 *J/l*, depending on the type of contaminant. For odour, the cost has shown to be lower. For liquids like water the energy density is between 5-100 *kJ/l*. The TUE transportable test unit with reactor is illustrated in figure 5-14.

AEA Technology Products & Systems (AEA (1999)) have recently commercialized what they call The Electrox Emission Abatement System (see figure 5-15), which is a device in which the gaseous phase contaminants are destroyed by a plasma generated between two concentric electrodes positioned axially within the ductwork. A pulsed high

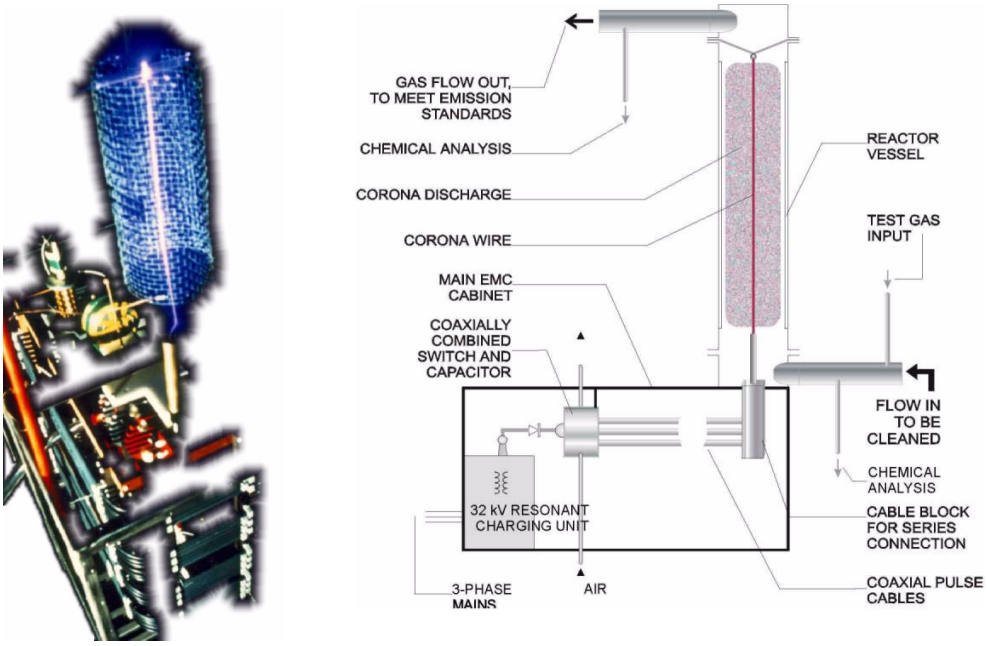

Figure 5-14: The TUE transportable test unit with reactor.

The unit is available for on-site testing and contains the power source and the controls for the electrical discharges. A reactor, specific for each application, can be designed on demand. The tailor made reactor will first be fine-tuned and pre-tested in the power engineering laboratory.

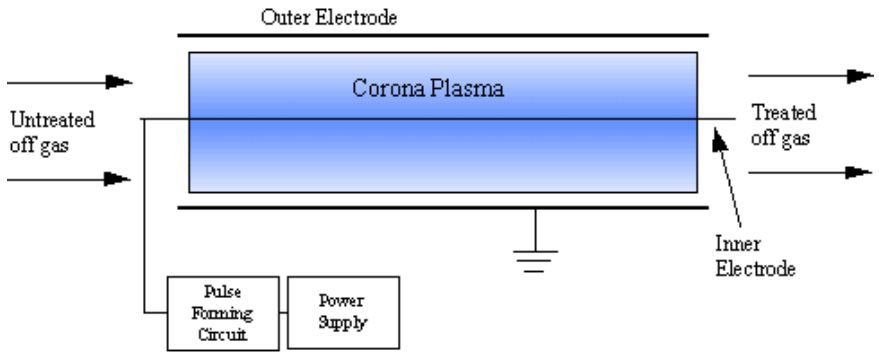

Figure 5-15: The Electrox Emission Abatement System, AEA (1999).

voltage is periodically applied to these electrodes leading to plasma formation and the appearance of corona streamers. In a typical reactor the average gas temperature has been found to rise by only around twenty degrees overall. The process claims to be highly efficient in removing species at the lower concentration range. From October 1998 to

March 1999 an Electrox demonstration system was evaluated at the South East London Combined Heat and Power (SELCHP) waste to energy plant. A portion of the exhaust was piped through a demonstration plant at a temperature of around 140 °*C*. During these tests the Electrox system was evaluated mainly for destruction of NO in anticipation of the future EC directive NO_x emission limits. The demonstration system showed that NO could be reduced down from 270 $mg\ Nm^{-3}$ to 30 $mg\ Nm^{-3}$ at a flow-rate of 1000 $Nm^3\ h^{-1}$ or 70 $mg\ Nm^{-3}$ at 1500 $Nm^3\ h^{-1}$ (i.e. to below all current and proposed European limits). Extensive testing and demonstration has also been successfully carried out for the destruction of VOC's present in the exhaust of industrial processes. They currently have designs for systems at flow-rates up to about 25 000 $m^3\ h^{-1}$.

A Norwegian company called Applied Plasma Physics AS claims to have a similar process consisting of a modular system where each module consists of two main components, the plasma generator and the reaction chamber (figure 5-16). The plasma generator is a specially designed 10 *kW* high voltage generator that supplies voltages of up to 40 *kV* (E-field up to 5 *kV/cm*). The voltage generated is either DC with high-frequency

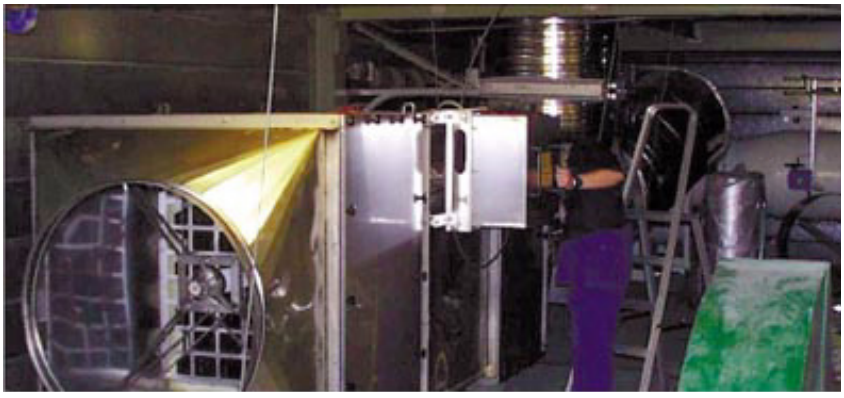

Figure 5-16: APP's reaction chamber, APP (1997).

AC harmonics or high frequency AC. The generator signal is fed into an oversized rectangular "chimney element" called the reaction chamber. Inside the reaction chamber the exhaust gas is divided and led into 50-100 parallel reaction zones. Each reaction zone works simultaneously as an oxidizing chamber and an electrostatic precipitator, where the relative split between the chambers acting as oxidizer versus precipitator will vary depending on the detailed chemical content of the exhaust. One module has the capacity to

process up to 50.000 m^3 exhaust per hour, and there are no restrictions as to the number of modules that can be integrated in one system. Thus, APP can deliver systems for processing exhaust gases from industrial facilities with emissions ranging from 10.000 m^3 to several millions m^3 per hour. APP is currently finishing a system for reducing the emission of particulate matter from Norton St. Gobain's SiC production facility in Lillesand, Norway (2000000 m^3 stack-gas emission per hour). The first modules are operating, and tests show a reduction in total particulate matter emitted of 75-85%. The installed system can be compared to that of an electrostatic precipitator with the only difference being how the free electrons are created. The plasma effect on decomposition/ oxidation has yet to be proved.

5.5.3 Silent (SDP)/Barrier discharge chemical decomposition

At Los Alamos scientists have been engaged in several advanced oxidation technology (AOT) projects since 1990. For the decomposition of gas-phase hazardous chemicals their strategy has concentrated on electrical-discharge driven non-thermal plasmas. Below are some specific technologies that are being developed (Rosocha (1996)):

- Non-thermal plasma treatment of hazardous/toxic pollutants
- Water treatment using electron beams
- Barrier discharge treatment of VOC's in oxygen lean gas mixtures
- Advanced oxidation technologies for chemical demilitarization

The treatment of acutely hazardous compounds, such as chemical warfare (CW) agents, requires destruction and removal efficiencies exceeding 99.999999 %, which are practically unobtainable using conventional treatment methods. Advanced oxidation technologies (AOTs) have recently been investigated for the removal of CW agents (Rosocha (1996)). This technology is now broadly used for processes involving highly reactive free radicals, some of which may even be reductive rather than oxidative. The concept used at Los Alamos was to introduce the hazardous chemicals into a selected carrier gas stream and treat the stream as part of a unique closed-loop system. The gas stream flowed through an non-thermal plasma unit, where a given fraction of entrained contaminant was destroyed. Chemical scrubbers then selectively removed the non-toxic treatment products after which the gas was recycled back to the starting point. The main approach was volatilization by a thermal packed-bed reactor, followed by oxidation or

reduction in a non-thermal plasma. The units were flamelessly operated in either oxidative or reductive modes at near-ambient pressure and were used with a large range of chemical forms (liquids, slurries, and pumpable sludges). Figure 5-17 shows the conceptual diagram of the closed-loop unit. It is well known that barrier discharges in humid air generate large quantities of both atomic oxygen (O_3P) and hydroxyls (OH), and for many air pollution control applications these radicals are ideally suited to oxidize air contaminants. The addition of fuel or oxidants are not required as the non-thermal plasma (NTP) uses the oxygen and hydrogen already present in the off-gas as the raw materials for radical production.

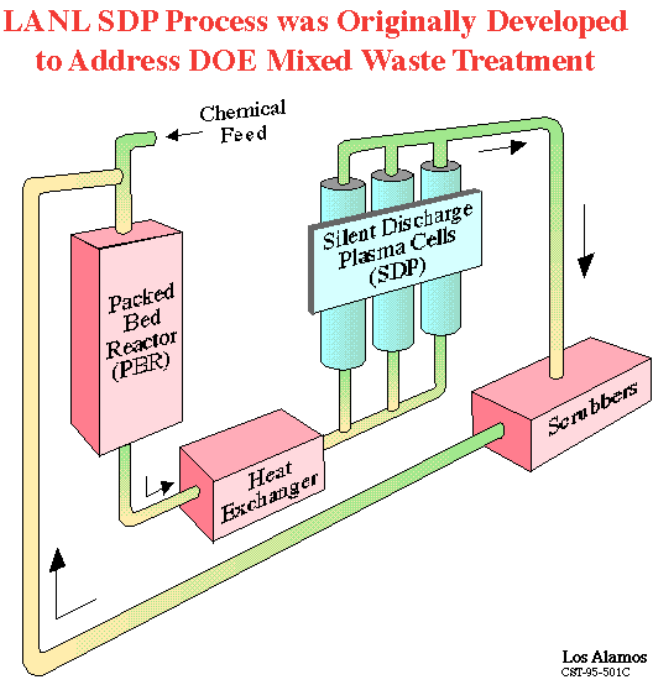

Figure 5-17: Closed loop PBR/NTP unit (Rosocha (1996)).

Another technique is applying the silent discharge process in an atmospheric pressure plasma jet (APPJ) that may provide a much needed method of CBW (Chem/Bio Warfare Decontamination) decontamination which, unlike traditional decon methods, is dry and non destructive to sensitive equipment and materials (Herrmann et al. (1999)). The APPJ discharge uses a high-flow feedgas consisting primarily of an inert carrier gas, such as He, and a small amount of a reactive additive, such as O_2, which flows between capacitively-coupled electrodes powered at 13.56 *MHz*. The plasma generates highly

reactive metastable and atomic species of oxygen which are then directed onto a contaminated surface. The reactive effluent of the APPJ has been shown to effectively neutralize VX nerve agent as well as simulants for anthrax and mustard blister agent. Research efforts are now being directed towards reducing He consumption and increasing the allowable stand-off distance. Recent results demonstrate that by replacing the O_2 reactive additive with CO_2, ozone formation is greatly reduced. This has the result of extending the lifetime of atomic oxygen by an order of magnitude or more. A recirculating APP Decon Chamber which combines heat, vacuum, forced convection and reactivity is currently being developed for enhanced decontamination of sensitive equipment. Several techniques are also being evaluated for use in an APP Decon Jet for decontamination of items which cannot be placed inside a chamber.

A recent process realized by the company PlasmaSol (2000) LLC is a non-thermal plasma reactor system comprised of a patented plasma reactor integrated with an extremely efficient power supply. They claim that their reactor system provides the performance level in the plasma region that scientists have been striving for, for over 30 years. It has long been understood that within the plasma region there are many attractive physical attributes to include destroying the molecular bond in NO_x and SO_x in combustion exhaust, breaking Volatile Organic Contaminants (VOC's) into their trace elements and cleaning surface contaminants from microelectronics, metals and other surfaces. What is the unique characteristics of the PLASMASOL system is that it is able to sustain a very diffuse, homogenous plasma at ambient temperature and atmospheric pressure. This operating characteristic allows the process to be applied to a number of practical industrial and consumer environmental applications. The PLASMASOL^{TM} NTP Reactor (figure 5-18) operates under ambient pressure and temperature, achieving total destruction of several VOC's including toluene, benzene, methanol, heptane and octane.

It has been long acknowledged that the NO_x and SO_x during combustion could be lowered, if not eliminated, by improving the efficiency of burning during the combustion cycle. PlasmaSol's method of generating NTP allows the pre-treatment of fuel/air mixtures. It is claimed that this method of excitation of the mixture prior to combustion will reduce the temperature of combustion. By lowering this temperature, NO_x and SO_x will not form.

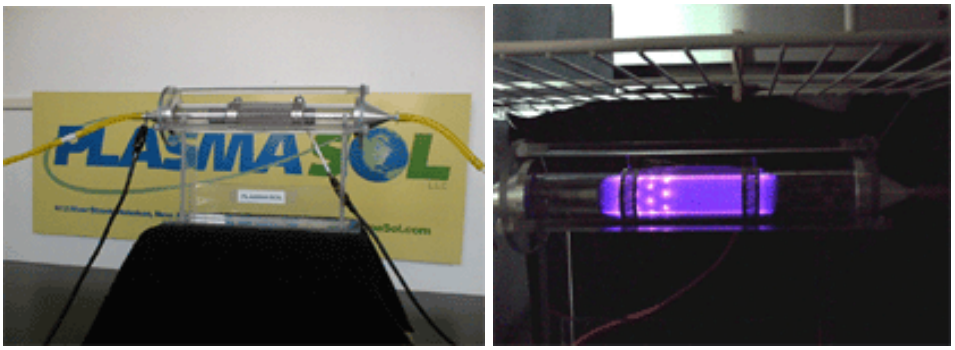

Figure 5-18: The PlasmaSOL reactor (PlasmaSol (2000)).

5.5.4 Electron beam chemical decomposition

This is a method where the energy of the electron beam is used directly to dissociate and ionize the background gas. During the ionization by the beam, a shower of secondary electrons is produced, which further produce a cascade of ionization and dissociation. This cascading effect produces a large volume of plasma that can be used to initiate the removal of various types of pollutant molecules. From the results of basic studies and pilot plant tests that have been done in Japan, Germany, Poland, and the USA, the electron beam process is considered to have an excellent potential for the simultaneous removal of NO_x and SO_2 from high-sulphur, coal-fired utility boiler combustion gases.

Three advanced pilot plant tests are now being conducted in Japan for electron-beam processing of flue gases. The first objective is to optimise the electron beam process for the treatment of flue gas from utility coal-fired boilers. The second objective is to expand the applications to other gases (Penetrante and Schultheis (1993)).

5.5.5 "Gliding Arc" chemical decomposition

Powerful electric arcs were gliding between great horn-shaped electrodes in the early part of this century. Industrial plants were using these "horn arcs" to produce nitrogen-based fertilizers. The technology involved the use of electricity in the high-temperature synthesis of NO_x from air. These arcs were forgotten when ammonia synthesis opened the door for a more efficient way to produce nitrogen compounds. In 1989 some scientists (Lesuer, Czernichowski and Chapelle (1989)) turned their attention back to the old horn arc, and using the shape of the antique electrode, they created a new plasma device they called "GlidArc", as described in previous chapters. These Gliding arcs are able to process

directly, at negligible pressure drop, different gases (Ar, air, water vapour, O_2 H_2, N_2, H_2S, CO, CO_2, hydrocarbons, and their mixtures), preheated and cold, in the pressure range 0.5-5 *atm* (Fridman et al. (1999)). Electrical energy is directly introduced into the reaction volume to create a non-equilibrium and very reactive environment for promoting the chemical transformations of interest. Up to 80 *%* of the electrical energy may be directly absorbed by endothermic chemical reactions. The average residence time of reagents in the reaction zone is approximately 10^{-3} *s*. This fact permits very high specific throughputs in the reaction zone, which generally exceeds by four orders of magnitude other chemical methods, including electrochemical and thermal ones.

The main aspect of using a gliding arc reactor is the way the chemical reactions are promoted by electrical discharges under thermally non-equilibrium conditions. The gliding arc reactor can be used for many industrial chemical applications. Some of the possible applications are being tested in laboratory and industrial scale reactors (Czernichowski (1994), Cormier, Richard, Chapelle and Dudemaine (1993)):

- Emission control of industrial volatile organic compounds (xylene, toluene, heptane, tetrachloroethylene, methyl ethyl ketone), ammonia, free or linked phenols, formaldehyde, organic nitrates, diluted mercap-tans and/or H_2S, diluted methane, etc.
- Emission control of soot, polyaromatic hydrocarbons, SO_x and NO_x
- Complete or partial incineration of concentrated H_2S or H_2S + CO_2 mixtures (gliding arc process);
- Conversion of natural gas to the syngas (H_2 + CO);
- Methane transformation to acetylene and hydrogen;
- Destruction of N_2O;
- Reforming of heavy petroleum residues;
- Decomposition and incineration of concentrated freons;
- CO_2 dissociation;
- Overheating of steam, oxygen, and other gases or flames;
- Ignition of propellants;

- UV generation;
- Decontamination of soil or industrial sands;
- Activation of organic fibers.

Some general features of these processes are:

- Electro burner
- Emission control of volatile organic compounds
- Cleaning of exhaust gases
- Incineration of sulphur compounds
- H_2S partial and complete oxidation
- Methane treatment

A gliding arc reactor can easily be substituted for a classical electro-burner for burning lean mixtures in cases when:

- The gas mixture to be burned has insufficient concentration of combustible gases (and therefore requires an extra energy supply);
- An addition of recirculated exhaust gases or extra air which dilutes the fumes and increases the volume, which leads to larger flue-gas treatment installation;
- Gas pulsation deteriorates the operation of the classical gas burner (when extra safety is required).

The gliding arc features can for example be added to chemical burners in order to:

- Achieve higher flame temperature;
- Control the temperature regime and hence the selectivity of chemical reactions;
- Stimulate reactions.

Fridman et al. (1994) estimated that a large part of the energy injected into the gliding arc, 75-80 %, corresponded to a non-equilibrium state for which the electron temperature, T_e, is about 10 000 *K* with a gas temperature, T_0, around 2000 *K*. Experience through more recent experiments and calculations have shown that the gliding arc concept more

likely will produce conditions with characteristic electronic, vibrational and transitional temperatures in non-equilibrium regime of 1-2 eV, 3-5000 ^{o}K and 800-1500 ^{o}K, respectively.

The parameters for the gliding arc are close to those for a non-equilibrium high frequency discharge at moderate pressures. Such processes are particularly adapted for stimulating molecular vibrational excitation. The authors are also working on the use of the gliding arc process on other decomposition and synthesis processes, e.g.:

- Decomposition of carbon-dioxide,

$$CO_2 \rightarrow CO + 1/2O \quad (5\text{-}1)$$

- Nitric oxide synthesis from air,

$$N_2 + O_2 \rightarrow 2\,NO \quad (5\text{-}2)$$

$$N_2O + O_2 \rightarrow NO_X \quad (5\text{-}3)$$

- Hydrogen production from water vapor,

$$H_2O \rightarrow H_2 + 1/2O \quad (5\text{-}4)$$

- Methane conversion to acetylene,

$$CH_4 \rightarrow 1/2C_2H_2 + 3/2\,H_2 \quad (5\text{-}5)$$

- Synthesis gas production from methane and other hydrocarbons,

$$CH_4 + CO_2 \rightarrow 2\,CO + 2\,H_2 \quad (5\text{-}6)$$

Some of these reactions have already been realized with interesting results. In the case of synthesis production from methane, previous results (Lesuer, Czernichowski and Chapelle (1989); Chapelle and Czernichowski (1992)) have showed that a conversion up to 45 % is possible. Another reaction which is important for the purification of natural gas, is the desulphurization of hydrocarbon gas-mixtures. Several authors (Lesuer, Czernichowski and Chapelle (1989) and in (1990); Chapelle and Czernichowski (1992)) have realized the following reaction in a gliding arc:

$$H_2S \rightarrow H_2 + S \quad (5\text{-}7)$$

The H_2S is either pure or mixed with O_2 or CO_2. For a mixture of H_2S/CO_2, almost complete removal of H_2S has been measured (99.8 %) with a energy cost of 0.6 kWh/nm^3.

Between 1993 and 1995, experiments were performed on exhausts gas, with focus on diluted buthane and methane molecules, from two industrial polymerization stoves. A six-stage prototype of 10 *kW* and a flow rate of 200 *scm/h* was used. It was found that the energy consumption depended on the initial concentration of the pollutant. Additional experiments using a smaller laboratory reactor were performed where both the dissipated electric energy and the destruction rate was measured (Czernichowski and Ranaivosoloarimanana (1996)). The purpose was to determine the specific energy requirement as a function of both initial hydrocarbon concentration and the specific energy input with focus on methane and butane molecules. They studied the destruction of very lean mixtures of methane and butane in air at a flow rate of 100 *scm/h* in a three-stage, 6 *kW* reactor at atmospheric pressure. Each stage of the reactor was connected to the high-voltage, 50 *Hz*, three-phase power supply with current control.

From the results a calculated b-value was deduced, which is an exponential factor for energy density as applied in a removal scaling relationship proposed by the Los Alamos group (Coogan et al. (1993)):

$$[X] = [X]_0 \cdot \exp(-SEI/b) \qquad \textbf{Eq. 5-3}$$

Here [X] is the concentration of the substance after the incineration process, $[X]_0$ is the initial hydrocarbon concentration, and SEI is the specific energy input.

It was clearly proven that energy costs (SER) of diluted VOC incineration were substantially lower for more concentrated vapours. The factor b initially proposed for very “cold” plasmas showed to be quite constant in GlidArc-based VOC removal, which should facilitate its scale-up capabilities.

* * *

CHAPTER 6.

EXPERIMENTAL STUDY ON THE NON-THERMAL PLASMA DECOMPOSITION OF STOCHIOMETRIC GASEOUS HYDROCARBON MIXTURES

6.1 INTRODUCTION

The present work consists of two experimental approaches regarding the decomposition of low-concentration hydrocarbons in air under atmospheric conditions. During the first experimental approach, the principle of the gliding arc to completely decompose methane in air was applied, while the second experimental approach exploited the barrier discharge principle. The latter also included the development of a high-frequency power generator and several different discharge reactors. The previous chapter have given an introduction to different plasma processes and applications of such. As an introduction to the following chapter dealing with current experiments on discharge induced decomposition, I would like to point out that even nowadays, after more than a hundred years of research on the ozone generation process in the dielectric-barrier discharge and despite a great number of scientific publications put forth mostly in the last 40-50 years, the knowledge of these processes still appears to be insufficient to provide an adequate quantitative theoretical description for such systems. It means that, for example, to solve an optimization problem for the operating conditions of an discharge reactor, or to develop a new, more efficient type of reactor, it is still not possible to use a computer simulation technique instead of the hard way of empirical search. The reason for this is not the lack of computer code, but actually our poor understanding of the physics of electrical breakdown, initial and determining stage of the general discharge process.

The discharge in an dielectric-barrier discharge is well known to consist of a number of tiny filaments (micro discharges), where each of these may be considered as a small reactor, almost independent of each other. Therefore, the mechanism of single micro discharge coming into being, development, and decay has become and still remains a major research topic in the field of physical chemistry of a general electric discharge device.

The removal of low-concentration hydrocarbons from gas mixtures still remains one of the most difficult type of air pollution problems. Since hydrocarbons are oxidizable atmospheric pollutants, they can be removed by combustion to give carbon dioxide and water. If the concentration of the hydrocarbons in an oxidant mixture is sufficiently high, that is in the flammable region, the oxidation process will be self-supported if allowed to ignite. If the concentration of the hydrocarbons in the gas mixture is below the lower flammable limit, the oxidation process must be supported by special means. The usual practice is to burn off the low-concentration hydrocarbon mixture in a pilot flame. An extension of this technique is catalytic combustion. It has the advantage that oxidation on the catalyst surface can occur at lower concentration and temperature than in conventional combustion. However, the cost and gradual deactivation of the catalyst decrease the attractiveness of the method.

An alternative approach to conventional methods for the removing of hydrocarbons contained in atmospheric air or flue gas is to decompose (completely or partly) them in electric plasma devices. Several methods are being investigated. The high efficiency of high-voltage alternating current silent discharge plasmas for cleaning methane-polluted air has earlier been demonstrated by several authors. Corona discharges has also been used by many investigators for the removal of hydrocarbons in air, e.g. car exhaust.

Another approach is to convert the hydrocarbons to something more useful than just carbon dioxide and water. The partial oxidation of hydrocarbons in a plasma reactor involves gas-phase free-radical reactions. Various radicals and reactive molecules, e.g. OH, H, O, CH, CH_2, CH_3, etc. are generated in the plasma. A variety of products are produced through many competing reaction pathways. Among them, partial oxidation products are usually not favoured, because the intermediates leading to the partial oxidation products can be oxidized further to carbon oxides easily. In the case of methane, which dimerization reactions are more favourable than methane oxidation when CH_x species are present in the reaction system in high concentrations. Therefore, it is important

to control the free-radical reactions in the plasma reactor by controlling the experimental conditions so that reactions leading to the desired products are the major pathways.

6.2 DECOMPOSITION OF AIR/METHANE MIXTURES IN A GLIDING ARC DISCHARGE REACTOR

6.2.1 Introduction

The purpose of the experimental part was to gain general knowledge of the gliding arc concept and it's operation in general. Besides this, two different aspects with the gliding arc was investigated. The first one was to measure the amount of NO_x formed in pure air during normal operating conditions equivalent to the size of the reactor e.g. flow rate. The operating conditions are described later. The second part was to investigate the ability of the gliding arc to decompose methane in lean to stoichiometric air-methane mixtures with the purpose of either:

- Transforming the CH_4 to heavier hydrocarbons e.g. methanol or formaldehyde by a two pass plasma-quenching process
- Production of synthesis gas

  $$CH_4 + 2O_2 \rightarrow CO_2 + 2H_2O$$

  $$CH_4 + CO_2 \rightarrow 2CO + 2H_2$$

- Achieving complete decomposition to final products, CO_2 and H_2O

Compared with similar discharge devices, the gliding arc concept is known to produce conditions with characteristic electronic, vibrational and transitional temperatures in non-equilibrium regime of 1-2 *eV*, 3-5000 ^oK and 800-2000 ^oK, respectively. The gliding arc should therefore be able to process reasonably well, all the above listed chemical processes. Investigation on the gliding arc discharge process are currently being performed at:

- The University of Orléans, France, Faculty of Sciences, Laboratory of Plasmas (contact: Dr. A. CZERNICHOWSKI)
- The Department of Mechanical Engineering (M/C 251), University of Illinois at Chicago, High Temperature Laboratory Plasma and Combustion Research Group (Contact: Dr. A. Fridman)

- Russian Research Center “Kurchatov Institute”, Hydrogen Energy & Plasma Technology Institute (HEPTI), Laboratory of Theoretical Investigations.

To investigate the efficiency of the gliding arc discharge reactor to oxidize low concentration methane (2-8 *vol%*) in air, a series of decomposition experiments have been performed by measuring the final products emerging from the discharge reactor.

6.2.2 Experimental setup

The reactor was build around three knife-shaped pairs of discharge electrodes situated in an annular cylindrical vessel with a high velocity gas-intake situated in the centre root of the electrodes and the gas-outlet on the opposite cylinder end-wall. The reactor pressure was held at 1 *atm* by adjusting the pressure drop over the main flue gas exit. The residence time for the gas passing through the reactor was calculated from the ratio of the reactor volume (V_{REAC}) to the gas flow rate (Q):

$$t_{residence} = V_{REAC} / \dot{Q} \qquad \textbf{Eq. 6-1}$$

and ranged from 1.36 to 15 *s*.

Besides several initial experiments, three sets (set 1a-3a) of experiments were performed with pure air (tot. of 27 exp. with pure air) and five sets (set 1b-5b) of experiments in air/methane mixtures (tot. of 27 exp. with air/CH_4 mixtures). Each set consists of a series of experiments with varying air or mixture flowrate (= residence time).

The experimental reactor

The reactor is illustrated in figure 6-1 and pictured in figure 6-3. It consisted of an annular cylindrical vessel in which the discharge was run in the innermost cylinder. The volume of the reactor was 2.5 *l*. A 2 *mm* nozzle was situated at the cylinder entrance. Mixture temperatures were measured with a mercury thermometer just before the inlet nozzle. The airstream was either lead through the annular space and thereby preheated up to between 130 and 260 ^{o}C depending on the flow rate, or taken directly from the ambient surroundings at room temperature of 20 ± 1 ^{o}C. The air was then mixed with the methane stream before entering the reactor through the nozzle.

Both the air- and the methane flows were controlled by mass flow controllers. The mixture inlet temperature and the reactor gas temperature and pressure were measured. To

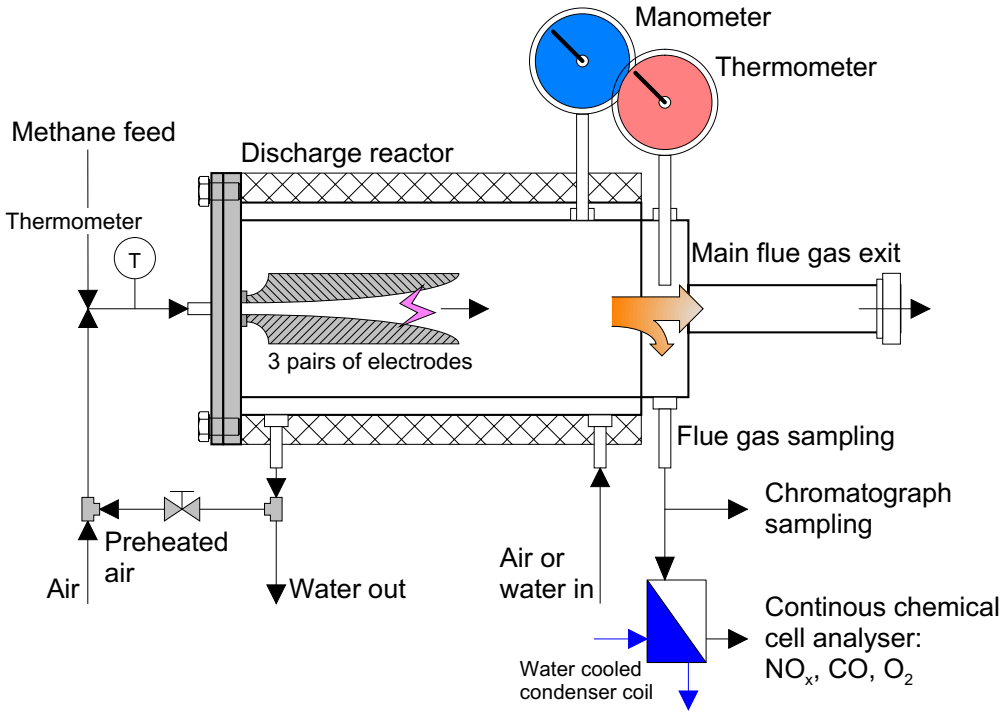

Figure 6-1: Schematic experimental setup.

minimize heat loss to the surroundings, the reactor was isolated on the outside with 2.5 *cm* rockwool.

The power supply and the plasma reactor

Inside the vessel three pairs of the knife-shaped electrode blades were symmetrically placed around the inlet nozzle, forming three 120 ^{o} spaced electrode planes. The shortest distance between the knife-shaped electrode was 3 *mm*, the longest one was about 10 *mm*. The electrodes were supplied form an AC 3-phase 50 *Hz* high-voltage power supply. The high-voltage was supplied by three high-voltage transformers in parallel ($\overline{V}$ = 384 *V*) giving a arc current of approximately $I_{arc} = (I_1 - I_0) \times 1/20$ (see figure 6-2). For the three transformers in parallel, the arc power is given as the input-power minus the transformer loss ($P_{loss} \approx 980$ *W*) as described by: $P_{primary} - P_{loss} = 3 \times I_2 \times V_{arc}$.

The principle of the gliding discharge has been illustrated in a previous section (chapter 5.4.6 and chapter 5.5.5). After the voltage has been switched on, an arc is formed between

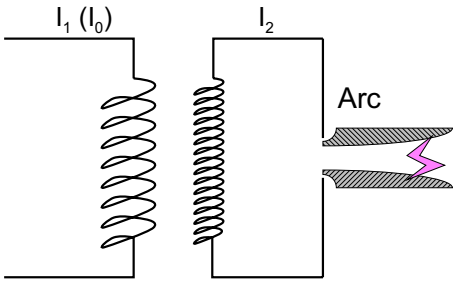

$I_{arc} = (I_1-I_0)\times 1/20$

I_0 = current without the secondary coil

$P_1-P_{loss} = 3 \times I_2 \times U_{arc}$

P_{loss} = 980 W (when all three transformers are used)

Figure 6-2: Power supply.

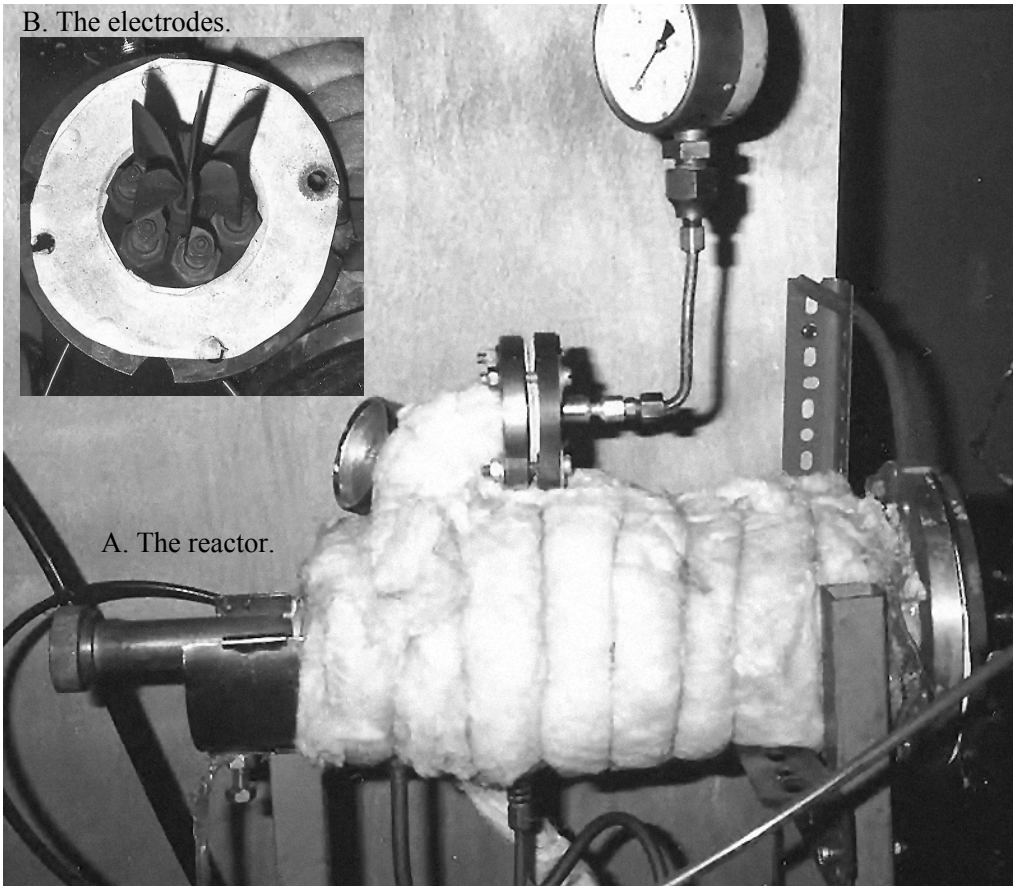

Figure 6-3: The reactor and the electrodes.

two opposite electrodes. The arc strikes where the distance between the electrodes is the shortest. Due to the fast gas flow of the operating gas (> 10 *m/s*) and the diverging form of the electrodes, the discharge moves (or "glides") along the electrodes in the direction of the gas flow until it extinguishes and a new arc is formed in a position defined by the parameters of the power supply, nature of the gas, gas flow rate and electrode geometry. The lifetime of a discharge is a few milliseconds. Several discharges are present at the same time because of the electrical phase shift at this multi-electrode system. This makes it possible to cover a large part of the inter-electrode space with discharges, increasing thus the efficiency of discharge interaction with the process gas.

Instrumentation of the rig

During all experiments the flue gas was continuously sampled with a portable chemical cell analyser of type TESTO 33. The analyser was equipped for continuous measuring of the three components, NO_x, CO and O_2 respectively. The measurement principle is based on chemical cell analysis, where each component is led through an electrochemical cell and thus initiating a reaction. The amount of a specific product formed by this reaction is then compared with a preset value. The ratio of the preset value to the measured then gives the concentration of the initial component. Some technical data for the instrument are given in table 6-1.

Table 6-1: Technical data for the chemical cell analyser, TESTO 33.

Measurement	**Spec.**
O_2 measurement	
Meas. range	0 to 21 *vol. %*
Accuracy	± 0.2 *vol. %* absolute
Resolution	0.1 *vol. %*
CO measurement (with H_2 compensation)	
Meas. range	0 to 8000 *ppm*
Resolution	1 *ppm*
NO measurement	
Meas. range	0 to 3000 *ppm*

The composition of the flue gas could additionally be sampled, by using evacuated

glass flasks, for analysis by gas chromatography. The chromatograph used a catharometer or flame ionization detector to measure the amounts of O_2, N_2, CO_2, CO and hydrocarbons in the flue gas.

The volume flow for both the air and the methane was controlled by mass flow controllers. For air, an AIR-LIQUID mass flow controller was used. For methane, a 4 channel TYLAN RO-28 0.01-200 *l/min*, was used. The mixture inlet temperature and the reactor gas temperature and pressure were measured. The mixture inlet temperature was measured with a mercury thermometer just before the inlet nozzle.

6.2.3 Results and discussion

In the experiments that involved only pure air, ambient air either at room temperature or preheated in the annular reactor was passed through the discharge reactor. The main purpose of running the reactor with pure air was to establish reference levels for the amount of NO_x produced at varying flow rates for both air- and water-cooled reactor annular (corresponding to preheated air or air at room temperature). Three sets of experiments were run, with a total of 27 experiments. The reactor was either water-cooled or air-cooled when used either with ambient air at room temperature or ambient preheated air, respectively.

Following the pure-air experiments, air/methane mixtures were processed. Five sets of experiments were performed, were the lowest and highest molar percentage of CH_4 was 2 and 8 *vol%*, respectively. Also here the reactor was either air- or water-cooled. During the first and second set, ambient air preheated in the annular reactor was mixed with methane before entering the reactor. Both sets used mixtures containing 2 *vol%* methane. In the third set ambient air at room temperature was mixed with methane to give a 2.6 *vol%* mixture. The fourth and fifth set was performed with ambient preheated air and air at room temperature with mixtures containing 3 and 2-8 *vol%* methane, respectively. During all five sets, a chemical cell analyser (TESTO 33) was used to measure the concentration of NO_x, CO and O_2 in the flue gas. During the first, fourth and fifth set, the composition of the flue gas was additionally measured by gas chromatography.

Measurements in pure air

Three sets of pure air experiments were performed. The conditions for these measurements are listed in table 6-2 with corresponding results in table 6-3 (and in

APPENDIX E). In the experiments that involved only pure air, ambient air either at room temperature or preheated in the annular reactor was passed through the discharge reactor. Due to the combination of the electric heat induction and the production of reactive species in the discharge, significant quantities of NO_x was formed. Preliminary measurements done with dräger tubes showed that with an air flow rate of 10 *l/min* (residence time, $\tau = 15$ *s*), NO_x concentrations in the order of 1000 to 1500 *ppm* could be expected.

Table 6-2: Conditions for measurements with pure air.

Set	Mixture	Method	Measured	Flow meter	Comments	Number of exp.
1a	Pure air	Chemical cell analyser	O_2 <vol%> NO_x <ppm> $T_{reactor}$ <degC> $T_{mixture\ in}$ <degC> P <kW>	AIR-LIQUID	Air preheated in annular reactor	7
2a	Pure air	Chemical cell analyser	O_2 <vol%> NO_x <ppm> $T_{reactor}$ <degC> $T_{mixture\ in}$ <degC> P <kW>	AIR-LIQUID	Air preheated in annular reactor	11
3a	Pure air	Chemical cell analyser	O_2 <vol%> NO_x <ppm> $T_{reactor}$ <degC> P <kW>	AIR-LIQUID	Ambient air with water-cooled reactor	9

The presence of ozone was also detected and measured to be ≥ 300 *ppm*, although these measurements may have been influenced by other similar species present in the flue gas. Further measurements with the chemical cell analyser, confirmed that significant quantities of NO_x was formed when the discharge was run in pure air, the maximum concentration being achieved at the lowest flow-rate. The results from the pure air experiments are shown in figure 6-4 and figure 6-5. Two different reactor configurations were used. The first two sets (1a and 2a) were run with air preheated in annular reactor (air cooled reactor) while the last set (3a) was run with air at room temperature being passed through a water cooled reactor. As can be seen, the difference in both oxygen concentration and produced NO_x for the two reactor configurations are very small. For all three sets, the NO_x concentrations levelled out at around 3300 *ppm* even when the residence time was increased beyond 4 s (37.5 *l/min*). The reason for this was most

Table 6-3: Experiments on pure air.

Species and variables measured for different configurations with pure air.

	Chromatograph						Chemical cell analyser						
	ResTime <s>	O_2 <vol%>	CH_4 <vol%>	CO_2 <vol%>	CO <vol%>	CH_4 conv. <%>	O_2 <vol%>	CO <ppm>	CO <vol%>	NO_x <ppm>	Treactor <degC>	Tmixture in <degC>	P <kW>
Set 1a	**Pure air (1)**						**Air preheated in annular reactor**						
	ResTime <s>	O_2 <vol%>	CH_4 <vol%>	CO_2 <vol%>	CO <vol%>	CH_4 conv. <%>	O_2 <vol%>	CO <ppm>	CO <vol%>	NO_x <ppm>	Treactor <degC>	Tmixture in <degC>	P <kW>
	7.14						20.00			3 334	312	165	1.87
	4.84						20.30			3 352	325	210	1.90
	3.66						20.40			2 917	325	226	1.93
	2.94			No chromatograph samples taken!			20.50			2 587	325	225	1.92
	2.42						20.60			2 280	318	212	1.90
	2.08						20.60			2 067	305	202	1.92
	1.83						20.60			1 895	298	190	1.93
	-						21.00						
Set 2a	**Pure air (2)**						**Air preheated in annular reactor**						
	ResTime <s>	O_2 <vol%>	CH_4 <vol%>	CO_2 <vol%>	CO <vol%>	CH_4 conv. <%>	O_2 <vol%>	CO <ppm>	CO <vol%>	NO_x <ppm>	Treactor <degC>	Tmixture in <degC>	P <kW>
	7.50						20.10			3 336	325	210	1.92
	7.50									3 312			
	5.00									3 150			
	3.75						20.40			3 189	325	229	1.93
	3.75									2 700			
	3.00									2 424			
	2.50			No chromatograph samples taken!			20.70			2 676	288	192	1.93
	2.50									2 426			
	2.14									1 730			
	1.88						20.73			2 358	268	168	1.92
	1.50						20.80			2 170	230	140	1.93
	-						21.00						
Set 3a	**Pure air (3)**						**Ambient air with water-cooled reactor**						
	ResTime <s>	O_2 <vol%>	CH_4 <vol%>	CO_2 <vol%>	CO <vol%>	CH_4 conv. <%>	O_2 <vol%>	CO <ppm>	CO <vol%>	NO_x <ppm>	Treactor <degC>	Tmixture in <degC>	P <kW>
	7.50						19.95			3 297	280		2.05
	3.75						20.30			3 265	250		2.03
	3.00						20.40			2 986	240		2.02
	2.50						20.50			2 666	230		2.00
	2.14			No chromatograph samples taken!			20.50			2 476	225		1.96
	1.88						20.60			2 257	220		1.92
	1.67						20.60			2 091	205		1.90
	1.50						20.60			2 014	180		1.90
	1.36						20.70			1 876	153		1.85
	-						21.00						

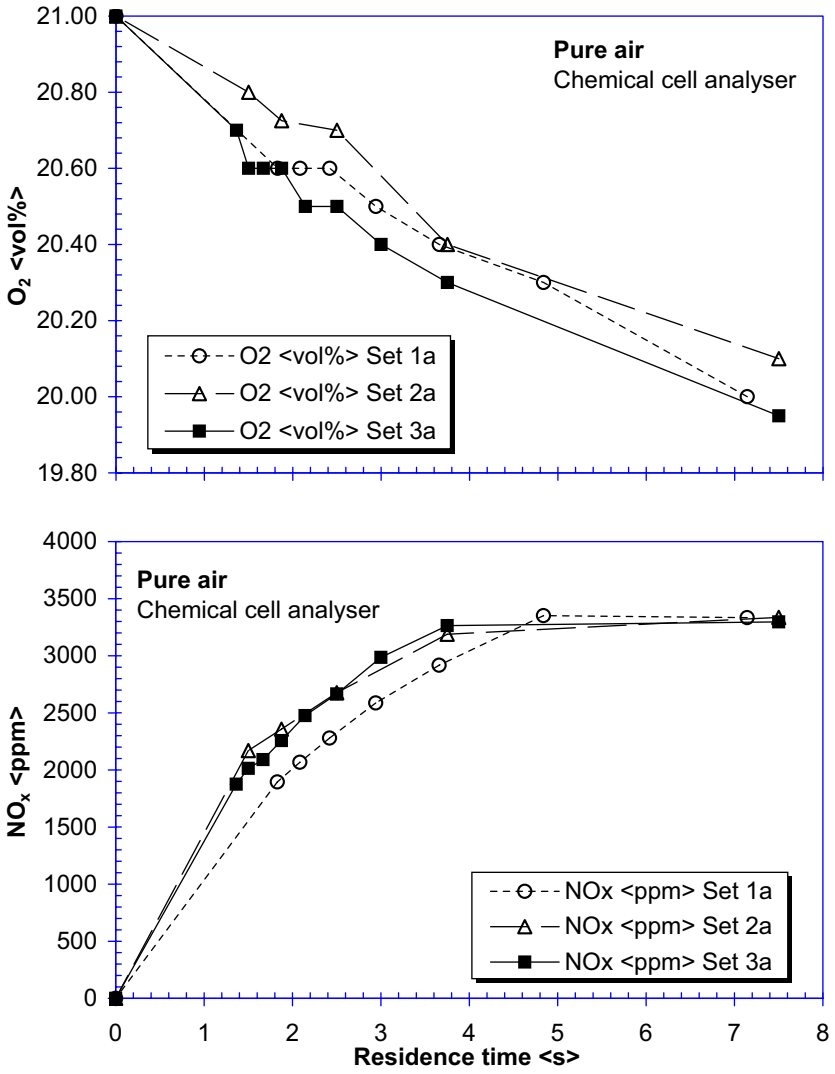

Figure 6-4: Pure air, O_2 and NO_x concentrations in flue gas.

O_2 and NO_x concentrations in flue gas as a function of residence time. Set 1a and 2a are for pure air with air preheated in annular reactor. Set 3a is for pure air at ambient temperature and water-cooled reactor as in table 6-3.

certainly caused by the chemical cell analyser being saturated when passing its upper range limit of 3000 *ppm* NO_x. The actual NO_x concentrations for the highest residence times were therefore probably higher. At the same time the O_2 concentrations showed a continues, almost linear decreasing trend up to even the highest residence times.

Although the gliding arc operation was highly unstable, the average electric input

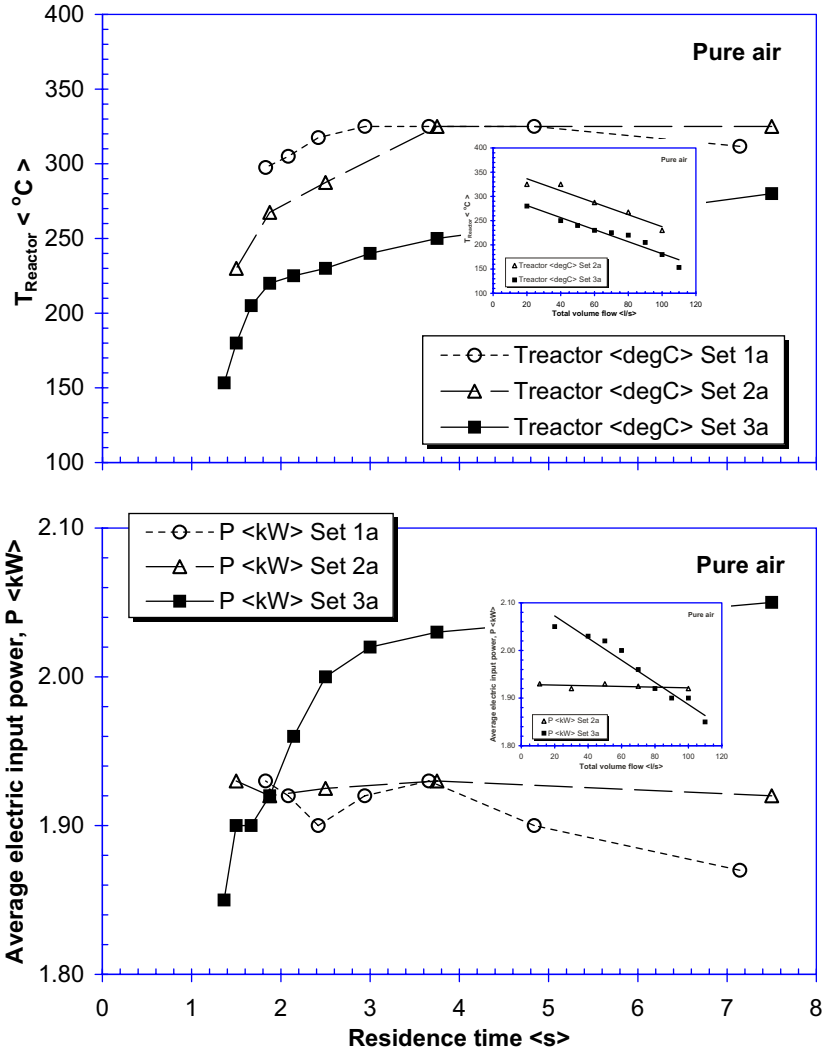

Figure 6-5: Pure air, reactor temperature and power.

Reactor temperature, $T_{reactor}$ <°C>, and average electric input power, P <kW>, as a function of residence time with conditions as given in table 6-3. Inlaid charts show the same variables as a function of flowrate in *l/min* (see eq. 6-1).

power readings showed a dependent behaviour on residence time and reactor configuration. Figure 6-5 shows the average electric input power as a function of residence time. For the two sets were preheated air was used (air-cooled reactor), the average electric input power showed only small variation with residence time. When ambient air at room temperature was used (water-cooled reactor, set 3a) the input power

rapidly increased from 1.85 *kW* at 1.4 *s* residence time before it levelled out at around 2 *kW* and 3 *s* residence time.

The reactor temperature was measured for all configurations but was not always as consistent in its dependence on electric input power as expected. This was probably caused by the large reactor mass, resulting in a system quite resistant to thermal changes. When the reactor was water-cooled the system became even more thermal resistant, and at least 30-45 *min* was required to reach stable conditions. Figure 6-5 also illustrates the somewhat linear variation (inlaid charts) with air flow rate for both reactor temperature and average electric input power.

Measurements in air-methane mixtures

Following the pure-air experiments, air/methane mixtures were processed. The purpose of running the air/methane mixture through the discharge reactor was to examine the characteristics of the methane decomposition and the amount of NO_x produced. The conditions for these measurements are listed in table 6-4 with corresponding results in table 6-5 (and in APPENDIX E). Methane mixed with air was reduced in the gliding discharge reactor mainly to CO_2 and CO as showed in figure 6-6 and figure 6-7 for 2 and 3 *vol%* CH_4 in air. Water, presumably containing negligible amounts of heavier hydrocarbons and reaction products, was observed to produce from the condenser outlet but was not quantified.

The CH_4 conversion rate was observed to increase with increasing residence time in the reactor (decreasing flow rate). To obtain a 90 % molar reduction with 2 *vol%* CH_4 in air, we can see from figure 6-8, that a residence time of approximately five seconds would be required with the conversion given as:

$$\text{Conversion} = \frac{[CH_4]_{in} - [CH_4]_{out}}{[CH_4]_{in}} \cdot 100\% \qquad \textbf{Eq. 6-2}$$

Comparing the results for the 2 and 3 *vol%* (figure 6-8) mixtures, we can observe that the CH_4 conversion is a little faster for the 3 *vol%* mixture. This corresponds to the results obtained by Czech, Czernichowski and Mizeraczyk (1994) with a similar reactor. With CH_4 concentrations in the range 0.98-2.93 *vol%* they found that the CH_4 conversion increased with increasing CH_4 concentration. However, the reason for this could not be

Table 6-4: Conditions for measurements in air-methane mixtures.

Set	Mixture	Method	Measured	Flow meter	Comments	Num of exp.
1b	2 vol% methane in air	Chemical cell	Chemical cell: T_{react}, $T_{air\ in}$, T_{gu}, T_g, O_2, CO, NO_x, P	TYLAN (Read): air/CH_4 = 0.72 AIR-LIQUID (Reg.)	Air preheated in annular reactor before being mixed with methane just before inlet nozzle.	7
2b	2 vol% methane in air	Chemical cell & Chrom.	Chemical cell: T_{react}, $T_{air\ in}$, T_g, O_2, CO, NO_x Chrom.: CH_4, C_2H_6, CO_2, CO, O_2, N_2	TYLAN (Read): air/CH_4 = 0.72 AIR-LIQUID (Reg.)	Air preheated in annular reactor before being mixed with methane just before inlet nozzle.	4
3b	2.6 vol% methane in air	Chemical cell	Chemical cell: O_2, CO, NO_x	TYLAN (Read): air/CH_4 = 0.72 AIR-LIQUID (Reg.)	Air at room temperature was mixed with methane just before inlet nozzle.	3
4b	3 vol% methane in air	Chemical cell & Chrom.	Chemical cell: T_{react}, $T_{air\ in}$, T_g, O_2, CO, NO_x Chrom..: CH_4, C_2H_6, CO_2, CO, O_2, N_2	TYLAN (Read): air/CH_4 = 0.72 AIR-LIQUID (Reg.)	Air preheated in annular reactor before being mixed with methane just before inlet nozzle. Five samples were taken. Sample No. 2 taken as reference for same conditions as sample 1, with no discharge running.	4
5b	2-8 vol% methane in air	Chemical cell & Chrom.	Chemical cell: T_{react}, T_g, O_2, CO, NO_x Chrom.: CH_4	TYLAN (Read): air/CH_4 = 0.72 AIR-LIQUID (Reg.)	Air at room temperature was mixed with methane just before inlet nozzle (water-cooled reactor). Only hydrocarbons were measured with chromatography. Produced gas observed to have a yellow- brownish colour. After some minutes in the glass bulb, this colour disappeared slowly. Liquid was formed during the experiment having a deep green colour. The current and power was unstable during the whole experiment.	9

Table 6-5: Experiments on air-methane mixtures.

Species and variables measured for different configurations with air-methane mixtures.

	Chromatograph						Chemical cell analyser							
ResTime <s>	O_2 <vol%>	CH_4 <vol%>	CO_2 <vol%>	CO <vol%>	CH_4 conv. <%>		O_2 <vol%>	CO <ppm>	CO <vol%>	NO_x <ppm>	Treactor <degC>	Tmixture in <degC>	P <kW>	
Set 1b	**2 vol% methane in**						**Air preheated in annular reactor**							
ResTime <s>	O_2 <vol%>	CH_4 <vol%>	CO_2 <vol%>	CO <vol%>	CH_4 conv. <%>		O_2 <vol%>	CO <ppm>	CO <vol%>	NO_x <ppm>	Treactor <degC>	Tmixture in <degC>	P <kW>	
7.35	15.60	0.01	2.00	0.21	99.5		15.10	2 934	0.29	2 207	410	156	1.97	
4.90	16.50	0.15	1.86	0.52	92.5		15.93	5 890	0.59	2 086	372	241	1.98	
3.67	16.90	0.42	1.70	0.61	79.0		16.45	7 104	0.71	2 219	370	262	1.97	
2.94	17.50	0.63	1.42	0.67	68.5		16.95	7 709	0.77	1 957	368	253	1.95	
2.45	17.70	0.99	1.20	0.80	50.5		17.25	7 968	0.80	1 778	352	235	1.94	
2.10	18.10	1.17	1.10	0.76	41.5		17.60	7 898	0.79	1 630	313	191	1.93	
1.84	18.50	1.26	0.90	0.60	37.0		17.85	7 292	0.73	1 554	250	130	1.96	
-	20.50	2.00	-	-	-		20.50	-	-					
Set 2b	**2 vol% methane in**						**Air preheated in annular reactor**							
ResTime <s>	O_2 <vol%>	CH_4 <vol%>	CO_2 <vol%>	CO <vol%>	CH_4 conv. <%>		O_2 <vol%>	CO <ppm>	CO <vol%>	NO_x <ppm>	Treactor <degC>	Tmixture in <degC>	P <kW>	
3.67							16.75	5 423		3 348	370	236		
2.45							17.30	6 223		2 916	315	187		
1.84			No chromatograph samples taken!				17.88	6 918		2 116	324	202		
1.47							17.90	6 921		1 761				
-							20.50	-						
Set 3b	**2.6 vol% methane in**						**Ambient air**							
ResTime <s>	O_2 <vol%>	CH_4 <vol%>	CO_2 <vol%>	CO <vol%>	CH_4 conv. <%>		O_2 <vol%>	CO <ppm>	CO <vol%>	NO_x <ppm>	Treactor <degC>	Tmixture in <degC>	P <kW>	
3.75							18.40	4 746		2 574				
3.00			No chromatograph samples taken!				18.60	4 858		2 185				
2.50							18.80	4 672		1 968				
-							20.50	-						
Set 4b	**3 vol% methane in**						**Air preheated in annular reactor**							
ResTime <s>	O_2 <vol%>	CH_4 <vol%>	CO_2 <vol%>	CO <vol%>	CH_4 conv. <%>		O_2 <vol%>	CO <ppm>	CO <vol%>	NO_x <ppm>	Treactor <degC>	Tmixture in <degC>	P <kW>	
2.42	15.80	1.30	2.10	1.10	56.7		14.95	11 417	1.14	1 826	365	220		
2.08	16.30	1.60	1.70	1.10	46.7		15.60	11 198	1.12	1 627	325	200	2.00	
1.82	16.10	1.55	1.80	1.50	48.3		15.53	12 732	1.27	1 490	360	230		
1.62	16.80	1.81	1.50	1.20	39.7		16.13	11 347	1.13	1 347	360	230		
-	20.40	3.00	-	-	-		20.40	-	-		350	210	2.11	
Set 5b	**2 - 8 vol% methane in**						**Ambient air with water-cooled reactor**							
ResTime <s>	O_2 <vol%>	$CH_{4\ out}$ <vol%>	$CH_{4\ in}$ <vol%>		CH_4 conv. <%>		O_2 <vol%>	CO <ppm>	CO <vol%>	NO_x <ppm>	Treactor <degC>	Tmixture in <degC>	P <kW>	
14.08	6.00	0.00	6.00		99.9		7.50	1 671		3 295	410		1.98	
9.80	2.00		2.00				16.50	2 826		3 301	335		2.00	
9.59	4.00	0.19	4.00		95.3		12.20	5 401		3 300	353		2.01	
9.39	6.00		6.00				7.20	4 911		3 297	388		2.03	
9.17	8.00	0.10	8.00		98.8		2.00	6 307		2 783	420		2.05	
7.35	2.00	0.36	2.00		82.0		16.85	3 341		3 219	345		2.02	
7.27	3.00	0.41	3.00		86.3		14.93	5 058		3 235	373		1.99	
7.19	4.00	0.33	4.00		91.8		12.63	6 928		3 184	393		1.96	
7.04	6.00	0.07	6.00		98.8		7.25	6 983		3 283	408		1.95	

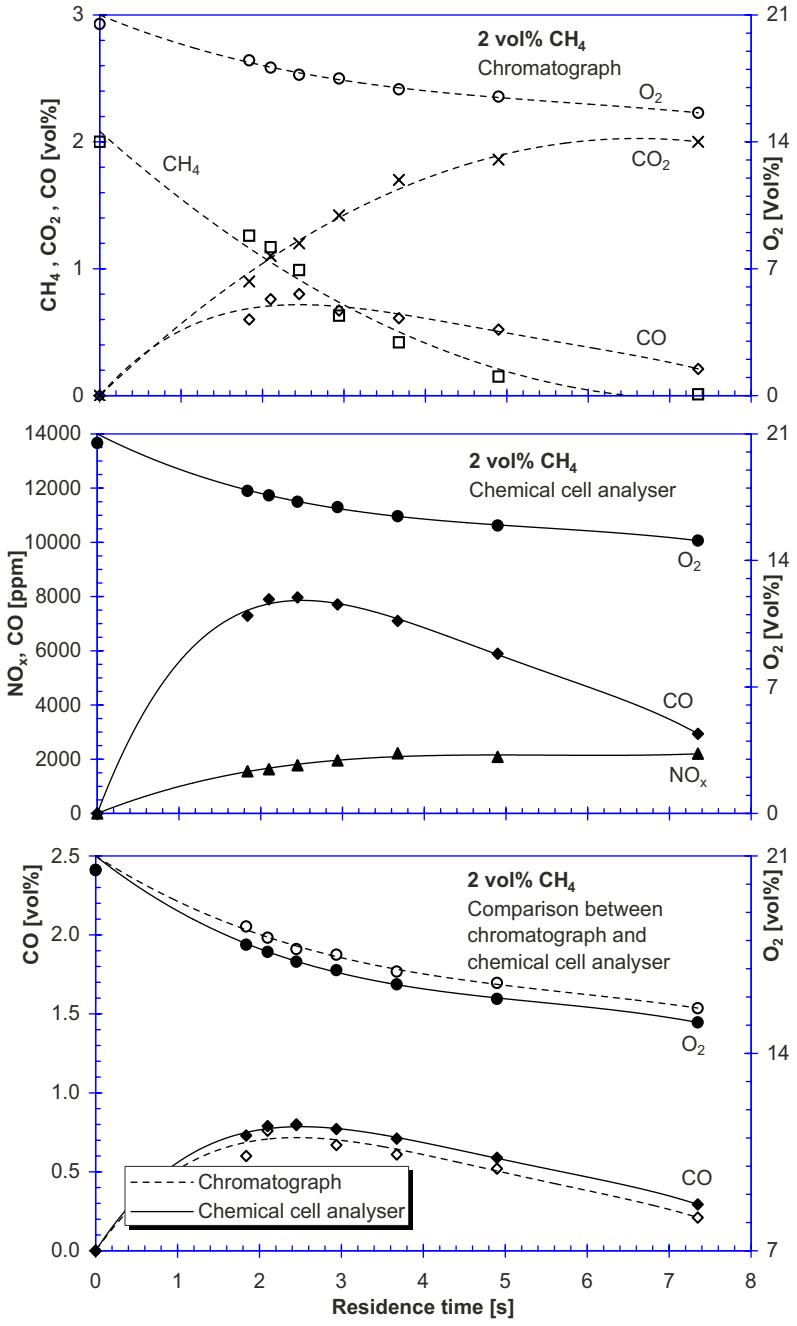

Figure 6-6: 2 *vol%* CH_4 in air.

Concentration of CH_4, CO_2, CO, O_2 and NO_x in dry flue gas as a function of residence time for the 2 *vol%* air/methane mixture measured with chromatography and chemical cell analyser. All lines are polynomial fits for the corresponding series.

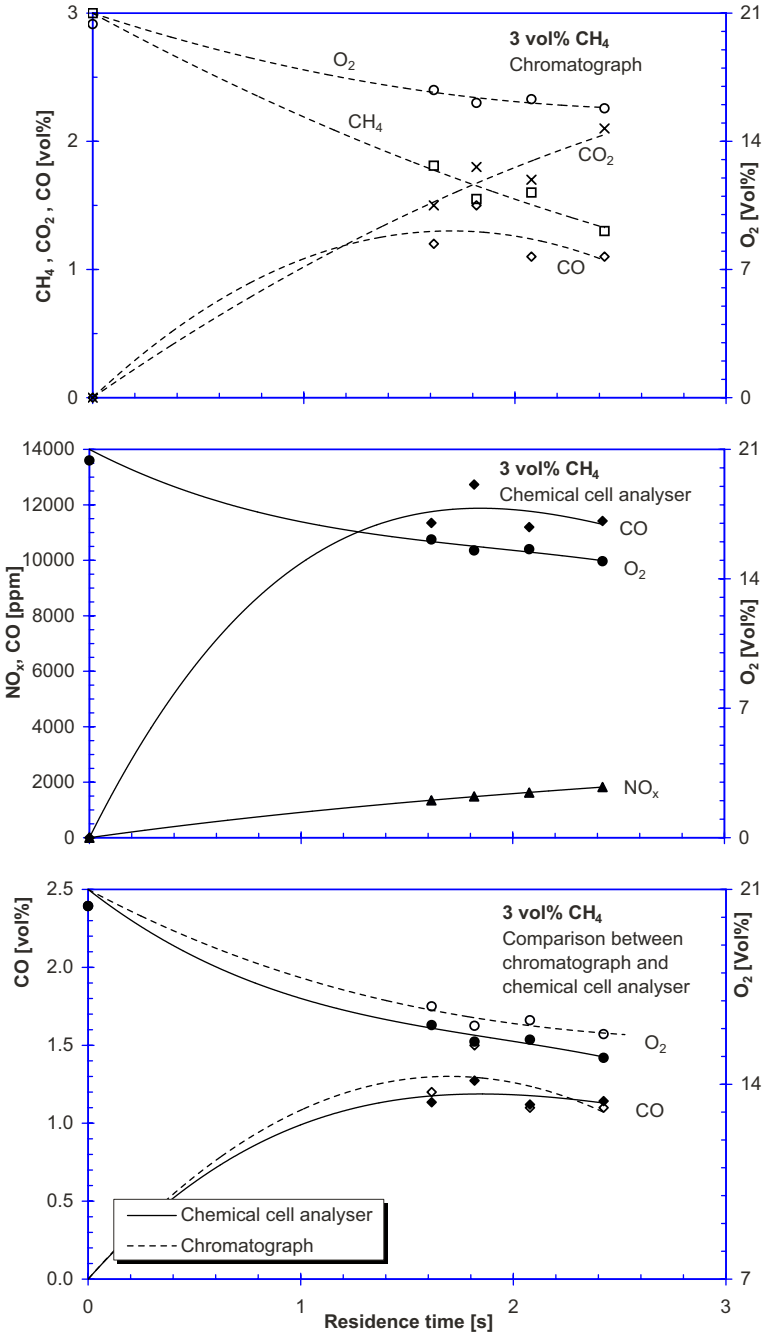

Figure 6-7: 3 *vol%* CH_4 in air.

Concentration of CH_4, CO_2, CO, O_2 and NO_x in dry flue gas as a function of residence time for the 3 *vol%* air/methane mixture measured with chromatography and chemical cell analyser. All lines are polynomial fits for the corresponding series.

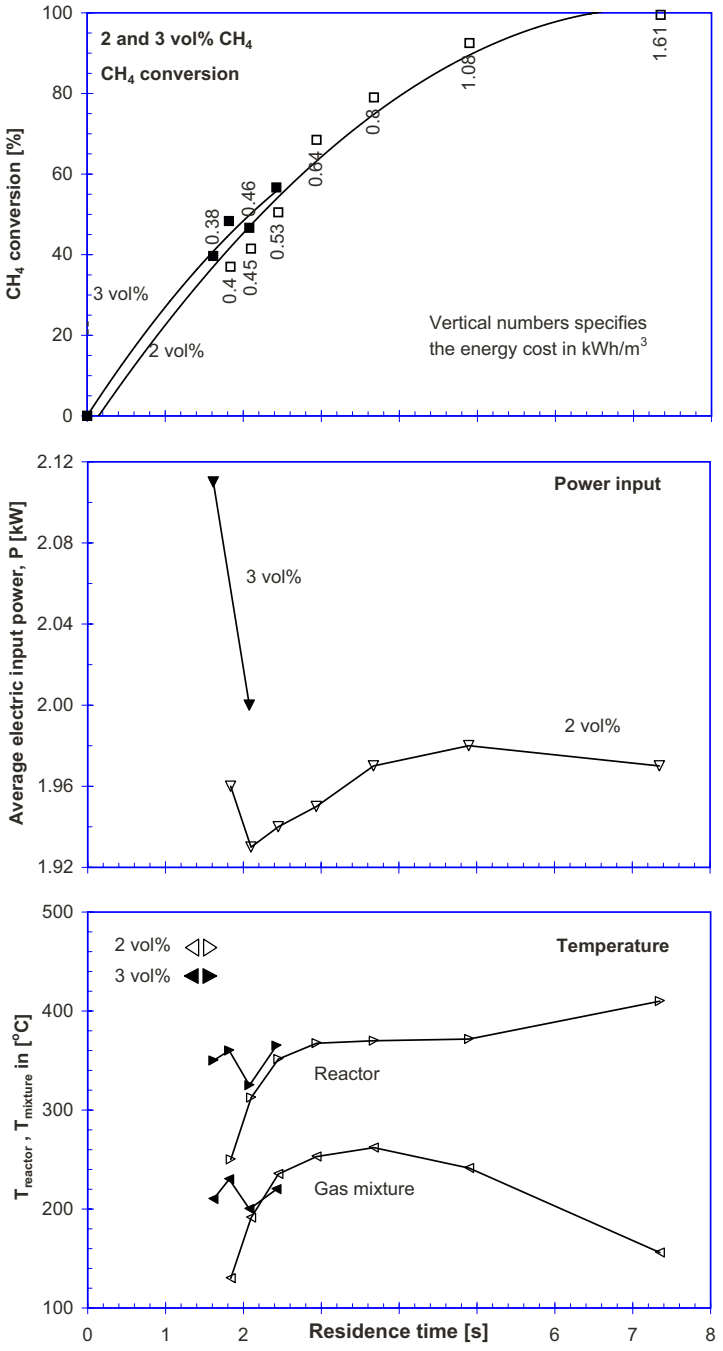

Figure 6-8: Conversion, Power and Temperature vs residence time.

CH_4 conversion, power input, P (*kW*), reactor- and mixture temperature, T_r and T_m in (^oC), as a function of residence time (*s*) in reactor. Comparison between 2 and 3 *vol %* CH_4 in air.

explained.

Besides the chromatography analysis, the final products from the reactor was continuously sampled through a 4 *m* long silicone hose to a chemical cell analyser, by a built-in pump in the apparatus. The results for the 2 and 3 *vol%* methane in air are shown in figure 6-6 and figure 6-7 for the NO_x, CO and O_2 concentration. The bottom charts in the same figures illustrates the different values obtained for CO and O_2 concentration when measured with either the chemical cell analyser or by chromatography. For the mixtures with 2 and 3 *vol%* CH_4 in air (set 1b and 4b, respectively), the difference in produced NO_x was insignificant. The right chart in figure 6-9 indicates that nearly equal amounts of NO_x was formed in the flue gas when processing mixtures of air and 2 to 3 *vol%* CH_4 at residence times up to 3 s.

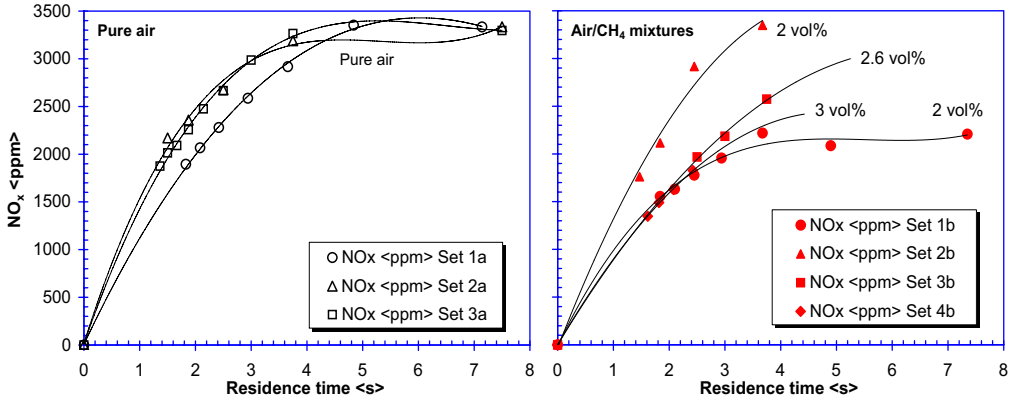

Figure 6-9: Comparison of NO_x production in air and air/CH_4 mixtures.

NO_x (*ppm*) concentration as a function of residence time (*s*) for pure air and air/methane mixtures. All lines are polynomial fits for the corresponding series.

The few experiments performed at higher residence times with air/methane mixtures indicate that the NO_x concentration will flatten off at levels between 2000-3000 ppm, depending on the different experimental conditions. The reason for the high NO_x concentrations for set 2b (2 *vol%* CH_4) cannot be justified neither by reactor configuration nor by the CH_4 content. Compared with experiments on pure air (figure 6-9, left chart), air/methane mixtures seems to produce less NO_x and at lower rates.

As for the measurements in pure air (air-cooled configuration) the average electric

input power for 2 *vol%* CH_4 (set 1b) in air slightly increased with residence time. The input power first decreased until a given residence time was reached (figure 6-8). From this on-set condition, the power then appeared to increase with increasing residence time, to stabilize at higher residence times. The mean power over all residence times was 1.96 *kW*, which is slightly higher than for the pure air configuration at 1.91 *kW*. For the 3 *vol%* mixture only two points are available because the power was too unstable to provide reasonable readings. For comparison, Czech, Czernichowski and Mizeraczyk (1994) measured an average power consumption of 1.11 *kW* for a CH_4 concentration of 1.98 *vol%*. The lower power consumption might be explained by the difference in reactor construction and the use of an internal fluegas recirculation chamber.

Also from figure 6-8, the reactor temperature can be seen first to increase at increasing residence times. The following decrease in temperature at higher residence times was probably because the reactor was not given enough time to reach steady state conditions before the temperature readings were taken.

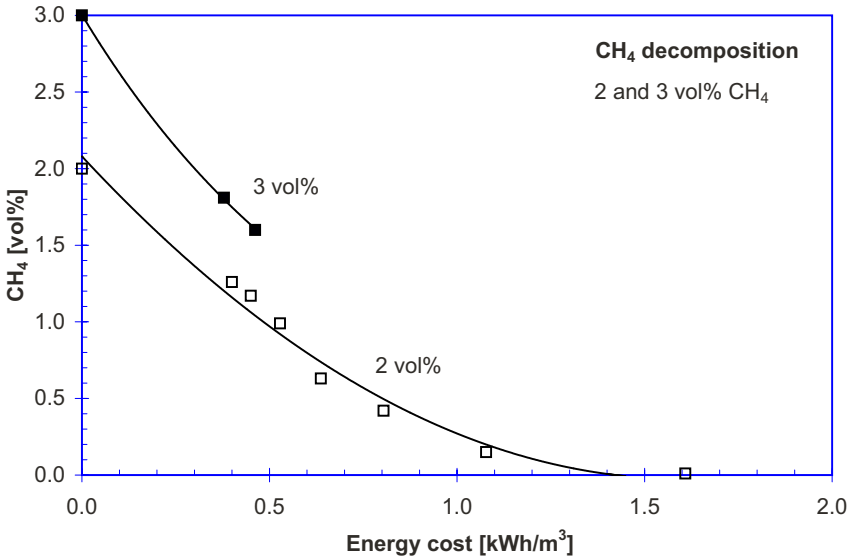

Figure 6-10: Specific energy cost for 2 and 3 *vol%* CH_4 in air.

Figure 6-10 illustrates the calculated specific energy cost (*kWh/m*^{3} mixture) for 2 and 3 *vol%* CH_4 in air. From this figure we can see that to achieve complete decomposition of CH_4 in 1 m^3 of the 2 *vol%* mixture, the energy cost is about 1.5 *kWh*. The figure also indicates that the higher the CH_4 concentration is in the initial mixture, the more energy is

needed for complete decomposition. However, a relative CH_4 reduction in either mixture seems to require about the same amount of energy.

For the last set of experiments (set 5b), the CH_4 concentration was varied between 2 and 8 *vol%* CH_4 while the residence time was held quite high. In figure 6-11, the calculated values for the conversion of CH_4 are shown for all the experiments (set 1b-5b). Because of the overall high residence time for all the experiments in set 5b, the conversion is quite high for all the CH_4 mixtures. The numbers enclosed in the symbols on figure 6-11 indicates the *vol%* CH_4 in the mixture.

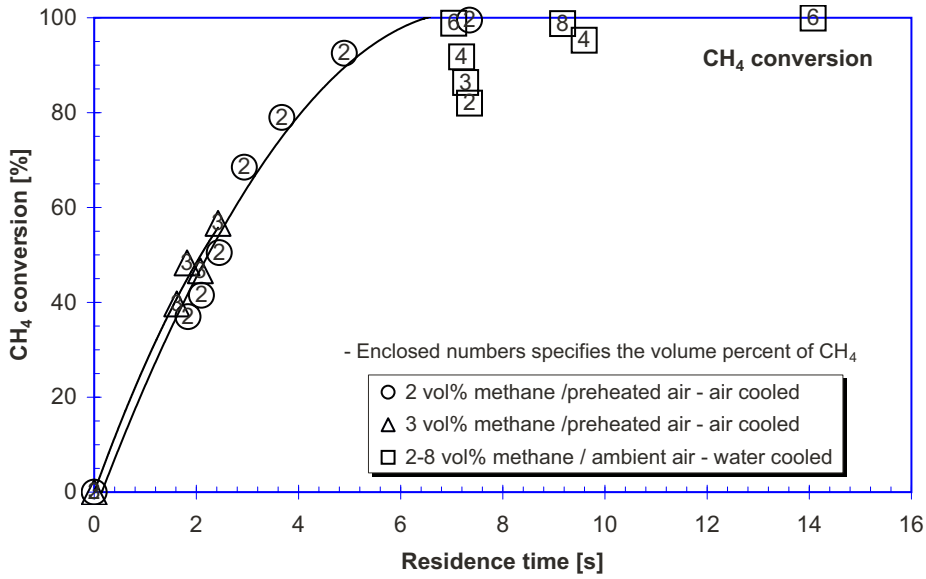

Figure 6-11: Conversion for all air/CH_4 mixtures.

Although the lower and upper flammability limits for CH_4 in air is 5 and 15 *vol%*, respectively, with a stoichiometric value of 9.47 *vol%*, there was no abrupt change in any of the measured values when the lower limit was passed. During these experiments rapid pulsed combustion was observed with flue gases expanding out through the main outlet in front, causing a rapid increase in pressure. This phenomena was only observed for mixtures in the flammable region. It was observed that when the CH_4 concentration exceeded the lower flammability limit, significant quantities of condensate was formed having a sharp green colour and a smell of hydrocarbons and formaldehyde. The green

colour most probably originate from a reaction between the copper tube and the condensate. Solid black carbon also was observed in the liquid. However, the liquid was not analysed. The amount of produced NO_x for all these experiments exceed the upper measurable limit for the chemical cell analyser, with values between 3200-3300 *ppm*.

Only negligible quantities of heavier hydrocarbons were produced, or at least measurable in the gaseous samples for the chromatography. The only time traces of heavier hydrocarbons were detected (0.003-0.04 *vol%* C_2H_6) was for the 3 *vol%* mixture at highest flow rate (80-90 *l mixture*/*min*).

Previous results obtained by Czech, Czernichowski and Mizeraczyk (1994) with a similar reactor are shown for comparison in figure 6-12 and figure 6-13. They investigated combustion of very lean methane-air mixtures (1 to 3 *vol%* CH_4), corresponding to coalmine exhausts) in an electro-burner built on the principle of gliding electrical discharges. The experiments were performed using either dry or wet methane-air mixtures initially at ambient temperature or preheated to 180 ^oC. The flow rate and pressure of the operating gas mixture was up to 120 *slm* and from 1 to 5 *bars*, respectively. They achieved almost complete decomposition of the methane for certain operational parameters.

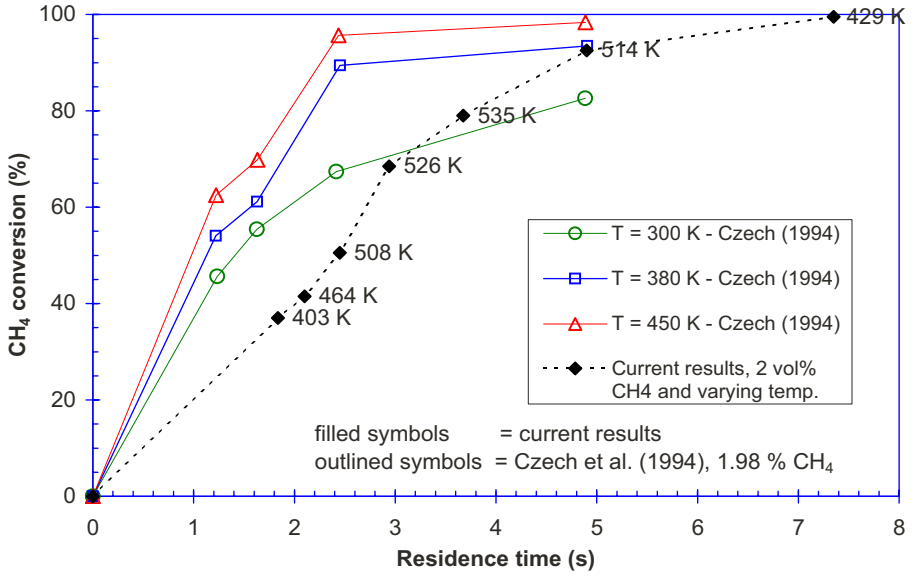

Figure 6-12: Comparison of results for CH_4 conversion.

The current experiments showed that the CH_4 conversion increased with increasing

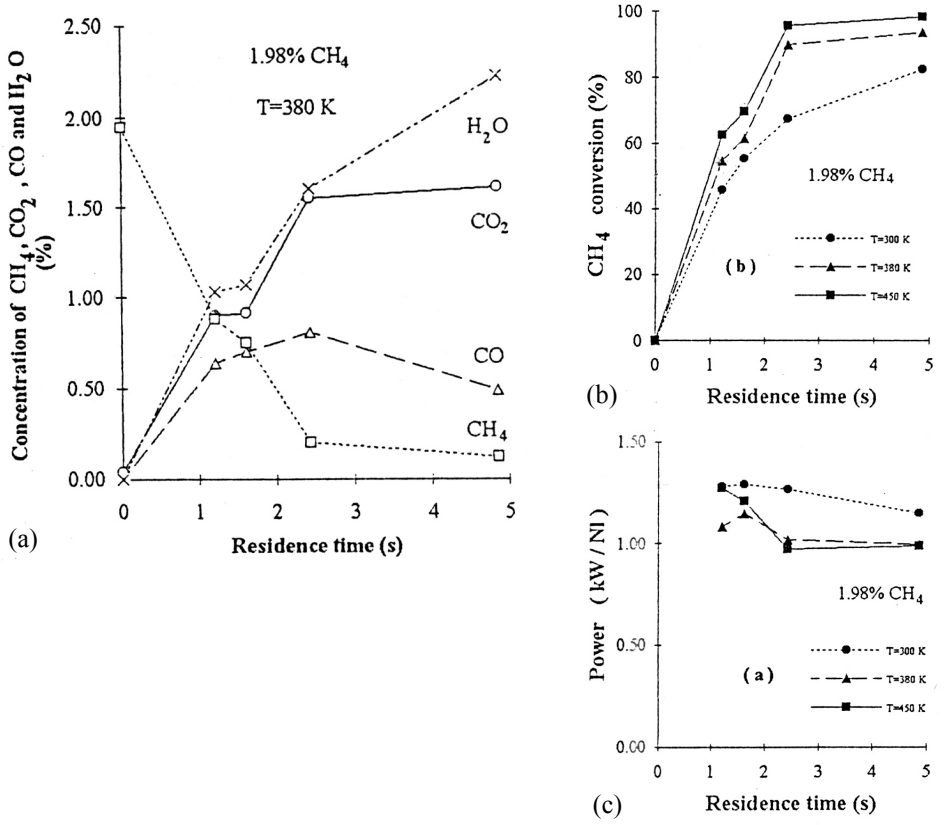

Figure 6-13: Measured species concentrations, conversion and power.

Concentrations of CH_4, CO_2, CO and H_2O as a function of gas residence time in the gliding discharges. Mixture: 1.98 *%* CH_4-air; gas temperature of 380 *K* (a), CH_4 conversion rate (b) and average electric input power (c) as a function of gas residence time in the gliding discharges for different gas temperatures. Experiments performed by Czech, Czernichowski and Mizeraczyk (1994)

CH_4 concentration (see figure 6-8). This is in accordance with previous experiments done by Czech, Czernichowski and Mizeraczyk (1994). Figure 6-12 shows that for the CH_4 conversion, the current results indicates that less conversion was achieved even if the gas temperatures was higher than those measured by Czech, Czernichowski and Mizeraczyk (1994). The authors do not mention or quantify any NO_x measurements.

The quantities of both CO and NO_x was produced in far higher concentrations when compared to conventional combustion at normal conditions, which for CO is around 100-200 *ppm* and for NO_x between 20-100 *ppm*. At relatively high flow rates the maximum CO concentration was measured to 8000 (50 *l/min*) and 13000 *ppm* (80 *l/min*)

for 2 and 3 *vol%* methane in air, respectively. The produced amount of both CO and NO_x were in such high quantities that they would constitute an important pollution threat if this process as of today was to be used in large scale CH_4 decomposition. Obviously other methods for measuring both formaldehyde's, hydrocarbons and other products contained in the condensed liquid from the process would be required to further investigate the process. There was no doubt about the existence of formaldehyde from the smell of the condensate. However, this was never quantified.

According to the chromatography measurements the actual reactor configuration was not very well adapted to perform only partly oxidation of the methane, that is, to convert low concentration methane to heavier hydrocarbons. The chain reactions are allowed to carry the reactions to final products (CO, CO_2 and H_2O), making the discharge process behave more or less like a normal combustion process. To avoid complete oxidation the residence time should be higher and the temperature of the reactor lower. Alternatively, intermediate products could be stopped in a "cold trap" before completion.

6.2.4 Conclusion and recommendations for further work

In these experiments decomposition of methane in very lean air/methane mixtures was studied in an electro-burner based on the gliding discharge principle. The presented results show that complete reduction of methane could be obtained if the residence time in the reactor was sufficiently long. The products of the methane decomposition were mainly CO_2, CO and H_2O. The methane conversion rate showed to increase with increasing residence time, temperature of the operating gas, and initial concentration of methane. To achieve complete decomposition of CH_4 in 1 m^3 of a 2 *vol%* mixture, the energy cost was about 1.5 *kWh*.

However, the formation of both CO and NO_x in the present gliding discharge system has been found to be significant. The produced amount of both CO and NO_x were in such high quantities that they would constitute an important pollution threat if this process as of today was to be used in large scale CH_4 decomposition.

According to the chromatography measurements the actual reactor configuration was neither very well adapted to perform only partly oxidation of the methane, that is, to convert low concentration methane to heavier hydrocarbons. The chain reactions are

allowed to carry the reactions to final products (CO, CO_2 and H_2O), making the discharge process behave more or less like a normal combustion process. To avoid complete oxidation the residence time should be higher and the temperature of the reactor lower. Alternatively, intermediate products could be stopped in a “cold trap” before completion.

More accurate temperature measurements of the temperature distribution in the reacting gas is required to determine which mechanisms are possible for the NO_x formation. In addition, deeper knowledge of the nature of the gliding discharge is necessary.

There is no doubt that more sophisticated measuring equipment is required to get a full understanding of the discharge process, at least equipment that is more adapted to the magnitude and time dependence of the measured variables. More time should be spend on getting a more complete physical understanding of the process with a reactor adapted for this purpose. A deeper understanding would make the approach to applications easier and results more predictable.

Numeric modelling of the decomposition should be performed, initially by using existing models and data for participant species.

* * *

6.3 DECOMPOSITION OF AIR/CH_4 AND AIR/C_3H_8 MIXTURES IN VARIOUS SILENT PLASMA DISCHARGE REACTORS

6.3.1 Introduction

The following experimental approach on hydrocarbon decomposition can be seen as a continuation of the experiments performed with the gliding arc discharge reactor, where the idea investigated being basically identical but with a different technical approach. The subject originated from discussions between me, my tutors and the Norwegian Defence Construction Service. The main initial idea was that plasma processing could have a potential as a method to deal with the threat from FAE weapons to defence blockhouse constructions by cold rapid decomposition of air-carried gaseous fuels. Another applicable area was to use plasma as a method for destruction of e.g. toxic military gases or other gaseous contaminants in centralized destruction plants. The technology can e.g. be applied as a part of a larger air treatment system for destruction of environmental air contaminants in advanced life support (ALS) systems.

In this part, techniques for hydrocarbon (CH_4 and C_3H_8) decomposition, known as the non-thermal discharge was considered. With this technique an electric field was applied to produce high energy electrons in the gas stream while leaving the bulk temperature of the gas unchanged. The high energy electrons served to generate reactive species such as O, OH, and HO_2 that attack the species in question through subsequent reactions.

It is the author's believe that substantial advances in effective manufacturing and environmental cleanup can be achieved by exploiting non-thermal plasma treatment. In such discharges, chemical change is driven by a variety of processes including ionization, molecular excitation, ion-electron recombination, fragmentation of ions and excited molecules, and reactions of radicals, atoms, and ions. Another prospect is the development of new, economical attractive processes for the conversion of natural gas to more valuable hydrocarbons such as methanol, ethylene and other organic compounds or higher hydrocarbons.

Several experiments were carried out to investigate the decomposition of methane and propane in stoichiometric air/methane and air/propane mixtures at room temperature and atmospheric pressure. Methane was intentionally selected because it stands out from most other hydrocarbons because it has a very large ionization energy, which is larger than the

ionization energy of molecular oxygen. Therefore, the charge transfer from molecular oxygen cation is impossible. Methane must therefore be activated either by the direct electron impact dissociation or via the free-radical processes. Propane on the other hand has a much lower ionization energy, and was selected as representative for the more simpler hydrocarbons.

In addition to actually performing the experiments, much time was also spend in constructing and assembling the high-frequency plasma power source and the different discharge reactors.

The specific device configurations investigated were all of the dielectric barrier discharge type either as simple or double barrier type as in figure 6-14, meaning the discharge is sustained between one or two dielectric surfaces respectively, that are backed by conductors. A high-frequency ac voltage is applied between the electrodes resulting in a series of short duration (100 *ns*) micro discharges that process the gas. In compliance with theory, the ratio of the electric field (E) to the number density of the gas (N) within the micro discharges should be rather large (E/N around 100 to 200 Townsend), thus producing electron energies well suited for excitation and dissociation of molecular gases.

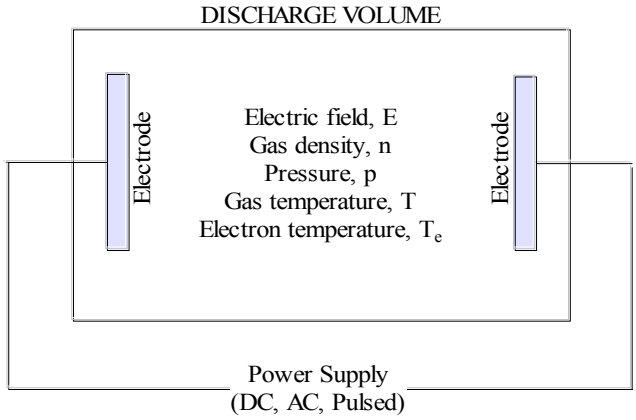

Figure 6-14: Circuit description of a double silent discharge device

Only little previous work have been reported on applying discharge generated plasma to decompose hydrocarbons in mixtures similar to those used in the current experiments. Thomas et al. (1993) studied the corona-induced oxidation of stoichiometric mixtures of ethylene, methane and acetylene in oxygen. They used a relatively low voltage system

with a very simple electrode geometry to produce the discharges. The discharges were able to run fairly well because of the low reactor pressure being used. However, lowering the system pressure is well known to promote the efficiency of the discharge. Total oxidation of the hydrocarbons in question were achieved, within a time interval in the order of many minutes. Gogolides et al. (1994) applied radio-frequency glow discharges to decompose methane in pure methane gas. The aim with these investigations was to develop a simplified gas-phase kinetic model that could confirm the experimental results. As Thomas et al. (1993) they used a low pressure system (80 *mTorr* - 1 *Torr*). The electrode spacing was between 2-6 *cm* and the power input between 0.06-0.15 W/cm_2. They proposed a mechanism where methane directly dissociated by electron attack to form CH_2 and CH_3 radicals, which further would contribute to the methane decomposition.

Other investigations of interest for the current studies are the recent reports on decomposition of hydrocarbons in air given by Chernova et al. (2001) and Krasnoperov and Krishtopa (2001). Chernova et al. (2001) investigated the destruction of ethane in a corona discharge both experimentally and by modelling, while Krasnoperov and Krishtopa (2001) have summarized experimental results on the kinetics of the "destruction" of a number of organic and inorganic compounds in a dielectric barrier discharge obtained by the NJIT (New Jersey Institute of Technology) group during the last seven years.

Several processes similar to the current experiments for treating different exhaustgases have been developed during the last decade (PlasmaSol (2000), AEA (1999), Up-To-Date Environmental Engineering AG (1999), Rosocha (1996), Eindhoven (1999), APP (1997), Litex (1999), Delphi Automotive Systems (2000)).

When it comes to the current experiments, I would like to emphasize that the use of the Tesla coil principle to generate the high-frequency low current (and high-voltage) which powers the electrodes, is rather unique when compared to earlier reported work. The main idea was to use a device that had a simple and rugged construction made up of inexpensive standard components, when compared to other common high-voltage power devices.

Another reason to use the Tesla coil was its ability for selective tuning to a specific high-voltage output frequency. The Tesla coil achieves a great gain in voltage in a very different way than a conventional transformer. A transformer's change in voltage is

dependent upon the turns ratio of the primary and secondary coils. If the primary coil of a transformer has 5 turns and the secondary coil has 100 turns, then the secondary voltage will be 20 times that of the primary. This does not fully apply to the interaction of the primary and secondary coils of a Tesla coil. Instead, a Tesla coil's voltage gain is based upon the different impedances of the primary and secondary circuit components. The resulting voltage in the discharge is around a couple hundred thousand volts for small coils and several millions for very large ones. A more through description of the Tesla coil principle will be given in the following chapters. Many of to days commercial Tesla coils are used in combination with lasers, to create spectacular lightening effects in movies and in public shows. In laboratories they are used to study high-voltage physics, radio waves and EMF phenomena.

Basic operation of a Tesla coil

The Tesla Coil is an air-core transformer with primary and secondary coils tuned to resonate. The primary and secondary function as a step-up transformer which converts relatively low-voltage high current to high-voltage low current at high frequencies. The Tesla Coil demonstrates the fundamental principles of high-frequency electrical phenomena. It illustrates the principles of ionisation of gases and behaviour of insulators and conductors in contact with high-frequency electrical fields. Its inventor, Nikola Tesla, conceived it to be a means to transmit electrical power without wires. An antenna would pull the transmitted electrical energy into the electrical system. One can also consider it a simple radio transmitter, operating within a broad range of high frequencies, which transmits power rather than information.

Components

A typical Tesla coil consists of a vibrator or transformer, one or several high-voltage capacitors, a primary, and a secondary connected to a ball terminal or antenna (see figure 6-15). The vibrator is composed of an air slot core around which coils of copper are wound; and a buzzer which consists of two tungsten points or contacts which open and close by means of a spring as alternating current and electricity passes through the core and discharges in the spark gap. For bigger Tesla coils at higher effects, a rotating spark gap is often used. The rotating spark-gap for the 8 *kW* TC can be seen in figure 6-15, with the 20 *kV* capacitor mounted at the back of the rack.

For the smallest coil, the capacitors were two large cylinders on either side of the spark gap. They are high-voltage capacitors of a predetermined size and value. The primary coil

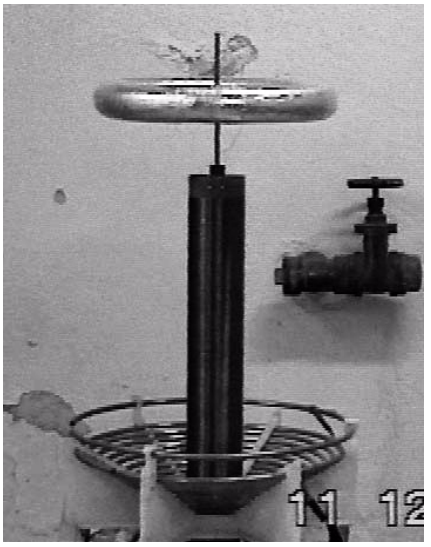

a) Primary, secondary and toroid

b, c) Rotating spark-gap and capacitor

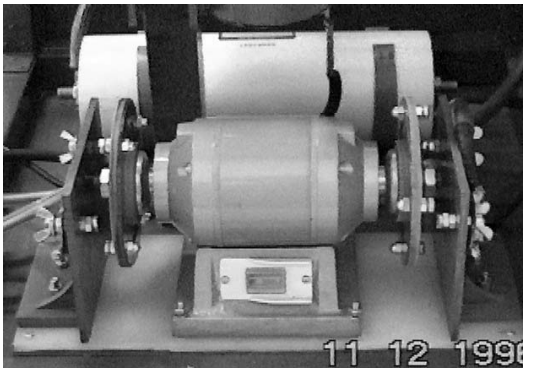

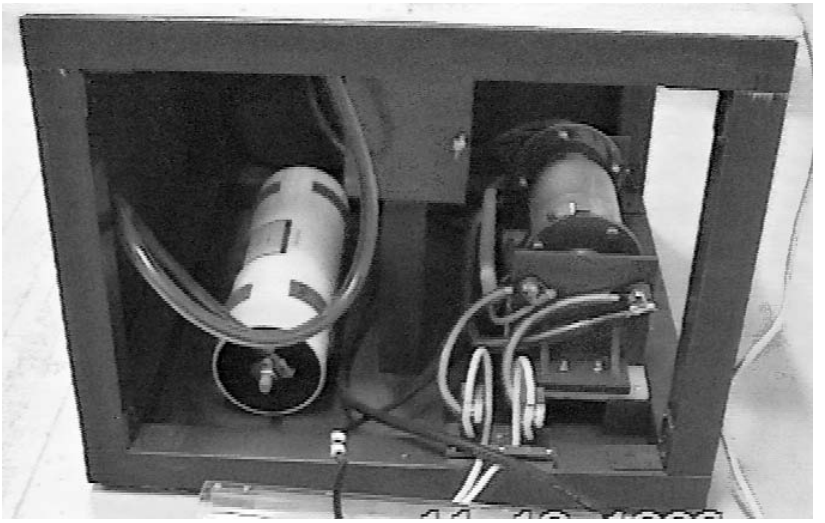

Figure 6-15: Tesla coil components

is a pair of thick insulated copper wires located next to, but not touching, the secondary and connected in series with the capacitors and spark gap. The secondary is a cone-shaped coil (cone-shaped to keep the coil compact and for manufacturing reasons as less wire is needed) consisting of about 400 turns of thin enamelled copper wire. It functions as a transformer by stepping up the voltage to high levels. The high-voltage produced is given off by the ball terminal.

How a Tesla Coil Works

The following gives a brief description of the manner of operation for the commercially available Edmund Scientific coil. When the plug is inserted into 110/220 *AC* current, electricity flows through the vibrator, an iron core with a hollow centre around which is wound many coils of copper wire. The iron core becomes an electromagnet. The buzzer, which consists of two tungsten contacts located opposite each other, not quite touching, pull apart when the electromagnet is activated and close when the magnetic field decays. This occurs at the rate of 120 s^{-1} to coincide with each time the AC current changes the polarity of the electromagnet. The capacitors charge up when the buzzer contacts are open, since the current passes into them to complete the electrical circuit. When the contacts are closed, the capacitors are shortened together and current does not pass into them. The open contacts allow the air in the spark gap the small space between open contacts to ionize, which permits a discharge that short circuits the transformer and capacitors. But the capacitors retain their electric charge, since the function of a capacitor is to store an electrical charge and thus provide energy to create an electromagnetic field.

The electromagnetic field is formed by the primary which converts the charge stored in the capacitors to magnetic energy. The electrical charge is transferred to the primary by the capacitors when the magnetic field in the iron core decays. When the magnetic field in the iron core is reactivated, the field generated in the primary is the one to decay, and the electrical charge is transferred back to the capacitors with every half cycle, a charge of increasingly higher voltage as each activation of the magnetic field adds to the charges previously generated. The vibrator also acts as an air core transformer, boosting the voltage to medium high levels with every half-cycle pulse of AC current. The high frequencies that are produced are rich in harmonics since each pulse of electricity across the spark gap of the buzzer is composed of many surges of electrical energy.

The capacitors have a particular size and value. They serve the dual function of storing electric charge and filtering through the high-frequency component of electrical current while blocking low frequency current. The result is that high-frequency electrical energy is built up by the generation and decay of the magnetic field in the primary every half cycle, reaching many million cycles per second. When the frequency is high enough and has reached the voltage pre-de-termined by the size and value of the capacitor, the primary induces a magnetic field in the secondary.

The Primary consists of two thick insulated copper wires which are resonated by the

capacitors to equal the natural resonant frequency of the secondary. When the resonance equals that of the secondary, a magnetic field is formed in the secondary. Resonance may be compared to a cymbal: when a cymbal selected for a certain size and weight is struck, it rings at a specific frequency. At the optimum resonant frequency, the *AC* resistance, or reactive impedance, is zero with the right coil and right capacitor, and now the maximum current can flow according to formula (also see APPENDIX F):

$$2\pi\frac{1}{\sqrt{LC}} = Fr \qquad \textbf{Eq. 6-3}$$

The secondary, like the vibrator, functions independently as a step-up transformer. Since it has many more coil turns of copper wire in its secondary from the primary voltage input, then electrical energy is supplied. As the electrical energy from the vibrator is fed to the capacitors of the primary air core transformer and its two-turn coil at its base, it now creates another independent circuit of the vibrator type transformer. The vibrator secondary output voltage is applied to this primary circuit, known as the air core Tesla resonant transformer or oscillator. Its energy is then induced to the cone shaped coil with the ball on top. It is the number of turns known as inductance and its self-capacitance. When the primary supply is properly tuned to the secondary, a high-voltage, high-frequency output is developed, which for the smallest coil is of around 50000 *V*. For this coil, the total primary capacitance is 0.25 *mF* at 3000 *V* and its secondary capacitance is 90 *pF* at 50000 *V*. It is the square root of the primary to the secondary capacitance that determines the approximate output voltage of 50000 *V*, according to the following formula:

$$\sqrt{\frac{C_p}{C_s}} = \sqrt{\frac{0.25\mu F}{90pF}} = \sqrt{\frac{0.025 \cdot 10^{-6}}{90 \cdot 10^{-12}}} = \sqrt{277} = 16.67 \qquad \textbf{Eq. 6-4}$$

which gives the secondary voltage: 16.67 x 3000 *V* = 50 000 *V*

APPENDIX F - Tesla Coil Formulas, presents the basic formulas describing the Tesla coil. They have ben collected from various sources on the internet.

With the current at maximum resonance, a high-voltage, high-frequency of one million impulses are produced at the ball of the secondary. The Tesla transformer does not function on turn ratio windings. It functions instead on the ratio of the primary capacitance to the secondary capacitance. The secondary, like the vibrator, functions as a transformer. Since it has more coils of wire than the primary, it boosts the high-voltage even higher.

The secondary is a cone-shaped coil located next to but not inside the primary. Only the first few turns are within the electromagnetic field created by the primary. Only a small difference in voltage exists between each turn of the coil and the one preceding it. This low voltage differential per turn prevents voltage from breaking down copper wire insulation and short-circuiting the secondary. The secondary produces a current called high-frequency electricity. high-frequency currents reverse their flow, or alternate, from 100 000 to one million times a second.

In typical Tesla coil designs, the frequency is adjusted by altering the primary coil's inductance. If the energy bursts are of the same frequency as the secondary, the energy transferred by the primary's magnetic field will start to build up in the secondary coil. Much like a laser, this energy grows and amplifies itself until there is an incredible voltage built up at the top of the coil, which dissipates into the air in the form of electrical sparks. The high-frequency voltage can also be transported through, or actually on the surface, of a insulated single-core cable to the reaction tube electrode. Figure 6-16 shows the current large 8 *kW* Tesla coil in action. We can see how the streamers emerge from the surface of the toroid.

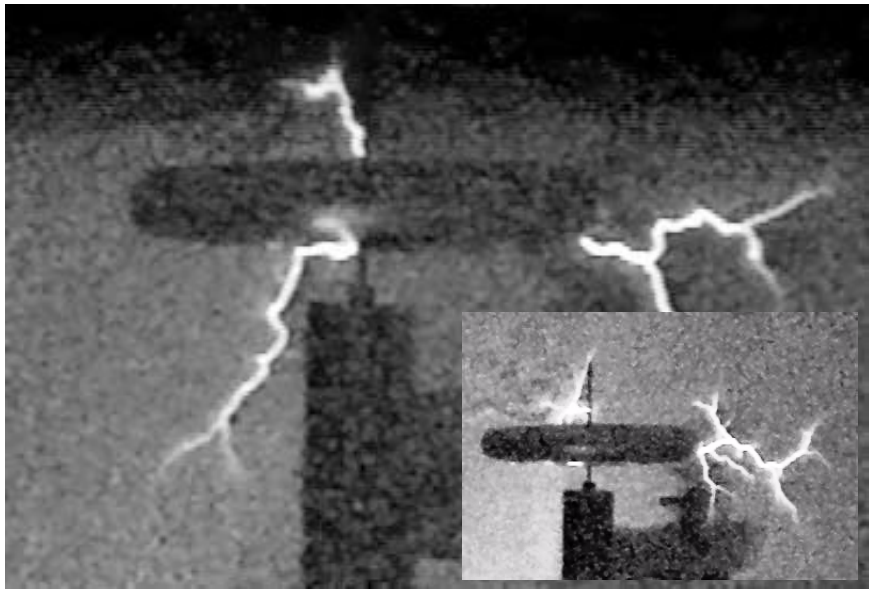

Figure 6-16: Image of the 8 *kW* Tesla coil in action.

Primary and secondary windings and toroid discharge-hat. The 20 000 V capacitor and the rotating spark-gap can be seen mounted inside a wooden frame, just under the primary and secondary.

Tesla constructed the first apparatus for the use of high-frequency currents in medical applications, a principle which is still used today. Small hand held Tesla coil devices were also used for many years as “leak detectors” in vacuum systems made of glass. A kind of Tesla coil is in nearly every circuit for feeding the CRT (PC-monitor, TV etc.) with high-voltage. In the industry, high-frequency currents are still used for dielectric heating, e.g. in furniture production. Many high-voltage test labs used and still use Tesla coils for high-voltage testing.

There have been found no other previous related work, where Tesla coils have been used as a source to power reactors for the decomposing of gaseous compounds. Therefore a lot of effort had to be put into the experimental setup, such as constructing and assembling the Tesla coils and arranging the high-voltage transfer to the reactor electrodes.

6.3.2 Experimental setup

Three different discharge configurations were investigated as explained from the context of table 6-6. All discharge reactor were based on the dielectric barrier discharge principle, which means that the voltage potensials are separated with a dielectric material such as glass, plexiglass etc. The effect of the discharge created plasma for configuration A were based only on visual observations and by video recordings (C_3H_8/CH_4 in air). For configuration B, the final species concentration after different exposure times in the plasma was sampled in glass containers and analysed by chromatography (C_3H_8 in air). For configuration C, The hydrocarbon concentration was continuously measured by infrared spectrophotometry (CH_4 in air).

Table 6-6: Experimental matrix.

	Configuration A	**Configuration B**	**Configuration C**
Type of discharge configuration	Simple dielectric barrier	Double dielectric barrier	Double dielectric barrier
Type of experiment	Ignition and flame propagation	decomposition	decomposition
Hydrocarbons	C_3H_8/CH_4	C_3H_8	CH_4
Diagnostics	HI-8 video camera	Gas chromography	MIRAN IR
Type of reactor	Wire-to-Plane	Double parallel plate	Double Annular

The gas flow system

The gas flow system is shown in figure 6-17. The removable reactor section had a length of 0.4 *m* and could be sealed of in both ends. A tube for observing flame propagation was connected to one end of the reactor section, having a length of 3 *m* and an inner diameter of 50 *mm*. The flow meter controlled the gas sources and made up a typical base stream consisting of stoichiometric mixtures of air-methane or air-propane. The system was set up to use either ambient air from the compressed air system (7 *bars*) or synthetic air. The intension with this was to investigate whether the water vapour in ambient air would have any effects on the decomposition. The calibration curves for the mass flow controllers are shown in APPENDIX F. All experiments presented here were conducted at room temperature.

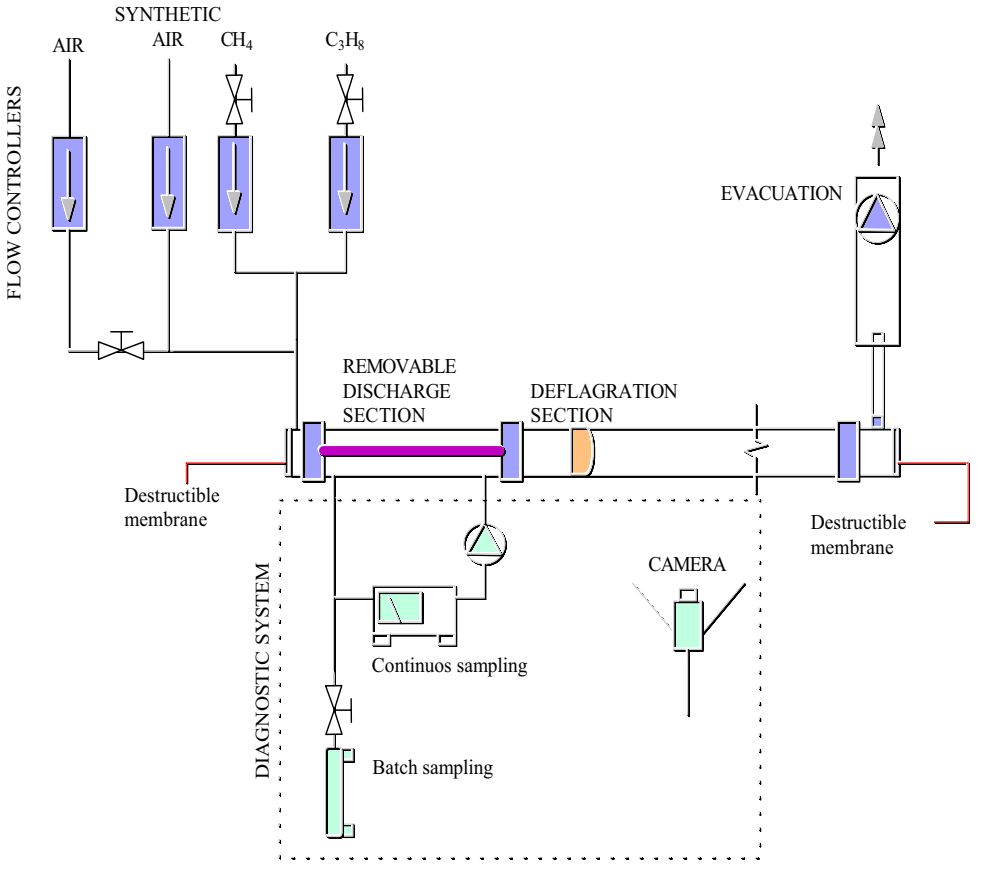

Figure 6-17: The gas handling system.

The concentration of either C_3H_8 or CH_4 could be continuously measured by the analyser which was a Foxboro Miran-1A infrared spectrophotometer. The Foxboro Miran-1A analyser is a general purpose, variable wavelength, infrared gas analyser designed for ambient analysis of gases or vapours which absorb infrared energy in the infrared region of 2.5 to 14.5 *microns*. Cell path length adjusts from 0-20 *m* in 13 increments enabling adjustment for sensitivity. Analog display and 0-1 *V* dc recorder output. The analyser measures either in absorbance units (AU) or in transmission (*%T*). The analyser can only measure one component at a time, and therefore had to be calibrated for either C_3H_8 or CH_4 when changing mixtures. The calibration curve for CH_4 is shown in figure 6-18 as an example. Continues measurements could not be logged but was read manually from the analog display. Each run lasted for a given amount of time (within minutes), or until the measured values for the concentration showed values close to zero.

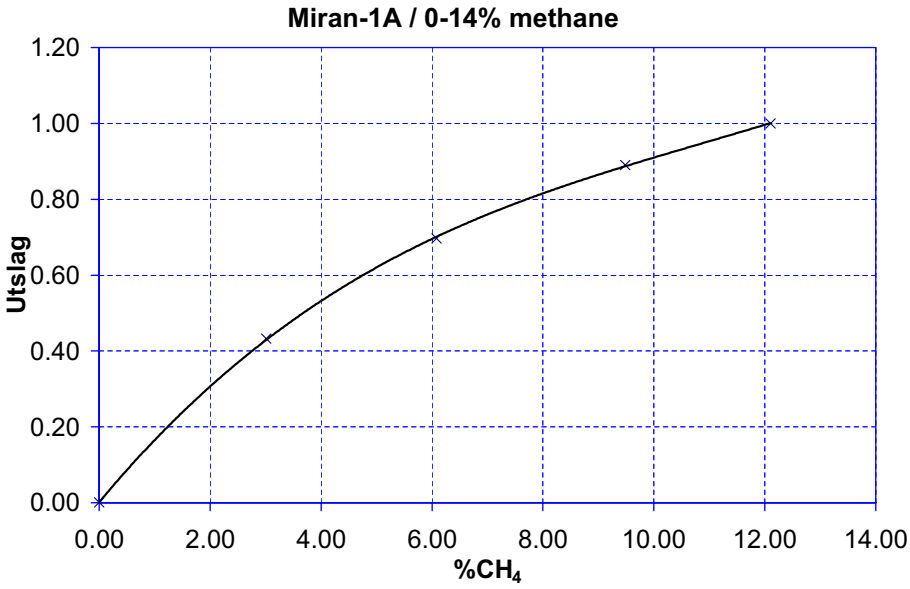

Figure 6-18: Miran-1A infrared spectrophotometer calibration for methane.

The power supply and HF generator

Two distinct power systems were used to power the two different high-frequency coils applied to the discharge system. A small 220/120 *V* transformer and a bigger three phase variable frequency power supply, capable of supplying a maximum of 20 *VA* at 260 *V*, was used to convert utility power to the desired frequency and voltage. Both the

high-frequency generators used, were of the Tesla coil type. The output of these supplies were then routed through a single-core cable to the respective Tesla coils and then delivered to the reaction tube electrode. The energy then discharges within the gas volume to the grounded opposite electrode.

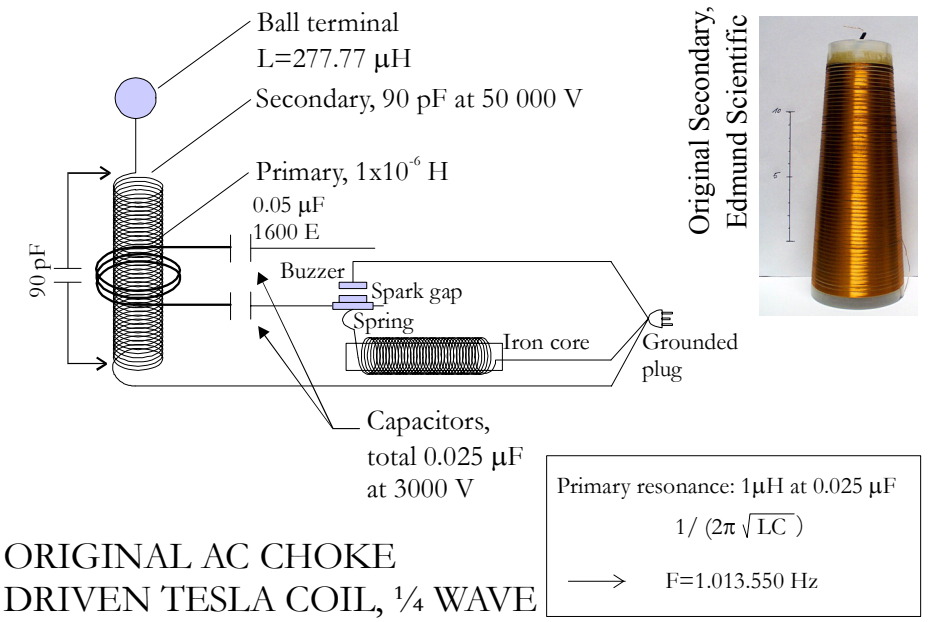

Figure 6-19: Circuit description of the smallest Tesla coil.

To produce the high-frequency voltage necessary for the discharge experiments, two Tesla coils had been obtained. The smallest coil had a power consumption of around 120 *W* and had been purchased from a U.S. store, Edmund Scientific Inc., which supplies a broad range of scientific equipment. The circuit description for the smallest Tesla coil is given in figure 6-19, with values for the main components. The coil was originally meant to be used in small-scale scientific experiments to show how low current high-frequency voltage is produced. Figure 6-20 gives a more illustrative picture. The voltage output from the smallest coil was 50 000 *V* at 1 000 000 *Hz*. The largest coil had been produced on exact specifications by a Finnish student from Helsinki, Kristian Ukkonen (studies computer science for MSc at HUT and runs his own company called KU - Resonant Research), and had a maximum power consumption of approximately 8 *kW*. The circuit description for the large TC is given in figure 6-21, also with values for the main components. The voltage output was 800 000 - 1000 000 *V* at 250-300 000 *Hz*.

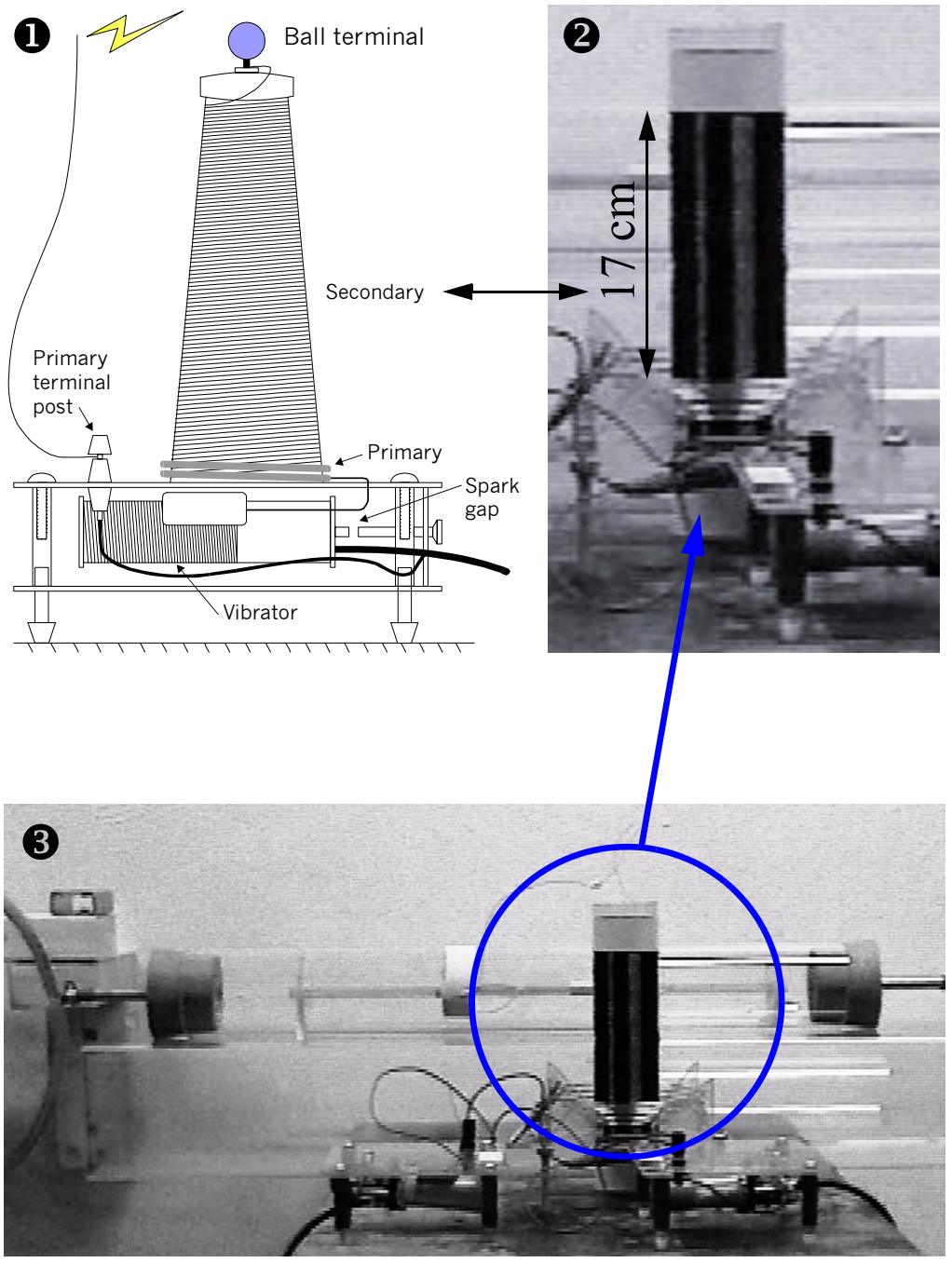

Figure 6-20: Commercially available Tesla coil, Edmund Scientific.

The experimental setup for the smallest Tesla coil with parallel plate copper electrodes and two step-up transformers in parallel connected to the secondary.

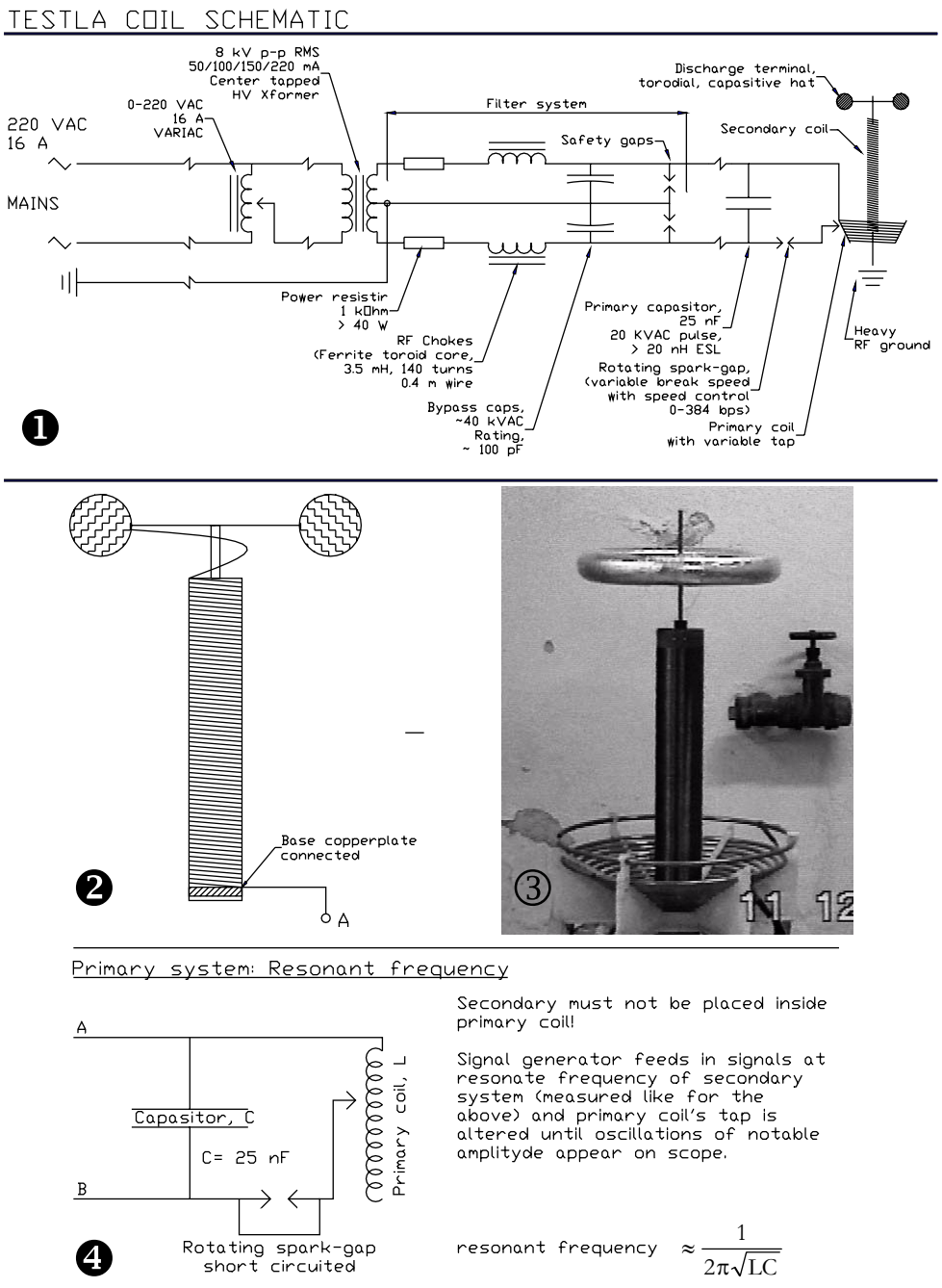

Figure 6-21: Big 8 *kW* home-made Tesla coil.

Discharge configurations

Two different discharge reactor configurations were used, based on the simple and the double barrier discharge configuration. The operation of the all the different reactors was achieved by grounding one of the electrodes while connecting the second to the high-voltage source.

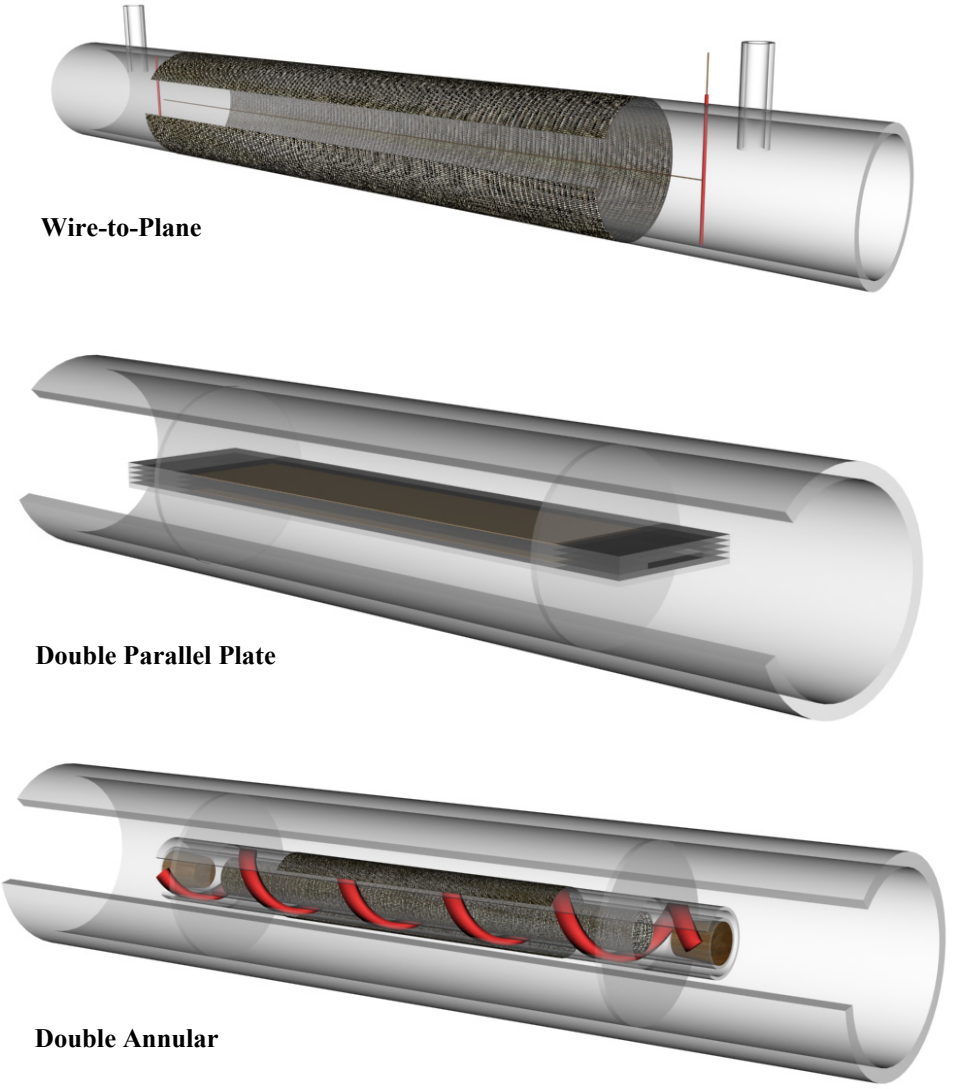

Figure 6-22: The plasma reactors investigated.

Three different types of dielectric barrier discharge reactors were developed for the decomposition experiments; a simple wire-to-plane, a double parallel plate and a double annular reactor

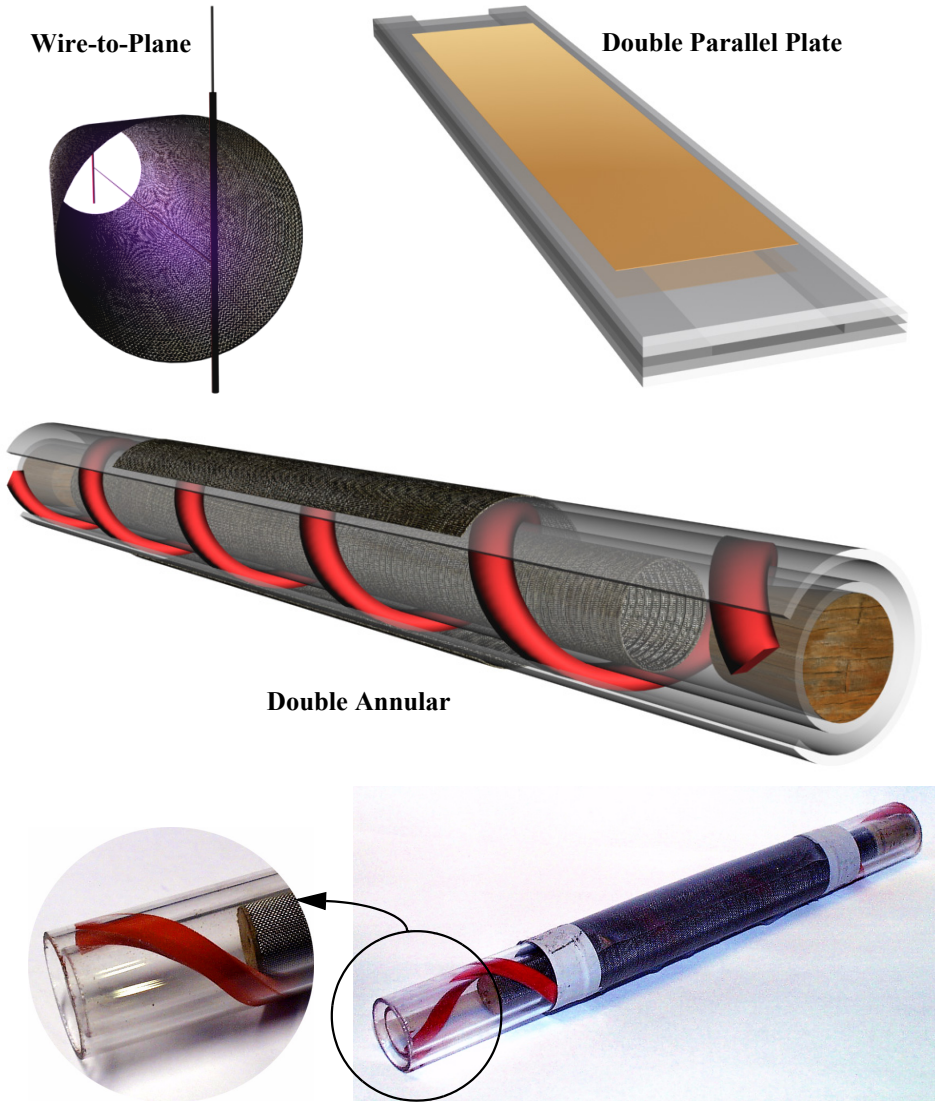

Figure 6-23: Plasma reactors - close-up.

The simple barrier discharge reactor consisted of a wire-to-plane system as shown by the uppermost picture in figure 6-22.

The double barrier discharge reactors were constructed by the plate-to-plate principle. In the first reactor, the discharge volume was formed between rectangular glass plates as shown on the picture in the middle of figure 6-22. The electrodes were made from 0.2 *mm* copper foil. The second double barrier discharge reactor consisted of two coaxial glass

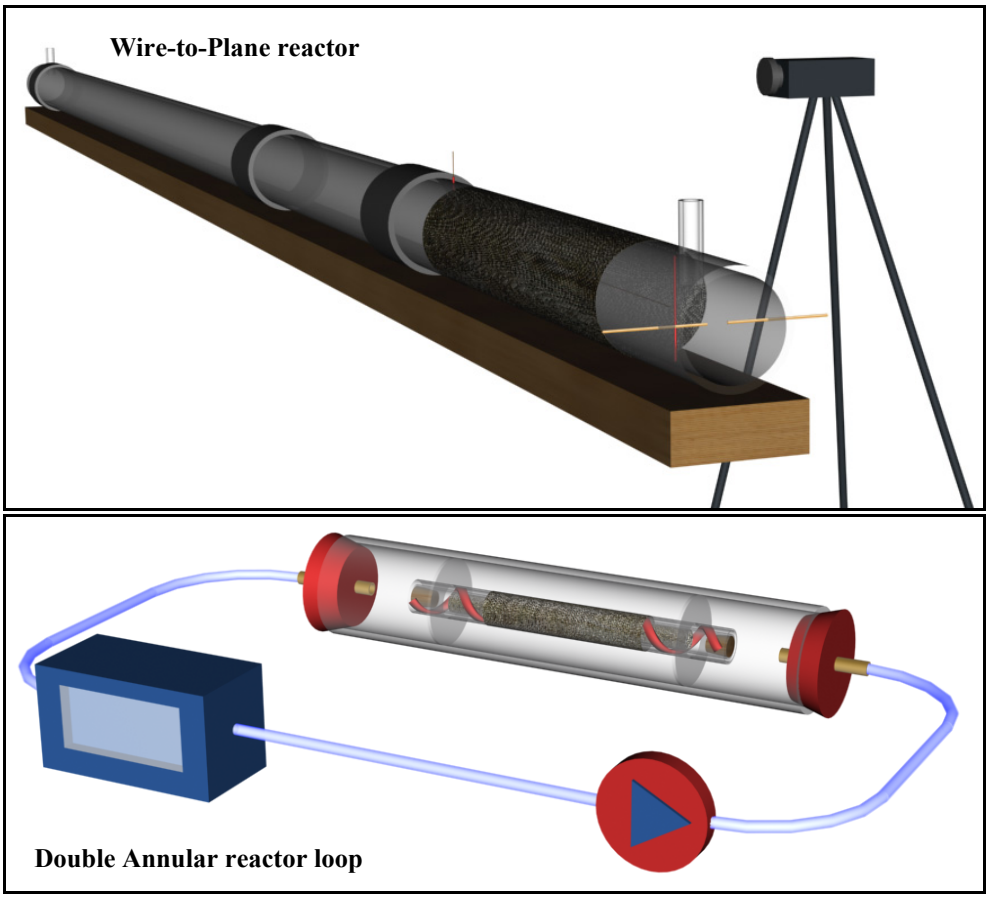

Figure 6-24: Experimental setup - configurations.

The upper image illustrates the setup for the ignition/propagation velocity experiments, while the bottom one shows the setup for one of the decomposition experiments.

tubes and was constructed so that gas flow was directed between the two cylinders as shown in the bottom picture in figure 6-22 and in figure 6-23. The inner tube had an outside diameter of 1.6 *cm* and the outer tube had an inside diameter of 1.95 *cm*.

The gas flow was between the cylinders in a gap of approximately 3.5 *mm* with a total active volume of 205 *ml*, forming the discharge volume. The centre electrode was a metallic wire sheet inside the inner cylinder. Both ends of the inner tube were sealed with the exception of a small hole for the penetration of the high-voltage connection. The outer tube was covered by copper foil connected to the grounded side of the high-voltage transformer secondary. These were the three types of reactors being used during the

experiments. The wire-to-plane reactor was mainly used with the propagation/ignition experiments (figure 6-24, topmost), while the double parallel plate and double annular reactors mainly were used in conjunction with the decomposition experiments (figure 6-24, bottom). The wire-to-plane reactor was developed in an early stage and had been adapted to work with both the small and the large Tesla coil.

6.3.3 Results and discussion

Intentionally the first experiments were supposed to be run with the large Tesla coil powering a central wire electrode in the largest wire-to-plane reactor shown topmost in figure 6-24. The large coil was first tuned as close as possible to its resonant frequency, as briefly explained in figure 6-21. Then immediately after connecting the power to the 3-phase powered variac, powerful lightening emerged from the toroid terminal extending up to several meters out from the terminal hat in an irregular pattern. The streamers were quite large, but fewer than expected and made quite a lot of noise (see images extracted from super-8 video in figure 6-16 and figure F- 9). Apparently these powerful discharges also produced large EMF-effects, and was able to ignite and illuminate the nearby fluorescent tubes several meters away. From the smell that arose in the in the room, important quantities of both ozone and NO_x were produced. Working several hours in the room with continues discharges had an irritating effect on both the throat and the head.

However, the power available at the surface of the toroid hat refused to be transported into the reactor to the wire electrode. Most of the effect was lost through the lightening bolts that still occurred even when the toroid was connected to the reactor wire. This was the main reason why the large coil was left in favour of the much smaller coils. The average tension on the surface of the toroid had been estimated to be between 800000 - 1000000 V and was probably too high for the available toroid surface. This surface should probably have been made larger to avoid the breakdown and subsequent boltening discharge. The power could then maybe have been canalized more effectively through the connecting conductor.

The following experiments were therefore accomplished by applying the previously described smaller coils. These could also be handled much easier and had no problems with transferring the power emerging from the terminal. As already mentioned, much time and work had been dedicated trying to enhance the Tesla coil operation, for both the small and the large system. The smallest commercial Tesla coil from Edmund Scientific was the

easiest to operate and try different configurations with. Several new secondary coils were constructed to try to enhance their operation. The basic formulas for calculating the dimensions of the secondary can be found in APPENDIX F. Two of the smallest Tesla coils were made to run in parallel, which seemed (by observation) to intensify the discharge effect. The smaller Tesla coils had much less power output then the larger coil, which also made them more safe to handle (120 *W* as compared to 8 *kW* power input). This smaller power output made it much easier to handle the transfer of the high-voltage from the top of the secondary coil to the discharge electrode (50 000 V at 1 000 00 *Hz* versus 800 000 - 1 000 000 *V* at 250-300 000 *Hz*). If the single core transfer cable was reasonable isolated, this would keep the current within the cable. The large coil had an output voltage which made it impossible to transfer the output energy within any cable. The current would flow outside on the surface of any object and dissipate in the surrounding air long before it reached the electrode inside the reactor. This made only the smallest Tesla coil suitable for the discharge experiments, on the cost of much less available power. Less power meant that smaller reactor volumes and gas quantities had to be considered.

The initial experiments on ignition and flame propagation, were performed on stoichiometric mixtures of CH_4 and C_3H_8 in air. The mixture was filled into both the reactor and flame propagation section and are referred to as configuration A (see table 6-6). The mixture was prepared by mixing the different gas flows through the mass flow controllers to make up the base streams consisting of stoichiometric mixtures of CH_4 and C_3H_8 in air. The mixture was then led through the reactor and flame propagation tube until the air had been evacuated. The end walls of the tube were then sealed off by a plastic film and the out- and inlets were closed with valves. The gas discharge (configured as in figure 6-23, wire-to-plane) was then allowed to run for a given time in the 0.4 *m* upper section of the tube, after which the end-mounted spark plug was lighted.

Then by theory, the gas discharge would produce both high energy electrons and free radicals that could break up and decompose the hydrocarbon molecules. Since the radicals must be produced from the species contained within the gaseous mixture, the radicals one could expect to be active in both these cases would be free oxygen atoms at different energy levels (O, $O(^3P)$, $O(^1D)$). Depending of the amount and energy level of the free electrons produced in the current discharge, direct attack of the hydrocarbons by electron or ion collisions was expected to have less effect than that of the radicals. If this was the

only active process initiated by the discharges, total decomposition times in the order of many minutes could be expected. However, if sufficient amounts of radicals were produced in the active discharge volume, a decomposition was expected to occur by the order of seconds. Decomposition of i.g. CH_4, as proposed by Gogolides et al. (1994), by direct electron-impact dissociation would produce additional radicals through the following reactions:

$$CH_4 + e \rightarrow CH_2 + 2H + e \quad (6\text{-}1)$$

$$CH_4 + e \rightarrow CH_3 + H + e \quad (6\text{-}2)$$

Assuming that some or all these processes were active during the discharge, this would then decrease the hydrocarbon concentration as a function of time. If the hydrocarbon concentration had reacted below the flammability range, no ignition would occur and no flame would propagate through the tube. Another purpose with these experiments was to investigate whether a discharge that had been run only for a short period of time, would affect the flame propagation properties. To record the observations, a high-8 video camera was situated normally to the tube as shown in figure 6-24 (topmost).

To actually quantify the capability of the barrier discharge to decompose either C_3H_8 or CH_4 in air, a circuit of tubes was set up as illustrated in figure 6-24 (bottom), also referred to as configuration B and C. The filling of the tube with each mixture was performed as previously explained, after which the circuit was sealed off. A pump provided a steady circulation of the gas mixture through the discharge volume and the analyser.

Experiments with configuration A were conducted on stoichiometric mixtures of C_3H_8/ air and CH_4/air by using a wire-to-plane discharge reactor as in figure 6-23 and figure 6-24. The results from these experiments are shown in table 6-7 and illustrated in figure 6-25. From the visual observations of flame propagation with the high-8 recordings, there were no measurable effect on the propagation velocity when this occurred. This was probably because the active plasma only was produced in the upper section of the tube. Any changes to the mixture contained in the reactor section did not seem to affect the mixture in the following tube within the time of operation. These experiments therefore ended up to become more of a qualitative approach which answered; propagation occurred=YES and no propagation=NO, were no propagation was attributed to the effect of hydrocarbon decomposition by reactive species generated by the discharge. The results showed that there were no distinct limit between when ignition and propagation occurred

and not. Causes for this could be inaccurate mixing, leakage or unstable operating performance of the power source. Another reason could be that the temperature gradient created in the plasma volume was sufficient to cause entrainment of the mixture contained inside the flame propagation section, and thereby altering the hydrocarbon concentration.

With C_3H_8 and runtimes from 3.5 *min* and upwards, experiments where no propagation was observed, were starting to occur. The mean runtime for experiments with no propagation was found to 4.3 *min*. This could indicate that at least some of the C_3H_8 had been completely or partly decomposed (or otherwise affected), so that the mixture was no longer flammable. The same pattern was found for the CH_4-mixture, with a necessary mean runtime of 5.1 *min* for experiments with no propagation to occur. One important finding pointed out by Krasnoperov and Krishtopa (2001) was how methane differed from the rest of the apparently similar species investigated. These molecules have ionization energy larger than the ionization energy of molecular oxygen. Therefore, a charge transfer from molecular oxygen cation is impossible. The authors therefore concluded that these molecules have to be activated either by direct electron impact dissociation or via the free-radical processes. Since direct electron impact dissociation is a slower process in diluted mixtures, we can presume that this mechanism was the most probable cause for the currently achieved results as in configuration A.

Experiments with reactor configuration B were performed in a double parallel plate reactor as in figure 6-23. A stoichiometric mixture of C_3H_8 in air was run in the loop illustrated in figure 6-24 (without the Miran-1A analyser), for different periods of time as tabulated in table 6-8. Gas was then sampled to evacuated glass bulbs and send for mass spectrometry analysis. The measured composition after given time exposures in the loop is illustrated in figure 6-26. According to these results, very little change in composition had occurred. Only some minor decrease in C_3H_8-concentration could be observed with increasing run-times. These indications of only very slow or non-existent decomposition can probably be attributed to the previously presumed mechanism. Free electrons are apparently produced, but probably loses most of their energy through collisions with the O_2 and N_2 molecules of the air. Any radicals produced are not in quantities high enough to have any substantial effect the concentration of the hydrocarbons. The type of reactor used here could also have been the cause for the very slow decomposition, if poorly designed.

The experiments for reactor configuration C were performed on stoichiometric CH_4

Table 6-7: Experimental results for configuration A.

Experimental results for configuration A

Oxidative experiments, CH4/air and C3H8/air (stoichiometric mixture). The mixture was introduced into the PVC tube and sealed off my a membrane on each side. The plasma apparatus was then run for a given time after which the mixture was ignited by a spark close to the tube inlet. Preliminary experiments were done by observing the effect of the discharge generated plasma on the flame deflagration velocity of a stoichiometric CH_4/air or C_3H_8/air mixture enclosed in a PVC tube. Flame velocities could be obtained from video images taken by a high-8 video camera.

Reactor: Wire-to-Cylinder
Temp. surr.: 10-15 °C

Exp. No.	Mixture (stoic.)	Run-time [min]	Deflagration [YES/NO]	Comments
1	C_3H_8/air (syntetic)	1.0	Y	
2	----"----	1.0	Y	leakage?
4	----"----	1.5	Y	
3	----"----	2.0	Y	
7	----"----	3.0	Y	
6	----"----	3.5	N	
16	----"----	3.5	N	out of calibration?
5	----"----	4.0	N	
14	----"----	4.0	N	
15	----"----	4.0	N	
8	----"----	4.5	N	
9	----"----	4.5	Y	
12	----"----	4.5	N	
13	----"----	4.5	Y	
10	----"----	5.0	N	
11	----"----	6.0	N	leakage?
Exp. No.	**Mixture (stoic.)**	**Run-time [min]**	**Deflagration [YES/NO]**	**Comments**
17	CH_4/air (syntetic)	1.5	Y	
18	----"----	2.0	Y	
19	----"----	3.0	Y	
20	----"----	4.0	N	
21	----"----	4.0	Y	
22	----"----	4.5	Y	
23	----"----	5.0	N	
24	----"----	5.0	Y	
25	----"----	6.0	N	
26	----"----	5.5	N	
27	----"----	4.5	Y	

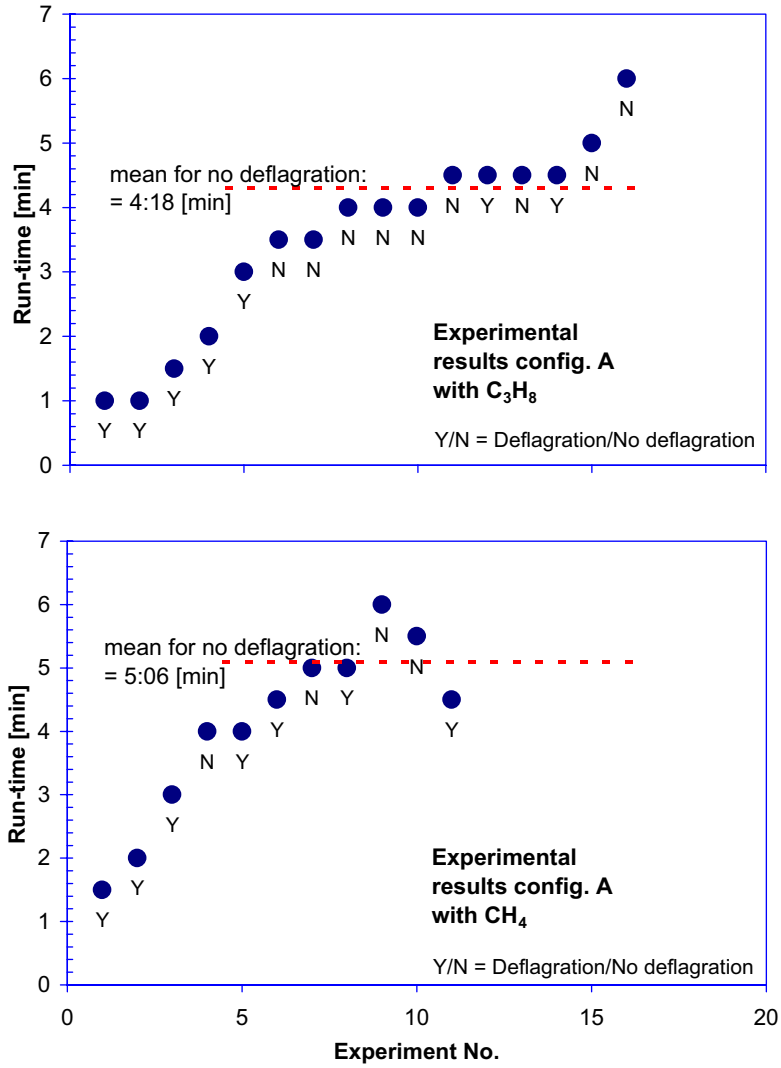

Figure 6-25: Experimental results for configuration A.

mixtures in either a double parallel plate or a double annular reactor as in figure 6-23. This time ambient air was used, containing some amount of water vapour. The aim with this was to see if the assumed effect of radical production from H_2O would improve the rate of decomposition. The reported results are from the experiments performed in the double annular reactor. The mixture was as before, run through the loop illustrated in figure 6-24, this time with the Miran-1A analyser connected. The obtained results are given in table 6-8 and illustrated in figure 6-27.

Table 6-8: Experimental results for configuration B and C.

Experimental results for configuration B

Oxidative experiments, C_3H_8/air, stoichiometric mixture, batch. Experiment run with C_3H_8 in air. The mixture was first enclosed in a loop and then recirculated through a continously running discharge. Sampled in glass bulb to measure species composition by gas cromogaphy.

Reactor: Double parallel plate
Temp. surr.: 10-15 °C

Run-time	C_3H_8	O_2	N_2	sum
0.0	3.73	18.35	77.87	99.95
0.5	3.75	18.31	77.28	99.34
1.0	3.72	18.28	77.93	99.93
3.0	3.72	18.15	77.98	99.85
5.0	3.48	18.05	77.28	98.81

Experimental results for configuration C

Oxidative experiments, CH_4/air, stoichiometric mixture, batch mode. The mixture was first enclosed in a loop and then recirculated through a continously running discharge. Methane concentration continously measured with Miran-1A infrared spectrophotometer.

Reactor: Double annular
Temp. surr.: 10-15 °C

Date	Exp. No.	Time to complete	Comments	
---- " ----	7	01:21	leakage?	
---- " ----	4	04:53		
8-9/4-97	6	05:02		
5/4-97	1	05:15		
---- " ----	5	05:34		
---- " ----	8	05:37		
---- " ----	2	05:47		
---- " ----	3	07:05	uncertain initial concentration?	
---- " ----	9	-	Ignition, spark ignited mixture and destroyed annular glas electrodes	
	10			
	11			
	12			
	13			

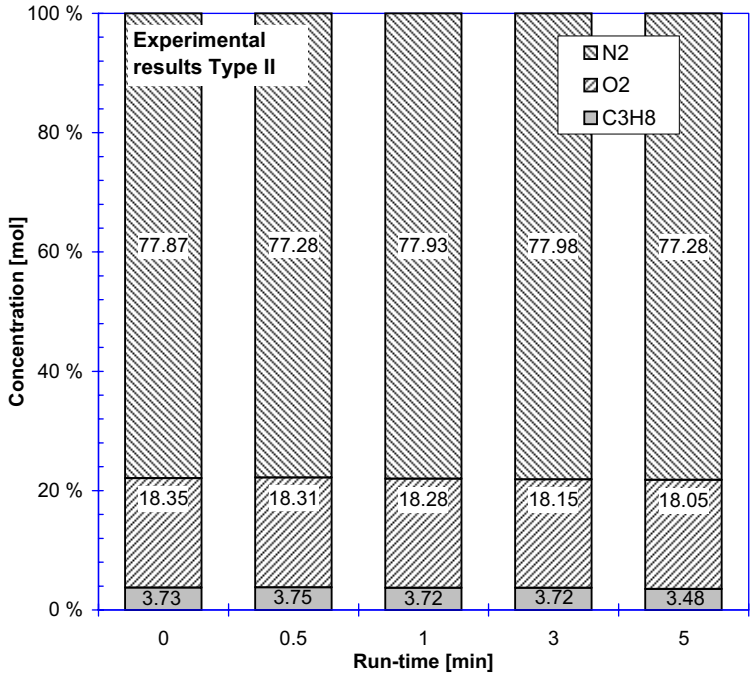

Figure 6-26: Experimental results for configuration B.

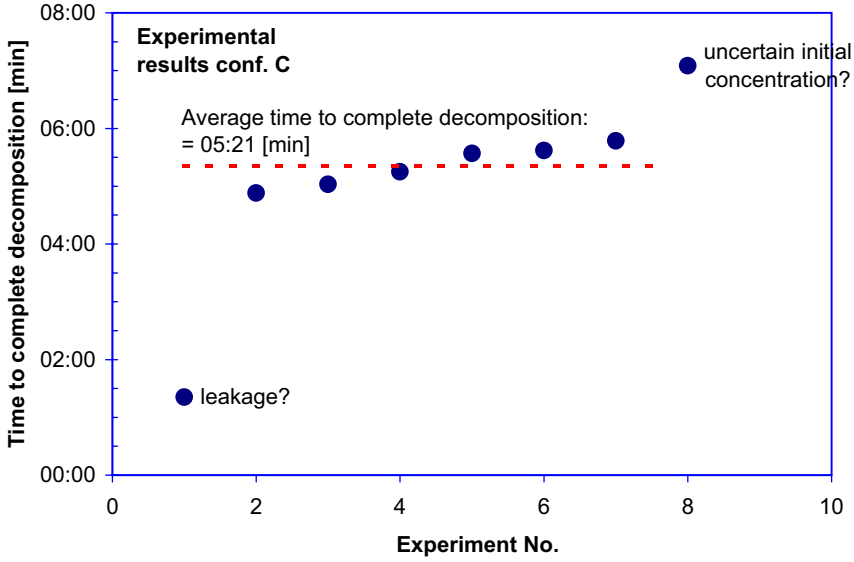

Figure 6-27: Experimental results for configuration C.

The results showed some similar behaviour as the results obtained with configuration A. From figure 6-27 we can se that complete removal of CH_4 was achieved after 5-6 *min* in the discharge loop. This new double annular reactor seemed to be more effective compared to the previous results from configuration B, where almost no decomposition of C_3H_8 were achieved. Decomposition of CH_4 could now be achieved even if this molecule apparently is much harder to destruct that C_3H_8, according to Krasnoperov and Krishtopa (2001). This obtained decomposition can probably be attributed to a more effective reactor design combined with the addition of water vapour to the mixture. According to Hammer (2000), radicals from water vapour can be produced by the following reactions:

$$e + H_2O \rightarrow e + H + OH \quad (6\text{-}1)$$

$$O(^1D) + H_2O \rightarrow 2\,OH \quad (6\text{-}2)$$

The hydroxyl radical is one of the most reactive species known, with an oxidizing potential of 2.80 *V*, and it can be made through a variety of processes including the electron impact dissociation of water. Ozone follows at 2.07 *V*.

Other examples of reactions besides 6-1 and 6-2, that are of importance to the radical formation are (Hammer (2000)):

$$e + O_2 \rightarrow e + O(^3P) + O(^3P) \quad (6\text{-}3)$$

$$e + O_2 \rightarrow e + O(^3P) + O(^1D) \quad (6\text{-}4)$$

$$e + N_2 \rightarrow e + N(^4S) + N(^4S) \quad (6\text{-}5)$$

$$e + N_2 \rightarrow e + N(^4S) + N(^2D) \quad (6\text{-}6)$$

$$e + CO_2 \rightarrow e + O + CO \quad (6\text{-}7)$$

$$O(^1D) + H_2O \rightarrow 2\,OH \quad (6\text{-}8)$$

O-radicals preferably react with hydrocarbon molecules thereby initiating a reaction chain forming several oxidizing radicals. One such reaction chain proposed for propylene e.g. is (Dorai and Kushner (1999), Penetrante et al. (1999))

$$O + C_3H_6 \rightarrow CH_2CO + CH_3 + H \quad (6\text{-}9)$$

$$H + O_2 \rightarrow HO_2 \quad (6\text{-}10)$$

$$CH_3 + O_2 \rightarrow CH_3O_2 \quad (6\text{-}11)$$

The results obtained through all three types of experiments have indicated that a discharge system based on the Tesla coil principle, has the capability to completely or partly decompose both the investigated hydrocarbon components (C_3H_8 and CH_4) within a time exposure in the discharge between 3-6 *min*. The time for complete decomposition to occur is in accordance with earlier observations made by Thomas et al. (1993). The different results achieved with configuration B and C also showed the importance of a good reactor design, and that the reactor must be properly adjusted to the characteristics of the power source. The results also indicated that addition of water vapour as a source for radical production, might enhance the hydrocarbon decomposition. Two possible physical explanations to the decomposition are therefore:

1. Direct electron impact: Plasma electrons + hydrocarbons (C_3H_8, CH_4) $\rightarrow$ Products
2. Chemical (radical-promoted) reactions: Radicals + hydrocarbons (C_3H_8, CH_4) $\rightarrow$ Products

where the first mechanism is the most plausible for explaining the current results.

When hydrocarbons other than methane are present in the gas mixture, O-radicals preferably react with hydrocarbon molecules thereby initiating a reaction chain forming several oxidising radicals. One such reaction chain for propylene have been proposed by Thomas et al. (2000):

$$C_3H_6 + O \rightarrow C_2H_5 + HCO \quad (6\text{-}12)$$

$$C_3H_6 + O \rightarrow CH_2CO + CH_3 + H \quad (6\text{-}13)$$

$$C_3H_6 + O \rightarrow CH_3CHCO + H + H \quad (6\text{-}14)$$

Some of the products of this oxidation subsequently react further with oxygen to produce peroxy (HO_2) radicals. The hydrocarbon reaction with O atoms is fast, but at least at the temperatures of relevance to barrier discharges, the reaction of hydrocarbons with OH radicals is even faster.

It is interesting to compare the present results with those reported in the NIRE Annual Report (1996). Here a pulse generator was used, which showed to be very effective, especially when the pulse rise time was less than 100 *ns*, the pulse peak voltage over 25 *kV*

and the pulse frequency over 70 *pulse/s*. The experiments showed that for this optimum pulse frequency, 30 *min* or longer retention time in the discharge reactor was necessary to achieve complete decomposition of the species in question (see figure 6-28).

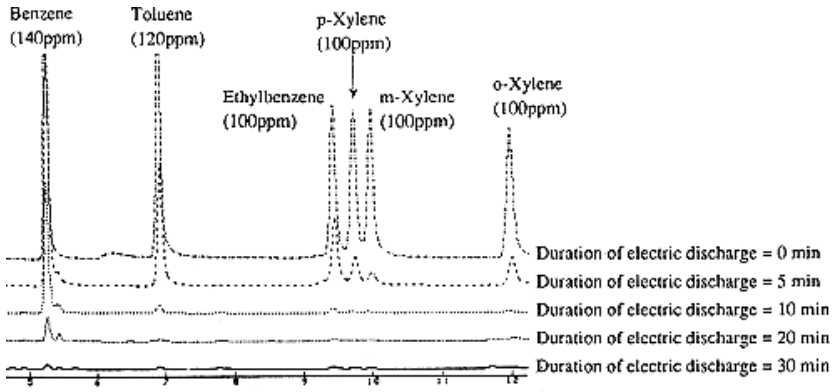

Figure 6-28: Decomposition of sample gas by electric discharge

6.3.4 Conclusion and recommendations for further work

An experimentally evaluation has been performed on a laboratory scale, single- and double dielectric-barrier discharge device as a means of removing CH_4 and C_3H_8 from a simulated reactive mixture inlet stream. The findings indicate that high-voltage high-frequency Tesla coil systems as power source for barrier discharge reactors, have a potentially reducing effect on the initial concentration of both CH_4 and C_3H_8. These experiments cannot however provide any specific or conclusive proof with regard to the physical mechanism or the kinetics of the process.

Stoichiometric air-methane (CH_4) and air-propane (C_3H_8) mixtures have been reduced in different batch-like barrier discharge systems developed at the local laboratory. The devices were all powered by an arrangement of commercially available Tesla coil units capable of high-voltage high-frequency output. The results from each of the different experiments are limited and sometimes only qualitative, but showed a tendency that the both CH_4 and C_3H_8 are reduced in a matter of a 3 to 6 *min* retention time. The most plausible mechanism for explaining the current achievements is the decomposition by direct electron impact. The slow rate of decomposition can be attributed to the

hydrocarbons being diluted in air and that much of the electrical energy therefore may have been wasted in producing unused radicals of the carrier gas. This is how most of the current non-thermal plasma processes work, through the ionization/dissociation of the carrier-gas molecules (N_2 and O_2) via collisions with energetic electrons and subsequent reaction of the radicals/ions thus produced with the target gas molecules.

Recommendations for further work

The work initiated at NTNU on dielectric barrier discharge techniques and high-frequency high-voltage technology indicated that there exists a potential of decomposing hydrocarbon molecules within a matter of minutes, at atmospheric pressure and low temperatures. The reason for using Tesla coils was that it is an inexpensive way of producing the necessary high-frequency voltages compared to commercially available power equipment. The disadvantage is the size of the apparatus. Extension of this work to high temperature gas streams and larger, more realistic flow rates should further be evaluated.

Several reputable laboratories, amongst them NIST-Physical and Chemical Properties Division, are making substantial advances in the area of plasma modelling and are now developing laboratory-validated databases for the purpose of modelling the processes associated with non-thermal plasma treatment of gas streams (Sieck et al. (1998)). Their program has focused on the creation and validation of an ion chemistry database for use in modelling plasma processes in addition to neutral-chemistry components that also will be pursued to describe more completely the total chemistry.

Any further advances on the work performed within this thesis should without doubt focus more towards the use of computer simulations before and in parallel to more extensive experiments with adequate measuring methods such as extensive use of mass spectrometry to verify some of the more qualitative observations obtained in this work. One such approach could be to use AURORA, which is a program that runs in conjunction with the CHEMKIN-III 3 and SURFACE CHEMKIN-III 4 packages, which handle the chemical reaction mechanisms for thermal and non-thermal systems. CHEMKIN-III allows for specification of electron-impact reactions, excitation losses, and elastic-collision losses for electrons. AURORA allows modelling of non-thermal, plasma reactors with the determination of ion and electron concentrations and the electron temperature, in addition to the neutral radical species concentrations.

CHAPTER 7.

SUMMARY, CONCLUSIONS AND RECOMMENDATIONS FOR FURTHER WORK

7.1 INTRODUCTION

This thesis was undertaken to study two different subjects both related to molecular decomposition, applying a shock tube- and non-thermal plasma to decompose selected hydrocarbons respectively. The first subject concerned thermal decomposition and oxidation of highly diluted nitromethane in a shock tube. The second subject concerned the application of non-thermal plasma to initiate reactions and decompose/oxidize selected hydrocarbons, methane and propane, in air and was sectioned into one theoretical and two experimental parts.

7.2 SHOCK TUBE EXPERIMENTS ON NITROMETHANE

The first subject concerned thermal decomposition and oxidation of highly diluted CH_3NO_2 (nitromethane, abbreviated as NM) in a shock tube. Physical and chemical properties were stated. The theory of nitromethane detonation structure, ignition process and the effect of additives on these parameters are reported. Some theories on nitromethane sensitising are discussed. The experimental part covered calibration of experimental apparatus, UV spectrum analysis and shock tube experiments.

The nitromethane spectrum was taken and analysed, showing that nitromethane do not absorb significantly at wavelengths above 350 *nm*, which is why nitromethane is transparent in the visible domain. The absorption minimum was located at approximately 242 *nm*. The spectrum was used when proper wavelengths was selected for the monochromator mounted on the shock tube, used for measuring nitromethane absorption during the course of decomposition.

By comparing the experimental against the calculated results it was verified that decomposition of highly diluted nitromethane at high-temperature conditions could be explained by the unimolecular dissociation reaction alone, given by the third body reaction as:

$$CH_3NO_2 + M \quad \rightarrow \quad CH_3NO_2 + M$$

Depending on the speed of the decomposition as calculated from the intensity profiles versus time, the decomposition experiments were separated into two groups: non-reactive and reactive. Experiments was found to be non-reactive when no decomposition was measured during 1 *ms* of registration for any given pressure and temperature. This was observed for reflected shock temperatures less than 990 *K*. Some experiments were lost because the decomposition was too fast to be registered by the preset oscilloscope time resolution.

Reflected shock experiments on NM decomposition, using mixtures of 0.2 to 1.5 *vol%* NM in nitrogen or argon were performed over the temperature range 850-1550 *K* and pressure range 190-900 *kPa*, with 46 experiments diluted in nitrogen and 44 diluted in argon. Out of these there were 9 experiments with no reaction. 54 (N_2/18, Ar/36) experiments were considered useful in the sense that they had been performed with no observable errors caused by external events and were within the range of measurability of the oscilloscope.

From the different plots of the experimental data, it can be seen that the experiments was performed in the transient region that is in the region between pressure dependent and independent rate constant. Heavy scattering was observed when the data were plotted over the entire pressure domain, both for NM decomposition and oxidation. By residual error analysis of the measured decomposition profiles it was found that NM decomposition ($CH_3NO_2 + M \rightarrow CH_3 + NO_2 + M$) corresponds well enough to a law of first order, verified down to the reaction half-life time. Arrhenius expressions were derived for the NM decomposition at different wavelengths and diluents from the plot of the best exponential fit of the experimental k-values versus the inverse of the temperature in the reflected shock, T_5.

Rate equations derived from experimental data with units in $cm^3/(mole \times s)$ in the Arrhenius form of $k = A \times \exp(-E_T/T)$ and $k = A \times \exp(-E_a/RT)$ with k in $cm^3/(mole \times s)$ were found as:

Diluent	Wavelength λ [nm]	The reaction rate constant, k $k = A \times \exp(-E_T/T(K))$ [$cm^3/(mole \times s)$]
N_2	220	$k = 1.026 \times 10^{17} \exp(-21960 / T(K))$
Ar	220-230	$k = 3.738 \times 10^{17} \exp(-24900 / T(K))$
For argon in separate wavelength domains		
Ar	220	$k = 2.820 \times 10^{17} \exp(-24480 / T(K))$
Ar	225	$k = 1.001 \times 10^{18} \exp(-26330 / T(K))$
Ar	230	$k = 5.867 \times 10^{16} \exp(-22420 / T(K))$

Parameters derived from the above Arrhenius expressions have further been extracted:

Diluent	Wavelength λ [nm]	A	E_T [K]	$E_a = E_T \times R$ $E_T \times R$ (kcal/mole×K) [kcal/mole]	 $E_T \times R$ (kJ/mole×K) [kJ/mole]
N_2	220	$10^{17.011}$	21960	43.6	182.6
Ar	220-230	$10^{17.574}$	24900	49.5	207.0
For argon in separate wavelength domains					
Ar	220	$10^{17.45}$	24480	48.6	203.6
Ar	225	10^{18}	26330	52.3	218.9
Ar	230	$10^{16.768}$	22420	44.5	186.4

In parallel to, and following the decomposition experiments, oxidative experiments on the ignition delay times of NM/O_2/Ar mixtures were investigated over high temperature and low to high pressure ranges. These experiments were carried out with eight different mixtures of gaseous NM and oxygen diluted in argon, with pressures ranging between

44.3-600 *kPa*, and temperatures ranging between 842-1378 *K*. Some experiments were carried out with highly diluted mixtures (mixture 5 at 98.65 *%* argon). The other experiments were carried out with mixtures diluted in 84 to 94 *%* argon at 235 *nm*. 76 experiments on nitromethane oxidation were carried out

The oxidation experiments were divided into three different types according to the type of decomposition signals achieved. For signals with emission (Type1: absorption signals with emission, Type 3: emission signals without light source) and for slightly or non-diluted mixtures the apparent quasi-constant activation energy was found from the correlations, to be 64.574 *kJ/mol* and 59.246 *kJ/mol*, respectively. For signals of type 1 and 3, the correlation for the ignition delay time was deduced as:

$$\tau = 0.3669 \cdot 10^{-2} \cdot [NM]^{-1.02}[O_2]^{-1.08}[Ar]^{1.42} \cdot \exp\left(\frac{7767}{T}\right)$$

,with an accuracy of 18.5 *%* and valid in the temperature and pressure domain between 44.3 <P< 277.94 *kPa* and 1026 <T< 1378 *K*, respectively. When the molar fraction of argon tends to unity ($z^{1.42} = 1$), and for slightly diluted mixtures, a different correlation may be derived as:

$$\tau = 0.3696 \cdot [NM]^{0.11}[O_2]^{-0.67}[Ar]^{0.0} \cdot \exp\left(\frac{7126}{T}\right)$$

, with an accuracy of 25 *%*.

For the absorption signals (Type 2: emission observed) a characteristic time was defined as the time interval between the arrival of the reflected shock and the instant when 10 *%* of the nitromethane had decomposed. By this definition the following correlation for the ignition delay time was found to be:

$$\tau_{10\%} = 0.3005 \cdot 10^{-2} \cdot [NM]^{-0.28}[O_2]^{0.12}[Ar]^{-0.59} \cdot \exp\left(\frac{13657}{T}\right)$$

, with an accuracy of 19.4 *%* and valid in the limited pressure and temperature domain between 52.48 <P< 483.29 *kPa* and 1001 <T< 1275 *K*, respectively. For slightly or non-diluted mixtures the correlation was found as:

$$\tau_{10\%} = 0.3844 \cdot 10^{-3} \cdot [NM]^{-0.12}[O_2]^{0.10}[Ar]^{0.0} \cdot \exp\left(\frac{13866}{T}\right)$$

, with an accuracy of 26.9 *%*.

A quasi-constant activation energy (ΔE) was deduced from the latter correlations to 113.544 *kJ/mol* and 115.282 *kJ/mol*, respectively.

Through computer simulations of the thermal NM decomposition it has been verified that the reaction mechanism indeed initiates through the third body decomposition of the nitromethane molecule as stated by previous authors. After the decomposition of the NM molecule, the reactions proceeds by two major and parallel pathways, which both includes radical reactions, to produce CH_2O. The latter acting as a source for further radicals when attacked by existing OH and H radicals, producing HCO radicals that will carry the reactions to completion. The simulated profiles correspond well to those obtained experimentally.

7.3 PROMOTION OF CHEMICAL REACTIONS BY NON-THERMAL PLASMA

The second subject of this thesis concerns the investigation of non-thermal plasma to initiate reactions and decompose/oxidize specific components in gaseous mixtures and is divided into one theoretical and two experimental parts. The process that has been investigated throughout this part is the decomposition of hydrocarbons, here represented as CH_4 and C_3H_8. It is the author's firm believe that substantial advances in the cleanup of low-concentration (below several percent) undesirable compounds from "contaminated" air streams can be achieved by exploiting non-thermal plasma treatment. In such discharges, chemical change is driven by a variety of processes including ionization, molecular excitation, ion-electron recombination, fragmentation of ions and excited molecules, and reactions of radicals, atoms, and ions.

The first approach to the subject concerning plasma decomposition was performed at the university of Orléans and covers a theoretical survey and experimental work done on the decomposition/reforming of low-to-stoichiometric concentration air/methane mixtures in a gliding arc discharge device. The basic theory and physical description of a gliding arc device is discussed. It was found that important quantities of NO_x were formed. When the discharge was run in pure air, the maximum concentration was achieved at the lowest flow-rate. Maximum NO_x concentration when cooling the reactor unit with either air or water, showed no significant differences. The NO_x production was found to be linear proportional to the air flow rate through the reactor, the highest flow rate giving the lowest

NO_x concentrations. At lower flow rates the residence time increases and more energy is distributed to the reacting volume resulting in higher temperature and thereby higher chemical activity and faster conversion to final products. NO_x was produced faster and in much larger quantities when the reactor was air cooled compared to water cooled.

Further, low-concentration methane in air, was partly reduced in a gliding discharge reactor at different residence times, the main products being CO_2 and CO (and H_2O, observed by not quantified). The CH_4 conversion rate was observed to increase with increasing residence time in the reactor (decreasing flow rate). The experiments indicated that the CH_4 conversion increases with increasing CH_4 concentration confirming previous experiments done by Tzech et al. (1994). As for the pure-air experiments, important quantities of NO_x was formed. Because of the methane content additional CO was produced. The quantities of these two components were produced in far higher concentrations when compared to conventional combustion. The NO_x concentration showed to increase with increasing residence time but with an insignificant difference for different methane concentrations. It was observed that when the methane concentration passed the lower flammability limit, important quantities of condensate was formed, having a sharp green colour and a smell of hydrocarbons and formaldehyde. Solid carbon was also observed. There is no doubt that more sophisticated measuring equipment is required to get a full understanding of the discharge process, at lest equipment that is more adapted to the magnitude and time dependence of the measured variables. More time should be spent on getting a more complete physical understanding of the process with a reactor adapted for this purpose. A deeper understanding would make the approach to applications easier and results more predictable.

Following the experiments on the gliding arc discharge device, a technique for hydrocarbon (CH_4 and C_3H_8) decomposition/conversion, known as the non-thermal discharge was considered. With this technique an electric field is utilized to produce high energy electrons in the gas stream while leaving the bulk temperature of the gas unchanged. The high energy electrons serve to directly decompose, and to generate reactive species such as O, OH, and HO_2 which again react with the species in question, through subsequent reactions.

The specific device configurations investigated were all of the dielectric barrier discharge type either as normal or double barrier type, meaning the discharge is sustained

between one or two dielectric surfaces respectively, that are backed by conductors. A high-frequency AC voltage is applied between the electrodes resulting in a series of short duration micro discharges that process the gas.

An experimentally evaluation has been performed on a laboratory scale, single- and double dielectric-barrier discharge device as a means of removing CH_4 and C_3H_8 from a simulated reactive mixture inlet stream. The findings indicate that high voltage high frequency Tesla coil systems as power source for barrier discharge reactors, have a potentially reducing effect on the initial concentration of both CH_4 and C_3H_8.

Stoichiometric air-methane (CH_4) and air-propane (C_3H_8) mixtures have been reduced in different batch-like barrier discharge systems developed at the local laboratory. The devices were all powered by an arrangement of commercially available Tesla coil units capable of high-voltage high-frequency output. The results from each of the different experiments are limited and sometimes only qualitative, but showed a tendency that the both CH_4 and C_3H_8 are reduced in a matter of a 3 to 6 *min* retention time. The most plausible mechanism for explaining the current achievements is the decomposition by direct electron impact. The slow rate of decomposition can be attributed to the hydrocarbons being diluted in air and that much of the electrical energy therefore may have been wasted in producing unused radicals of the carrier gas. This is how most of the current non-thermal plasma processes work, through the ionization/dissociation of the carrier-gas molecules (N_2 and O_2) via collisions with energetic electrons and subsequent reaction of the radicals/ions thus produced with the target gas molecules.

The initial experiments on ignition and flame propagation, were performed on stoichiometric mixtures of CH_4 and C_3H_8 in air in a wire-to-plane reactor. By theory, the gas discharge would produce both high energy electrons and free radicals that could break up and decompose the hydrocarbon molecules. Since the radicals must be produced from the species contained within the gaseous mixture, the radicals one could expect to be active in both these cases would be free oxygen atoms at different energy levels (O, $O(^3P)$, $O(^1D)$). Depending of the amount and energy level of the free electrons produced in the current discharge, direct attack of the hydrocarbons by electron or ion collisions was expected to have less effect than that of the radicals. If this was the only active process initiated by the discharges, total decomposition times in the order of many minutes could be expected. However, if sufficient amounts of radicals were produced in the active

discharge volume, a decomposition was expected to occur by the order of seconds. Decomposition of i.g. CH_4 by direct electron-impact dissociation would produce additional radicals through the following reactions:

$$CH_4 + e \rightarrow CH_2 + 2H + e \quad (7\text{-}1)$$

$$CH_4 + e \rightarrow CH_3 + H + e \quad (7\text{-}2)$$

Assuming that some or all these processes were active during the discharge, this would then decrease the hydrocarbon concentration as a function of time. If the hydrocarbon concentration had reacted below the flammability range, no ignition would occur and no flame would propagate through the tube. Another purpose with these experiments was to investigate whether a discharge that had been run only for a short period of time, would affect the flame propagation properties. To record the observations, a high-8 video camera was situated normally to the tube. From the visual observations of flame propagation with the high-8 recordings, there was no measurable effect on the propagation velocity when this occurred. This was probably because the active plasma only was produced in the upper section of the tube. Any changes to the mixture contained in the reactor section did not seem to affect the mixture in the following tube within the time of operation. These experiments therefore ended up to become more of a qualitative approach which answered; propagation occurred = YES and no propagation = NO, were no propagation was attributed to the effect of hydrocarbon decomposition by reactive species generated by the discharge. The results showed that there were no distinct limit between when ignition and propagation occurred and not. Causes for this could be inaccurate mixing, leakage or unstable operating performance of the power source. Another reason could be that the temperature gradient created in the plasma volume was sufficient to cause entrainment of the mixture contained inside the flame propagation section, and thereby altering the hydrocarbon concentration.

With C_3H_8 and runtimes from 3.5 *min* and upwards, experiments where no propagation was observed, were starting to occur. The mean runtime for experiments with no propagation was found to 4.3 *min*. This could indicate that at least some of the C_3H_8 had been completely or partly decomposed (or otherwise affected), so that the mixture was no longer flammable. The same pattern was found for the CH_4-mixture, with a necessary mean runtime of 5.1 *min* for experiments with no propagation to occur. Methane, among others, os known to have ionization energy larger than the ionization energy of molecular

oxygen. Therefore, a charge transfer from molecular oxygen cation is impossible. Previous work has concluded that these molecules have to be activated either by direct electron impact dissociation or via the free-radical processes. Since direct electron impact dissociation is a slower process in diluted mixtures, we can presume that this mechanism was the most probable cause for the currently achieved results.

To actually try to quantify the capability of the barrier discharge to decompose either C_3H_8 or CH_4 in air, recycling circuit of tubes was set up. Experiments in a double parallel plate reactor were performed. A stoichiometric mixture of C_3H_8 in air was run in the loop for different periods of time. According to these results, very little change in composition had occurred. Only some minor decrease in C_3H_8-concentration could be observed with increasing run-times. These indications of only very slow or non-existent decomposition can probably be attributed to the previously presumed mechanism. Free electrons are apparently produced, but probably lose most of their energy through collisions with the O_2 and N_2 molecules of the air. Any radicals produced are not in quantities high enough to have any substantial effect the concentration of the hydrocarbons. The type of reactor used here could also have been the cause for the very slow decomposition, if poorly designed.

Further experiments were performed on stoichiometric CH_4 mixtures in a double annular reactor using the same loop as previously mentioned. This time ambient air was used, containing some amount of water vapour. The aim with this was to see if the assumed effect of radical production from H_2O would improve the rate of decomposition. These results showed some similar behaviour as for the results obtained with the wire-to-plane reactor. Complete removal of CH_4 was achieved after 5-6 *min* in the discharge loop. This new double annular reactor seemed to be more effective compared to the previous results with the double parallel plate reactor, where almost no decomposition of C_3H_8 was achieved. Decomposition of CH_4 could now be achieved even if this molecule apparently is much harder to destruct that C_3H_8, according to previous work. This obtained decomposition can probably be attributed to a more effective reactor design combined with the addition of water vapour to the mixture. It is known that radicals from water vapour can be produced by the following reactions:

$$e + H_2O \rightarrow e + H + OH \quad (7\text{-}3)$$

$$O(^1D) + H_2O \rightarrow 2\,OH \quad (7\text{-}4)$$

The hydroxyl radical is one of the most reactive species known, with an oxidizing potential of 2.80 *V*, and it can be made through a variety of processes including the electron impact dissociation of water. Ozone follows at 2.07 *V*.

Other examples of reactions besides 7-1 and 7-2, that are of importance to the radical formation are:

$$e + O_2 \rightarrow e + O(^3P) + O(^3P) \quad (7\text{-}5)$$

$$e + O_2 \rightarrow e + O(^3P) + O(^1D) \quad (7\text{-}6)$$

$$e + N_2 \rightarrow e + N(^4S) + N(^4S) \quad (7\text{-}7)$$

$$e + N_2 \rightarrow e + N(^4S) + N(^2D) \quad (7\text{-}8)$$

$$e + CO_2 \rightarrow e + O + CO \quad (7\text{-}9)$$

$$O(^1D) + H_2O \rightarrow 2\ OH \quad (7\text{-}10)$$

O-radicals preferably react with hydrocarbon molecules thereby initiating a reaction chain forming several oxidizing radicals. One such reaction chain have been proposed in earlier work:

$$O + C_3H_6 \rightarrow CH_2CO + CH_3 + H \quad (7\text{-}11)$$

$$H + O_2 \rightarrow HO_2 \quad (7\text{-}12)$$

$$CH_3 + O_2 \rightarrow CH_3O_2 \quad (7\text{-}13)$$

The results obtained through all three types of experiments have indicated that a discharge system based on the Tesla coil principle, has the capability to completely or partly decompose both the investigated hydrocarbon components (C_3H_8 and CH_4) within a time exposure in the discharge between 3-6 *min*. The time for complete decomposition to occur is in accordance with earlier observations.

The different results achieved with the double parallel plate (without water vapour) and the double annular reactor (with water vapour), also showed the importance of a good reactor design, and that the reactor must be properly adjusted to the characteristics of the power source. The results also indicated that addition of water vapour as a source for radical production, might enhance the hydrocarbon decomposition. Two possible physical explanations to the decomposition are therefore:

1. Direct electron impact: Plasma electrons + hydrocarbons (C_3H_8, CH_4) → Products
2. Chemical (radical-promoted) reactions: Radicals + hydrocarbons (C_3H_8, CH_4) → Products

where the first mechanism is the most plausible for explaining the current results.

When hydrocarbons other than methane are present in the gas mixture, O-radicals preferably react with hydrocarbon molecules thereby initiating a reaction chain forming several oxidising radicals. One such reaction chain for propylene has earlier been proposed:

$$C_3H_6 + O \rightarrow C_2H_5 + HCO \quad (7\text{-}14)$$

$$C_3H_6 + O \rightarrow CH_2CO + CH_3 + H \quad (7\text{-}15)$$

$$C_3H_6 + O \rightarrow CH_3CHCO + H + H \quad (7\text{-}16)$$

Some of the products of this oxidation subsequently react further with oxygen to produce peroxy (HO_2) radicals. The hydrocarbon reaction with O atoms is fast, but at least at the temperatures of relevance to barrier discharges, the reaction of hydrocarbons with OH radicals is even faster.

Recommendations for further work

The work initiated at NTNU on di-electric barrier discharge techniques and high frequency high voltage technology indicated that there exists a potential of decomposing hydrocarbon molecules at atmospheric pressure and low temperatures.

The reason for using Tesla coils was that it is an inexpensive way of producing the necessary high-frequency voltages compared to commercially available power equipment. The disadvantage is the size of the apparatus. Extension of this work to high temperature gas streams and larger, more realistic flow rates should further be evaluated.

Several reputable laboratories, amongst them NIST-Physical and Chemical Properties Division, are making substantial advances in the area of plasma modelling and are now developing laboratory-validated databases for the purpose of modelling the processes associated with non-thermal plasma treatment of gas streams (Sieck et al. (1998)). Their program has focused on the creation and validation of an ion chemistry database for use in

modelling plasma processes in addition to neutral-chemistry components that also will be pursued to describe more completely the total chemistry.

Any further advances on the work performed within this thesis should without doubt focus more towards the use of computer simulations before and in parallel to more extensive experiments with adequate measuring methods such as extensive use of mass spectrometry to verify some of the more qualitative observations obtained in this work. One such approach could be to use AURORA, which is a program that runs in conjunction with the CHEMKIN-III 3 and SURFACE CHEMKIN-III 4 packages, which handle the chemical reaction mechanisms for thermal and non-thermal systems. CHEMKIN-III allows for specification of electron-impact reactions, excitation losses, and elastic-collision losses for electrons. AURORA allows modelling of non-thermal, plasma reactors with the determination of ion and electron concentrations and the electron temperature, in addition to the neutral radical species concentrations.

* * *

LIST OF REFERENCES

AEA Technology Products & Systems, www-paper at http://www.aeat-prodsys.com/subdivisions-div/ELECTROX1.html , 1999

Akshi, K., Pure Appl. Chem., 57 1197, 1985

Alston, L.L., High Voltage Technology, Oxford University Press (London, England), 1968

Amir-Ebrahimi, V., Booney, J. J., J.Mol.Catal. 50, L17, 1989

APP, APPLIED PLASMA PHYSICS AS, www-paper at http://www.app.no, 1997

Atkinson, R., Chem. Rev. 86, 69, 1986

Baddour, R.F., Timmius, R.S., "The Application of Plasma to Chemical Processing", MIT Press: Cambridge, MA, 1, 1967

Bardo, R., "Proceedings of the Eighth Symposium (Int) on Detonation", 1, 230, 1985

Blaustein, B. D.,"Chemical reactions in electrical discharges", Advances in chemistry, series 80, Miami Beach, 1969

Boenig, H.V., "Fundamentals of Plasma Chemistry and Technology", Technomic: Lancaster, 1988

Borisov, A., Kogarko, S.M., Skachkov, G., Kinet i Katal., 7:521, Russia, 1966

Bouios, M.I., "In High Energy Density Technologies in Materials Science; Garbassi, F., Occhiello, E., Eds.; Kluwer Academic: Dordrecht, The the Netherlands, p.49, 1990

Bradley D., Advanced Combustion Methods, Academic press, The effects of electric fields on combustion processes, kap 6, 1986

Brown, M.J., Parkyns, N.D., Catal Today 8, 305, 1991

Burcat, A. and Mc Bride, B., "1994 Ideal Gas Thermodynamic Data for Combustion and Air Pollution Use", Rapport Technion Aerospace Engineering, 697, 1994

Burch, R., Squire, C.D., Tsang, S.C., J.Chem.Soc., Faraday Trans.1 85, 3561, 1989

Calcote H. F., *Ion-molecule reactions*, Butterworths (London), vol. 2, Ions in flames, kap. 15, 1972

Cesser, H.D., Hunter, N.R., In Methane Conversion by Oxidative Processes, Wolf, E.E., Ed., Van Nostrand ReinhoId:New York, p.403, 1992

Chang, C.D., Hydrocarbons from Methanol; Marcel Dekker: New York, 1983

Chapelle, J. and Czernichowski A., Industrie, “Cahiers Francais de l’Electricité”, No. 4, p.20-21, 1992

CHEMKIN Collection CHEMKIN manual, Ed. Ellen Meeks, 1999

CHEMKIN-III file therm.dat V.3.0 January 1997, CVS Revision: 3.0 created Date 1997/05/01 21:31:14, 1997

Chernova A.A., Krishtopa L.G., Korobeinicheva O.P., Krasnoperov L.N., “Destruction of Ethane in Corona Discharge: Experiment and Modeling”, 5th International Conference on Chemical Kinetics, NIST, Gaithersburg, MD 20899 USA,16-20 July 2001

Choen, N., Dissertation, Univ. of California, Berkley, 1963

Coogan, J. J., Rosocha, L. A., Brower, M. J., Kang, M., Schmidt, C. A. “Proceedings of the ACS Special Symposium on Emerging Technologies in Hazardous Waste Management V”, Atlanta, GA, 27--29 Sept. 1993, American Chemical Society: Washington, DC, p. 642-645, 1993

Cook, M.D. and Haskins, P.J., “Decomposition of Nitromethane. A critical Study of the Initial Steps.”, 12th International Pyrotechnics Seminar, Juan les Pins, 43-48, 1987

Cook, M.D., “Shock Initiation of Nitromethane”, 12th International Pyrotechnic Seminar, Juan Les Pins, 393, 1987

Cormier M., Richard F., Chapelle J., Dudemaine M., Proc 2nd Int Conf on Electrical contacts, Arcs, Apparatus and Applications, 40-2, May 1993

Cotrell T., Graham T. and Reid T., “The thermal decomposition of Nitromethane”, Trans. Farad. Soc., 47, p. 584-590, 1951

Crawforth C.G, Waddington D.J, Trans. Far. Soc., 65:1334, 1969

Czech T., Czernichowski A., Mizeraczyk J., “Electrical assisted combustion of very lean methane-air mixtures”, GREMI, Internal paper, The University of Orléans, France, 1994

Czernichowski A, Pure Appl Chem, 66(6):1301, 1994

Czernichowski, A. and Ranaivosoloarimanana, A., “Zapping VOCs with a discontinuous electric arc”, CHEMTECH 1996, 26(4), p.45-49, 1996

Danner, G.A., Ed., Methanol Technology and Economics; AIChE: New York, 1970

Dechaux, J.C, Perche,A. “The modelling-Simulation Approach for the Determination of Kinetic Mechanisms; Two Examples: Oxidative Pyrolysis of Nitromethane and end of Reaction Phenomenon During Oxidation og Alkanes”, Oxidation Communications 3, No.2, p. 77-87, 1983

Delphi Automotive Systems, www-paper at http://www.delphiauto.com, September 2000

Dorai, R. and Kushner, M.J., "Plasma remediation of nox from diesel exhausts: Effects of propene and propane", Presentation, University of Illinois Department of Electrical and Computer Engineering Urbana, IL 61801, 1999

Dorai, R., Kushner, M.J., SAE paper no. 1999-01-3683, 1999

Dorko, E.A., Bass, D.M., Crosseley. R.W., Scheller, K., Combust. Flame, vol. 24, p. 173, 1975

Dremin, A.N., Rozanov, O.K. and Trofinov, V.S., Combustion & Flame, 7, 153, 1963

Edmund Scientific, Coil Manual for small Tesla coil

Edwards, T.H., Foster, N.R., FuelSci. Technol. Int. 4, 365, 1986

Eliasson, B. and Kogelschatz U., "Nonequilibrium volume plasma chamical processing", IEEE Trans. on plasma Science, vol. 19, No. 6, 1991a

Eliasson, B. and Kogelschatz, U., "Modeling and applications of silent Discharge plasmas", IEEE Trans. on plasma Science, vol.19, No. 2, 1991b

Engelke R. and Bdzil, Phys. Fluids, 26, 1210, 1983

Engelke, R., "Effect of a Chemical Inhomogeneity on Steady-State Detonation", Phys. Fluids, 23, 875, 1980

Engelke, R., Earl, W.L., and Rohlfing, C.M., J. Phys. Chem, 90, 545, 1986

Flinn, J.E., Ed. Engineering, Chemistry, and Use of Plasma Reactors; AIChE: New York, 1971

Fliszar, S., Minichino, C., "Bond Energies and Bond Dissociation Energies", Journal de Physique, 48, 9, 1987

Forshey, D.R., Cooper, J.C., Doyak, W.J., Explosivstoffe, 6, 125, 1969

Foster, N. R., Appl. Catal 19, 1., 1985

Frejacques, C., C.R. Acad. Sci. 231:1061, Thèse de Doctorat d'etat, Paris, 1953

Fridman A., Nester S., Kennedy L.A. , Saveliev A., Mutaf-Yardimci O., "Gliding arc gas discharge", Progress in energy and combustion science, Vol.25, No.2, p. 211-231, 1999

Fridman, A.A., Petrousov, A., Chapelle, J., Cormier, J.M., Czernichowski, A., Lesueur, H., Stevefelt, J., "Modèle physique de l'arc glissant", J.Phys. III, France 4, p. 1449-1465, 1994

Gentile, A. Catherine , “Kinetic processes and plasma remediation of toxic gases”, Thesis submitted at the University of Illinois at Urbana-Champaign, 1995

Glänzer, K. and Troe, J., “Thermische Zerfallsreaktionnen von Nitroverbindungen. I: Dissoziation von Nitromethan.”, Helvetica Chimica Acta, 55, (8), 1972

Granovsky, V.L., “Electrical current in Gas. Direct current”, Nauka, Moscow, 1971

Gogolides E., Buteau C. Rhallabi A. and Turban G., “Radio-frequency glow discharges in methane gas: modelling of the gas-phase physics and chemistry”, J. Pys. D: Appl. Phys. 27 p.818-825, 1994

Grothaus, M.G. and Fanick, E.R., “Harmful Compounds Yield to Nonthermal Plasma Reactor”, Southwest Research Institute (SwRI), www-paper at http://http://www.swri.org/3pubs/ttoday/spring96/ttoday2.htm, 1996

Guirguis R., Hsu D., Bogan D. and Oran E., “Investigation of the thermal initiation of detonation in Nitromethane”, JAYCOR, Naval Research Laboratory, 1983

Guirguis R., Hsu D.S.Y., Bogan D. and Oran E., “A Mechanism for Ignition of High Temperature Gaseous Nitromethane. The Key Role of the Nitro Group in Chemical Explosives”, Combustion & Flame, 61, 51-62, 1985

Guirguis, R., Oran, E.S. and Kailasanath, K., “The Effect of Energy Release on the Regularity of Detonation Cells in Liquid Nitromethane.” 21st Symposium (Int) on Combustion, 1659-1668, 1986

Hammer, T., “Non-thermal plasma treatment of automotive exhaust gases”, The VII-th International Symposium on High Pressure, Low Temperature Plasma Chemistry, Greifswald / Germany, September 2000

Hardesty, D.R., Combustion & Flame, 27, 229, 1976

Heinsohn R. S., Becker P. M., *Combustion tecnology - some modern developments* , Effects of electric fields on flames, kap. 9, Academic press (London), 1974

Herrmann, H.W., Henins, I. , Park, J. , Selwyn, G.S., “Atmospheric Pressure Plasma Jet for Chem/Bio Warfare Decontamination”, Poster, 41st Annual Meeting of the Division of Plasma Physics, November 15-19, Seattle, WA, 1999

Hillenbrandt, L.,Kirkpatrick,M.,J.Chem.Phys. 21:525, 1953

Howe, P., Frey, R. and Melani, G., “Observation Concerning Transverse Waves in Solid Explosives.”, Combust., Sci. Technol., 14, 63-74, 1976

Hsu, D.S.Y. and Lin, M.C., “Laser Probing and Kinetic Modeling of NO and CO Production in Shock-Wave Decomposition of Nitromethane under Highly Diluted Conditions.”, J.of Energetic Materials, 3, 95-127, 1985

Huang J., Badani M.V., Suib S.L., Harrison J.B. and Kablauoi M., “Partial Oxidation of Methane to Methanol through Microwave Plasmas. Reactor Design To Control Free-Radical Reactions”, J.Phys.Chem., 98, p.206-210, 1994

Huang, J., Suib, S.L., Proceedings of GRI Conference, Florida, 1992

ISPC-7 Eindhoven, Paper number P-1-6 “Studies On Non-Initiator Methane Oxidatioh To Formaldehyde In Non-Equilibrium Plasma” Liu Wanying, Huang Dairong, Zhang Jiren, Zhang JiB Chengdu Institute of Organic Chemistry,Academia Si, July 1985

Junl-Dam, T and Brockmeier, N.F., Ind. Eng. Chem Prod Res. Dev, 9, 388, 1970

Kang, J.G., Lee, S.W., Yun, S.S., Choi, S.N., and Kim, C.S., Combust. Flame, vol. 85, p. 275-278, 1991

Kato, Y., Bauer, P., Brochet, C., Bouriannes, R., “Brightness Temperature of Detonation Wave in Nitromethane Mixtures and in Gaseous Mixtures at High Initial Pressure”, Seventh Symposium (Int.) on Combustion, 1981

Kato, Y., Bouriannes, R., Brochet, C., “Mesure de la Temperature de Luminance des Détonations d'Explosifs Transparents et Opaques”, Actes du Symp. H.D.P., C.E.A., 139, 1979

Kato, Y., Brochet, C., “Cellular Structure of Detonation in Nitromethane Containing Aluminium Particles” in Proceedings of the Sixth Int. Symposium on Detonation, 124, 1976

Khan, M.M., Somorjai, C.A., J.Catal 91, 263., 1985

Kharas, K.C.C., Lunsford, J.H.J., Am. Chem. Soc. 111, 2336., 1989

Kieffer, L.J. , “A Compilation of Electron Collision Cross Section Data for Modeling of Gas Discharge Lasers”, JILA report no. ICR 13, NTIS, Springfield, Virginia, 1973

Klein, M., “Barrierenentladungen zur Entstickung motorischer Abgase, Dissertation”, Universität Karlsruhe, 1995

Kondrikov, B.N., Kozak, G.D., Raikova, V.M. and Starshinov, A.V., Sov. Phys. Dokl, 233, 315, 1977

Krasnoperov, L.N. and Krishtopa, L.G., “Kinetic and Mechanism of Hydrocarbons Transformation in Dielectric Barrier Corona Discharge”, 5th International Conference on Chemical Kinetics, NIST, Gaithersburg, MD 20899 USA,16-20 July 2001

Lawton J., Weinberg F. J., Electrical aspects of combustion, Clarendon press (Oxford), 1969

Lee, J.J., Frost, D.L. and Lee, J.H.S., “Propagation of Nitromethane Detonations in Porous Media” 14th. Int. Colloquium on the Dynamics of Explosions and Reactive Systems, Coïmbria, 1993

Lelevkin, V.M., Otorbaev D.K., Schram, D.C., “Physics of non-equlibrium plasmas”, Elsevier Science Publishers B.V. Amsterdam, ISBN 0444895337, 1992

Lesuer H., Czernichowski A. and Chapelle J., Brevet Francais 2639172, 1989

Lesuer H., Czernichowski A. and Chapelle J., J.Phys., Colloq. France 51, C5, 1990

Lifshitz,A., “Shock Tubes and Waves”, Proc. 14th Int. Symp. on Shock Tubes and Waves, p. 26-40, New South Wales Univ. Press, Kensington, Aust. 1984

Litex, Inc., 340 North Westlake Boulevard, Westlake Village, CA 91362, www-paper at www.litexcorp.com, 1999

Liu, H.F., Liu, R.S., Liew, K.Y., Johnson, R.E., Lunsford, J.H., J.Am.Chem.Soc. 106, 4117. Morton, L A. Prep. Symp. on Methane, 1984

McCarthy, R.J., J. Chem. Phys. 22, 1360, (1954)

Melius, C.F, “Molecular Decomposition of Energetic Materials.”, ONR Workshop on Energetic Materials, 1988

Moulard, H., Fauquignon, C., Lichtenberg, M., Lombard, J.M., “Détonation de Mélanges Al-NO_2”, Actes du Symp. H.D.P., C.E.A., 293, 1979

Mukkavilli, S., Lee C.K., Varghese K., Tavlarides L.L., Modeling of the electrostatic corona discharge reactor, IEEE Trans. on plasma Science, vol. 16, No. 6, 1988

NIST Standard Reference Database 17, NIST Chemical Kinetics Database Version 5.0 - Data coverage through 1992, Data and bibliographic citations abstracted and edited by: F.Westley, D.H.Frizzell, J.T.Herron, R.F.Hampson, W.G.Mallard; Chemical Kinetics & Thermodynamics Division - NIST, Database developed by: W.G. Mallard, Chemical Kinetics & Thermodynamics Division NIST. Distributed by: NIST Standard Reference Data Gaithersburg, MD 20899 USA, 1992

Penetrante B.M., Schultheis S.E., “Non-Thermal Plasma Techniques for Pollution Control”, Nato ASI series, Springer-Verlag, Series G: Ecological Sciences, Vol. 34, Part A (Proceedings of the NATO Advanced Research Workshop on Non.Thernal Plasma Tecniques for Pollution Control, held at Cambridge, England 1992), 1993

Penetrante et al., SAE paper no. 1999-01-3687, 1999

Perche, A., Tricot, J.C. and Lucquin, M., “The Pyrolysis of Nitromethane. Part 1. Experimental Study : Nitromethane Alone and in the Presence of Additives.”, J. Chem. Research, (S), 116-117, 1979, + (M), 1555-1578, 1979a

Perche, A., Tricot, J.C. and Lucquin, M., “The Pyrolysis of Nitromethane. Part 2. Determination of a Simplified Mechanism; Bibliographic Review of Rate Constants.”, J. Chem. Research, (S), 304-305, 1979, + (M), 3219-3256, 1979b

Periana, R.A., Taube, D.J., Evitt, E.R., Loffler, D.G., Wentrcek, Masuda, T., Science 259, 340.P. R., Voss, C., 1993

Pitchai, R., Klier, K., Catal. Rev-Sci. Eng. 28, 13., 1986

PlasmaSol, LLC, www-paper at http://www.plasmasol.com/, 2000

Power Engineering Group, Eindhoven University of technology, P.O.Box 513, 5600MB Eindhoven, “Pulsed corona, a new technology to clean gas and liquid flows”, www-paper at http://www.ele.tue.nl/evt/ehc/corona/corona.htm, 1999

Presles H.N, Desbordes D., Guirard M., Guerraud C.; “Nitromethane and nitromethane-oxygen mixtures: a new detonation structure.”, Communication presented at 15th ICDERS, Boulder, Colorado, 1995

Presles, H.N., Brochet, C., “Influence of Additives on Nitromethane Detonation Characteristics”, Seventh Symposium (Int.) on Combustion, 583, 1981

Presles, R.N., Campos, J., Heuze, O. and Bauer, P., “Effects of Microballoons Concentration on the Detonation Characteristics of Nitromethane-PMMA Mixtures”, in Proceedings of the Ninth Int. Symposium on Detonation, 362, 1989

Ritter E.R. and Bozzeli J.W., THERM: Thermodynamic property estimation for radicals and molecules, New Jersey Institute of Technology, 1987

Rogers, John W.; Nejezchleb, Allen J.; Rolader, Glenn E.; Federle, Steven P.; Littrell, Donald M; Neely, William C.; Newhouse, E. Irene, “Barrier Discharge Optimization for Nitric Oxide Destruction”, accepted for publication in a special non-thermal discharge issue of the Journal of Advanced Oxidation Technologies, 1996

Rosocha L. A., Los Alamos National Laboratory LA-UR 96-595, 96-728, 96-729, 94-4278, (Online) Available http://mwanal.lanl.gov/CSTftp/094031/rosocha/aot_overview.html, May 6 (1996)

Shchelkin, K.I., Zh. Eksperim. i Teor. Fiz., 36, 600, 1959

Shilov, A.E., In The Activation of Saturated Hydrocarbon by Transition Metol Complexes, D. ReideI: Dordrecht, The NetherIands, 1984

Sieck, L.W.; Herron, J.T.; Green, D.S. (U. Md); Buckley T.J. and Hunter E. P., "Experimentally Validated Database for Neutral/Ion Kinetics for Plasma Processes", NIST Technical Highlights, www-paper at http://properties.nist.gov/TAR/file12.html, 1998

Sigmond, R.S., "Corona discharge induced physical and chemical processes : plasma-chemical gas treatment and depolution", Project ELION 16 (updated june 1993), 1993

Sigmond, R.S., Kompendie i faget ladete partikler, Inst. for Fysikk, NTNU, rev. 1996

Skjørli V., "Study of Thermal Decomposition and Oxdation og Gaseous Nitromethane, by using the shock tube method", Laboratoire de Combustion et Systèmes Réactifs, CNRS - France, 1995

Society of Automotive Engineers, "Non-Thermal Plasma for Exhaust Emission Control: NOx, HC, and Particulates", SAE special publication no. SP-1483, 1999

Society of Automotive Engineers, "Plasma Exhaust Aftertreatment", SAE special publica-tion no. SP-1395,1998

Suib S.L., Zhang S., U.S Patent 5, 015, 349 May 14, 1991

Suib S.L., Zhang Z., U.S. Patent 5,131,993' July 21, 1992

Taylor H. and Vesselovsky V., "The pyrolysis of Nitromethane", J. Phys. Chem., 39, p. 1095-1101, 1935

Thomas G.O., Edwards M.J., Jones S.A., "Corona-Induced Oxidation of Reactive Gaseous Mixtures", Brief communication, Combustion and Flame, 92:197-200, 1993

Thomas G.O, Suzanne E., Martin A.R., Raybone D., Shawcross J.T., Ka L., Beech P., Whitehead J.C., "Non-Thermal Plasma Aftertreatment of Particulates Theoretical Limits and Impact on Reactor Design", prepared for submittal to the SAE Spring Fuels and Lubes Conference, Paris, 19-22, June 2000

Tricot J.C, Perche A., Lucquin M., "Gas Phase Oxidation of Nitromethane", Combust. and Flame,vol. 40, p.269-291, 1981

Ullmann's Encyclopedia of Industrial Chemistry, article on “Oxidation”, Release 2000, Sixth Edition, 1998

Up-To-Date Umwelttechnik AG, Linthlistr. 9, CH-8868 Oberurnen, Web-paper at http://www.up-to-date.ch/utd.nsf/Alle/eHomepage, 1999

Urtiew P.A., Kusubov A.S. and Duff R.E., Combustion & Flame, 14, 117, 1970

van Heesch E.J.M., Pemen A.J.M., Yan Keping, van Paasen S.V.B, Ptasinski K.J., Matyáš Z., Huijbrechts P.A.J.H., Hultermans B.J., Nicoletti A., “Experimental Program Of The Pulsed Corona Tar Cracker”, Eindhoven University of Technology, The Netherlands. P. Zacharias, ISET, Institute for Solar Energy Development, Kassel, Germany, Accepted for 12 th IEEE International Pulsed Power Conference, Monterey CA, 1999

Venugopalan, M., . Veprek, 5. Top. Curr Chem. 107, 1983

Vogtlin, George E., Internet paper, Defense Sciences Engineering Division, Electronics Engineering, 1994

von Engel , A., “Electric plasmas: Their nature and uses”, Taylor & Francis Ltd., London and NY, 1983

Worthen, R., Internet paper, “A Study of the Removal of Nitric Oxide in the Corona Discharge”, University of New Hampshire, Chemical Dep., 1996

Xu, X. and Kushner, M., “Plasma remediation of toxic gases”, Department of electrical and computer engineering, University of Illinois at Urbana/ Champaign, www-paper at http://uigelz.ece.uiuc.edu/Projects/PRTG/, 1999

Yarlagadda, PS., Morton, L.A., Hunter, N.R., Cesser, H.D., Ind.Eng.Chem.Res. 27, p.252, 1988

Zaslonko, I.S., Kogarko, S.M., Mozzhukhin, E.B. and Petrov, Y.P., “Thermal Decomposition of Nitromethane in Shock Waves”, Kinet. Katal, 13, (5), p.1113-1118, 1972

Zerger, R.P., Suib, S.L, Zhang, Z., Symposium On Natural Gas upgrading II, Preprint ACS, Div. Pet. Chem., San Francisco, April 5-10, p.344-348, 1992

APPENDIXES

APPENDIX A

Shock Tube Calculations

- The Law Of Beer-Lambert
- Concentration from the decomposition signals
- Calculating the parameters of the reflected shock
- Incident Shock Parameter Calculations
- Reflected Shock Parameter Calculations

The Law of Beer-Lambert

The Beer-Lambert law (or Beer's law) is the linear relationship between absorbance and concentration of an absorbing species. Modern absorption instruments can usually display the data as either transmittance, %-transmittance, or absorbance. An unknown concentration of an analyte can be determined by measuring the amount of light that a sample absorbs and applying Beer's law. The Beer-Lambert law can be derived from an approximation for the absorption coefficient for a molecule by approximating the molecule by an opaque disk whose cross-sectional area, σ, represents the effective area seen by a photon of frequency ω. If the frequency of the light is far from resonance, the area is approximately 0, and if ω is close to resonance the area is a maximum (see figure).

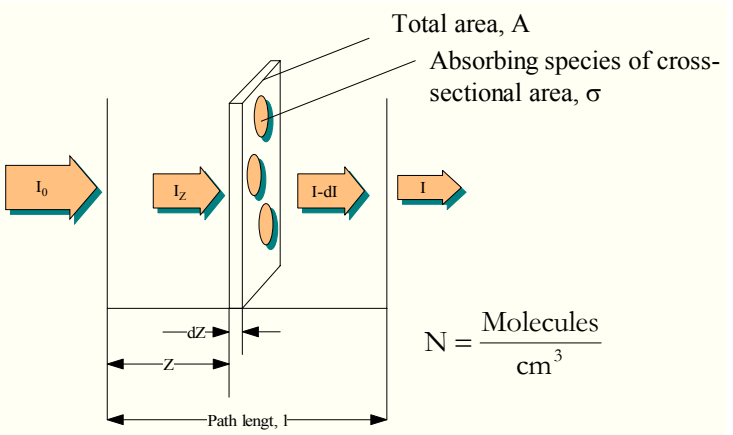

From the measured absorption signal and from knowledge of the molecular extintion coefficients, it is possible to determine the evolution of the concentration as a function of time. The concentration can be calculated from the BEER-LAMBERT expression for the optical density as deduced from the above figure and given by :

$$D = \varepsilon \cdot l \cdot C \qquad \textbf{A-1}$$

where :

C : reactant concentration [mol/m^3]

l : optical distance (tube diameter) [m]

ε : molecular extinction or absorption coefficient [m^2/mol]

The optical desity is also defined as :

$$D = \log\left(\frac{I_0}{I}\right) \qquad \textbf{A-2}$$

Where :

I_0 : incident intensity

I : transmitted intensity

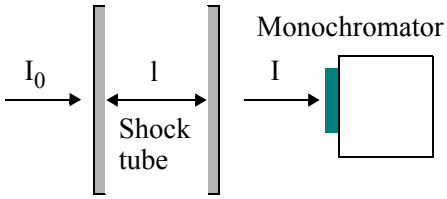

Experimental measurements are usually made in terms of transmittance (T), which is defined as:

$$T = \frac{I}{I_0} \qquad \textbf{A-3}$$

Modern absorption instruments can usually display the data as either transmittance, %-transmittance, or absorbance. An unknown concentration of an analyte can be determined by measuring the amount of light that a sample absorbs and applying Beer's law.

The intensity is directly proporsional to the amplitude of the signal from the photomultipliater for a given imposed voltage. We can write :

$$I_0 = k \cdot (V_f - V_0) \qquad \textbf{A-4}$$

$$I = k \cdot (V_f - V(t)) \qquad \textbf{A-5}$$

where:

V_0 : signal measured with PM when the tube is empty

V_f : signal measured with PM closed

$V(t)$: signal measured with PM as a function of time during the thermal decomposition

The optical density as a function of time, D(t), can then be written as:

$$D(t) = \log\left[\frac{I_0}{I}\right] = \log\left[\frac{V_f - V_0}{V_f - V(t)}\right] \qquad \textbf{A-6}$$

The initial concentration behind the reflected shoc is :

$$C_i = \frac{x_i \cdot p}{R \cdot T} \qquad \textbf{A-7}$$

where x_i is the initial molar fraction for specie i.

Knowing the pressure and the temperature in the differents states, the molecular extinction coeffisient, ε_i, is determined from the following expression:

$$\varepsilon_i = \frac{D_i}{C_i \cdot l} = \frac{D_i \cdot R \cdot T_i}{X_i \cdot p_i \cdot l} \qquad \textbf{A-8}$$

With i = 1, 2 or 5 (1 :initial unshocked condition, 2 :insident shock, 5 : reflected shock).

After having determined ε_i, the concentration as a function of time is given by:

$$C_i(t) = \frac{\log\left[\frac{V_f - V_0}{V_f - V(t)}\right]}{\varepsilon_i \cdot l} \qquad \textbf{A-9}$$

or in terms of the natural logarithm as:

$$C_i(t) = \frac{\ln\left[\frac{V_f - V_0}{V_f - V(t)}\right]}{\varepsilon_i \cdot l} \cdot \frac{1}{\ln 10} \qquad \textbf{A-10}$$

where ε_i is considered constant during the decomposition.

The normalized concentration in the decomposition region after the reflected shock, can then be expressed as:

$$\frac{C_i(t)}{C_5} = \frac{\ln\left[\frac{V_f - V_0}{V_f - V(t)}\right]}{\ln\left[\frac{V_f - V_0}{V_f - V_5}\right]} = \frac{\ln\left[\frac{V_f - V_0}{V_f - V(t)}\right]}{\ln 10} \cdot \frac{1}{D_5} \qquad \textbf{A-11}$$

If the absorbtion due to the reaction products after an infinite time interval, V_∞, is significantly different from the absorbtion at t=0, the correlation is must be extended to take this into account:

$$\frac{C(t)}{C_0} = \frac{\ln\left[\frac{V_f - V_0}{V_f - Vt}\right] - \ln\left[\frac{V_f - V_0}{V_f - V_{t=\infty}}\right]}{\ln\left[\frac{V_f - V_0}{V_f - V_{t=0}}\right] - \ln\left[\frac{V_f - V_0}{V_f - V_{t=\infty}}\right]} \qquad \textbf{A-12}$$

Limitations of the Beer-Lambert law

The linearity of the Beer-Lambert law is limited by chemical and instrumental factors. Causes of nonlinearity include:

- deviations in absorptivity coefficients at high concentrations (>0.01M) due to electrostatic interactions between molecules in close proximity.
- scattering of light due to particulates in the sample.
- fluoresecence or phosphorescence of the sample.
- changes in refractive index at high analyte concentration.
- shifts in chemical equilibria as a function of concentration.
- non-monochromatic radiation, deviations can be minimized by using a relatively flat part of the absorption spectrum such as the maximum of an absorption band.
- stray light.

Calculating the Concentration from the Decomposition Signals

Procedure, “lecture”, in turbopascal from “CONC.PAS” which reads data registred by the oscilloscope and calculates the concentration, in mol/m^3, of CH_3NO_2 for each time point registred.

Explanation:

Line 18, 19: Density, D_5, and maximum start concentration in the reflected shock, C_5, is entered.

Line 34-47: Mean lower and upper densities are calculated from measurements with tube evacuated and tube filled with given mixture of NM/dilutant.

Line 48- : From the law of Beer-Lambert, the relative concentration profile, $C(t)/C_5$, is calculated and saved to file.

```
8   ------------------------------------
9        procedure lecture;
10  ------------------------------------
11  var
12   fd1,fd2,fd3                  :file of byte;
13   d1,d2,d3                     :byte;
14   dd1,dd2,dd3,somd1,somd2      :real;
15   fic_trait                    :array[1..3] of string;
16   temps, D5, C5                :real;
17   kk                           :integer;
18   fd36                         :text;
19   lnrelcon                     :array[1..4001] of real;
20  begin
21   closegraph;
22   window(1,1,80,24);
23   textbackground(0);textcolor(blanc);
24   clrscr;
25   Write('D5  :');readln(D5); {calculated density from exp. data}
26   Write('C5  :');readln(C5); {calculated start conc. in the refl. shock}
27   Writeln(ln(10));
28   fic_trait[1]:=nomfich+'ZV1';
29   assign(fd1,fic_trait[1]);
30   reset(fd1);
31   fic_trait[2]:=nomfich+'ZV2';
32   assign(fd2,fic_trait[2]);
33   reset(fd2);
34   fic_trait[3]:=nomfich+'V1';
35   assign(fd3,fic_trait[3]);
36   reset(fd3);
37   seek(fd1,npi);
38   seek(fd2,npi);
39   seek(fd3,npi);
40   j:=npi;
41   somd1:=0;
```

```
42   somd2:=0;
43   kk:=0;
44   for i:=npi to npf do
45    begin
46     read(fd1,d1);
47     read(fd2,d2);
48     somd1:=somd1+d1;
49     somd2:=somd2+d2;
50    end;
51   dd1:=somd1/(npf-npi);
52   dd2:=somd2/(npf-npi);
53   close(fd1);
54   close(fd2);
55   assign(fd36,nomfich + 'titi.dat');
56   rewrite(fd36);
57   Writeln(fd36,'Time',' ','LNrelcon',' ','relcon',' ','conc_[mol/m^3]');
58   Repeat
59    read(fd3,d3);
60    relcon[j]:=ln((dd2-dd1)/(dd2-d3))/D5;
61    lnrelcon[j]:=ln(relcon[j]);
62    temps:=(j-npi)*vs*10/4000;
63    IF (relcon[j] >= 0.4)
64     THEN
65     Writeln(fd36,temps*0.000001,' ',lnrelcon[j],' ',relcon[j],' ',relcon[j]*C5/1E6);
66    j:=j+1;
67   Until (j=npf);
68   close(fd36);
69   close(fd3);
```

* * *

Calculating the Parameters of the Reflected Shock

The temperature dependent heat capasity

```
70  FUNCTION CP(T:DOUBLE):DOUBLE;
71
72  VAR
73       VALEUR1:REAL;
74
75  BEGIN
76      IF T<1000 THEN
77      BEGIN
78          VALEUR1:=0;
79          FOR J:=1 TO NBCP DO
80          BEGIN
81              VALEUR:=0;
82              FOR I:=1 TO 5 DO
83                 VALEUR:=VALEUR+(COEF_F[INC[J],I]*EXP((I-1)*LN(T)));
84              VALEUR1:=VALEUR1+X[J]*VALEUR*R;
85          END;
86           CP:=VALEUR1;
87      END
88      ELSE
89      BEGIN
90      VALEUR1:=0;
91      FOR J:=1 TO NBCP DO
92      BEGIN
93          VALEUR:=0;
94          FOR I:=1 TO 5 DO
95              VALEUR:=VALEUR+(COEF_I[INC[J],I]*EXP((I-1)*LN(T)));
96          VALEUR1:=VALEUR1+X[J]*VALEUR*R;
97      END;
98      CP:=VALEUR1;
99      END;
100 END;
```

The enthalpy at 298 K

```
101 FUNCTION H298(K:integer):DOUBLE;
102
103
104 VAR
105      VALEUR1:REAL;
106      i1:integer;
107
108 BEGIN
109         VALEUR1:=0;
110         VALEUR:=0;
111         FOR I1:=1 TO 5 DO
112               VALEUR:=VALEUR+COEF_F[K,I1]*EXP(I1*LN(298))/I1;
113         VALEUR1:=(COEF_F[K,6]+VALEUR)*8.314;
114         H298:=VALEUR1;
115 end;
```

The temperature dependent entalpy

```
116 FUNCTION H(T:DOUBLE):DOUBLE;
117
118 VAR
119      VALEUR1:REAL;
120
121 BEGIN
122     IF T<1000 THEN
123     BEGIN
124         VALEUR1:=0;
125         FOR J:=1 TO NBCP DO
126         BEGIN
127           VALEUR:=0;
128           FOR I:=1 TO 5 DO
129               VALEUR:=VALEUR+COEF_F[INC[J],I]*EXP(I*LN(T))/I;
130            VALEUR1:=VALEUR1+X[J]*(COEF_F[INC[J],6]+VALEUR)*8.314;
131         END;
132         H:=VALEUR1;
133     END
134     ELSE
135     BEGIN
136         VALEUR1:=0;
137         FOR J:=1 TO NBCP DO
138         BEGIN
139             VALEUR:=0;
140             FOR I:=1 TO 5 DO
141                 VALEUR:=VALEUR+COEF_I[INC[J],I]*EXP(I*LN(T))/I;
142             VALEUR1:=VALEUR1+X[J]*(COEF_I[INC[J],6]+VALEUR)*8.314;
143         END;
144         H:=VALEUR1;
145     END;
146 END;
```

The speed of the incident shock

```
147 FUNCTION U1(T1A,T2A:REAL):DOUBLE;
148
149 VAR
150     KSI: DOUBLE;
151
152 BEGIN
153      H2:=H(T2A);
154      H1:=H(T1A);
155      KSI:=2*(H2-H1)/R+T1A-T2A;
156      RO21:=(KSI+SQRT(KSI*KSI+4*T1A*T2A))/(2*T2A);
157      U1:=SQRT(RS*(RO21*T2A-T1A)/(1-1/RO21));
158 END;
```

The speed of the reflected shock

```
159 FUNCTION U5(T2A,T5A:REAL):DOUBLE;
160 VAR KSI: DOUBLE;
161 BEGIN
162      H5:=H(T5A);
163      H2:=H(T2A);
164      KSI:=2*(H5-H2)/R+T2A-T5A;
165      RO52:=(KSI+SQRT(KSI*KSI+4*T2A*T5A))/(2*T5A);
166      U5:=SQRT(RS*(RO52*T5A-T2A)/RO52/(RO52-1));
167 END;
```

The ρ, γ, Mach numbers and the temperature of the reflected shock

```
168 PROCEDURE CALCUL;
169
170 BEGIN
171     FENETRE(5,2,77,24,4);
172     VS:=LONG*1E3/TEMPS;
173     RS:=R*1E3/MASSE_MOY;
174     GAMMA:=CP(T1)/(CP(T1)-R);
175     A1:=SQRT(GAMMA*R*T1*1000/MASSE_MOY);M:=VS/A1;M2:=M*M;
176     RO1:=P1/(T1*RS);
177      IF M>1 THEN
178      BEGIN
179           T21:=(1+M2*(GAMMA-1)/2)*(M2*2*GAMMA/(GAMMA-1)-1)/
180                (M2*(GAMMA+1)*(GAMMA+1)/(2*(GAMMA-1)));
181           T2:=T21*T1;
182           DT:=100;
183           REPEAT
184                T2:=T2-DT+2*DT*(VS-U1(T1,T2-DT))/(U1(T1,T2+DT)-U1(T1,T2-DT));
185                DT:=DT/2;
186           UNTIL ABS(DT)<1E-2;
187           U2:=U1(T1,T2)/RO21;
188           T5:=2*T2;
189           DT:=100;
190           REPEAT
191                ERR1:=U2*(1-RO21)-U5(T2,T5-DT)*(1-RO52);
192                ERR2:=U2*(1-RO21)-U5(T2,T5+DT)*(1-RO52);
193                T5:=T5+ERR1*2*DT/(ERR1-ERR2);
194                DT:=DT/2
195           UNTIL ABS(DT)<1E-2;
196 END;
197
198 END;
```

* * *

Incident Shock Parameter Calculations

The velocity before and after the shock front, in shock-fixed coordinates, can be expressed as:

$$u_1 = U_s - U_1 \quad \textbf{A-13}$$

$$u_2 = U_s - U_2 \quad \textbf{A-14}$$

The laws of mass, momentum and energy conservation are:

$$\rho_1 u_1 = \rho_2 u_2 \quad \textbf{A-15}$$

$$p_1 + \rho_1 u_1^2 = p_2 + \rho_2 u_2^2 \quad \textbf{A-16}$$

$$h_1 + \frac{1}{2}u_1^2 = h_2 + \frac{1}{2}u_2^2 \quad \textbf{A-17}$$

By eliminating u_2 in eq. A-16 and combining with eq. A-17 leads to the Rankine-Hugoniot equation:

$$h_2 - h_1 = \frac{1}{2}(p_2 - p_1)\left(\frac{1}{\rho_1} + \frac{1}{\rho_2}\right) \quad \textbf{A-18}$$

The enthalpy is a fuction of temperature alone, hence:

$$H_i = C_p T_i = C_p \cdot \frac{p_i W_i}{\rho_i R} \quad \textbf{A-19}$$

$$h_i = \frac{H_i}{W_i} = \frac{C_p}{C_p - C_v} \cdot \frac{p_i}{\rho_i} \quad \textbf{A-20}$$

$$h_i = \frac{\gamma}{\gamma - 1} \cdot \frac{p_i}{\rho_i} \quad \textbf{A-21}$$

Elininating u_1 and u_2 from eq. A-15 and eq. A-16 and rewriting eq. A-17 with the latter equation gives:

$$\frac{\rho_1 p_2 - \rho_2 p_1}{\rho_2 p_2 - \rho_1 p_1} = \frac{\gamma - 1}{\gamma + 1} \quad \textbf{A-22}$$

which by rearrangement gives:

$$\frac{\rho_2}{\rho_1} = \frac{\left(\frac{\gamma-1}{\gamma+1} + \frac{p_2}{p_1}\right)}{\left(\frac{\gamma-1}{\gamma+1}\right) \cdot \frac{p_2}{p_1} + 1} \qquad \textbf{A-23}$$

Given the Mach number as: $M_1 = \frac{u_1}{a_1} = \frac{U_s}{a_1}$,

where a_1 is the speed of sound in the test gas.

gives:

$$a_1 = \sqrt{\frac{\gamma R T_1}{M}} = \sqrt{\frac{\gamma \cdot p_1}{\rho_1}} \qquad \textbf{A-24}$$

and the Mach number as:

$$M_1 = u_1 \sqrt{\frac{\rho_1}{\gamma \cdot p_1}} \qquad \textbf{A-25}$$

We then obtain from eq. A-15 and eq. A-16:

$$\frac{p_2}{p_1} = 1 + \frac{\rho_1 \cdot u_1}{p_1}\left(1 - \frac{\rho_1}{\rho_2}\right) \qquad \textbf{A-26}$$

Introducing eq. A-25 gives:

$$\frac{p_2}{p_1} = 1 + \gamma \cdot M_1^2 \cdot \left(1 - \frac{\rho_1}{\rho_2}\right) \qquad \textbf{A-27}$$

We then combine eq. A-23 and eq. A-27 to yield:

$$\frac{p_2}{p_1} = \frac{2 \cdot \gamma \cdot M_1^2 - (\gamma - 1)}{\gamma + 1} \qquad \textbf{A-28}$$

From the last two equations:

$$\frac{\rho_2}{\rho_1} = \frac{(\gamma + 1) \cdot M_1^2}{(\gamma - 1) \cdot M_1^2 + 2} \qquad \textbf{A-29}$$

By introducing the ideal gas law into the last two equations:

$$\frac{T_2}{T_1} = \frac{\left(\gamma \cdot M_1^2 - \frac{\gamma - 1}{2}\right)\left(\frac{\gamma - 1}{2} M_1^2 + 1\right)}{\left(\frac{\gamma + 1}{2}\right)^2 \cdot M_1^2} \qquad \textbf{A-30}$$

These relations are only valid for gases having constant specific heats, like monatomic gases, which can be predicted up to temperatures of 8000 *K*. In shock tube experiments this is achieved by using mixtures highly diluted with given monatomic gases like argon.

Reflected Shock Parameter Calculations

In shock fixed coordinates, the denote the velocity of the gas by u'. The relationship between the two velocities can be expressed as:

$$u_2' = U_r - U_2 \quad \textbf{A-31}$$

$$u_5 = U_r - U_5 \quad \textbf{A-32}$$

giving the conservation equations as:

$$\rho_2 u_2' = \rho_5 u_5 \quad \textbf{A-33}$$

$$p_2 + \rho_2 (u_2')^2 = p_5 + \rho_5 u_5^2 \quad \textbf{A-34}$$

$$h_2 + \frac{1}{2}(u_2')^2 = h_5 + \frac{1}{2}u_5^2 \quad \textbf{A-35}$$

As for the incident shock, the above equations leads to the Rankine-Hugoniot equation:

$$h_5 - h_2 = \frac{1}{2}(p_5 - p_2)\left(\frac{1}{\rho_5} + \frac{1}{\rho_2}\right) \quad \textbf{A-36}$$

By writing the Mach number for the reflected shock as $Mr=u_2'/a_2$, the temperature and pressure ratio may be expressed as:

$$\frac{p_5}{p_2} = \frac{\frac{\gamma+1}{\gamma-1} + 2 - \frac{p_1}{p_2}}{1 + \frac{\gamma+1}{\gamma-1}\cdot\frac{p_1}{p_2}} \quad \textbf{A-37}$$

$$\frac{T_5}{T_2} = \frac{p_5}{p_2}\left(\frac{\frac{\gamma+1}{\gamma-1} + \frac{p_5}{p_2}}{1 + \frac{\gamma+1}{\gamma-1}\cdot\frac{p_5}{p_2}}\right) \quad \textbf{A-38}$$

APPENDIX B

Experimetal results - CNRS

	P_1	P_4	Memb.	Dilutent	NM	Wavel.	P_2	T_2	D_2	C_2	ε_2	P_5	T_5	D_5	C_5	ε_5	$\varepsilon_2/\varepsilon_5$	$V_{incident}$
	[Torr]	[bar]	[µm]		[vol %]	[nm]	[kPa]	[K]		[mol/m^3]	[m^2/mol]	[kPa]	[K]		[mol/m^3]	[m^2/mol]		[m/s]
Man #6	50.49	1.40	12	N2	1.00	220	57.42	624	0.48	0.11	82.87	247.90	989	2.15	0.30	136.18	1.64	923.3
Man #7	30.95	1.40	12	N2	1.00	220	39.51	733	0.34	0.06	100.21	193.43	1211	0.99	0.19	97.83	0.98	1004.2
Man #8	45.53	1.40	12	N2	1.00	220	51.52	684	0.46	0.09	96.18	239.58	1110	1.43	0.26	104.92	1.09	947.0
Man #9	70.30	1.40	12	N2	1.00	220	60.50	589	0.46	0.12	70.54	248.00	917	1.43	0.33	83.75	1.19	829.6
Man #10	59.74	1.40	12	N2	1.00	220	57.42	624	0.53	0.11	91.94	247.90	989	1.65	0.30	104.57	1.14	874.8
Man #11	59.99	1.20	8	N2	1.00	220	50.25	580	0.27	0.10	49.05	202.74	899	0.98	0.27	68.50	1.40	818.2
Man #12	64.35	1.60	12	N2	0.50	220	62.97	633	0.34	0.06	106.77	273.47	1010	1.19	0.16	139.05	1.30	885.8
Man #13	40.50	1.20	8	N2	0.50	220	46.10	690	0.23	0.04	107.48	214.31	1124	0.78	0.11	129.83	1.21	953.4
Man #14	40.31	1.60	12	N2	0.50	220	51.88	741	0.28	0.04	128.16	253.99	1229	0.71	0.12	108.30	0.85	1012.1
Man #15	50.10	1.20	8	N2	0.50	220	50.65	645	0.27	0.05	106.88	223.31	1033	1.09	0.13	159.70	1.49	900.0
Man #16	98.88	2.40	18	N2	0.50	220	92.83	619	0.53	0.09	110.94	395.36	981	1.85	0.24	145.11	1.31	868.2
Man #18	83.12	2.30	18	N2	0.50	220	86.69	656	0.51	0.08	121.52	387.65	1056	2.08	0.22	179.59	1.48	913.7
Man #21	70.09	2.30	12	N2	0.50	220	81.76	699	0.45	0.07	120.87	384.09	1144	1.43	0.20	134.62	1.11	964.8
Man #22	56.30	2.20	12	N2	0.50	220	67.08	708	0.36	0.06	120.25	318.02	1162	1.18	0.16	136.23	1.13	974.9
Man #23	50.12	1.20	8	N2	0.30	220	48.89	633	0.10	0.03	65.89	211.79	1011	0.37	0.08	93.57	1.42	885.8
Man #24	69.97	1.20	8	N2	0.30	220	56.24	571	0.10	0.04	51.47	221.61	883	0.40	0.09	83.49	1.62	806.5
Man #25	30.20	1.10	8	N2	0.30	220	38.67	741	0.07	0.02	67.57	188.69	1229	0.21	0.06	72.80	1.08	1011.2
Man #26	54.85	1.20	8	N2	0.30	220	38.67	741	0.09	0.02	91.15	188.69	1229	0.36	0.06	125.42	1.38	855.7
Man #27	45.17	1.20	8	N2	0.30	220	46.47	652	0.09	0.03	66.35	206.32	1050	0.29	0.07	77.73	1.17	909.1
Man #28	39.86	1.20	8	N2	0.30	220	44.20	681	0.08	0.02	68.45	202.89	1107	0.29	0.07	84.87	1.24	942.8
Man #29	80.00	2.30	18	N2	0.30	220	83.00	655	0.15	0.05	64.03	369.00	1056	0.53	0.13	80.23	1.25	912.8
Man #30	99.80	2.30	18	N2	0.30	220	91.94	613	0.20	0.05	70.99	385.81	969	0.64	0.14	84.89	1.20	859.4
Man #31	99.80	2.30	18	N2	0.30	220	88.86	603	0.18	0.05	65.65	368.54	948	0.62	0.14	84.88	1.29	847.5
Man #32	72.45	2.30	18	N2	0.30	220	76.75	663	0.13	0.04	59.82	345.30	1072	0.48	0.12	79.27	1.33	922.1
Man #33	50.00	1.40	12	N2	0.33	220	54.62	675	0.15	0.03	91.64	249.12	1095	0.55	0.09	116.52	1.27	935.6
Man #34	70.00	1.40	12	N2	0.33	220	61.42	598	0.20	0.04	94.32	252.97	938	0.72	0.11	128.61	1.36	841.1
Man #35	90.00	1.40	12	N2	0.33	220	69.04	558	0.23	0.05	90.04	265.54	855	0.78	0.12	120.52	1.34	788.1
Man #36	100.00	3.00	18	N2	0.33	220	105.15	660	0.33	0.06	98.66	471.52	1066	1.04	0.18	112.57	1.14	918.4
Man #37	120.00	3.00	18	N2	0.33	220	118.60	638	0.39	0.07	101.40	516.93	1020	1.31	0.20	123.74	1.22	891.1
Man #38	90.00	3.00	18	N2	0.33	220	104.42	698	0.30	0.06	97.52	488.91	1143	0.86	0.17	96.51	0.99	963.6
Man #39	60.00	1.40	12	N2	0.33	220	58.58	633	0.20	0.04	101.62	253.89	1011	0.67	0.10	127.80	1.26	885.8
Man #40	55.00	1.40	12	N2	0.33	220	54.35	638	0.17	0.03	96.82	236.93	1020	0.65	0.09	134.36	1.39	891.1
Man #41	50.00	1.40	12	N2	0.33	220	50.41	645	0.13	0.03	81.03	221.80	1034	0.50	0.09	111.08	1.37	900.0
Man #42	40.00	1.40	12	N2	0.33	220	48.30	715	0.10	0.03	68.49	230.03	1177	0.35	0.08	85.84	1.25	982.5
Man #43	95.12	3.00	18	N2	0.33	220	105.21	679	0.28	0.06	85.46	482.52	1105	0.88	0.17	97.06	1.14	941.4
Man #44	100.00	4.00	18	N2	0.33	220	129.90	747	0.32	0.07	89.38	637.60	1241	0.59	0.20	55.42	0.62	1018.1
Man #45	125.00	4.00	18	N2	0.33	220	141.95	690	0.38	0.08	88.01	658.60	1126	1.16	0.23	94.77	1.08	953.4
Man #46	131.00	4.00	18	N2	0.33	220	142.40	673	0.38	0.08	86.23	647.90	1091	1.44	0.24	116.65	1.35	933.6

Table B-1: Diluted in nitrogen - decomposition experiments Nº 1-46.

	P_1 [Torr]	P_4 [bar]	Memb. [µm]	Dilutent	NM [vol %]	Wavel. [nm]	P_2 [kPa]	T_2 [K]	D_2	C_2 [mol/m^3]	ε_2 [m^2/mol]	P_5 [kPa]	T_5 [K]	D_5	C_5 [mol/m^3]	ε_5 [m^2/mol]	$\varepsilon_2/\varepsilon_5$	$V_{incident}$ [m/s]
Man #47	80.00	1.20	8	Ar	0.50	220	69.20	738	0.34	0.06	115.66	252.30	1306	0.75	0.12	122.45	1.06	741.4
Man #48	100.00	1.20	8	Ar	0.50	220	71.70	656	0.35	0.07	102.71	241.00	1113	0.99	0.13	145.42	1.42	677.7
Man #49	90.00	1.20	8	Ar	0.50	220	64.30	655	0.36	0.06	117.35	215.70	1204	0.80	0.11	141.49	1.21	708.7
Man #50	100.00	1.40	12	Ar	0.50	220	79.40	700	0.39	0.07	109.87	279.60	1214	0.94	0.14	129.01	1.17	712.0
Man #51	130.00	1.40	12	Ar	0.50	220	81.90	607	0.41	0.08	96.08	259.00	998	1.11	0.16	135.00	1.41	637.4
Man #52	115.00	1.40	12	Ar	0.50	220	81.40	651	0.43	0.08	108.43	271.90	1100	1.10	0.15	140.48	1.30	673.7
Man #53	86.90	1.40	12	Ar	0.50	220	74.10	732	0.37	0.06	114.89	268.50	1290	0.75	0.13	114.31	0.99	736.5
Man #54	80.20	1.20	8	Ar	0.30	220	69.50	743	0.22	0.03	124.12	253.50	1320	0.48	0.07	133.10	1.07	743.8
Man #55	100.00	1.20	8	Ar	0.30	220	72.63	666	0.26	0.04	126.32	245.98	1138	0.71	0.08	172.32	1.36	684.9
Man #57	200.00	3.00	18	Ar	0.20	220	156.45	697	0.30	0.05	105.07	546.05	1212	0.69	0.11	121.87	1.16	708.7
Man #58	200.00	3.00	18	Ar	0.20	220	156.98	698	0.30	0.05	106.67	548.68	1216	0.71	0.11	125.43	1.18	709.8
Man #59	181.50	2.40	18	Ar	0.20	220	120.42	629	0.25	0.05	105.27	389.94	1053	0.72	0.09	153.91	1.46	655.0
Man #60	240.00	3.00	18	Ar	0.20	220	171.03	657	0.33	0.06	100.06	572.64	1119	0.83	0.12	127.96	1.28	677.7
Man #61	220.00	3.00	18	Ar	0.20	220	164.97	678	0.31	0.06	101.46	565.22	1169	0.80	0.12	130.52	1.29	694.4
Man #62	158.00	2.40	18	Ar	0.20	220	116.20	670	0.22	0.04	99.22	394.80	1150	0.60	0.08	138.19	1.39	688.1
Man #63	250.00	3.50	18	Ar	0.20	220	192.40	690	0.30	0.07	86.26	666.79	1195	0.65	0.13	92.32	1.07	703.1
Man #64	248.00	3.40	18	Ar	0.20	220	184.18	674	0.32	0.07	92.65	628.33	1159	0.70	0.13	102.88	1.11	691.2
Man #65	250.30	3.38	18	Ar	0.20	220	185.89	674	0.33	0.07	95.63	634.16	1159	0.78	0.13	112.49	1.18	691.2
Man #66	245.50	3.20	18	Ar	0.20	220	174.95	657	0.31	0.06	92.96	585.76	1119	0.84	0.13	126.96	1.37	677.7
Man #67	150.00	3.00	18	Ar	0.30	220	139.42	778	0.43	0.06	127.03	522.62	1403	0.60	0.13	85.69	0.67	769.2
Man #68	160.00	3.00	18	Ar	0.30	220	147.14	772	0.44	0.07	124.61	549.31	1390	0.65	0.14	87.75	0.70	769.2
Man #69	170.00	3.00	18	Ar	0.30	220	147.26	743	0.44	0.07	117.75	536.78	1319	0.78	0.14	103.02	0.87	743.6
Man #70	50.00	1.00	8	Ar	0.30	220	52.01	840	0.13	0.02	110.18	203.38	1549	0.21	0.05	84.84	0.77	812.3
Man #71	80.00	1.00	8	Ar	0.30	220	60.10	678	0.16	0.03	95.87	206.19	1166	0.44	0.06	132.29	1.38	694.4
Man #72	70.00	0.90	8	Ar	0.30	220	54.95	697	0.17	0.03	117.28	192.19	1211	0.41	0.06	137.84	1.18	709.2
Man #73	62.00	0.90	8	Ar	0.30	220	50.23	711	0.15	0.03	111.77	178.06	1245	0.38	0.05	143.28	1.28	720.0
Man #74	70.00	1.20	8	Ar	1.50	227	64.67	755	0.29	0.15	36.01	244.06	1329	0.74	0.33	42.37	1.18	758.6
Man #75	100.00	1.20	8	Ar	1.50	230	70.30	637	0.17	0.20	16.13	235.33	1058	0.86	0.40	40.72	2.52	665.7
Man #76	80.00	1.20	8	Ar	1.50	230	68.46	719	0.17	0.17	18.54	250.34	1246	0.75	0.36	39.65	2.14	731.4
Man #77	90.00	1.20	8	Ar	1.50	230	70.47	680	0.18	0.19	18.50	247.99	1157	0.91	0.39	44.94	2.43	700.8
Man #78	90.00	1.00	8	Ar	1.50	230	63.84	641	0.15	0.18	15.91	214.73	1066	0.76	0.36	40.07	2.52	668.6
Man #79	80.20	1.00	8	Ar	1.50	230	59.64	659	0.14	0.16	16.61	205.10	1109	0.78	0.33	44.74	2.69	683.9

Table B-2: Diluted in argon - decomposition experiments Nº 47-79.

	P_1 [Torr]	P_4 [bar]	Memb. [µm]	Dilutent	NM [vol %]	Wavel. [nm]	P_2 [kPa]	T_2 [K]	D_2	C_2 [mol/m^3]	ε_2 [m^2/mol]	P_5 [kPa]	T_5 [K]	D_5	C_5 [mol/m^3]	ε_5 [m^2/mol]	$\varepsilon_2/\varepsilon_5$	$V_{incident}$ [m/s]
Man #80	354.10	4.60	23	Ar	0.30	225	266.04	678	0.38	0.14	50.53	912.75	1166	1.23	0.28	82.67	1.64	694.4
Man #81	354.10	4.20	23	Ar	0.30	225	251.05	654	0.43	0.14	59.04	838.92	1110	1.30	0.27	90.99	1.54	675.4
Man #82	354.10	4.00	23	Ar	0.30	225	237.55	632	0.49	0.14	68.33	773.64	1059	1.59	0.26	114.84	1.68	657.9
Man #83	330.00	4.00	23	Ar	0.30	225	236.34	658	0.40	0.13	59.45	793.55	1120	1.20	0.26	89.14	1.50	678.7
Man #84	330.00	4.20	23	Ar	0.20	225	240.82	667	0.31	0.09	67.69	815.10	1142	0.92	0.17	102.28	1.51	685.5
Man #85	214.00	3.00	18	Ar	0.20	225	164.05	688	0.21	0.06	71.23	567.67	1191	0.61	0.11	100.81	1.42	701.8
Man #86	340.00	3.80	23	Ar	0.20	225	222.77	625	0.30	0.09	67.62	717.04	1042	0.98	0.17	112.91	1.67	651.1
Man #87	208.30	3.00	18	Ar	0.20	225	163.01	697	0.25	0.06	83.54	569.03	1213	0.68	0.11	114.70	1.37	708.8
Man #88	340.00	4.40	23	Ar	0.20	225	254.96	678	0.40	0.09	84.48	873.52	1169	1.15	0.18	122.21	1.45	694.4
Man #89	208.90	2.80	18	Ar	0.20	225	148.86	657	0.22	0.05	77.78	498.43	1119	0.75	0.11	133.45	1.72	677.7
Man #90	220.00	3.20	18	Ar	0.20	225	165.50	680	0.25	0.06	81.20	567.83	1172	0.71	0.12	116.75	1.44	695.5

Table B-3: Diluted in argon - decomposition experiments Nº 80-90

No	P_1 [torr]	P_1 [bar]	mem [µm]	NM	O_2	Ar	I	P_2 [kPa]	T_2 [K]	P_5 [kPa]	T_5 [K]	Speed [m/sec]	Delay [µs]	Signal type
1	80.00	1.00	8	4.00	3.00	93.00	230	57.89	619	200.09	995	662.54		no decomposition
2	83.00	1.50	12	4.00	3.00	93.00	230	71.20	683	266.40	1 135	718.39	100.00	2
3	64.95	1.20	12	4.00	3.00	93.00	230	61.74	726	241.57	1 230	754.65	30.00	2
4	40.00	1.00	8	4.00	4.08	91.92	235	53.75	636	190.94	1 033	679.96	208.00	2
5	55.00	1.00	8	4.00	4.08	91.92	235	52.33	724	205.17	1 225	755.03	233.50	1
6	75.00	1.00	8	4.00	4.08	91.92	235	58.65	645	210.63	1 051	687.55	213.00	2
7	48.80	1.00	8	4.00	4.08	91.92	235	48.85	747	195.63	1 275	773.59	182.30	1
8	66.40	1.00	8	5.00	8.00	87.00	235	52.07	630	189.35	1 011	684.51	392.00	2
10	56.40	1.00	8	5.00	8.00	87.00	235	51.86	690	203.04	1 140	738.55	90.60	1
11	59.90	1.00	8	5.00	8.00	87.00	235	51.37	663	194.88	1 081	714.40	172.10	1
14	192.80	3.00	18	5.00	8.56	86.44	235	160.25	651	599.52	1 054	703.89	66.00	other
16	91.30	1.40	12	5.00	8.56	86.44	235	74.80	645	277.95	1 042	699.08	170.60	1
17	66.20	1.00	8	3.90	4.13	91.97	235	54.48	665	200.25	1 096	705.00	137.00	2
18	60.45	1.00	8	3.90	4.13	91.97	235	55.87	713	216.20	1 200	745.16	214.10	1
19	72.50	1.00	8	3.90	4.13	91.97	235	54.85	634	193.82	1 027	677.30	435.00	2
20	69.85	1.40	12	3.90	4.13	91.97	235	69.59	746	277.94	1 274	772.40	101.70	1
21	80.05	1.40	12	3.90	4.13	91.97	235	70.93	695	269.49	1 161	730.28	207.00	1
22	85.10	1.40	12	3.90	4.13	91.97	240	76.26	700	291.16	1 172	734.21	202.60	other
23	72.00	1.40	12	3.90	4.13	91.97	240	69.93	735	276.40	1 249	763.10	136.60	other
24	60.00	1.00	8	2.04	4.07	93.89	235	55.48	734	211.68	1 275	755.79	22.20	2
25	76.90	1.00	8	2.04	4.07	93.89	235	59.50	661	210.08	1 103	694.02	112.00	2
26	70.15	1.00	8	2.04	4.07	93.89	235	59.25	697	217.53	1 184	723.71	39.30	2
27	64.81	1.00	8	2.04	4.07	93.89	235	55.00	699	202.38	1 189	723.39	32.00	2
28	184.80	2.60	18	2.04	4.07	93.89	233	138.77	649	483.29	1 077	684.20	106.00	2
29	163.10	2.60	18	2.04	4.07	93.89	235	130.11	673	465.81	1 130	704.23	42.00	2
31	100.00	2.40	18	0.30	1.05	98.65	235	98.66	806	379.55	1 073	801.00	56.00	2
33	166.60	2.40	18	0.30	1.05	98.65	220	126.51	680	436.66	1 170	697.89		
35	180.00	1.40	8	0.30	1.05	98.65	235	92.12	540	261.25	842	578.78		
36	180.10	1.40	8	0.30	1.05	98.65	220	92.12	540	261.25	842	578.78		
41	19.82	2.20	18	6.40	5.68	87.92	235	16.54	644	62.31	1 033	698.32	415.70	1
42	23.27	2.40	18	6.40	5.68	87.92	235	19.28	641	72.43	1 028	696.06	479.80	1
43	20.19	3.00	23	6.40	5.68	87.92	235	20.65	724	85.32	1 202	769.63	199.80	1
44	24.70	2.80	23	6.40	5.68	87.92	235	20.85	648	79.01	1 042	702.25	451.60	1
45	19.93	2.80	23	6.40	5.68	87.92	235	19.07	696	76.50	1 143	745.40	269.70	1
46	21.27	3.40	23	6.40	5.68	87.92	235	22.51	739	94.38	1 234	782.34	138.40	
47	19.50	3.80	23	6.40	5.68	87.92	235	21.59	759	92.25	1 277	799.43	95.60	1
49	21.39	4.40	36	6.40	5.68	87.92	235	22.41	734	93.55	1 224	778.55	145.00	1

Table B-4: Experimental data - NM/O_2/Ar oxidation Nº 1-49

No	P_1 [torr]	P_1 [bar]	mem [mm]	NM	O_2	Ar	I	P_2 [kPa]	T_2 [K]	P_5 [kPa]	T_5 [K]	Speed [m/sec]	Delay [µs]	Signal type
50	21.33	4.80	36	6.40	5.68	87.92	235	22.93	746	96.78	1 249	788.23	117.00	1
51	19.72	5.00	50	6.40	5.68	87.92	235	22.51	773	97.35	1 307	811.10	78.20	1
54	13.85	1.20	8	6.40	5.68	87.92	235	11.69	648	44.30	1 042	702.25	588.30	1
58	19.50	1.40	12	3.56	12.40	84.00	235	14.74	623	52.48	1 001	679.86	437.00	2
59	22.82	2.00	12	3.56	12.40	84.00	235	19.03	659	70.98	1 079	712.48	297.00	2
64	22.57	2.80	18	3.56	12.40	84.00	235	20.65	696	80.31	1 159	744.79	107.00	2
66	21.44	3.20	18	3.56	12.40	84.00	235	21.71	739	88.18	1 254	781.86	32.00	2
67	19.44	2.80	18	3.56	12.40	84.00	235	19.50	735	78.92	1 245	778.41	40.00	2
70	20.44	2.20	18	3.56	12.40	84.00	235	17.01	658	63.42	1 077	711.91	198.00	2
71	20.00	2.30	18	3.56	12.40	84.00	235	16.57	657	61.65	1 074	710.40	365.00	2
73	19.67	2.60	23	3.56	12.40	84.00	235	18.59	709	73.33	1 188	756.43	74.00	2
74	19.68	2.60	18	3.56	12.40	84.00	235	17.73	689	68.53	1 145	739.46	60.00	2
75	20.00	4.00	23	3.56	12.40	84.00	235	21.32	763	88.49	1 306	801.50	74.70	1
79	20.07	3.50	23	3.56	12.40	84.00	306	21.55	767	89.71	1 314	804.51	64.90	3
80	21.10	2.80	18	3.56	12.40	84.00	306	19.39	698	75.59	1 163	746.45	207.90	3
81	21.08	2.80	18	3.56	12.40	84.00	235	20.00	711	79.06	1 192	757.96	201.20	3
82	20.09	3.50	23	3.56	12.40	84.00	235	21.82	772	91.22	1 325	808.63	58.40	3
83	20.00	5.00	50	3.56	12.40	84.00	306	21.54	768	89.74	1 317	805.37	61.80	3
84	20.81	3.10	23	3.56	12.40	84.00	306	21.17	742	86.19	1 259	783.70	64.00	3
87	21.58	2.40	18	3.56	12.40	84.00	306	17.34	645	63.56	1 049	699.95	424.90	3
88	20.07	2.40	18	3.56	12.40	84.00	306	16.94	664	63.55	1 089	716.67	335.90	3
90	20.07	2.40	18	6.40	3.20	90.40	235	18.47	692	73.13	1 136	737.10	509.10	1
91	19.86	3.00	18	6.40	3.20	90.40	235	20.13	725	82.54	1 206	765.70	523.70	1
92	20.18	3.40	23	6.40	3.20	90.40	235	22.30	763	94.84	1 289	798.08	231.10	1
93	21.00	4.00	23	6.40	3.20	90.40	235	21.59	731	89.03	1 219	770.81	241.50	1
94	20.04	4.60	50	6.40	3.20	90.40	235	21.09	741	87.89	1 242	779.63	299.80	1
95	19.88	5.80	50	6.40	3.20	90.40	235	23.26	790	101.20	1 346	820.12	160.10	1
96	19.72	6.00	50	6.40	3.20	90.40	235	23.77	805	104.66	1 378	831.95	81.80	1
97	20.42	2.20	18	6.40	3.20	90.40	235	16.66	640	61.94	1 026	690.45	959.00	1
98	19.68	2.40	18	6.40	3.20	90.40	235	16.79	656	63.70	1 060	705.22	576.90	1
99	18.96	2.40	18	6.40	3.20	90.40	235	16.87	672	65.27	1 093	719.42	616.30	1
100	18.96	2.40	18	6.40	3.20	90.40	235	17.03	667	65.49	1 083	714.97	529.60	1
101	20.13	2.30	18	6.40	3.20	90.40	235	17.12	655	64.90	1 058	704.23	755.60	1
102	20.00	5.00	50	6.40	3.20	90.40	235	22.29	767	95.11	1 297	801.28	224.70	1
103	20.00	5.40	50	6.40	3.20	90.40	235	23.45	791	102.14	1 349	821.02	183.20	1
104	20.06	5.20	50	6.40	3.20	90.40	235	22.28	766	94.95	1 294	800.00	291.20	1
105	21.06	3.00	23	6.40	3.20	90.40	235	21.27	723	87.07	1 203	764.33	547.40	1

Table B-5: Experimental data - NM/O_2/Ar oxidation Nº 50-105

Signals type 1 and 3				Signals type 2		
	Y	Y			Y	Y
1/T	Type 1&3	Type 1&3 SD		1/T	Type 2	Type 2 SD
8.16E-04	8.84E-01	5.35E+00		8.81E-04	6.51E+00	4.64E+00
7.84E-04	5.76E-01	5.05E+00		8.13E-04	5.28E+00	3.43E+00
8.77E-04	1.02E+00	4.86E+00		9.68E-04	7.16E+00	5.33E+00
9.25E-04	1.67E+00	5.51E+00		9.51E-04	7.20E+00	5.36E+00
9.59E-04	2.01E+00	5.76E+00		9.89E-04	7.62E+00	5.93E+00
8.33E-04	8.34E-01	5.31E+00		9.12E-04	6.74E+00	4.91E+00
7.85E-04	2.22E-01	4.67E+00		9.73E-04	7.90E+00	6.07E+00
8.61E-04	9.75E-01	5.42E+00		7.84E-04	5.09E+00	3.01E+00
9.68E-04	1.66E+00	5.52E+00		9.07E-04	6.75E+00	4.64E+00
9.73E-04	1.91E+00	5.75E+00		8.45E-04	5.70E+00	3.59E+00
8.32E-04	1.04E+00	4.88E+00		8.41E-04	5.47E+00	3.38E+00
9.60E-04	1.90E+00	5.73E+00		9.29E-04	6.85E+00	4.60E+00
8.75E-04	1.30E+00	5.15E+00		8.85E-04	5.91E+00	3.67E+00
8.10E-04	7.23E-01	4.55E+00		9.32E-04	6.91E+00	3.86E+00
7.83E-04	3.14E-01	4.15E+00		9.99E-04	7.47E+00	6.07E+00
8.17E-04	7.69E-01	4.60E+00		9.27E-04	7.17E+00	5.55E+00
8.01E-04	5.64E-01	4.39E+00		8.63E-04	6.16E+00	4.53E+00
7.65E-04	1.34E-01	3.97E+00		7.97E-04	4.95E+00	3.32E+00
9.60E-04	1.77E+00	5.67E+00		8.03E-04	5.16E+00	3.54E+00
7.47E-04	-8.29E-03	4.11E+00		9.28E-04	6.74E+00	5.14E+00
7.66E-04	3.38E-01	4.46E+00		9.31E-04	7.35E+00	5.75E+00
7.61E-04	2.03E-01	4.33E+00		8.42E-04	5.77E+00	4.16E+00
8.60E-04	1.33E+00	5.46E+00		8.73E-04	5.55E+00	3.95E+00
8.39E-04	1.31E+00	5.44E+00				
7.54E-04	1.03E-01	4.22E+00				
7.60E-04	1.53E-01	4.28E+00				
7.94E-04	1.91E-01	4.31E+00				
9.54E-04	2.00E+00	6.14E+00				
9.18E-04	1.74E+00	5.88E+00				
8.80E-04	1.25E+00	5.37E+00				
8.29E-04	1.32E+00	5.44E+00				
7.76E-04	5.48E-01	4.66E+00				
8.20E-04	5.86E-01	4.70E+00				
8.05E-04	7.81E-01	4.90E+00				
7.43E-04	1.95E-01	4.30E+00				
7.26E-04	-4.69E-01	3.64E+00				
9.75E-04	1.87E+00	6.00E+00				
9.44E-04	1.32E+00	5.46E+00				
9.15E-04	1.38E+00	5.52E+00				
9.23E-04	1.24E+00	5.38E+00				
9.46E-04	1.61E+00	5.74E+00				
7.71E-04	5.17E-01	4.63E+00				
7.41E-04	3.35E-01	4.44E+00				
7.73E-04	7.77E-01	4.89E+00				
8.31E-04	1.40E+00	5.51E+00				

Table B-6: Ignition delay time data for NM/O_2/Ar mixtures.

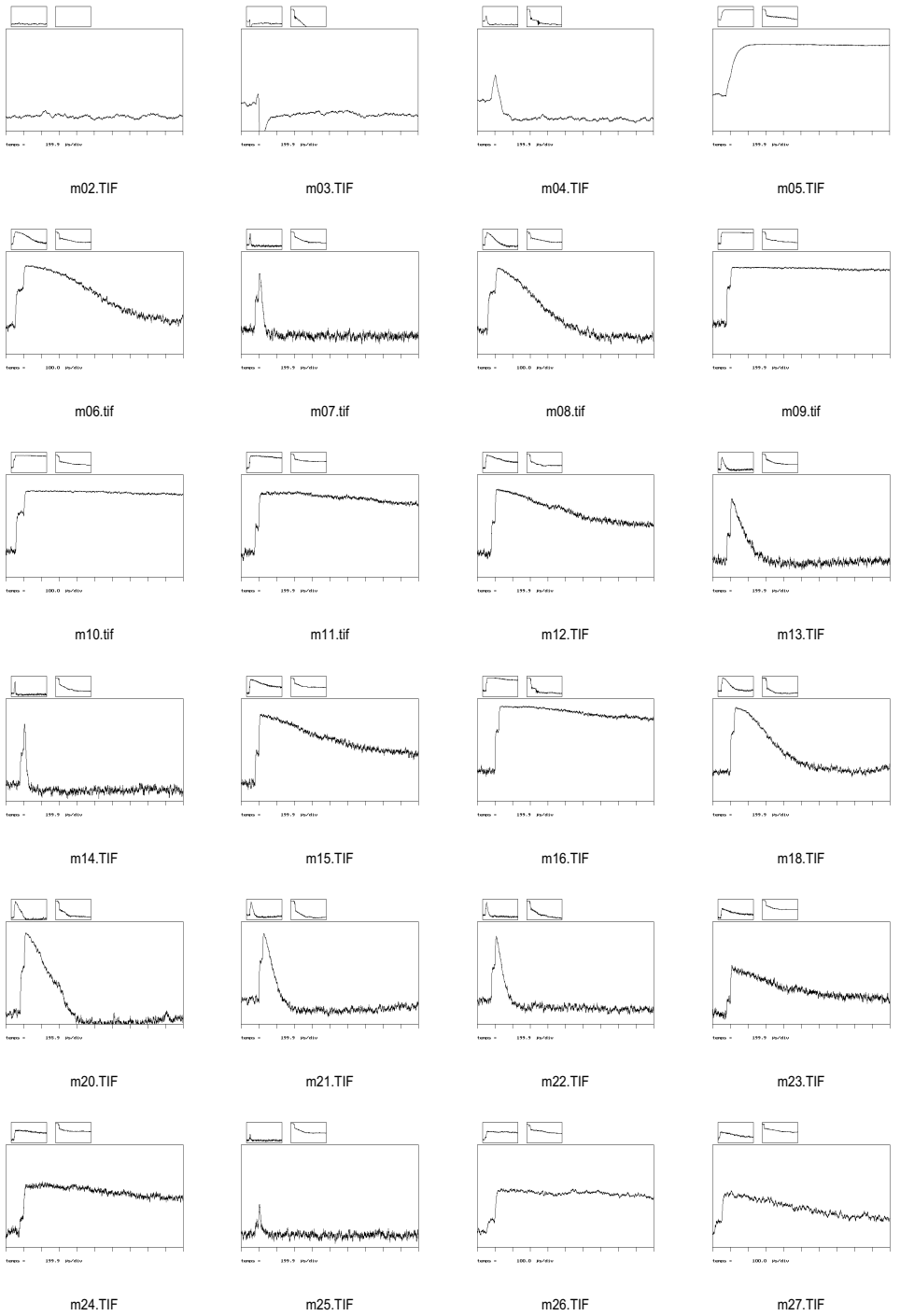

Figure B - 1: Absorption signals from the oscilloscope - Exp. 2 to 27.

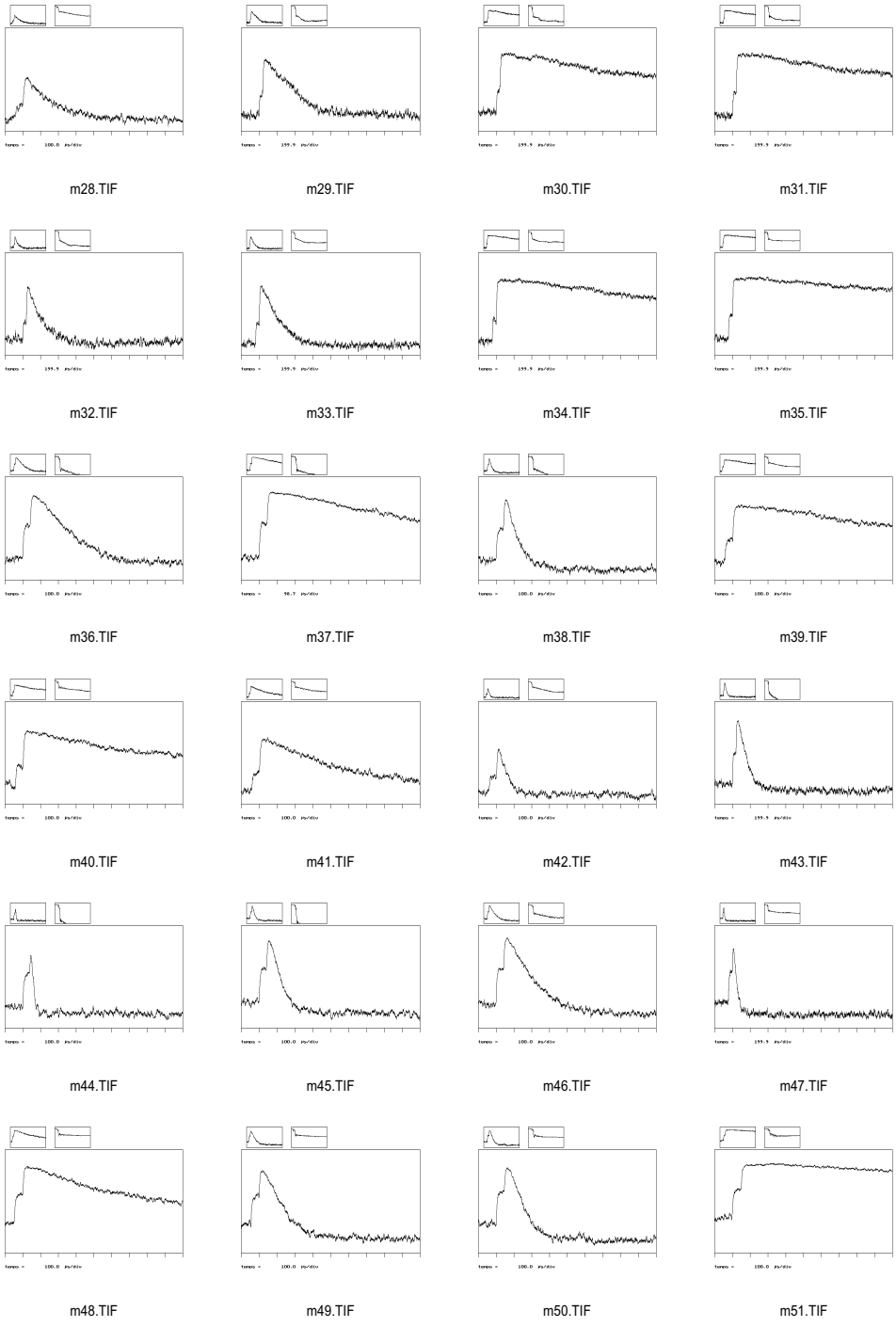

Figure B - 2: Absorption signals from the oscilloscope - Exp. 28 to 51.

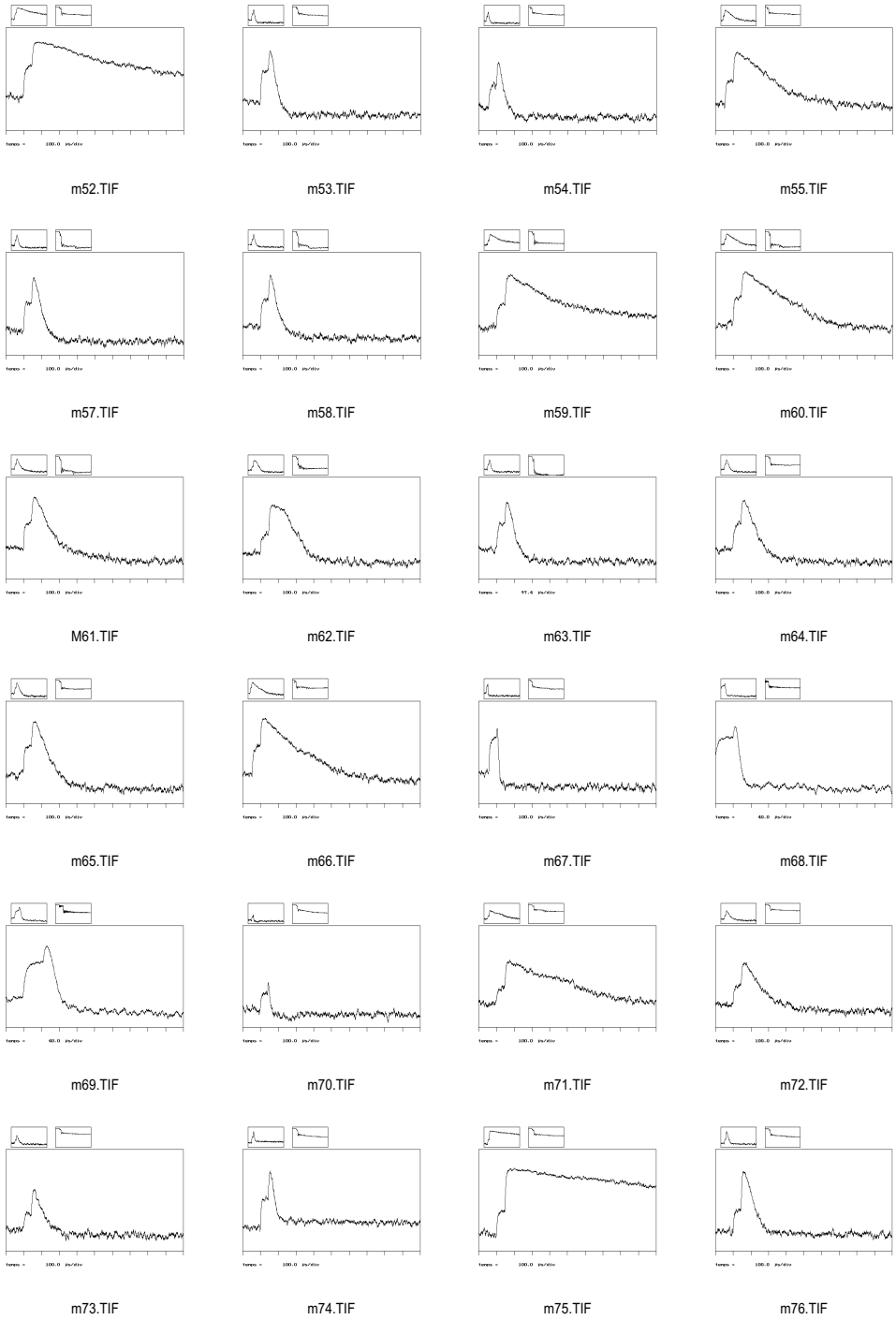

Figure B - 3: Absorption signals from the oscilloscope - Exp. 52 to 76.

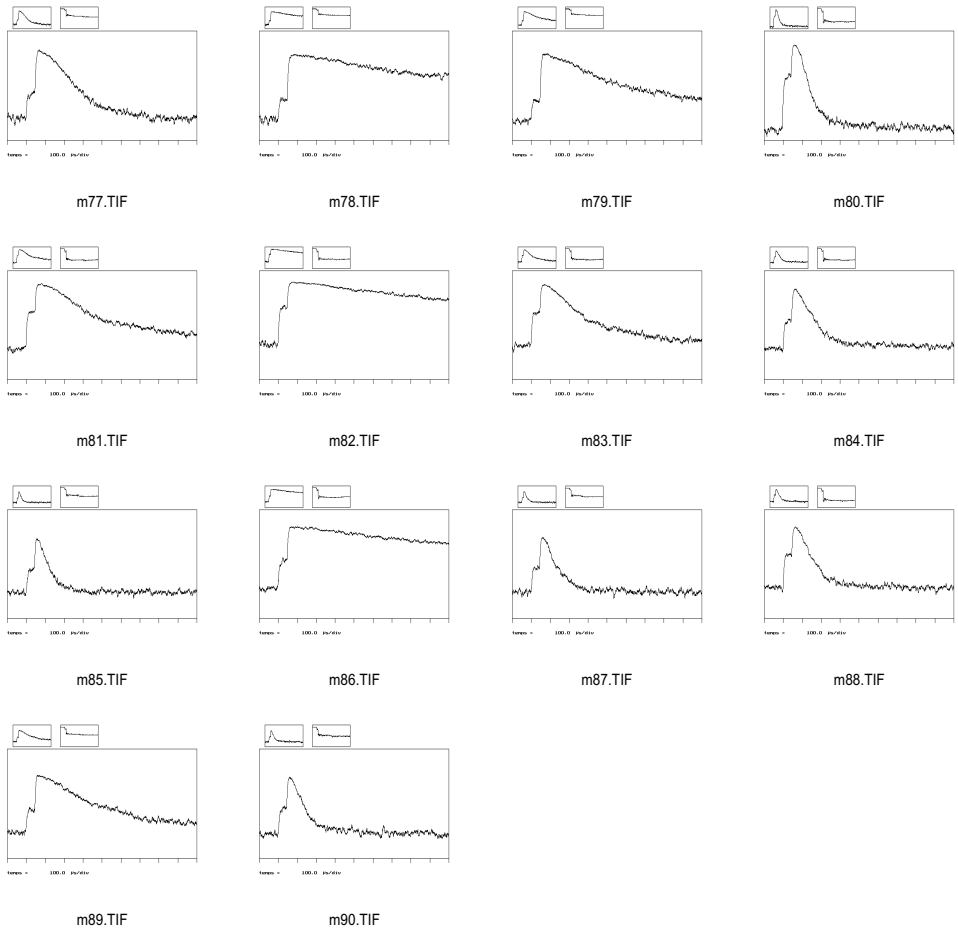

Figure B - 4: Absorption signals from the oscilloscope - Exp. 77 to 90.

APPENDIX C

Reaction Mechanisms

- Original Reaction Mechanisms
- Differenses Between The Three Mechanisms
- Mechanism Used In Simulations

Original Reaction Mechanisms

Mechsenk.101

GUIRGUIS, RAAFAT H., "Investigation of the thermal initiation of detonation in Nitromethane", JAYCOR, Naval Research Laboratory, 1983

```
CHEMKIN INTERPRETER OUTPUT: CHEMKIN-II Version 3.9  Aug. 1994
                            DOUBLE PRECISION

                          --------------------
                          ELEMENTS     ATOMIC
                          CONSIDERED   WEIGHT
                          --------------------
                           1. C       12.0112
                           2. H       1.00797
                           3. N       14.0067
                           4. O       15.9994
                          --------------------
```

SPECIES CONSIDERED	PHASE	CHARGE	MOLECULAR WEIGHT	TEMPERATURE LOW	TEMPERATURE HIGH	ELEMENT COUNT C	H	N	O
1. N2	G	0	28.01340	300	5000	0	0	2	0
2. CH3NO2	G	0	61.04056	300	4000	1	3	1	2
3. CH3	G	0	15.03506	300	5000	1	3	0	0
4. NO2	G	0	46.00550	300	5000	0	0	1	2
5. NO	G	0	30.00610	300	5000	0	0	1	1
6. CO	G	0	28.01055	300	5000	1	0	0	1
7. CO2	G	0	44.00995	300	5000	1	0	0	2
8. CH2O	G	0	30.02649	300	6000	1	2	0	1
9. HCO	G	0	29.01852	300	5000	1	1	0	1
10. CH4	G	0	16.04303	300	5000	1	4	0	0
11. CH2NO2	G	0	60.03259	300	5000	1	2	1	2
12. H	G	0	1.00797	300	5000	0	1	0	0
13. H2	G	0	2.01594	300	5000	0	2	0	0
14. H2O	G	0	18.01534	300	5000	0	2	0	1
15. OH	G	0	17.00737	300	5000	0	1	0	1
16. HNO	G	0	31.01407	300	5000	0	1	1	1
17. CH3OH	G	0	32.04243	300	6000	1	4	0	1
18. C2H6	G	0	30.07012	300	4000	2	6	0	0
19. C2H5	G	0	29.06215	300	5000	2	5	0	0
20. C2H4	G	0	28.05418	300	5000	2	4	0	0
21. CH3O	G	0	31.03446	300	3000	1	3	0	1
22. CH3NO	G	0	45.04116	300	6000	1	3	1	1
23. HNO2	G	0	47.01347	200	6000	0	1	1	2
24. O	G	0	15.99940	300	5000	0	0	0	1
25. CH3ONO	G	0	61.04056	300	4000	1	3	1	2

	REACTIONS CONSIDERED	(k = A T**b exp(-E/RT)) A	b	E
1.	CH3NO2+M=>CH3+NO2+M	1.30E+17	0.0	42.0
2.	CH3+NO2=>CH3NO2	5.00E+11	0.0	0.0
3.	CH3+NO2=CH3O+NO	1.30E+13	0.0	0.0
4.	CH3O+M=>CH2O+H+M	4.00E+40	-7.5	22.6
5.	CH2O+H+M=>CH3O+M	4.75E+37	-6.9	0.1
6.	NO2+H=NO+OH	2.90E+14	0.0	0.8
7.	CH3O+NO=>CH2O+HNO	3.20E+12	0.0	0.0
8.	CH2O+HNO=>CH3O+NO	2.85E+12	0.0	28.8
9.	H+NO+M=>HNO+M	5.40E+15	0.0	-0.6
10.	HNO+M=>H+NO+M	2.88E+16	0.0	48.8
11.	CH3O+NO2=CH2O+HNO2	4.00E+11	0.0	0.0
12.	HNO2+M=>NO+OH+M	3.00E+18	0.0	46.7
13.	NO+OH+M=>HNO2+M	7.91E+15	0.0	-2.2
14.	CH3+NO=>CH3NO	4.00E+12	0.0	0.0
15.	CH3NO=>CH3+NO	7.00E+13	0.0	38.0
16.	CH3O+NO=>CH3ONO	6.30E+13	0.0	0.0
17.	CH3ONO=>CH3O+NO	4.00E+15	0.0	41.1
18.	CH3O+H=CH2O+H2	1.00E+14	0.0	0.0
19.	CH3O+H=CH3+OH	9.09E+17	0.0	15.2
20.	CH3+OH=CH2O+H2	8.00E+12	0.0	0.0
21.	CH3O+OH=CH2O+H2O	3.20E+13	0.0	0.0
22.	H2+OH=>H2O+H	5.20E+13	0.0	6.5
23.	H2O+H=>H2+OH	2.22E+14	0.0	21.8
24.	CH3O+CH3O=CH3OH+CH2O	1.10E+13	0.0	0.0
25.	CH3NO2+CH3=CH2NO2+CH4	2.40E+11	0.0	9.0
26.	CH3NO2+NO2=>CH2NO2+HNO2	3.07E+12	0.0	18.3
27.	CH2NO2+HNO2=>CH3NO2+NO2	1.00E+12	0.0	0.0
28.	CH3NO2+H=>CH2NO2+H2	2.50E+09	1.3	2.6
29.	CH2NO2+H2=>CH3NO2+H	6.20E+05	2.2	9.5
30.	CH3NO2+OH=CH2NO2+H2O	6.90E+04	2.6	-1.9
31.	CH2NO2=CH2O+NO	1.00E+13	0.0	36.0
32.	CH2O+H=HCO+H2	2.50E+09	1.3	2.6
33.	CH2O+OH=HCO+H2O	6.90E+04	2.6	-1.9
34.	CH2O+NO=>HCO+HNO	2.86E+14	0.0	42.0
35.	HCO+HNO=>CH2O+NO	3.20E+13	0.0	1.4
36.	CH2O+CH2NO2=HCO+CH3NO2	2.50E+13	0.0	10.0
37.	HCO+NO2=HNO2+CO	1.00E+14	0.0	0.0
38.	HCO+NO2=H+CO2+NO	1.00E+14	0.0	0.0
39.	HCO+NO2=OH+CO+NO	1.00E+14	0.0	0.0
40.	HCO+M=>H+CO+M	1.00E+15	0.0	14.7
41.	H+CO+M=>HCO+M	1.67E+15	0.0	0.3
42.	HCO+NO=>HNO+CO	2.00E+11	0.5	2.0
43.	HNO+CO=>HCO+NO	7.60E+11	0.6	36.8
44.	CO+OH=CO2+H	1.50E+07	1.3	-0.8
45.	CO+O+M=CO2+M	2.80E+13	0.0	-4.5
46.	CH3+CH3=C2H6	2.50E+12	0.0	0.0
47.	CH3+CH3=>C2H5+H	8.00E+14	0.0	26.6
48.	C2H5+H=>CH3+CH3	5.26E+16	0.0	15.1
49.	CH3+CH3=C2H4+H2	1.00E+16	0.0	32.0
50.	C2H6+CH3=>C2H5+CH4	5.50E+14	0.0	21.5
51.	C2H5+CH4=>C2H6+CH3	3.25E+15	0.0	28.4
52.	C2H6+OH=>C2H5+H2O	6.30E+13	0.0	3.6
53.	C2H5+H2O=>C2H6+OH	6.32E+13	0.0	25.4
54.	C2H6+H=>C2H5+H2	1.30E+14	0.0	9.4
55.	C2H5+H2=>C2H6+H	3.05E+13	0.0	16.0
56.	C2H5+M=>C2H4+H+M	4.70E+14	0.0	26.6
57.	C2H4+H+M=>C2H5+M	9.54E+13	0.0	-10.8
58.	C2H5+OH=C2H4+H2O	2.00E+13	0.0	0.0
59.	C2H4+OH=>CH2O+CH3	5.00E+12	0.0	0.0
60.	CH2O+CH3=>C2H4+OH	2.84E+12	0.0	16.6
61.	CH4+OH=>CH3+H2O	3.20E+13	0.0	5.0
62.	CH3+H2O=>CH4+OH	5.43E+12	0.0	19.9

NOTE: E units Kcal/mole, A units mole-cm-sec-K

Mechsenk.201

(CO+OH = CO2+H ! WARNATZ79)

```
GUIRGUIS, RAAFAT H. AND HSU D., BOGAN D. AND ORAN E., "A mechanism for igni-
tion of high-temperature gaseous Nitromethane - The key role of the Nitro
group in chemical explosives", Combustion and Flame 61, p.51-62, 1985
-------------------------------------------------------------------------------

CHEMKIN INTERPRETER OUTPUT: CHEMKIN-II Version 3.9  Aug. 1994
                            DOUBLE PRECISION

                           --------------------
                           ELEMENTS     ATOMIC
                           CONSIDERED   WEIGHT
                           --------------------
                            1. AR      39.9480
                            2. C       12.0112
                            3. H       1.00797
                            4. N       14.0067
                            5. O       15.9994
                           --------------------
 -------------------------------------------------------------------------------
                              C
                           P  H
                           H  A
                           A  R
 SPECIES                   S  G  MOLECULAR  TEMPERATURE  ELEMENT COUNT
 CONSIDERED                E  E  WEIGHT     LOW    HIGH  AR C  H  N  O
 -------------------------------------------------------------------------------
   1. AR                   G  0   39.94800   300    5000   1  0  0  0  0
   2. CH3NO2               G  0   61.04056   300    4000   0  1  3  1  2
   3. CH3                  G  0   15.03506   300    5000   0  1  3  0  0
   4. CH4                  G  0   16.04303   300    5000   0  1  4  0  0
   5. C2H6                 G  0   30.07012   300    4000   0  2  6  0  0
   6. H2                   G  0    2.01594   300    5000   0  0  2  0  0
   7. H                    G  0    1.00797   300    5000   0  0  1  0  0
   8. O                    G  0   15.99940   300    5000   0  0  0  0  1
   9. C2H5                 G  0   29.06215   300    5000   0  2  5  0  0
  10. C2H4                 G  0   28.05418   300    5000   0  2  4  0  0
  11. OH                   G  0   17.00737   300    5000   0  0  1  0  1
  12. H2O                  G  0   18.01534   300    5000   0  0  2  0  1
  13. HNO                  G  0   31.01407   300    5000   0  0  1  1  1
  14. NO                   G  0   30.00610   300    5000   0  0  0  1  1
  15. NO2                  G  0   46.00550   300    5000   0  0  0  1  2
  16. CO                   G  0   28.01055   300    5000   0  1  0  0  1
  17. CO2                  G  0   44.00995   300    5000   0  1  0  0  2
  18. HCO                  G  0   29.01852   300    5000   0  1  1  0  1
  19. CH3O                 G  0   31.03446   300    3000   0  1  3  0  1
  20. CH2O                 G  0   30.02649   300    6000   0  1  2  0  1
  21. CH2NO2               G  0   60.03259   300    5000   0  1  2  1  2
  22. CH3NO                G  0   45.04116   300    6000   0  1  3  1  1
  23. CH3OH                G  0   32.04243   300    6000   0  1  4  0  1
  24. HNO2                 G  0   47.01347   200    6000   0  0  1  1  2
  25. C2H3                 G  0   27.04621   300    6000   0  2  3  0  0
  26. C2H2                 G  0   26.03824   300    6000   0  2  2  0  0
  27. CH2OH                G  0   31.03446   300    6000   0  1  3  0  1
  28. CH2NO                G  0   44.03319   300    6000   0  1  2  1  1
  29. HCN                  G  0   27.02582   300    6000   0  1  1  1  0
```

	REACTIONS CONSIDERED	(k = A T**b exp(-E/RT)) A	b	E
1.	CH3NO2+M=CH3+NO2+M	1.30E+17	0.0	42.0
2.	CH3+NO2=CH3O+NO	1.30E+13	0.0	0.0
3.	CH3O=CH2O+H	3.31E+15	0.0	27.5
4.	NO2+H=NO+OH	3.50E+14	0.0	1.5
5.	CH3O+OH=CH2O+H2O	3.20E+13	0.0	0.0
6.	H2+OH=>H2O+H	2.20E+13	0.0	5.2
7.	H2O+H=>H2+OH	9.30E+13	0.0	20.4
8.	CH3O+NO2=CH2O+HNO2	4.00E+11	0.0	0.0
9.	CH3O+NO=CH2O+HNO	3.20E+12	0.0	0.0
10.	HNO2+M=>NO+OH+M	3.00E+18	0.0	46.7
11.	NO+OH+M=>HNO2+M	7.91E+15	0.0	-2.2
12.	HNO+M=>H+NO+M	2.88E+16	0.0	48.8
13.	H+NO+M=>HNO+M	5.40E+15	0.0	-0.6
14.	CH3NO2+CH3=CH2NO2+CH4	1.60E+11	0.0	10.8
15.	CH3NO2+H=CH2NO2+H2	6.30E+13	0.0	9.7
16.	CH3NO2+OH=CH2NO2+H2O	1.85E+12	0.0	1.6
17.	CH2NO2=CH2O+NO	1.00E+13	0.0	36.0
18.	CH2O+CH3=HCO+CH4	3.10E+10	0.0	4.9
19.	CH2O+H=HCO+H2	1.26E+13	0.0	3.8
20.	CH2O+OH=HCO+H2O	7.53E+12	0.0	0.2
21.	HCO+M=>H+CO+M	1.00E+15	0.0	14.7
22.	H+CO+M=>HCO+M	6.90E+14	0.0	-1.7
23.	HCO+NO2=HNO2+CO	1.00E+14	0.0	0.0
24.	HCO+NO=HNO+CO	2.00E+11	0.5	2.0
25.	HCO+HNO=CH2O+NO	3.20E+13	0.0	1.4
26.	CO+OH=CO2+H	4.40E+06	1.5	-0.7
27.	CH4+OH=CH3+H2O	1.45E+12	0.0	3.4
28.	CH3+CH3=C2H6	3.16E+13	0.0	0.0
29.	C2H6+CH3=C2H5+CH4	3.20E+11	0.0	10.8
30.	C2H6+H=C2H5+H2	1.26E+14	0.0	9.7
31.	C2H6+OH=C2H5+H2O	1.10E+13	0.0	2.4
32.	C2H5+H=CH3+CH3	3.71E+13	0.0	0.0
33.	C2H5+M=C2H4+H+M	4.70E+14	0.0	26.6
34.	C2H4+OH=CH2O+CH3	4.50E+12	0.0	0.2
35.	C2H4+OH=C2H3+H2O	7.33E+12	0.0	7.8
36.	C2H3+M=C2H2+H+M	8.00E+14	0.0	31.5
37.	CH3+OH=CH3OH	8.00E+12	0.0	0.0
38.	CH3OH+CH3=CH2OH+CH4	3.15E+10	0.0	6.4
39.	CH3OH+H=CH2OH+H2	1.50E+13	0.0	5.3
40.	CH3OH+OH=CH2OH+H2O	4.23E+12	0.0	0.8
41.	CH2OH=CH3O	1.00E+13	0.0	39.5
42.	CH2OH+H=CH2O+H2	7.50E+13	0.0	0.0
43.	CH3+NO=>CH3NO	4.00E+12	0.0	0.0
44.	CH3NO=>CH3+NO	7.00E+13	0.0	38.0
45.	CH3NO+CH3=CH2NO+CH4	1.60E+11	0.0	10.8
46.	CH3NO+H=CH2NO+H2	6.30E+13	0.0	9.7
47.	CH3NO+OH=CH2NO+H2O	1.85E+12	0.0	1.6
48.	CH2NO=HCN+OH	3.98E+11	0.0	33.0

NOTE: E units Kcal/mole, A units mole-cm-sec-K

Mechsenk.301

```
Hsu, D.S.Y.; Lin, M.C., "Laser probing and kinetic modeling og NO and CO
production C   in shock-wave decompositin of Nitromethane under higly
diluted conditions", Naval research laboratory, 1985
--------------------------------------------------------------------------------

CHEMKIN INTERPRETER OUTPUT: CHEMKIN-II Version 3.9  Aug. 1994
                            DOUBLE PRECISION

                           --------------------
                           ELEMENTS     ATOMIC
                           CONSIDERED   WEIGHT
                           --------------------
                            1. AR      39.9480
                            2. C       12.0112
                            3. H       1.00797
                            4. N       14.0067
                            5. O       15.9994
                           --------------------
 --------------------------------------------------------------------------------
                        C
                      P H
                      H A
                      A R
 SPECIES              S G  MOLECULAR  TEMPERATURE  ELEMENT COUNT
 CONSIDERED           E E  WEIGHT     LOW    HIGH  AR C  H  N  O
 --------------------------------------------------------------------------------
   1. AR              G  0   39.94800   300   5000   1  0  0  0  0
   2. CH4             G  0   16.04303   300   5000   0  1  4  0  0
   3. CH3             G  0   15.03506   300   5000   0  1  3  0  0
   4. CH3NO2          G  0   61.04056   300   4000   0  1  3  1  2
   5. CH2NO2          G  0   60.03259   300   5000   0  1  2  1  2
   6. CH3O            G  0   31.03446   300   3000   0  1  3  0  1
   7. CH3OH           G  0   32.04243   300   6000   0  1  4  0  1
   8. CH3NO           G  0   45.04116   300   6000   0  1  3  1  1
   9. C2H6            G  0   30.07012   300   4000   0  2  6  0  0
  10. C2H5            G  0   29.06215   300   5000   0  2  5  0  0
  11. C2H4            G  0   28.05418   300   5000   0  2  4  0  0
  12. CH2O            G  0   30.02649   300   6000   0  1  2  0  1
  13. NO              G  0   30.00610   300   5000   0  0  0  1  1
  14. NO2             G  0   46.00550   300   5000   0  0  0  1  2
  15. CO              G  0   28.01055   300   5000   0  1  0  0  1
  16. CO2             G  0   44.00995   300   5000   0  1  0  0  2
  17. OH              G  0   17.00737   300   5000   0  0  1  0  1
  18. H               G  0    1.00797   300   5000   0  0  1  0  0
  19. H2              G  0    2.01594   300   5000   0  0  2  0  0
  20. H2O             G  0   18.01534   300   5000   0  0  2  0  1
  21. HNO             G  0   31.01407   300   5000   0  0  1  1  1
  22. HCO             G  0   29.01852   300   5000   0  1  1  0  1
  23. HONO            G  0   47.01347   300   5000   0  0  1  1  2
  24. HCN             G  0   27.02582   300   6000   0  1  1  1  0
 --------------------------------------------------------------------------------
```

	REACTIONS CONSIDERED	(k = A T**b exp(-E/RT)) A	b	E
1.	CH3NO2+M=>CH3+NO2+M	6.00E+16	0.0	44.0
2.	CH3+NO2+M=>CH3NO2+M	1.20E+14	0.0	-12.6
3.	CH3+NO2=>CH3O+NO	1.30E+13	0.0	0.0
4.	CH3O+M=>CH2O+H+M	4.00E+40	-7.5	22.6
5.	CH3O+NO2=>CH2O+HONO	4.00E+11	0.0	0.0
6.	CH3O+NO=>CH2O+HNO	3.20E+12	0.0	0.0
7.	CH3O+OH=>CH2O+H2O	3.20E+13	0.0	0.0
8.	NO2+H=>NO+OH	2.90E+14	0.0	0.8
9.	CH3+OH=>CH2O+H2	8.00E+12	0.0	0.0
10.	CH3+OH=>CH3O+H	2.00E+16	0.0	27.4
11.	CH3NO2+CH3=>CH2NO2+CH4	2.40E+11	0.0	9.0
12.	CH3NO2+H=>CH2NO2+H2	2.50E+09	1.3	2.6
13.	CH3NO2+OH=>CH2NO2+H2O	1.70E+04	2.5	-2.4
14.	CH2NO2=>CH2O+NO	1.00E+13	0.0	36.0
15.	CH3+NO+M=>CH3NO+M	8.20E+31	-5.2	3.8
16.	CH3NO=>HCN+H2O	7.90E+12	0.0	39.3
17.	CH3NO+M=>CH3+NO+M	7.50E+40	-6.8	48.4
18.	CH2O+H=>HCO+H2	2.50E+09	1.3	2.6
19.	CH2O+OH=>HCO+H2O	6.90E+04	2.6	-1.9
20.	CH2O+CH3=>HCO+CH4	1.10E-03	4.9	3.5
21.	HNO+M=>H+NO+M	2.88E+16	0.0	48.8
22.	H2+OH=>H2O+H	5.20E+13	0.0	6.5
23.	H2O+H=>H2+OH	2.20E+14	0.0	21.8
24.	HONO+M=>NO+OH+M	1.80E+30	-3.9	52.3
25.	HCO+M=>H+CO+M	1.60E+14	0.0	14.7
26.	HCO+NO2=>HONO+CO	1.00E+14	0.0	0.0
27.	HCO+NO=>HNO+CO	2.00E+11	0.5	2.0
28.	CO+OH=>H+CO2	6.30E+07	1.3	-0.8
29.	CO+NO2=>NO+CO2	1.90E+12	0.0	29.3
30.	CH3O+CH3O=>CH3OH+CH2O	1.10E+13	0.0	0.0
31.	CH3+CH3=>C2H6	3.00E+12	0.0	0.0
32.	CH3+C2H6=>CH4+C2H5	5.50E+14	0.0	21.5
33.	C2H6+OH=>H2O+C2H5	6.30E+13	0.0	3.6
34.	C2H5+M=>C2H4+H+M	4.70E+14	0.0	26.6
35.	C2H5+NO2=>CH3+CH2O+NO	1.30E+13	0.0	0.0
36.	C2H4+OH=>CH2O+CH3	5.00E+12	0.0	0.0
37.	CH4+OH=>CH3+H2O	3.20E+13	0.0	5.0

NOTE: E units Kcal/mole, A units mole-cm-sec-K

Mechanism used in computer simulations

For different dilutants:

					A	b	E
Nitrogen:	CH3NO2 + M	=	CH3	+ NO2 + M	**1.03E17**	0.00	**43.60**
Argon:	CH3NO2 + M	=	CH3	+ NO2 + M	**3.75E17**	0.00	**49.50**

SPECIES CONSIDERED:
AR/N2 CH3NO2 CH3 NO2 NO CO CO2 CH2O HCO CH4 CH2NO2 H H2 H2O OH HNO CH3OH
C2H6 C2H5 C2H4 CH3O CH3NO HNO2 O CH3ONO

	REACTIONS CONSIDERED	(k = A T**b exp(-E/RT)) A	b	E
1.	CH3NO2+M=CH3+NO2+M	**1.03E17/3.75E17**	**0.0**	**43.6/49.5**
2.	CH3+NO2=CH3O+NO	1.30E+13	0.0	0.0
3.	CH3O+M=CH2O+H+M	4.00E+40	-7.5	22.6
4.	NO2+H=NO+OH	2.90E+14	0.0	0.8
5.	CH3O+NO=CH2O+HNO	3.20E+12	0.0	0.0
6.	H+NO+M=HNO+M	5.40E+15	0.0	-0.6
7.	CH3O+NO2=CH2O+HNO2	4.00E+11	0.0	0.0
8.	HNO2+M=NO+OH+M	3.00E+18	0.0	46.7
9.	CH3+NO=CH3NO	4.00E+12	0.0	0.0
10.	CH3O+NO=CH3ONO	6.30E+13	0.0	0.0
11.	CH3O+H=CH2O+H2	1.00E+14	0.0	0.0
12.	CH3O+H=CH3+OH	9.09E+17	0.0	15.2
13.	CH3+OH=CH2O+H2	8.00E+12	0.0	0.0
14.	CH3O+OH=CH2O+H2O	3.20E+13	0.0	0.0
15.	H2+OH=H2O+H	5.20E+13	0.0	6.5
16.	CH3O+CH3O=CH3OH+CH2O	1.10E+13	0.0	0.0
17.	CH3NO2+CH3=CH2NO2+CH4	2.40E+11	0.0	9.0
18.	CH3NO2+NO2=CH2NO2+HNO2	3.07E+12	0.0	18.3
19.	CH3NO2+H=CH2NO2+H2	2.50E+09	1.3	2.6
20.	CH3NO2+OH=CH2NO2+H2O	6.90E+04	2.6	-1.9
21.	CH2NO2=CH2O+NO	1.00E+13	0.0	36.0
22.	CH2O+H=HCO+H2	2.50E+09	1.3	2.6
23.	CH2O+OH=HCO+H2O	6.90E+04	2.6	-1.9
24.	CH2O+NO=HCO+HNO	2.86E+14	0.0	42.0
25.	CH2O+CH2NO2=HCO+CH3NO2	2.50E+13	0.0	10.0
26.	HCO+NO2=HNO2+CO	1.00E+14	0.0	0.0
27.	HCO+NO2=H+CO2+NO	1.00E+14	0.0	0.0
28.	HCO+NO2=OH+CO+NO	1.00E+14	0.0	0.0
29.	HCO+M=H+CO+M	1.00E+15	0.0	14.7
30.	HCO+NO=HNO+CO	2.00E+11	0.5	2.0
31.	CO+OH=CO2+H	1.50E+07	1.3	-0.8
32.	CO+O+M=CO2+M	2.80E+13	0.0	-4.5
33.	CH3+CH3=C2H6	2.50E+12	0.0	0.0
34.	CH3+CH3=C2H5+H	8.00E+14	0.0	26.6
35.	CH3+CH3=C2H4+H2	1.00E+16	0.0	32.0
36.	C2H6+CH3=C2H5+CH4	5.50E+14	0.0	21.5
37.	C2H6+OH=C2H5+H2O	6.30E+13	0.0	3.6
38.	C2H6+H=C2H5+H2	1.30E+14	0.0	9.4
39.	C2H5+M=C2H4+H+M	4.70E+14	0.0	26.6
40.	C2H5+OH=C2H4+H2O	2.00E+13	0.0	0.0
41.	C2H4+OH=CH2O+CH3	5.00E+12	0.0	0.0
42.	CH4+OH=CH3+H2O	3.20E+13	0.0	5.0

NOTE: E units Kcal/mole, A units mole-cm-sec-K

APPENDIX D

Simulations vs. Experiments

Comparison between measured and calculated decomposition of CH_3NO_2 for the reactive experiments. The concentration is in *mole/cm3* and is plotted as a function of time (in *s*). Experiments numbered up to 46 were diluted in nitrogen, while the rest were diluted in argon. The number in the upper right corner of each figure corresponds to the number of each experiment. Data for all experiments are found in APPENDIX B. These simulations were achieved by using the following values for the thirdbody decomposition of NM as extracted from the experimental data:

		A	n	E (kcal/mole)
with nitrogen:	$CH_3NO_2 + M = CH_3 + NO_2 + M$	1.03E17	0.00	43.60
with argon:	$CH_3NO_2 + M = CH_3 + NO_2 + M$	3.74E17	0.00	49.50

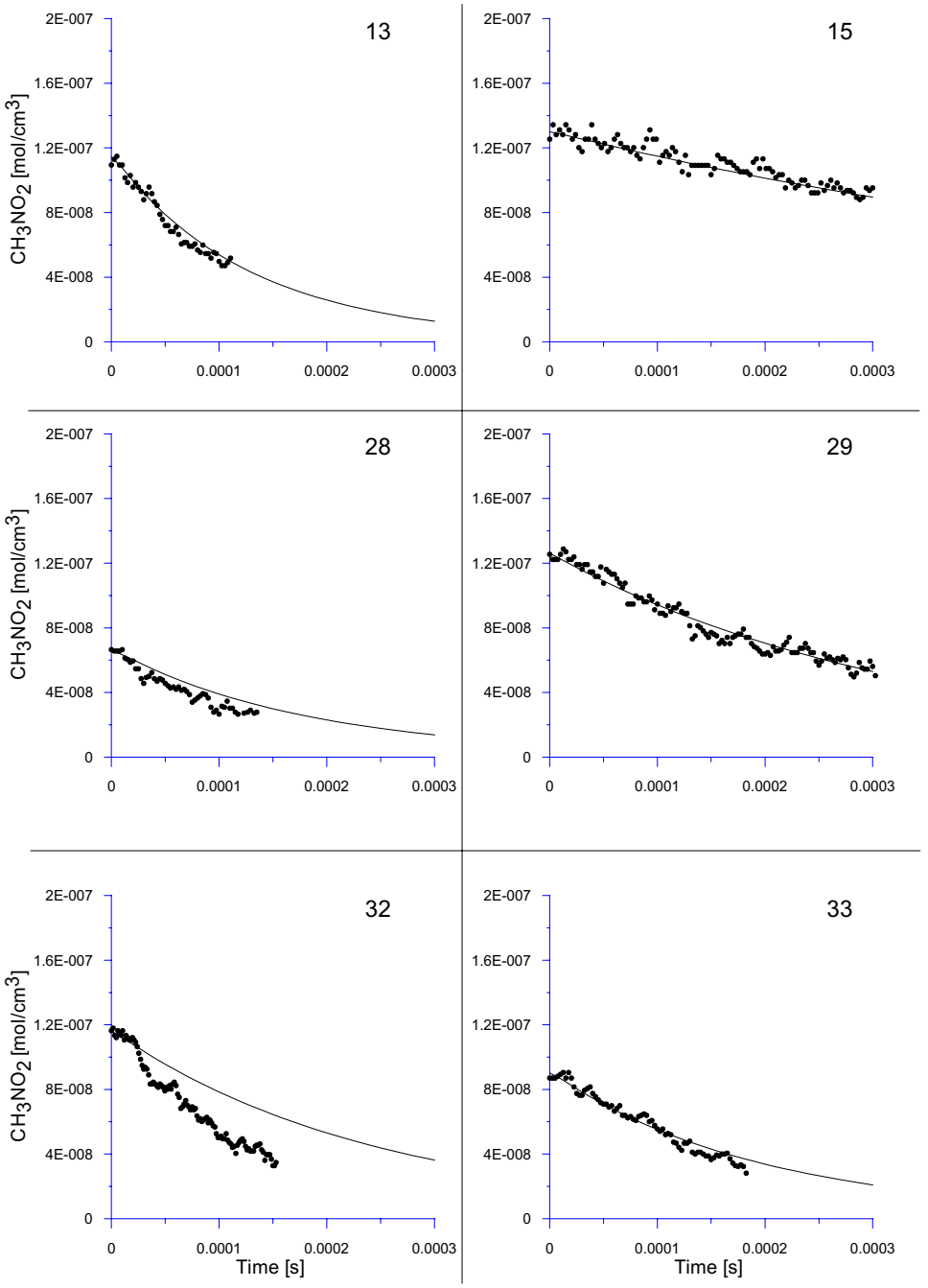

Figure D - 1: Simulated vs. experimental results. Exp. 13-33 diluent: N_2.

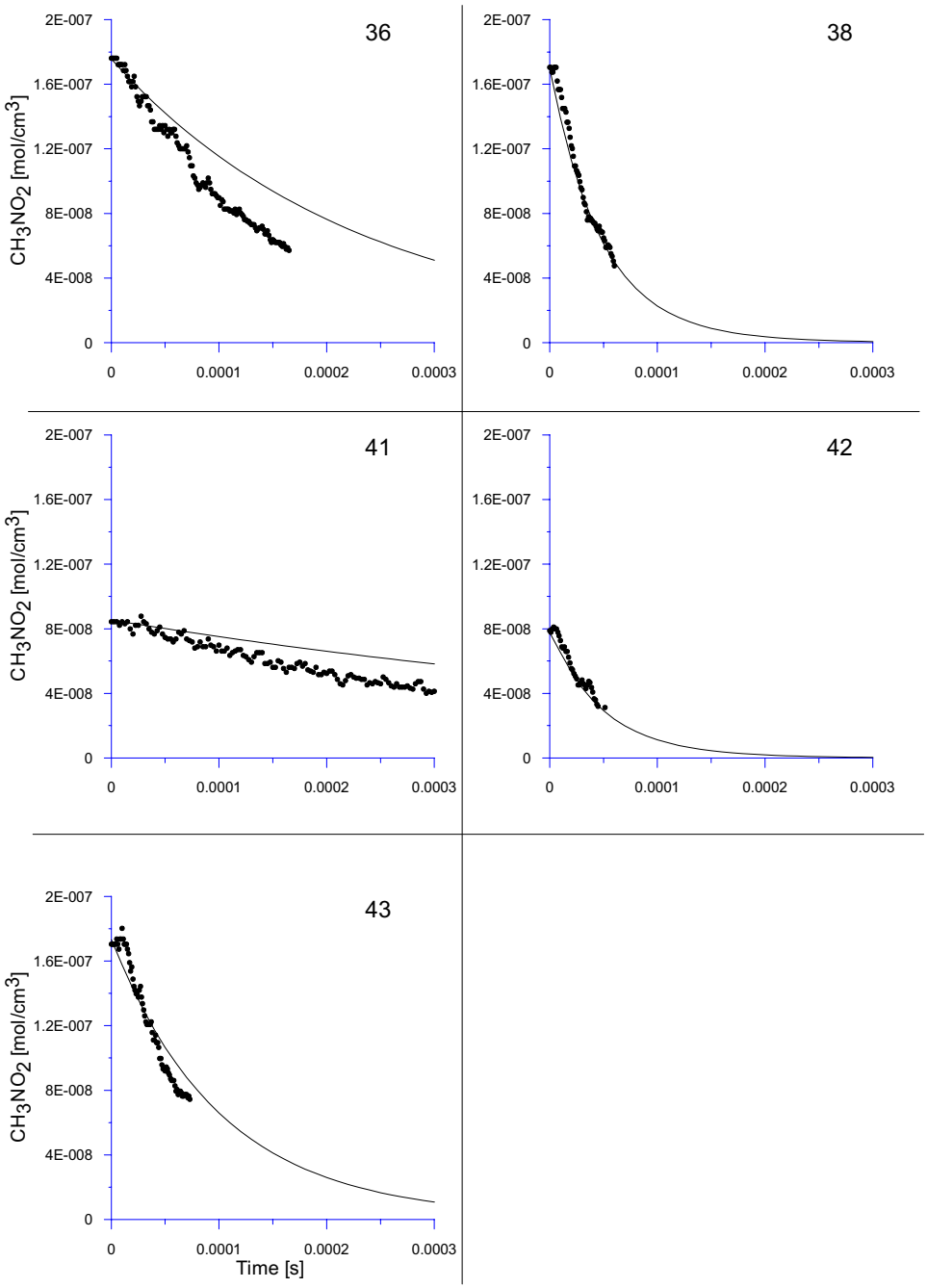

Figure D - 2: Simulated vs. experimental results. Exp. 36-43 diluent: N_2.

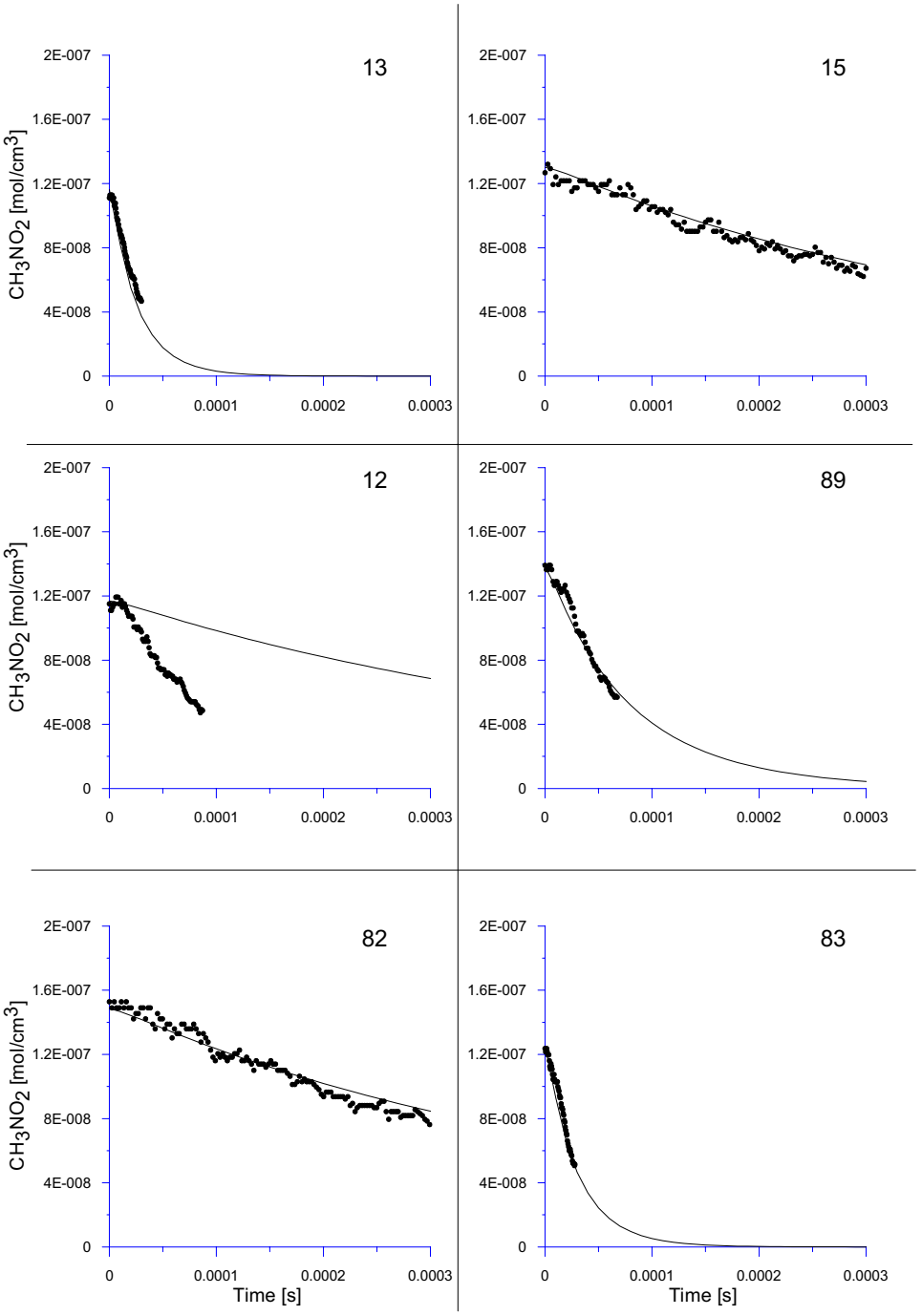

Figure D - 3: Simulated vs. experimental results. Exp. 47-53 diluent: Ar

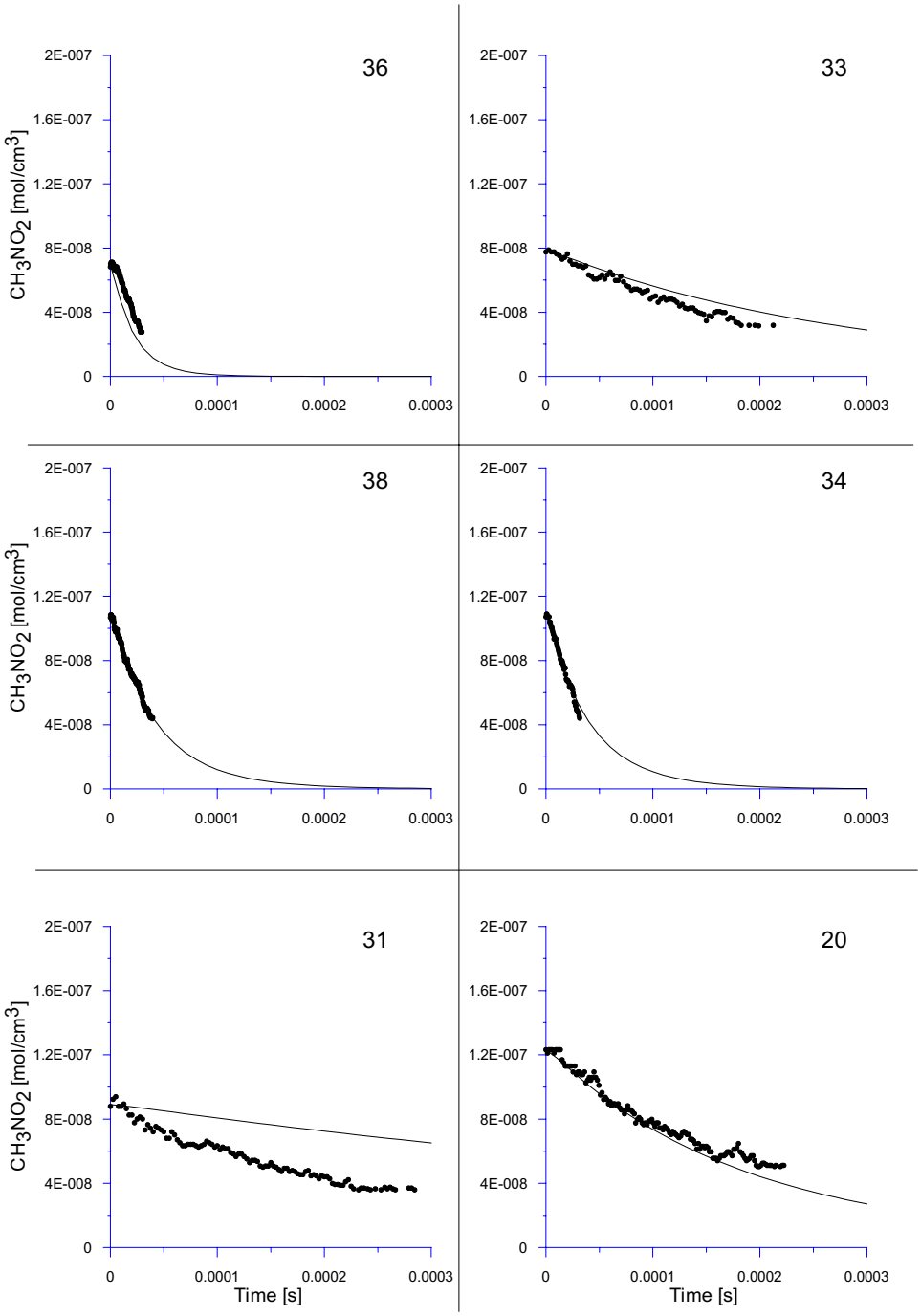

Figure D - 4: Simulated vs. experimental results. Exp. 54-60 diluent: Ar

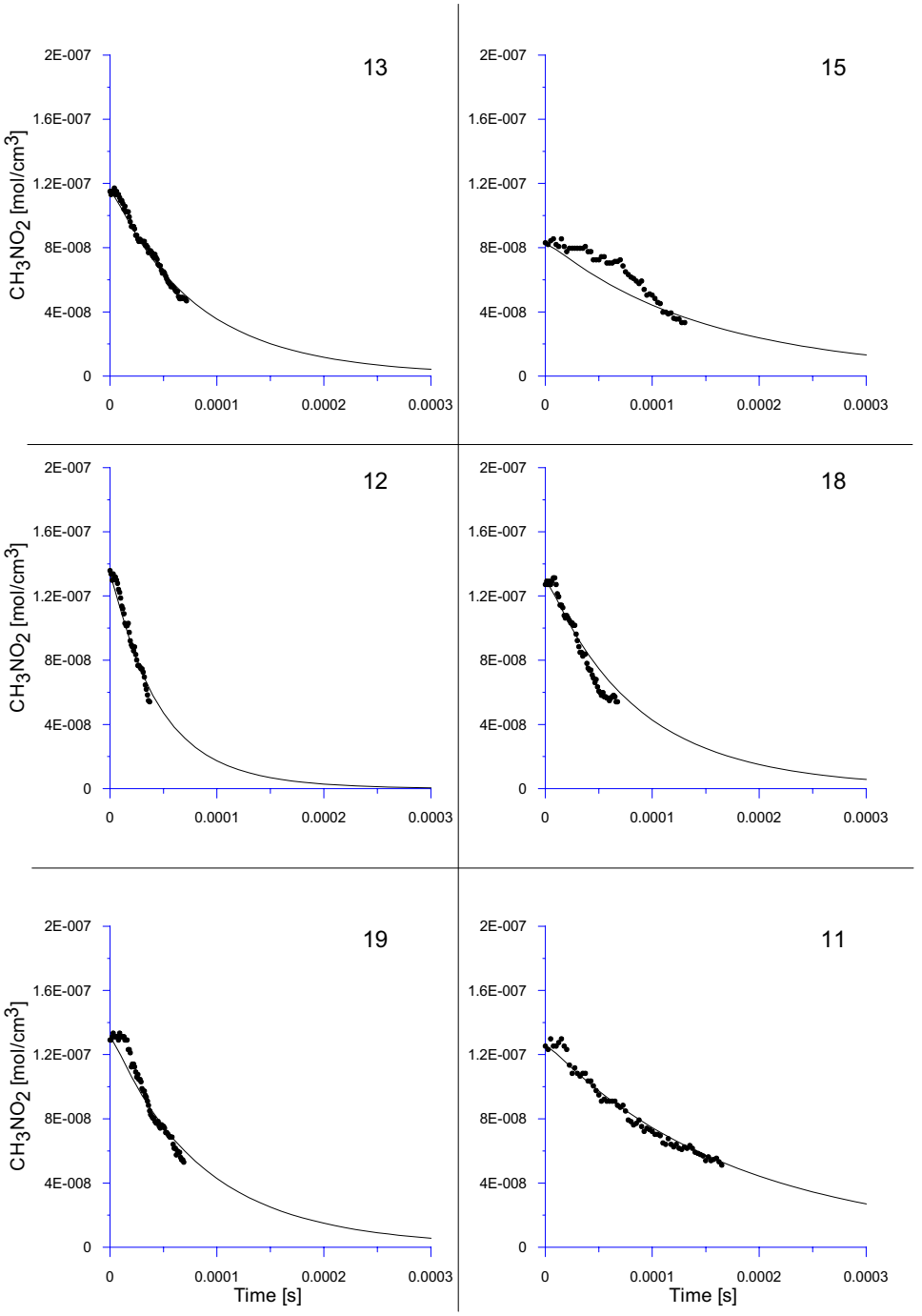

Figure D - 5: Simulated vs. experimental results. Exp. 61-66 diluent: Ar

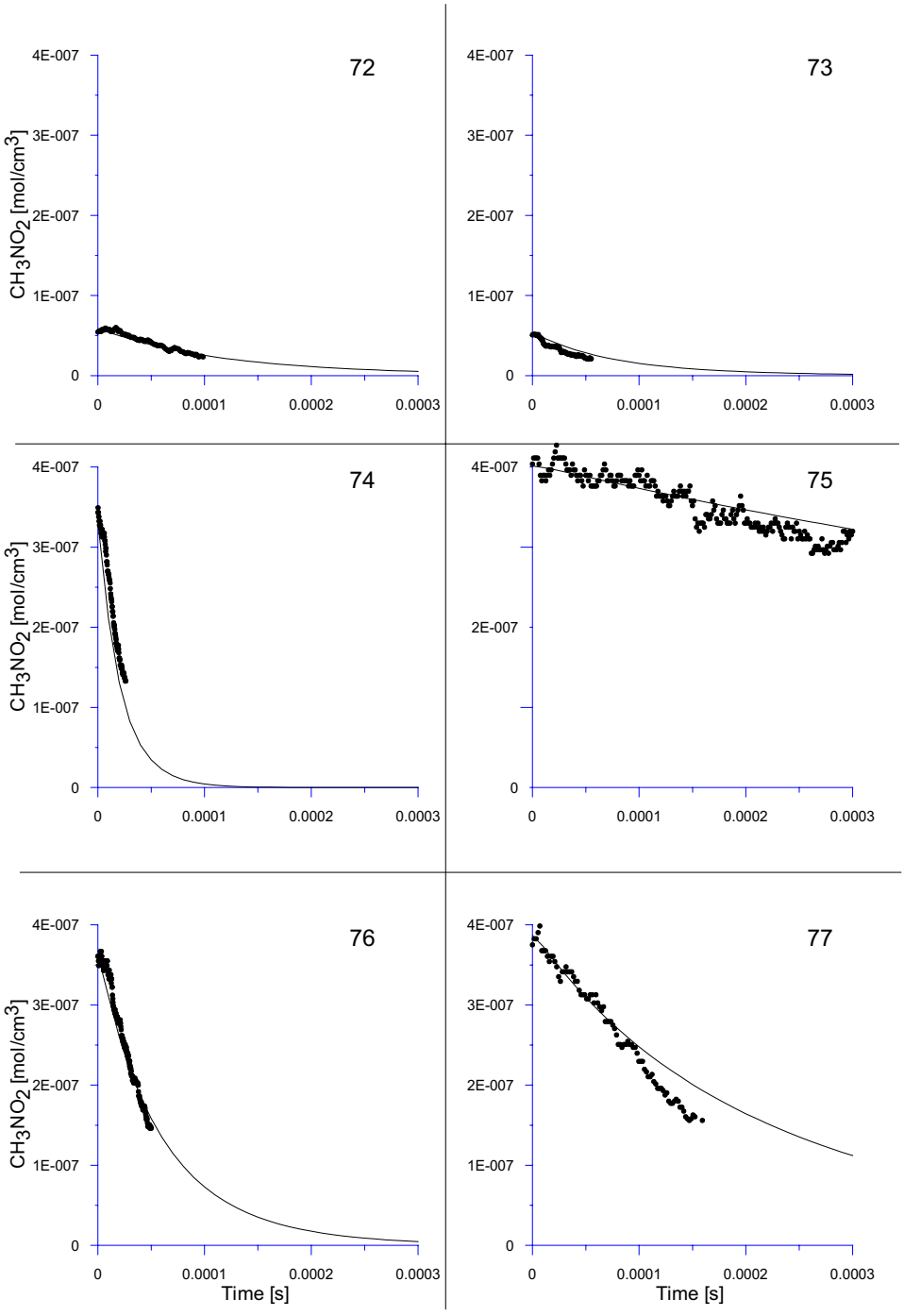

Figure D - 6: Simulated vs. experimental results. Exp. 72-77 diluent: Ar

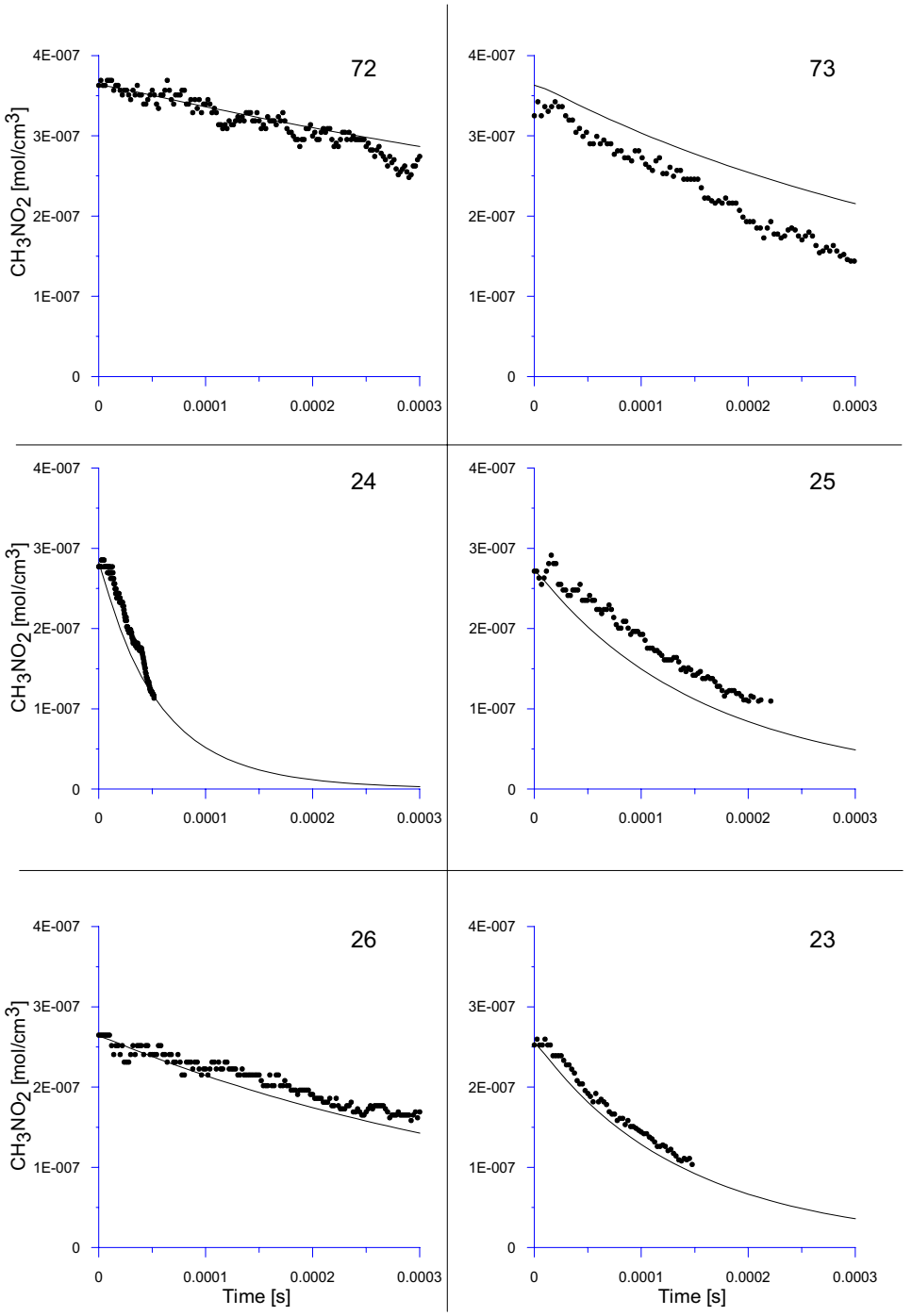

Figure D - 7: Simulated vs. experimental results. Exp. 78-83 diluent: Ar

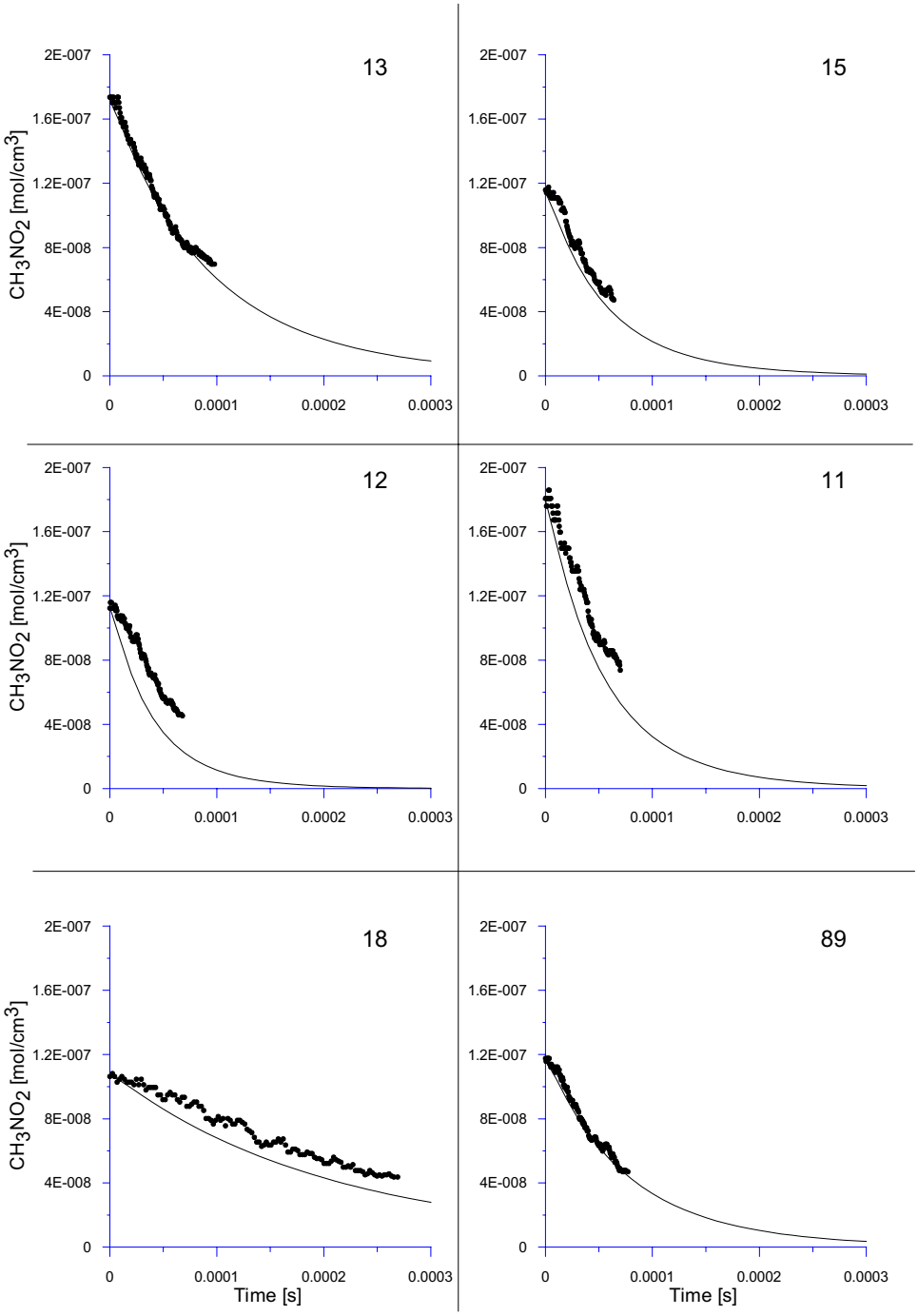

Figure D - 8: Simulated vs. experimental results. Exp. 84-90 diluent: Ar

APPENDIX E

Experimental Results - GREMI

Air 1.0 | Methode DRÄGER TUBES
Mixture Pure air
Flow Meter AIR-LIQUID
Comments Preliminary measurements in pure air. Airstream preheated in annular reactor. No opening in front.

N°	Q_{air}	$Q_{Methane}$	$T_{Reactor}$	$T_{Mixture\ in}$	T_{Sample}	O_2	CO_2	CO	N_2	NO_x	CH_4	P	V - I - ϕ
	l/min	l/min	gr.C	gr.C	gr.C	vol%		ppm		ppm	vol%	kW	
	9,3									>10 ppm		1,69	384 - 15,7 - 0,160
	9,3									>100 ppm		1,69	384 - 15,7 - 0,160
	9,3									>50 ppm		1,69	384 - 15,7 - 0,160
	9,3									>500 ppm		1,69	384 - 15,7 - 0,160
	9,6									1400 ppm		1,69	382 - 15,6 - 0,160
	19,8									1000 ppm		1,80	383 - 15,5 - 0,175

Air 2.0 | Date 1-6;6/5/94, 7-11;2-3/6/94
Methode TESTO33
Mixture Pure air
Measured Treact, Tair in, Tgu, Tg, O2, CO, NOx, P, Qgu, tgu
Flow Meter AIR-LIQUID
Comments Preliminary measurements in pure air. Airstream preheated in annular reactor. No opening in front. Temperature of preheated air-stream measured with mercury thermometer just before mixing vane.

N°	Q_{air}	$Q_{Methane}$	$T_{Reactor}$	$T_{Mixture\ in}$	T_{Sample}	O_2	CO_2	CO	N_2	NO_x	CH_4	P	V - I - ϕ
	l/min	l/min	gr.C	gr.C	gr.C	vol%				ppm		kW	
1	20									3312			
2	30									3150			
3	40									2700			
4	50									2424			
5	60									2426			
6	70									1730			
7	20		325	210	17,40	20,1				3336		1,92	385 - 15,8 - 0,18
8	40		325	229	17,20	20,4				3189		1,93	386 - 15,7 - 0,18
9	60		288	192	18,83	20,7				2676		1,93	
10	80		268	168	18,68	20,7				2358		1,92	
11	100		230	140	19,80	20,8				2170		1,93	384 - 15,7 - 0,18

Table E-1: Air No 1 & 2

Air 3.0

Date 24/6/94
Methode TESTO33
Mixture Pure air
Measured Treact, Tg, O2, NOx, P
Flow Meter TYLAN (Read),f(air/Methane)=0.72; AIR-LIQUID (Reg.)
Comments Water-cooled reactor. Room tempered air is mixed with Methane just before inlet nozzle. Main out-let in front.

N°	Q_{air}	$Q_{Methane}$	$T_{Reactor}$	$T_{Mixture\ in}$	T_{Sample}	O_2	CO_2	CO	N_2	NO_x	CH_4	P	V - I - ϕ
	l/min	l/min	gr.C	gr.C	gr.C	vol%		ppm		ppm	vol%	kW	
1	20		280,0		21,9	20,0				3297		2,05	385 - 15,7 - 0,19
2	40		250,0		21,8	20,3				3265		2,03	386 - 15,5 - 0,19
3	50		240,0		21,8	20,4				2986		2,02	386 - 15,4 - 0,2
4	60		230,0		21,8	20,5				2666		2,00	386 - 15,5 - 0,19
5	70		225,0		21,8	20,5				2476		1,96	384 - 15,4 - 0,19
6	80		220,0		21,7	20,6				2257		1,92	384 - 15,3 - 0,19
7	90		205,0		21,8	20,6				2091		1,90	382 - 15,2 - 0,19
8	100		180,0		21,8	20,6				2014		1,90	382 - 15,1 - 0,19
9	110		153,3		21,5	20,7				1876		1,85	380 - 14,9 - 0,19

Air/ Methane 1.0

Date 2,6 Vol%.27/5/94, 2 vol%: 7/5-6/6/94
Methode TESTO33
Mixture 2/2,6 vol% Methane in air
Measured Treact, Tair in, Tgu, Tg, O2, CO, NOx, P
Flow Meter TYLAN (Read), f(air/Methane)=0.72; AIR-LIQUID (Reg.)
Comments Room tempered air is mixed with Methane just before inlet nozzle. No samples taken for cromatograph.

N°	Q_{air}	$Q_{Methane}$	$T_{Reactor}$	$T_{Mixture\ in}$	T_{Sample}	O_2	CO_2	CO	N_2	NO_x	CH_4		
	l/min	l/min	gr.C	gr.C	gr.C	vol%		ppm		ppm	vol%		
	2,6 vol% Methane in air				1-3: 27/05/94								
1	38,96	1,04				18,4		4746		2574			
2	48,70	1,30				18,6		4858		2185			
3	58,44	1,56				18,8		4672		1968			
	2 vol% Methane in air				1: 3/6/94, 2-4: 6/6/94, 5: 7/5/94								
1	40	0,82	370	236,0	17,5	16,8		5423		3348			
2	60	1,24	315	186,7	17,7	17,3		6223		2916			
3	80	1,65	324	202,4	18,3	17,9		6918		2116			
4	100	2,07				17,9		6921		1761			

Table E-2: Air N^o 3 and Air-Methane N^o 1

Air/ Methane 2.0

Date	Pure air: 9/6/94 2 vol%: 8/6/94
Methode	TESTO33 / Samples taken for Cromatograph
Mixture	Pure air / 2 vol% Methane in air
Measured	TESTO33 ; Treact, Tair in, Tg, O2, CO, NOx
	Cromatograph ; CH4, C2H6, CO2, CO, O2, N2
Flow Meter	TYLAN (Read),f(air/Methane)=0.72; AIR-LIQUID (Reg.)
Comments	Air preheated in annular reactor before beeing mixed with Methane just before inlet nozzle.

N°	Q_{air}	$Q_{Methane}$	$T_{Reactor}$	$T_{Mixture\ in}$	T_{Sample}	O_2	CO_2	CO	N_2	NO_x	CH_4	P
	l/min	l/min	gr.C	gr.C	gr.C	vol%		ppm		ppm	vol%	kW
	21		312	165	16,3	20,0				3334		1,87
	31		325	210	16,3	20,3				3352		1,90
	41		325	226	16,5	20,4				2917		1,93
	51		325	225	16,6	20,5				2587		1,92
	62		318	212	16,4	20,6				2280		1,90
	72		305	202	16,6	20,6				2067		1,92
	82		298	190	16,8	20,6				1895		1,93
2 vol% Methane in air: TESTO 33												
3	20	0,41	410	156	19,4	15,1		2934		2207		1,97
2	30	0,62	372	241	19,3	15,9		5890		2086		1,98
1	40	0,82	370	262	19,5	16,5		7104		2219		1,97
5	50	1,03	368	253	19,6	17,0		7709		1957		1,95
9	60	1,23	352	235	19,6	17,3		7968		1778		1,94
4	70	1,44	313	191	19,3	17,6		7898		1630		1,93
7	80	1,65	250	130	19,4	17,9		7292		1554		1,96
2 vol% Methane in air: CHROMATOGRAPH												N_2
						vol%	vol%	vol%			vol%	vol%
3						15,60	2,00	0,21			0,01	80,00
2						16,50	1,86	0,52			0,15	79,30
1						16,90	1,70	0,61			0,42	77,50
5						17,50	1,42	0,67			0,63	76,90
9						17,70	1,20	0,80			0,99	76,40
4						18,10	1,10	0,76			1,17	76,90
7						18,50	0,90	0,60			1,26	76,30

Table E-3: Air-Methane N° 2

Air/ Methane 3.0																				
	Date	7/6/94																		
	Methode	TESTO33 / Samples taken for Cromatograph																		
	Mixture	3 vol% Methane in air																		
	Measured	TESTO33 ; T react, T air in, T g, O2, CO, NOx																		
		Cromatograph ; CH4, C2H6, CO2, CO O2, N2																		
	Flow Meter	TYLAN (Read), f(air/Methane)=0.72; AIR-LIQUID (Reg.)																		
	Comments	Air preheated in annular reactor before beeing mixed with Methane just before inlet nozzle. 5 Samples were taken. Sample 2 taken as reference for same conditions as sample 1, with no discharge running.																		
	3 vol% Methane in air: TESTO 33																			
N°	Q_{air}	$Q_{Methane}$	$T_{Reactor}$	$T_{Mixture\ in}$	T_{Sample}	O_2	CO_2	CO	N_2	NO_x	CH_4	P								
	l/min	l/min	gr.C	gr.C	gr.C	vol%		ppm		ppm	vol%	kW								
1	60	1,87	365	220	20,7	15,0		11417		1826										
3	70	2,18	325	200	20,7	15,6		11198		1627		2,00								
4	80	2,52	360	230	21,0	15,5		12732		1490										
5	90	2,83	350	210	21,1	16,1		11347		1347		2,11								
	2 vol% Methane in air: CHROMATOGRAPH																	N_2	C_2H_6	
						vol%	vol%	vol%			vol%							vol%	vol%	
1						15,8	2,10	1,1			1,30							77,30		
3						16,3	1,70	1,1			1,60							76,00		
4						16,1	1,80	1,5			1,55							76,70	0,00	
5						16,8	1,50	1,2			1,81							76,40	0,04	
2						13,6	3,63	0,9			0,22							79,40		

Table E-4: Air-Methane N^{o} 3

Table E-5: Air-Methane N° 4

Air/ Methane 4.0	Date	30/6/94
	Methode	TESTO33 / Samples taken for Cromatograph
	Mixture	2-8 vol%Methane in air
	Measured	TESTO33 ; TReactor, TSample, O2, CO, NOx
		Chromatograph ; CH4
	Flow Meter	TYLAN (Read), f(air/Methane)=0.72; AIR-LIQUID (Reg.)
	Comments	Water-cooled reactor. Only HC's (CH_4) were measured with Cromatograph (CO_x considered to be in too low concentrations to be detected with reasonable accuracy). Produced gas observed to have a Yellow-brownish color except for exp. 8 (blanc). After som minutes in the glasbulb, this color disapeared slowly. Liquid was formed during the experiment having a deep green color. The front outlet was almost completly closed. The current and power was unstable during the whole experiment. No. 8 gave transparant gas. Inlet-flow controlled by air-liquid and adjusted with Tylan.

N°	CH_4	Q_{air}	$Q_{Methane}$	$T_{Reactor}$	T_{Sample}	O_2	CO	NO_x	CH_4	P	Liquid formed
	Vol%	l/min	l/min	gr.C	gr.C	vol%	ppm	ppm	vol%	kW	
1	6	20	1,31	408	21,8	7,3	6983	3283	0,070	1,95	Liquid is formed
2	4	20	0,85	393	21,9	12,6	6928	3184	0,330	1,96	Litle or no liquid
3	3	20	0,63	373	21,9	14,9	5058	3235	0,410	1,99	no liquid
4	2	20	0,41	345	21,8	16,9	3341	3219	0,360	2,02	—"—
5	2	15	0,31	335	21,9	16,5	2826	3301		2,00	—"—
6	4	15	0,63	353	22,0	12,2	5401	3300	0,190	2,01	—"—
7	6	15	0,98	388	22,0	7,2	4911	3297		2,03	Liquid is formed
8	8	15	1,35	420	22,0	2,0	6307	2783	0,100	2,05	Important quantities of liquid is formed
9	6	10	0,66	410	22,5	7,5	1671	3295	0,004	1,98	Litle or no liquid

APPENDIX F

NTNU Experimental

- Calibration Curves
- Tesla Coil Formulas

Calibration Curves

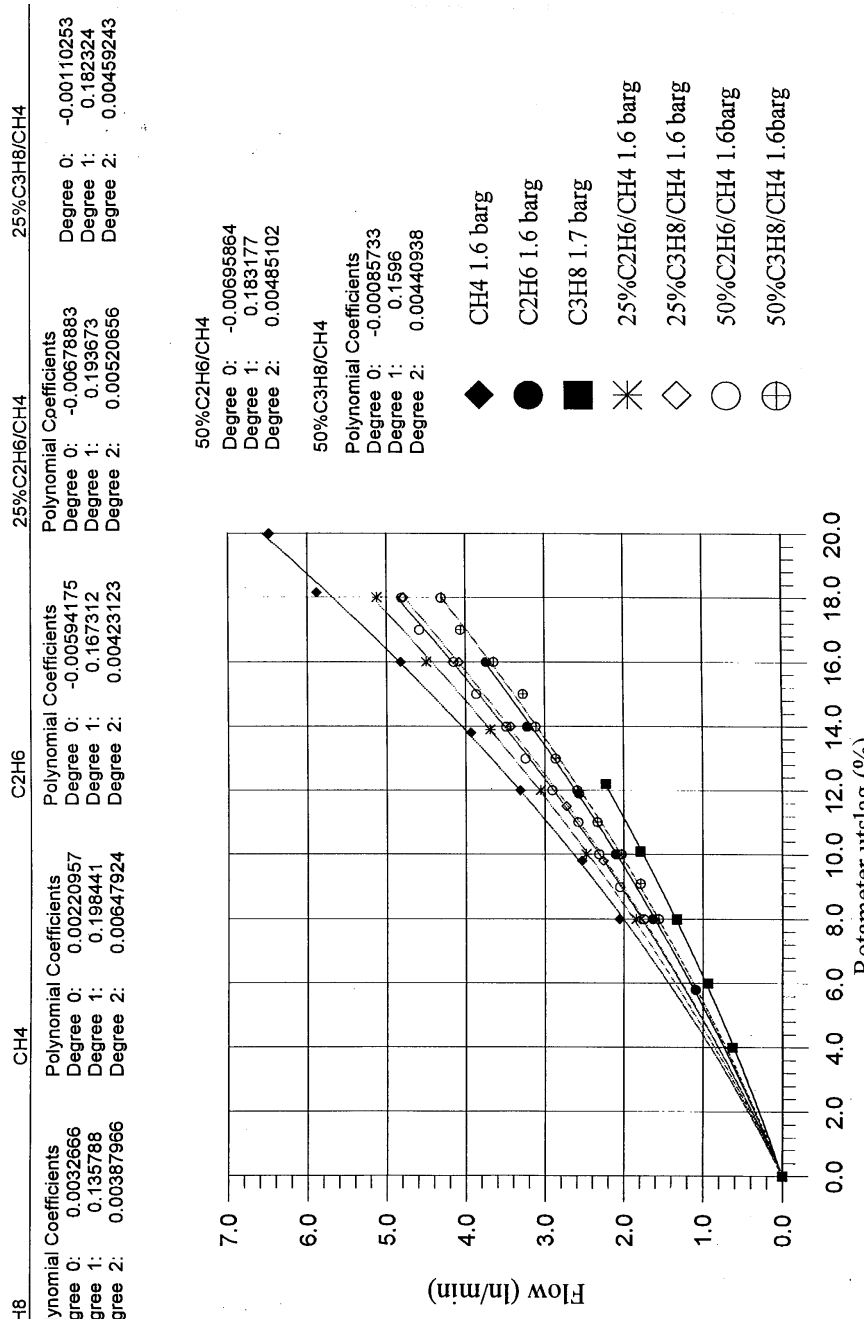

Figure F - 1: Rotameter calibration.

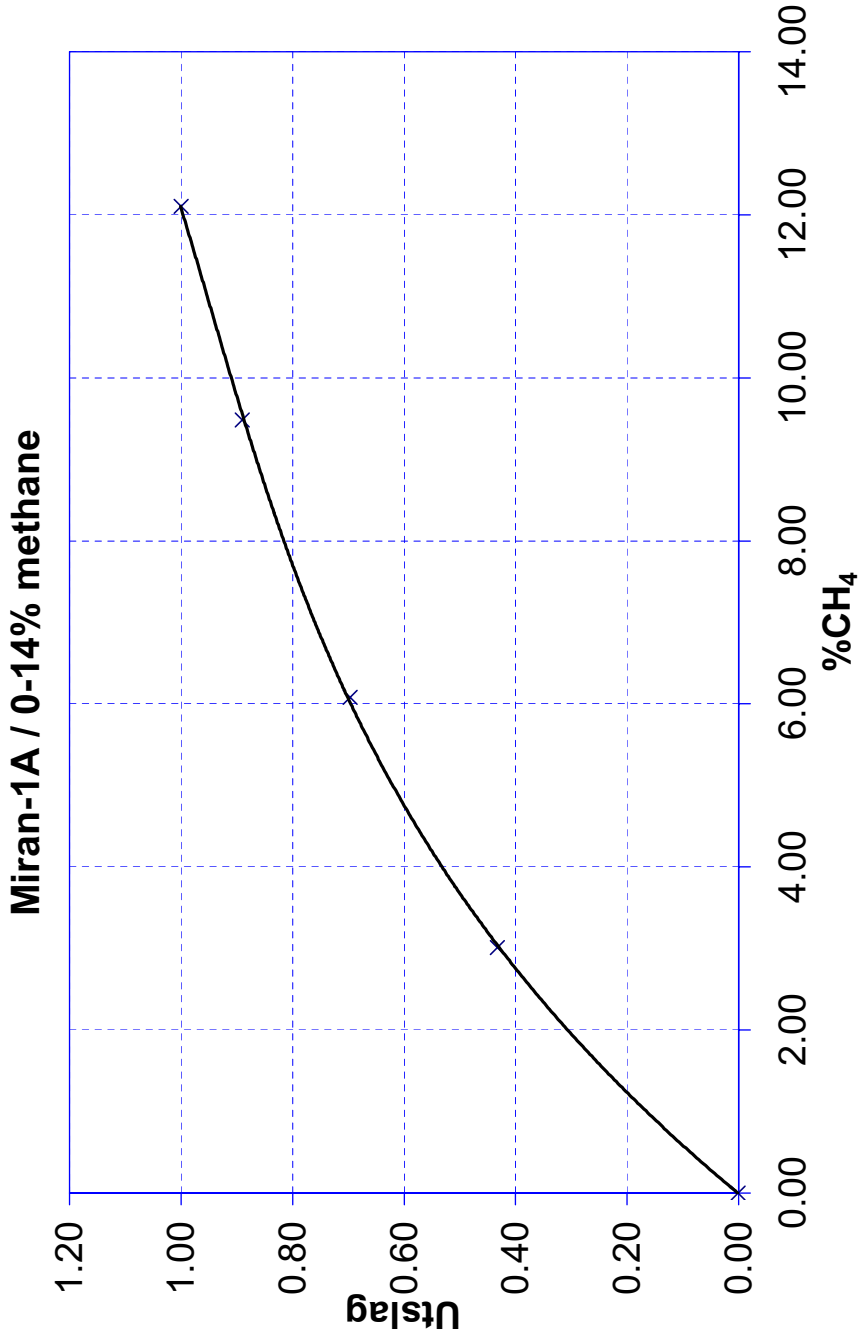

Figure F - 2: Miran-1A Infrared Spectrophotometer calibration for methane.

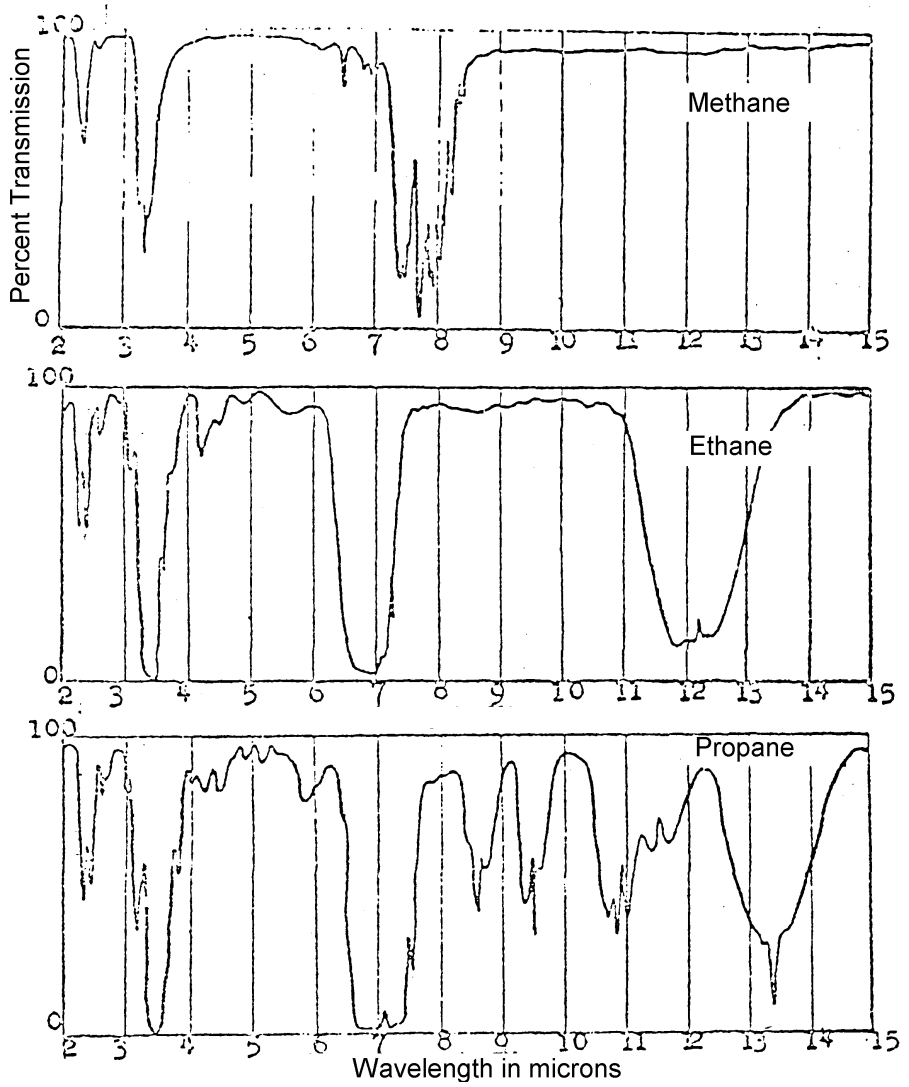

Figure F - 3: Transmission properties for different hydrocarbons.

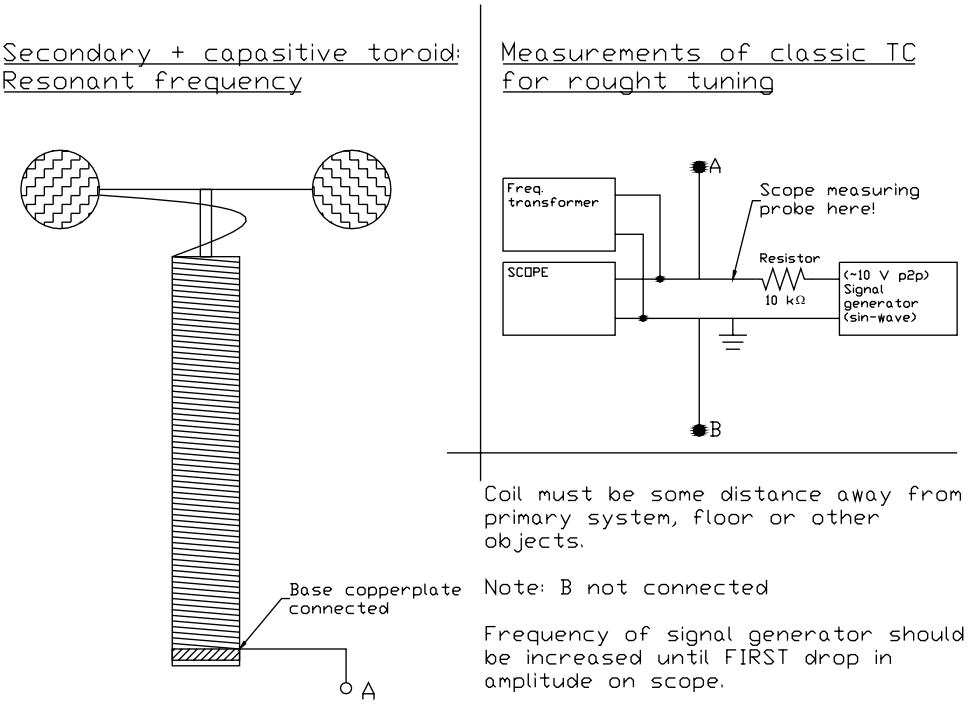

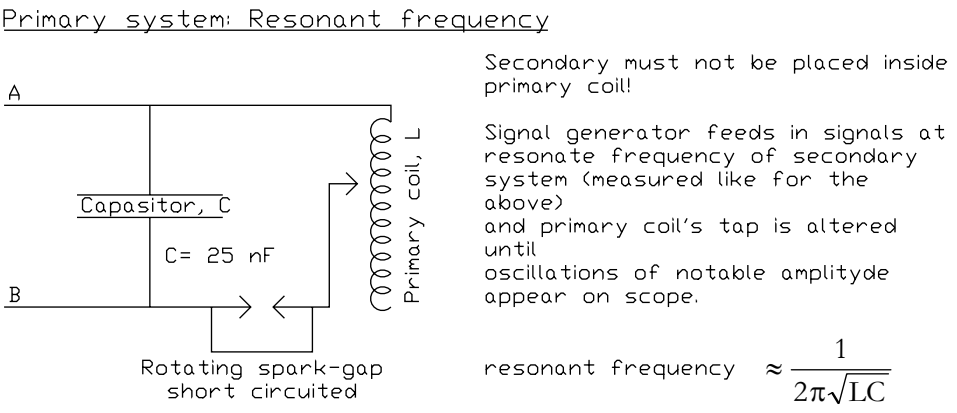

NOTE: Power supply MUST NOT be connected!

Figure F - 4: Tuning the 8 *kW* tesla coil.

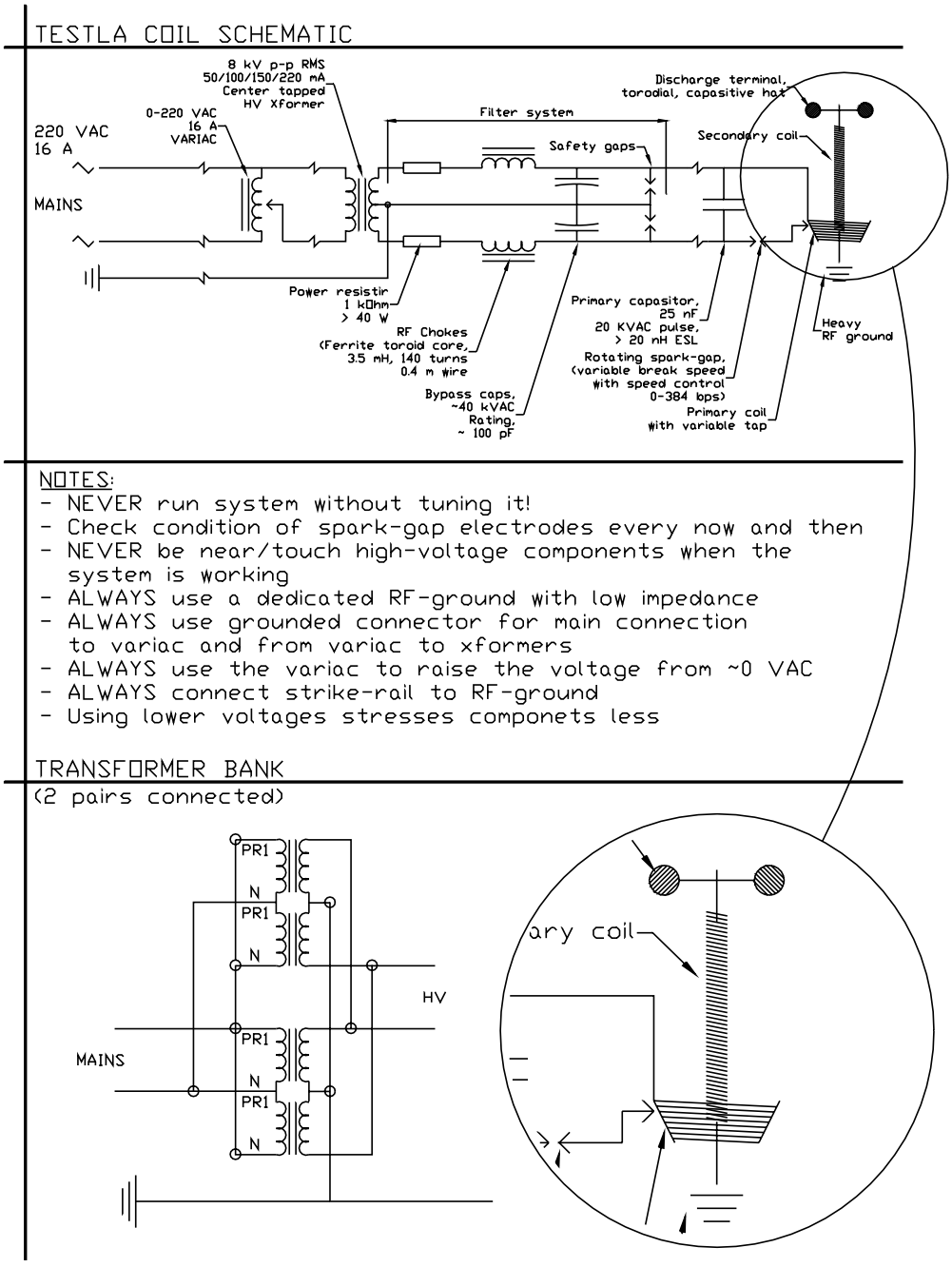

Figure F - 5: Schematic diagram of 8 *kW* tesla coil.

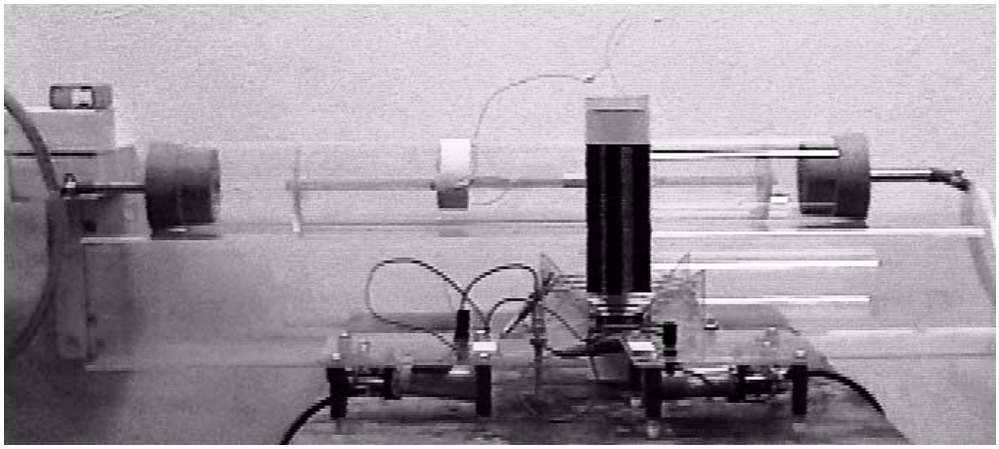

Figure F - 6: An image of the small tesla coil.

Small tesla coil set up for one of the experimental configurations, with flat electrodes (copper + glass) in the duct centre and gas inlet and outlet at each end of the plexiglass tube.

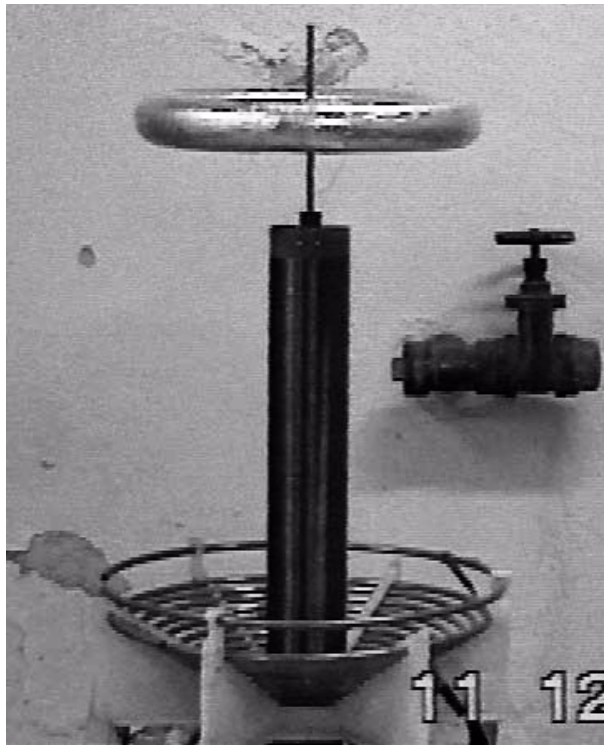

Figure F - 7: An image of the 8 *kW* tesla coil.

Primary and secondary windings and toroid discharge-hat.

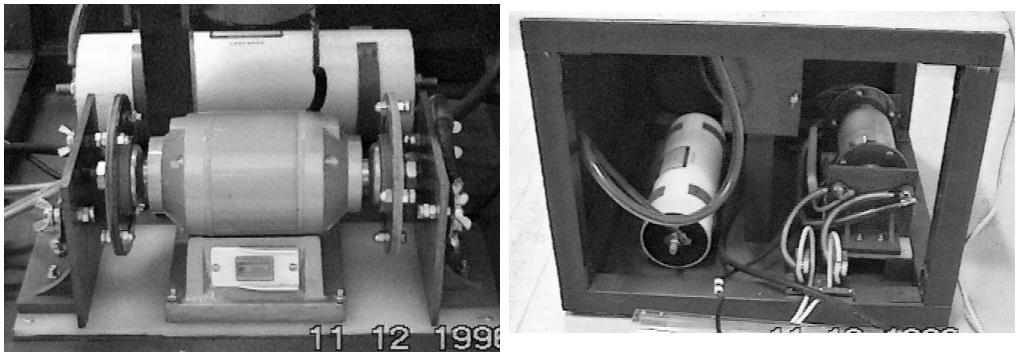

Figure F - 8: The variable speed rotating spark-gap.

Left and right image show the front and side view of the variable speed rotating spark-gap with the capacitor situated behind.

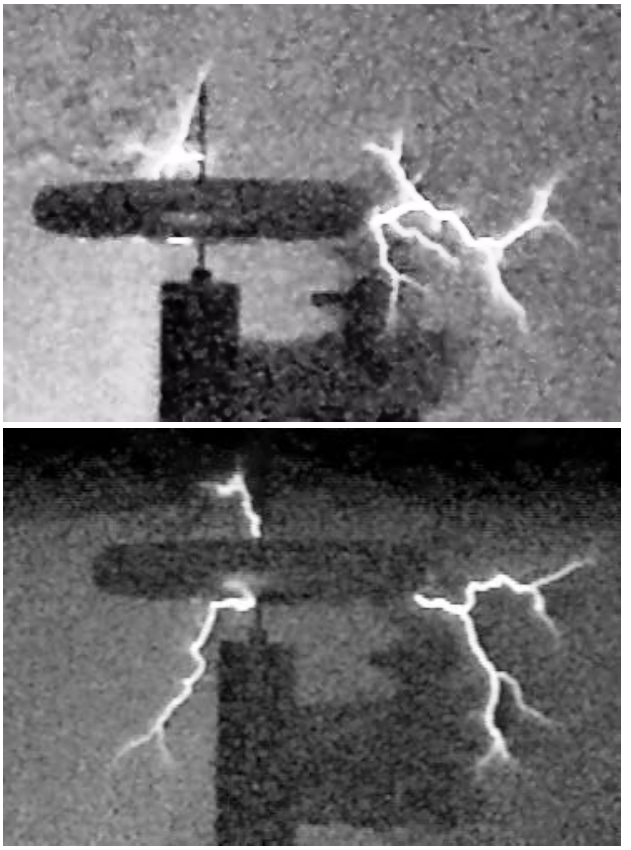

Figure F - 9: The 8 *kW* tesla coil in action.

Tesla Coil Formulas

These formulas have been collected from various litterature sources on the Tesla coils, and applied when performing secondary coil design for the experimental system.

Ohm's Law

$E = IZ$ $P = IE$

E = volts
I = current in amps
Z = impedance or resistance in ohms
P = power in watts

Transformer Input and Output

$E_P I_P = E_S I_S$

E_P = primary voltage
I_P = primary current in amps
E_S = secondary voltage
I_S = secondary current in amps

Capacitive Reactance

$$X_C = \frac{1}{2\pi FC}$$

X_C = capacitive reactance in ohms
F = frequency in hertz
C = capacitance in farads

Inductive Reactance

$$X_L = 2\pi FL$$

X_L = inductive reactance in ohms
F = frequency in hertz
L = inductance in henrys

Figure F - 10: Tesla coil formulas (1/5)

Resonant Circuit Formula

$$4\pi^2F^2LC = 1$$

$$F = \frac{1}{2\pi\sqrt{LC}}$$

F = frequency in hertz
L = inductance in henrys
C = capacitance in farads

Archimedes Spiral Coil Inductance

$$L = \frac{(NR)^2}{8R + 11W}$$

L = inductance of coil in microhenrys (μH)
R = average radius of the coil in inches
N = number of turns
W = width of the coil in inches

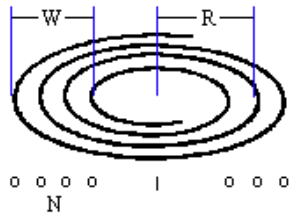

Helical Coil Inductance

$$L = \frac{(NR)^2}{9R + 10H}$$

L = inductance of coil in microhenrys (μH)
N = number of turns
R = radius of coil in inches (Measure from the center of the coil to the middle of the wire.)
H = height of coil in inches

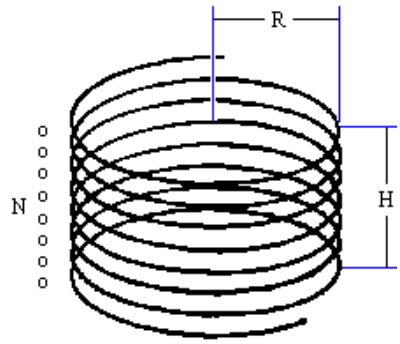

Figure F - 11: Tesla coil formulas (2/5)

Inverse Conical Coil Inductance

$$L_1 = \frac{(NR)^2}{9R + 10H} \qquad L_2 = \frac{(NR)^2}{8R + 11W}$$

$$L = \sqrt{(L_1 \sin(x))^2 + (L_2 \cos(x))^2}$$

L = inductance of coil in microhenrys (μH)
L_1 = helix factor
L_2 = spiral factor
N = number of turns
R = average radius of coil in inches
H = effective height of the coil in inches
W = effective width of the coil in inches
X = rise angle of the coil in degrees

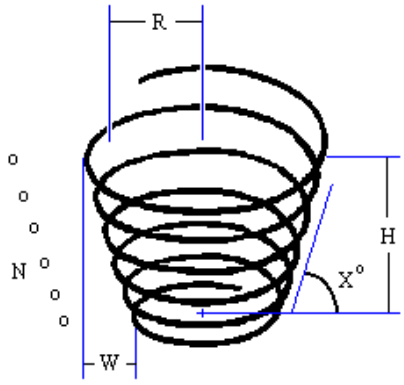

Secondary Coil Dimensions

$$L = \frac{\pi DAH}{12} \qquad T = AH \qquad A = \frac{1}{B}$$

L = length of wire in feet
D = outer diameter of coil form in inches
H = height of windings in inches
A = number of turns per inch
T = total number of turns
B = thickness of wire in inches

Medhurst

$$C = 0.29\,L + 0.41\,R + 1.94\sqrt{\frac{R^3}{L}}$$

C = self capacitance in picofarads
R = radius of secondary coil in inches
L = length of secondary coil in inches

Figure F - 12: Tesla coil formulas (3/5)

Toroid Capacitance

$$C = 1.4\left(1.2781 - \frac{D_2}{D_1}\right)\sqrt{\pi D_2(D_1 - D_2)}$$

C = capacitance in picofarads
D_1 = outside diameter of toroid in inches
D_2 = diameter of cross section of toroid in inches
This equation courtesy Bert Pool.

Sphere Capacitance

$$C = \frac{25.4R}{9}$$

C = capacitance in picofarads
R = radius in inches

Plate Capacitors

$$C = \frac{0.224KA(N - 1)}{1{,}000{,}000D}$$

C = capacitance in microfarads
K = dielectric constant
A = area of each plate in square inches
N = number of plates
D = distance between plates in inches (thickness of dielectric)

Leyden Jar Capacitors

$$C = \frac{0.224\pi KD(H + 0.25D)}{1{,}000{,}000T}$$

C = capacitance in microfarads
K = dielectric constant
D = diameter of jar in inches
H = height of jar in inches
T = thickness of jar in inches

Figure F - 13: Tesla coil formulas (4/5)

AC RMS and Peak Voltage

$E_{RMS} = 0.7071 \cdot E_P$

E_{RMS} = RMS voltage
E_P = peak voltage

Rotary Spark Gap Firings per Second

$$F = \frac{RE}{60}$$

F = firings per second (hertz)
R = motor RPM rating
E = number of rotary electrodes

Rotary Spark Gap Electrode Speed

$$S = \frac{\pi RD}{1056}$$

S = electrode speed (MPH)
R = motor RPM rating
D = diameter of electrode placement circle (inches)

Joules for L and C

Capacitance	Inductance
$J = 0.5\ V^2\ C$	$J = 0.5\ I^2\ L$

J = joules of energy stored
V = peak charge voltage
I = peak current
C = capacitance in farads
L = inductance in henries

The energy stored at any given time is : $J(t) = 0.5\ [V(t)]^2\ C$ and $J(t) = 0.5\ [I(t)]^2\ L$.

Figure F - 14: Tesla coil formulas (5/5)